

Manipulating beam propagation in slow-light media

by

Ryan Hogan

A thesis
submitted to the University of Ottawa
in partial fulfillment of the
thesis requirement for the degree of
Doctor of Philosophy
in
Physics

Ottawa, Ontario, Canada, 2023

© Ryan Hogan, Ottawa, Canada, 2023

Examining Committee

The following served on the Examining Committee for this thesis.

External Examiner: Miles Padgett
Professor, Dept. of Physics, University of Glasgow

Internal Examiners: Jeff Lundeen
Professor, Dept. of Physics, University of Ottawa
Giulio Vampa
Professor, National Research Council of Canada
Khaled Mnaymneh
Professor, Dept. of Physics, Carleton University

Other Member(s): President of the Committee
Christopher Boddy
Professor, Dept. of Chemistry and Biomolecular Sciences
University of Ottawa

Supervisor: Robert W. Boyd
Professor, Dept. of Physics, University of Ottawa

Abstract

Materials with resonant features can have a rapidly changing refractive index spectrally or temporally that gives rise to a changing group index. Depending on the wavelength of the input light, this light can see regimes of normal or anomalous dispersion. Within these regions, the group index can become large, depending on the optical effect used, and give rise to slow or fast light effects.

This thesis covers two platforms that exhibit the use of slow and fast light. Slow and fast light are used to manipulate and enhance other optical effects in question. As the focus of this thesis, we examine a rotating ruby rod and spaceplates based on multilayer stacks, both considered as slow- and fast-light media. Light propagation through each platform is modelled and simulated to compare to the experiment. The simulation results for both platforms match well with the measured experimental effects and show the feasibility and utility of slow or fast light to manipulate or enhance optical effects.

We simulate light propagation in a rotating ruby rod as a rotating, anisotropic medium with thermal nonlinearity using generalized nonlinear Schrodinger equations, modelling the interplay of many optical effects, including nonlinear refraction, birefringence, and a nonlinear group index. The results are fit to experimentally measured results, revealing two key relationships: The photon drag effect can have a nonlinear component that is dependent on the motion of the medium, and the temporal dynamics of the moving birefringent nonlinear medium create distorted figure-eight-like transverse trajectories at the output.

We observe light propagation through a rotating ruby rod where the light is subject to drag. Light drag is often negligible due to the linear refractive index but can be enhanced by slow or fast light, i.e., a large group index. We find that the nonlinear refractive index can also play a crucial role in the propagation of light in moving media and results in a beam deflection. An experiment is performed on the crystal that exhibits a very large negative group index and a positive nonlinear refractive index. The negative group index drags the light opposite to the motion of the medium. However, the positive nonlinear refractive index deflects the beam along with the motion of the medium and hinders the observation of the negative drag effect. Therefore, it is deemed necessary to measure not only the transverse shift of the beam but also its output angle to discriminate the light-drag effect from beam deflection. This work could be applied to dynamic control of light trajectories, for example, beam steering and velocimetry.

For the following two chapters, we will focus on a different slow-light platform. This platform focuses on optics that we developed and tested that compress the amount of free-space propagation using multilayered stacks of thin films known as spaceplates. We design

and characterize four multilayer stack-based spaceplates based on two design philosophies: coupled resonators and gradient descent. Using the transfer-matrix method, we simulate and extract the angular and wavelength dependence of the transmission phase and transmittance to extract and predict compression factors for each device. A brief theoretical investigation is developed to predict resonance positions, spacing, and bandwidth.

We measure the transverse walk-off to extract the compression factor of four multilayer stack-based spaceplates as a function of angle and wavelength. One of the devices was found to have a compression factor of $R = 176 \pm 14$, more than ten times larger than previous experimental records. We increased the numerical aperture of one of the devices by ten times, and we still observed a compression factor of $R = 30 \pm 3$, two times larger than the most recent experimental measurements. We also measured focal shifts up to 800 microns, more than 40 times the device size, typically 10-12 microns thick. The multilayer stack-based spaceplates we studied here show great promise for ultrathin flat optical systems that can easily be integrated into a modern-day imaging system.

Résumé

Les matériaux avec des caractéristiques résonnantes peuvent avoir un indice de réfraction qui change rapidement spectralement ou temporellement, ce qui donne lieu à un indice de groupe changeant. Selon la longueur d'onde de la lumière d'entrée, cette lumière peut voir des régimes de dispersion normaux ou anormaux. A l'intérieur de ces régions, l'indice de groupe peut devenir important, selon l'effet optique utilisé, et donner lieu à des effets lumineux lents ou rapides.

Cette thèse porte sur deux plates-formes qui présentent l'utilisation de la lumière lente et rapide. La lumière lente et rapide est utilisée pour manipuler et améliorer d'autres effets optiques en question. Au centre de cette thèse, nous examinons une tige de rubis rotative et des lames d'espace basées sur des empilements multicouches, tous deux considérés comme des milieux à lumière lente et rapide. La propagation de la lumière à travers chaque plate-forme est modélisée et simulée pour être comparée à l'expérience. Les résultats de simulation pour les deux plates-formes correspondent bien aux effets expérimentaux mesurés et montrent la faisabilité et l'utilité de la lumière lente ou rapide pour manipuler ou améliorer les effets optiques.

Nous simulons la propagation de la lumière dans une tige de rubis en rotation en tant que milieu anisotrope en rotation, avec une non-linéarité thermique à l'aide d'équations de Schrödinger non linéaires généralisées, modélisant l'interaction de nombreux effets optiques, notamment la réfraction non linéaire, la biréfringence et un indice de groupe non linéaire. Les résultats sont adaptés aux résultats mesurés expérimentalement révélant deux relations clés: l'effet de traînée de photons peut avoir une composante non linéaire qui dépend du mouvement du milieu, et la dynamique temporelle du milieu non linéaire biréfringent en mouvement crée une distorsion transversale en forme de huit. trajectoires en sortie.

Nous observons la propagation de la lumière à travers une tige de rubis en rotation où la lumière est soumise à une traînée. La traînée lumineuse est souvent négligeable en raison de l'indice de réfraction linéaire, mais peut être améliorée par une lumière lente ou rapide, c'est-à-dire un indice de groupe important. Nous trouvons que l'indice de réfraction non linéaire peut également jouer un rôle crucial dans la propagation de la lumière dans les milieux en mouvement et se traduit par une déviation du faisceau. Une expérience est réalisée sur le cristal qui présente un très grand indice de groupe négatif et un indice de réfraction non linéaire positif. L'indice de groupe négatif entraîne la lumière à l'opposé du mouvement du milieu. Cependant, l'indice de réfraction non linéaire positif dévie le faisceau avec le mouvement du milieu et gêne l'observation de l'effet de traînée négatif. Par conséquent, il est jugé nécessaire de mesurer non seulement le décalage transversal du

faisceau mais également son angle de sortie pour discriminer l'effet de traînée lumineuse de la déviation du faisceau. Ces travaux pourraient être appliqués au contrôle dynamique des trajectoires lumineuses, par exemple, l'orientation du faisceau et la vélocimétrie.

Pour les deux chapitres suivants, nous nous concentrerons sur une plate-forme de lumière lente différente. Cette plate-forme se concentre sur l'optique que nous avons développée et testée et qui comprime la quantité de propagation dans l'espace libre à l'aide d'empilements multicouches de couches minces appelées lames d'espace. Nous concevons et caractérisons quatre lames d'espace multicouches basées sur des piles basées sur deux philosophies de conception; Résonateurs couplés et descente de gradient. À l'aide de la méthode de matrice de transfert, nous simulons et extrayons la dépendance angulaire et en longueur d'onde de la phase de transmission et de la transmittance pour extraire et prédire les facteurs de compression pour chaque appareil. Une brève étude théorique est développée pour prédire les positions de résonance, l'espacement et la bande passante.

Nous mesurons le walk-off transversal pour extraire le facteur de compression de quatre lames d'espace multicouches en fonction de l'angle et de la longueur d'onde. L'un des appareils s'est avéré avoir un facteur de compression de $R = 176 \pm 14$, plus de dix fois supérieur aux enregistrements expérimentaux précédents. Nous avons multiplié par dix l'ouverture numérique de l'un des appareils, et nous avons tout de même observé un facteur de compression de $R = 30 \pm 3$, deux fois supérieur aux mesures expérimentales les plus récentes. Nous avons également mesuré des décalages focaux jusqu'à 800 microns, soit plus de 40 fois la taille de l'appareil, généralement de 10 à 12 microns d'épaisseur. Les lames d'espace multicouches à base de piles que nous avons étudiées ici sont très prometteuses pour les systèmes optiques plats ultra-minces qui peuvent facilement être intégrés dans un système d'imagerie moderne.

Acknowledgements

Firstly, I wish to thank my supervisor, Prof. Robert W. Boyd, for his gracious support and his guidance throughout my pursuit of a doctorate degree in physics. The candor that he has brought to each and every one of our meetings has always been a breath of fresh air. He encouraged me to be inquisitive and study topics in a scientifically sound but wonderful way. His joy for physics is truly unmatched, and I am glad that I was able to work under his supervision. I would have not had the chance to travel and share my work and also participate in group retreats all around Canada if it wasn't for him. It was also a great pleasure of mine to have had the opportunity to study nonlinear optics directly from the author himself. It was an honor to work in Bob's group among many great physicists, and I believe that this allowed me to succeed in my endeavors at the University of Ottawa.

I would also like to thank Prof. Jeff Lundeen for allowing me to collaborate on the spaceplate project. It was through this collaboration that I received valuable advice and countless resources on how to write articles, have good organizational skills, and how to do good science overall. It was a pleasure working with Jeff, and our work together has now become an integral part of my thesis. I am very appreciative of the time and effort that Jeff has given to help me. I very much appreciate Jeff allowing me to conduct research in his lab and use the equipment readily available throughout to see the project through.

I would like to extend thanks to Dr. Jeremy Upham. He has helped me navigate the interweaving pathway that extends to all of the requirements of a Ph.D. Jer has been there to see to the many managerial tasks that often go unnoticed in the works. Whether it be putting me in contact with the right person, advice on the troubles of a project, or just day-to-day conversations that create a pleasant work environment, Jer has helped in creating a space that has kindled my progress throughout the years of my Ph.D. I am also appreciative of his efforts and advice toward our work together. My projects would have not reached their full potential without his help.

I would like to thank my collaborator Orad Reshef. His advice, both professionally as a colleague and personally as a friend, has been greatly appreciated. I would also like to thank my other collaborators, Boris Braverman, Akbar Safari, and Giulia Marcucci, for their guidance and advice to see through our work together. Their demeanor toward my progression as a Ph.D. student has made me into a well-rounded scientist with a variety of skill sets. With each their own experimental and analysis preferences, I have become adept in many languages and learned many interesting experimental and theoretical techniques that I will keep close in the future. This thank you also extends out to my other friends and colleagues that I've met over the years. Each and every person has made my academic

development richer and the environment in which it was done more fun, leading to the success of my degree.

I'd also like to thank everyone who read my thesis and gave me insightful suggestions and comments, particularly Akbar Safari, Boris Braverman, Girish Kulkarni, Orad Reshef, Varun Sharma and Xiaoqin Gao.

I would like to acknowledge the indigenous community that has supported me throughout my years as an academic. They have seen me through my many years of school and had faith that I would one day be successful in leading another generation of indigenous students in the future. Therefore, to pay respects, I would like to acknowledge that my Ph.D. work was done at the University of Ottawa, which is situated on the unceded land of the Algonquin and Anishinaabe People.

I would like to acknowledge my fiancée Xiaoqin Gao. Without her endless help, advice, and suggestions, I wouldn't be here writing this thesis. Her love has not only supported me emotionally but has given me the drive to complete my Ph.D. Through the good and bad, she has been by my side and pushed me to be my best. This acknowledgment is ever deserving, and I am truly happy that I can share my successes and my life with her.

Finally, I would also like to acknowledge my dad and my grandmother for supporting me all through my academic career. The support to see me through leaving my hometown and pursuing further education is felt each and every day. Their love and support allowed me to continue in a field that I love and reach the goals that I wish to attain in the future.

Dedication

This is dedicated to the one I love, Xiaoqin Gao. I have never met such a heartwarming, and intelligent person and I am truly happy that she is by my side. She has helped me achieve success on many occasions during my Ph.D., and I wouldn't want to share it with anyone else except her. She is the love of my life, and this is all possible with her love and care.

Table of Contents

List of Tables	xiv
List of Figures	xv
List of Publications	xxxi
1 Introduction	1
1.1 Motivation of Slow Light	1
1.2 Wave Theory	2
1.2.1 Maxwell's Equations	3
1.2.2 Wave Equation: Linear to Nonlinear	4
1.3 Nonlinear Refraction	7
1.4 Dispersion	10
1.4.1 Wave Properties	10
1.5 Nonlinear Schrödinger Equation	13
1.6 Slow Light and its Applications	15
1.6.1 Kramers-Kronig Relations	16
1.6.2 Slow-Light Media	17
1.6.3 Optical Effects for the Creation of Slow-Light	18
1.7 Thesis Outline	20

2	Photon Drag Theory and Nonlinear Propagation	22
2.1	Background	22
2.2	Photon Drag Theory	24
2.2.1	Linear Drag	24
2.2.2	Nonlinear Drag	26
2.3	Media in Rotation	27
2.3.1	Rotation and Anisotropy	28
2.3.2	Electric Fields in Rotating Media	31
2.3.3	Nonlinear Group Index Contributions to NLSE	38
2.4	Influence of Nonlinear Group Index	40
2.4.1	Definition of the Nonlinear Group Index of the COI	40
2.4.2	Rotation Speed and Intensity Dependence of Nonlinear Group Index	40
2.4.3	Thermal Nonlinear Response	45
2.5	Simulation Methods	48
2.5.1	Linear and Nonlinear Propagators	48
2.6	Simulation Results	50
2.6.1	Fields along Propagation in Space and Time	50
2.6.2	Birefringence and the Associated Trajectories	54
2.6.3	Trajectories of the COI	54
2.6.4	Transverse Shifts at the Crystal Output	57
2.7	Summary	57
3	Photon Drag, Nonlinear Deflection, and Nonlinear Refraction	59
3.1	Background	59
3.2	Methodology	62
3.3	Results	63
3.3.1	COI Trajectories	63
3.3.2	Transverse Shift	69

3.3.3	Transverse Shift at Different Longitudinal Positions	71
3.3.4	Fitting Function for Effective Group Index	75
3.3.5	Townes Profile and Calculation of Nonlinear Refractive Index	77
3.4	Summary	80
4	Theory and Design of Multilayer Stack-Based Spaceplates	81
4.1	Background	82
4.1.1	Basic Theory of Spaceplates	82
4.1.2	Lens Phase vs. Spaceplate Phase	84
4.1.3	Types of Spaceplates	84
4.2	Transfer Matrix Method	86
4.2.1	Interface Matrix	89
4.2.2	Propagation Matrix	91
4.3	Device Design	93
4.3.1	Ideal Spaceplate Phase	93
4.4	Characterization of Spaceplates	98
4.4.1	Design Philosophies	98
4.4.2	TMM Characterization of Devices	101
4.4.3	Spectral Response of Devices	109
4.5	Group Velocity and Group Delay in Spaceplates	111
4.6	Summary	113
5	Experimental Observation of Spatial Compression using Multilayer Stack-Based Spaceplates	114
5.1	Background	115
5.2	Methodology	117
5.2.1	Design and Characterization	117
5.2.2	Experimental Setup	120

5.2.3	Measured Transmittance	122
5.3	Results and Discussion	123
5.3.1	Angular Dependence of Transverse Walk-off	123
5.3.2	Wavelength Dependence of Compression Factor	127
5.3.3	Focal Retraction and Imaging	127
5.3.4	Full Description of Transverse Walk-off	130
5.4	Summary	133
6	Conclusion and Outlook	134
6.1	Conclusion	134
6.2	Outlook	137
	Bibliography	139

List of Tables

2.1	Results of the phenomenological fit for the n_g^{NL}. Fit variables for the expressions in Eq. (2.59) in the nonlinear ($P = 100$ mW, $I = 3.3 \times 10^4$ W/cm ²) and highly nonlinear ($P = 520$ mW, $I = 6.4 \times 10^5$ W/cm ²) regimes for low-to-mid speeds ($\Omega = 5 \sim 100$ deg/s) and mid-to-high speeds ($\Omega = 100 \sim 9000$ deg/s) are shown.	44
2.2	Summary of the relevant variables used to calculate the index gradient Δn_{NL} due to a thermal nonlinearity. The definition of the variables is used to clarify the function of each variable within the derivative.	47
3.1	Results of the fitting parameters are shown for the highly nonlinear regime. a, b, c, d, f, g and h for the effective group index in the highly nonlinear ($P_0 = 520$ mW) regime for all rotation speeds ($\Omega = 1 \sim 9000$ deg/s). We fit a continuous function consisting of two exponentials and a constant offset of the form: $f(\Omega) = a - be^{-\Omega/c} + de^{-\Omega/f}$	76
5.1	Device parameters for four devices: CR1 and CR2 comprise integer-valued multiples of quarter-waves for low and high index layers represented as L and H , respectively, and two other devices of an alternating index, with thicknesses determined by gradient descent. The number of unit cells indicates the repetition count of the unit cell. The compression factor denotes the effective to the real device length ratio. The number of layers is indicated with a star for the gradient descent devices. The device's angular range is also displayed. Note that all devices are quoted for p -polarized light, although s -polarized light exhibits comparable performance in a limited angular range of $\theta_{\text{device}} \leq 10^\circ$	119

List of Figures

1.1	Schematic of the spectral response of the absorption α, the refractive index n, and the group index n_g. By Kramers-Kronig, the Lorentzian lineshape in the absorption spectrum gives the swing in the refractive index. This variation in the refractive index will give a non-zero slope and, therefore, a variation in the group index. The region in red for the group index shows a region of normal dispersion and slow light behaviour. The blue region, on the other hand, shows anomalous dispersion and a fast-light effect. These slow and fast light regions can enhance the light-matter interaction in specific spectral regions.	19
2.1	Schematic of the linear, transverse photon drag effect. A beam of light passing through an isotropic, lossless medium of length L , moving transversely with speed v , gets laterally shifted by Δy due to a small angle deviation, θ	25
2.2	A laser beam incident on a rotating medium far from the center of rotation. Far from the center, the beam experiences the tangential component of the velocity in the direction according to the sign of the angular velocity, Ω , that rotates about the z -axis. Two frames of reference are also shown. The lab frame is shown in (x, y, z) and the crystal frame is (x', y', z') . 27	27
2.3	Schematic of two different frames of reference. The reference frames are laboratory (x, y, z) and crystal (x', y', z') . The wave vector comes in at an angle θ in the xz plane. The reference frames become tilted by Ωt , where Ω is the rotation speed, and t , time, and γ , the crystal orientation with respect to the optic axis. Ωt shifts the coordinates in xy plane, and γ in xz plane.	30

2.4	The refractive index ellipsoid in the lab's frame. Four refractive indices are labeled on the ellipsoid, n_o as a projection onto the z -axis, n_e , which is equal to the length from O to N , defined as \overline{ON} , and $n_{e,1}$ and $n_{e,2}$ defined in Eq. (2.22). The point N is on the edge of the index ellipsoid such that \overline{ON} is perpendicular to \vec{k} , and therefore corresponds to the point at which the refractive index is n_e	33
2.5	Transverse movement of the ordinary (o) and the extraordinary (e) beam upon rotation and the walk-off angle β. The o-beam propagates straight through the crystal, while the e-beam revolves around it in a circular pattern. Also depicted schematically is the centre of intensity (COI) of their intensities, tracing out figure-eight-like patterns for the linear dynamics of the system.	35
2.6	Schematic optical beam distributing heat over a rotating ruby rod crystal face. The heat distribution circles about the crystal cause an index gradient with varying magnitude depending on speed. The heat reaches different distances depending on the rotation speed until it reaches fully around the crystal, producing a smaller magnitude of index gradients at higher rotation speeds. The distribution can also reach a steady-state-like response where the heat is equally distributed.	42
2.7	Schematic of curved trajectory induced by a moving index gradient created by the nonlinear refraction. (a) shows the trajectory at very slow speeds, (b) shows the largest transverse shift around $\Omega = \Omega_c$, and (c) shows a smaller transverse shift at high speeds.	44

2.8	Numerical results for propagation and rotation effects on the electric field distribution.	The total electric field of the o- and e-beams is plotted for three z -positions, $z = L/3$ cm, $z = 2L/3$, and $z = L$, where $L = 2$ cm, and over eight different frames along the rotation in time for a rotation speed of $\Omega = 100$ deg/s for three regimes: (a) Linear ($P = 0.2$ mW), (b) Nonlinear ($P = 100$ mW) and (c) Highly Nonlinear ($P = 520$ mW). Nonlinear effects can be observed leaving imprinted beams when the input power is sufficiently high $P > 100$ mW. The field trajectories widen with increasing power due to the nonlinear deflection as a result of the nonlinear group index. For a given z , the time evolution shows beam rotation in the xy plane. Field structure is complicated for the o- and e-beams overlapped, and therefore, the centre of intensity is favourable to track the dynamics, seen in Fig. 2.10. For a given t , the field evolution increases in size and moves more in the xy plane with higher powers. The field value is maximum in the yellow regions and zero in the dark blue. The faint beam seen in the highly nonlinear regime is an index gradient imprinted on the crystal.	52
2.9	Simulated transverse trajectories of the o- (blue) and e- (red) beams for three input powers at positive/negative low/high rotation speeds.	Linear regime shows no transverse shift drag in either beam for different speeds, while nonlinear and highly nonlinear regimes show increasing shifts for a given speed. The amount of shift is seen more clearly in the o-beam movement. At the same time, the e-beam shows deviations from a circular trajectory, which is due to the nonlinear response of the system. Opposite speeds show opposing translations of each beam.	53
2.10	Transverse trajectories for three input powers and three input speeds (a) $\Omega = \pm 10$ deg/s, (b) $\Omega = \pm 100$ deg/s, and (c) $\Omega = \pm 9000$ deg/s.	Simulated curves for the linear ($P = 0.2$ mW) regime show a figure-eight-like trajectory for the COI, while nonlinear ($P = 100$ mW) and highly nonlinear ($P = 520$ mW) regimes show deviations from a figure-eight, as well as transverse shifting along y . Blue and orange curves correspond to positive and negative rotation speeds, respectively.	55

2.11	The transverse shift in the nonlinear and highly nonlinear regime for various rotation speeds. The distribution shows a log-normal-like distribution about $\Omega = 100$ deg/s. The phenomenological fit (dashed lines) suggests a peak closer to $\Omega = 150$ deg/s, while the simulation values suggest $\Omega = 100$ deg/s. About the peak rotation speed, considered as some characteristic rotation speed of the system, the amount of shift drops exponentially. The exponential behaviour is comprised of both optical and thermal nonlinear response and is modelled using the nonlinear group index discussed in Sec. 2.4.2. Several points are highlighted along the curve for comparison of the amount of drag when considering different input powers. These shifts are taken as half the difference between positive and negative rotation speeds.	56
------	--	----

3.1	Schematics of the dynamics in the system. (a) A schematic showing laser beam propagation in i) a stationary medium versus ii) a moving medium which exhibits a transverse shift of Δy . For simplicity of illustration, we show the laser beams as pulses. (b) The edge of a rotary ruby rod is used to achieve an approximately linear motion in the $-y$ ($+y$) direction when the crystal rotates clockwise (counterclockwise). (c) A single frame imaged at the input face of the crystal ($z = -2$ cm) that shows the o- and e-beams propagated through the 2-cm-long ruby crystal. (d) A diagram showing the trajectories of o- and e-beams at different crystal orientations highlighting each beam's intensity change at 45-degree intervals. The red "x" shows the centre of intensity (COI) position for different crystal orientations, highlighting the emergence of a figure-eight-like pattern. In contrast, o- and e-beams are shown by green and blue dots, respectively, with varying transparency to signify their relative intensities.	60
-----	--	----

3.2	Experimental setup for measurement of transverse shifts.	A 520 mW continuous-wave laser beam at 473 nm is focused using a 100 mm focal length plano-convex lens L_1 to a spot size of 20 μm onto the input face of a rotating ruby rod. The rod spins around its axis, driven by a stepper motor. The laser beam at the output of the crystal is imaged onto a CCD camera with unity magnification using a 4-f system consisting of two lenses L_2 and L_3 of focal length $f = 150$ mm. The CCD camera captures the beam, with a frame rate of 1000 fps, as the stepper motor is rotated at various speeds. An ND filter is placed between the dielectric mirror and lens L_2 for nonlinear measurements and between L_1 and the ruby for linear measurements. The CCD camera images at different z -positions using a translation stage. Measurements are taken at $z = 0$, $z = 0.762$ cm, and $z = 1.524$ cm to measure the transverse shift, as well as the output angle of the beam as it exits the crystal. Input beam power was controlled by a half-wave plate and a polarizing beam-splitter before the ruby crystal. (M: Mirror, HWP: Half-wave plate, PBS: Polarizing beam-splitter, BD: Beam dump, L_1 : Plano-convex lens [$f = 100$ mm], L_2 : Plano-convex lens [$f = 150$ mm], L_3 : Plano-convex lens [$f = 150$ mm], FF: Fluorescence filter, DM: Dielectric mirror, ND: Neutral density filter [O.D. 1], and a CCD: Charge-coupled device.)	62
3.3	(a) Measured COI trajectories in linear ($P_0 = 0.2$ mW) regime. (b) Simulated COI trajectories in the linear regime. Legend of different rotation rates (deg/s) applies to (a) and (b). Looking into the beam, (counter) clockwise rotation speeds are (negative) positive. No significant shift is observed in y for trajectories at different speeds because the group index and the nonlinear refraction are negligible.	64	
3.4	(a) Measured COI trajectories in nonlinear ($P_0 = 100$ mW) regime. (b) Simulated COI trajectories in the nonlinear regime. Legend of different rotation rates (deg/s) applies to (a) and (b). Trajectories at low speeds are distorted due to the index gradient formed by each beam at its respective max intensity. The gradient diminishes at high speeds, and thus, the figure eights are recovered but transversely shifted from one another based on the nonlinear deflection for a given rotation speed.	65	

3.5	Experimentally measured (a) and simulated (b) COI trajectories in the nonlinear regime (input laser power of 520 mW) for different rotational speeds (Ω) in units of deg/s.	At low speeds, trajectories are significantly distorted and have similar paths to the 100 mW results but with more distortion due to stronger nonlinear coupling between the beams. At high speeds, the coupling between the beams is weaker due to the finite response time of the medium. For slow speeds, $\Omega \leq 100$ deg/s, the trajectories are very noisy, and no discernable pattern is easily observed. This behaviour is mainly due to the thermal gradient impressed on the crystal by the intense illumination, and therefore, the transverse beam shape is drastically modified.	66
3.6	Experimental and simulated amount of shift in the beam's transverse position at the end of the crystal for 0.2 mW, 100 mW, and 520 mW input beam laser power.	The measured shift for the linear regime (i.e., $P_0 = 0.2$ mW) for both experiment and simulations is multiplied by a factor of 10, showing no discernible deviation from zero shift. The magnitude of the transverse shift is shown against the magnitude of the rotation speed. This shift is calculated between the position with no rotation, i.e. $\Omega = 0$ deg/s, and the respective transversely shifted position. Simulations are plotted using dotted lines in green and red for the nonlinear and highly nonlinear regimes for better comparison to experimental data. The fits were based on a phenomenological exponential function in Eq. (3.2). The fit is not a perfect match due to the simulated nonlinear response of the material acting on the beams upon propagation through the crystal. . .	67
3.7	Power dependence of experimental and simulated transverse shifts.	The evolution of the transverse shift with power for various rotation speeds is shown for both experiment and simulation.	68
3.8	Schematic showing the three positions imaged by translating a CCD fast camera.	With a frame rate of 1000 frames/s, we measure three positions moving away from the output face of the crystal by using a 4-f system of lenses 2 and 3. A single frame of a video of the beam at the output face (i.e. $z = 0$ mm) is shown in the inset of which the COI is taken to show the movement of the COI and the amount the beam is dragged over many frames. The frame shows a single large beam encompassing the o- and e-beams. The two beams expand significantly upon propagation through 2 cm in the ruby crystal, so they are no longer distinguishable on the camera.	70

3.9	Measurement of the output angle versus input power and rotation speed.	(a) a schematic showing the output beam's angle after leaving the crystal. The nonlinear response of the crystal changes the angle at the interface of the crystal output face and, therefore, changes the propagation pathway. (b) The output angle and its uncertainty are calculated from the beams' transverse positions measured at three points along the z -axis ($z = 0$, $z = 0.762$ cm, and $z = 1.524$ cm). The output angle increases as the laser's power increases, as expected from nonlinear deflection.	72
3.10	Experimentally measured transverse shift in nonlinear ($P_0 = 100$ mW), and highly nonlinear ($P_0 = 520$ mW) regimes at different z-positions.	Measurements were taken at $z = 0$, 7.62 mm, and 15.24 mm to calculate the output angle. The transverse shift approaches $\Delta y = 10 \sim 15$ μm for an input power $P_0 = 100$ mW, and $\Delta y = 60$ μm for $P_0 = 520$ mW. The curve takes shape similar to a log-normal distribution, but is modelled as the sum of two decaying exponentials with different decay rates centred around a rotation speed of $\Omega = 100$ deg/s.	73
3.11	Extrapolation of transverse shift for input laser powers of $P_0 = 100$ mW, and $P_0 = 520$ mW.	Evolution of the amount of transverse drag at three points, including the crystal output face, and two positions hereafter, as shown in Fig. 3.8. The extrapolation of these points in the highly nonlinear regime ($P_0 = 520$ mW) also shows a linear dependence on the transverse shift as the propagation distance increases, consistent with a straight-line propagation of the COI. The difference from the nonlinear regime is the magnitude of the slopes is much larger due to a larger nonlinear response in the system for input powers of 520 mW. One could extrapolate these curves as a linear regression back to the crystal input face $z = -20$ mm and see that the value does not reach zero. It is clear in the range of speeds from $\Omega = 50 \sim 1000$ deg/s, where the value would be non-zero at the crystal input face, and thus a nonlinear trajectory is suspected.	74

3.12 A continuous fitting function consisting of the sum of two exponentials. The transverse shift is plotted for the highly nonlinear regime $P_0 = 520$ mW for three positions along z : $z = 0$ (blue), $z = 7.62$ mm (yellow), and $z = 15.24$ mm (green). Similar behaviour can be seen in the case of an input power of $P_0 = 100$ mW with transverse shifts of smaller magnitude. The form of the fitting function is $f(\Omega) = a - be^{-\Omega/c} + de^{-\Omega/f}$, where a , b , c , d , and f are fitting constants. One can see that the maximum drag should be closer to $\Omega_c \approx 150$ deg/s, while discrete points in Fig. 3.11 suggest 100 deg/s. It is clear that the two exponentials indeed fit the discrete points from low to high rotation speeds and provide strong evidence that the transverse shift scales with a sum of exponentials.

75

3.13 The effect of input beam power on beam shape in a stationary medium for a beam waist of 3 mm. Four powers are shown (a) $P_0 = 10$ mW, (b) $P_0 = 12$ mW, (c) $P_0 = 398$ mW, and (d) $P_0 = 520$ mW, where the blue ($P_0 = 10$ mW) and cyan ($P_0 = 12$ mW) curves do not meet the threshold power to show nonlinear refraction and thus self-focusing. Increasing laser power causes the input beam to self-interact and self-focus, creating a spatial soliton. This solitonic behaviour is seen in the yellow ($P_0 = 398$ mW) and red ($P_0 = 520$ mW) curves, which are significantly more intense and show a change to the beam's transverse profile. One can see that moderate intensity ($P_0 = 398$ mW) shows slightly less self-focusing than the red curve ($P_0 = 520$ mW). The red curve approaches a stable solitonic-type solution known as the Townes Profile. The tapering and stabilization of the beam waist for a Gaussian beam due to a self-focusing nonlinearity is a well-known characteristic of spatial solitons. The Townes profile observation here indicates a considerably large nonlinear index in the system at an input wavelength of $\lambda_0 = 473$ nm. A lens does not focus the beam in this case and is the straight output of the laser with a beam diameter of 3 mm. Townes profile formation with CW lasers is uncommon as most soliton solutions are formed using pulsed lasers that need sufficiently long propagation distances to stabilize.

78

4.1	A schematic of how an SP device of thickness d acts as an effective distance of free space propagation, d_{eff}. The distance w represents the lateral shift over a certain distance propagated in free space where the angle of the input ray, θ , is conserved for both free space and the SP. The distance between an apparent ray, in dashed lines, and the actual ray is the transverse walk-off, Δx	83
4.2	Schematics of the incident, reflected and transmitted fields for (a) a single interface and (b) a multilayer stack interface. An incident field \vec{E}_i interacts with a surface at an angle θ_i for the normal, and creates a reflected field \vec{E}_r , at angle $\theta_r = \theta_i$, and a transmitted field \vec{E}_t , at an angle θ_t . For a single interface of infinitely thin thickness, the interaction is governed by Snell's Law in Eq. (4.7) relating the refractive indices n_1 and n_2 and the angles θ_i, θ_r , and θ_t . The fields are related by Fresnel coefficients, discussed in Eqs. (4.8)- (4.11). For a multilayer stack, the stack is described by a matrix, M , calculated using TMM to relate the inward and outward fields discussed in more detail later in the chapter. Propagation and interface matrices can be defined in between layers i and $i + 1$, which will be used to calculate the full matrix M of the device.	88
4.3	Fitting an ideal SP phase to the transmission phase of a device. Phase is shown over the full angular range of $\theta = 0 \sim 90^\circ$ and a smaller region $\theta = 0 \sim 5^\circ$ for both s - and p -polarization. The smaller angular range allows for a better fit to the device's phase and, therefore, provides a correct quantification of the compression factor for this given device.	94
4.4	A schematic of the transverse walk-off for a given incident angle θ. The measured transverse walk-off Δx_{sp} comprises components of the addition of the apparent walk-off, Δx and the SP walk-off, $\Delta x'_{sp}$ [1].	95
4.5	A schematic of the evolution of the transverse walk-off for an SP. Spatial compression is witnessed in the blue region, denoted SP region. The device's NA, $\pm\theta_{\text{device}}$, is set based on the region between where the slope of the transverse walk-off goes to zero. $\Delta x_{\text{max/min}}$ show the maximum and minimum transverse walk-off measured within the SP region. The yellow regions show a region where R starts to decrease from its maximum value until the device reaches a zone where it is no longer spatially compressing but acting larger than its given size, indicated in red. This region is usually seen after $\pm 2\theta_{\text{device}}$	96

4.6	<p>Schematic representation of a Gaussian beam waist evolution for three cases for a beam with a waist $w_0 = 10 \mu\text{m}$. The beam waist evolution of free space is plotted in black, and the waist is situated at $z = 0$. The evolution of beam waist for a 3 mm thick piece of glass is shown in red and for a 10 μm thick SP ($R = 80$) in blue. These two cases for a piece of glass and an SP highlight the focal advance and retraction, respectively. The advance in focus is denoted as ΔF_{gl}, and the focal retraction is denoted ΔF_{sp}.</p>	97
4.7	<p>Unit cells of two SP devices using a coupled resonator approach. The unit cell in (a) is repeated four times, resulting in three peaks in the wavelength dependence of the transmittance for device CR1. The unit cell in (b) is repeated eight times, resulting in seven peaks in the wavelength dependence of the transmittance for device CR2. The resonance peaks result from interference of multiple cavities formed in the device, and the amount of peaks is governed by $n - 1$ unit cells. $n_H > n_L$, where n_H are the blue layers, and n_L are the orange layers.</p>	99
4.8	<p>Unit cells of two SP devices using gradient descent. (a) shows a design (MS1) with a moderate angular range ($\theta \pm 10^\circ$), and a modest compression factor ($R = 18$), while (b) shows a design (MS2) with a small angular range ($\theta = \pm 1^\circ$) and a large compression factor ($R = 238$).</p>	101
4.9	<p>An example of the simulated characterization methods for an SP (CR1) is shown. (a) shows transmission phase calculated from TMM is plotted in blue and fitted to an ideal SP phase (See. Eq. (4.27)). The device is fit over $\theta = 3.5^\circ$; however, the fit is shown for twice that range. (b) shows the transmittance as a function of angle. The inset in the plot shows the device that is characterized, showing one unit cell comprised of varying layer thicknesses and alternating low/high index. (c) shows the transmittance as a function of wavelength, where five resonance peaks are shown. The unit cell in b) is repeated eight times, resulting in seven peaks in the wavelength dependence of the transmittance; however, only five are shown near the operating range of the laser. The resonance peaks result from coupling because the cavity is formed in the device, and the amount of peaks is governed by $n - 1$ unit cells. (d) shows the corresponding compression factor as a function of wavelength.</p>	102

4.10	<p>An example of the simulated characterization methods for an SP (CR2) is shown. (a) shows the transmission phase calculated from TMM plotted in blue and fitted to an ideal SP phase. The operating angular range of the device is $\theta = \pm 1^\circ$. (b) shows the transmittance as a function of angle. The inset in the plot shows the device that is characterized, showing one unit cell comprised of varying layer thicknesses and alternating low/high index. (c) shows the transmittance as a function of wavelength, where three resonance peaks are shown. The unit cell in (b) is repeated four times, resulting in three peaks in the wavelength dependence of the transmittance. The resonance peaks result from coupling because the cavity is formed in the device, and the amount of peaks is governed by $n - 1$ unit cells. (d) shows the corresponding compression factor as a function of wavelength. The resonant features are more narrow due to a large compression factor.</p>	105
4.11	<p>An example of the simulated characterization methods for an SP (MS1) is shown. (a) shows the transmission phase, TMM in blue, and the ideal SP phase in red. The device is fit over $\theta = 10^\circ$. (b) shows the transmittance as a function of angle. (c) shows the transmittance as a function of wavelength, where one peak with a much larger bandwidth is shown, compared to the central peak of CR1 and CR2. (d) shows the corresponding compression factor as a function of wavelength. The maximum compression factor was found to be $R = 40$, roughly two times the size of the predicted R by gradient descent.</p>	106
4.12	<p>An example of the simulated characterization methods for an SP (MS2) is shown. (a) shows the transmission phase, TMM in blue, and the ideal SP phase in red. The device is fit over $\theta = 1^\circ$. (b) shows the transmittance as a function of angle. (c) shows the transmittance as a function of wavelength, where one peak with a more narrow bandwidth is shown, compared to CR1 and CR2. (d) shows the corresponding compression factor as a function of wavelength. The maximum compression factor was $R = 238$, matching the predicted R by gradient descent.</p>	107
4.13	<p>Spectral behaviour when changing the number of unit cells for CR2. (a)-(d) shows a long range spectral response of CR2 with increasing amount of unit cells from $n = 1$, to $n = 4$. (e)-(h) show only the region near the design wavelength of $\lambda = 1.55 \mu\text{m}$ with an increasing amount of unit cells according to (a) through (d). Peaks present resonance locations according to constructive and destructive interference positions, with the number of peaks determined by $n - 1$ unit cells.</p>	108

4.14	Transmittance for devices MS2 and MS1 are plotted around their design wavelengths and over a larger range. (a) shows the design range of MS2, while (b) shows an extended range with rich, resonant features in lower and higher wavelengths. (c) shows the design range of MS1, while (d) also shows an extended range with rich, resonant features in lower and higher wavelengths, but features are much more narrow than MS1. This reflects the sharp feature seen around the design wavelength.	110
5.1	Schematic of beam propagation for three different cases. A different focal plane is shown in the case of a beam propagating (a) in free space, (b) through a tilted 3-mm long piece of glass, (c) through a tilted 10- μm multilayer stack based SP, and (d) the combined tilted system comprised of the glass and the SP. With respect to the imaging plane of free space, the glass advances the focus and positively shifts the beam to a different transverse position. The focus retracts in the case of the SP, and the beam negatively shifts in the transverse plane. The combined system shows that a 10 μm SP can undo the effects of the glass slide, leading to an unaffected beam.	115
5.2	Characterization methods for an SP. (a) Transmission phase calculated from TMM is plotted in blue and fitted to an ideal SP phase in red. The device is fit over the SP region shown in light blue. (b) Transverse walk-off is calculated from the derivative of the phase in (a). (c) Transmittance as a function of angle is plotted and maximized over the SP region. (d) The corresponding SP multilayer stack unit cell is shown with low (n_L) and high (n_H) refractive indices layers quarter-wave thickness. The device consists of a unit cell repeated four times, creating a coupled resonator-like response with sharp resonances that exhibit larger compression factors. (e) Transmittance as a function of wavelength is plotted, showing three resonance peaks. The number of peaks follows $n - 1$ unit cells. (f) The corresponding compression factor is shown calculated from (b) for various wavelengths. .	118

5.3 Experimental setup to measure transverse walk-off and focal shifts.

A 1.6 mW continuous-wave tunable laser at 1550 nm with a spot size of 7 mm is minified by a factor of five by a telescope consisting of two plano-convex lenses L_1 ($f = 25$ cm), and L_2 ($f = 5$ cm). The beam is then sent through a quarter wave plate (QWP) to set the input polarization, followed by a half-wave plate (HWP) and polarizing beam-splitter (PBS) to control the power. The beam is then sent through another QWP, and HWP, set such that p -polarization illuminates the sample. The QWP and HWP can have p - and s -polarization and circular polarization if needed. The beam is then focused by a plano-convex lens L_3 ($f = 25$ cm) down to a spot size of approximately $2w_0 = 310 \mu\text{m}$, with a half angle divergence of $\theta_{\text{half}} = 0.2^\circ$. At the focus, an SP is placed on a rotation mount controlled by a K-cube to measure the transverse walk-off as a function of the angle. The beam is then recollimated by another plano-convex lens L_4 ($f = 10$ cm) and refocused using a plano-convex lens L_5 ($f = 15$ cm) to be imaged on a camera situated on a translation stage with 2.54 cm range of motion, controlled by another k-cube. The imposed magnification was calibrated to be $M = 1.48$, and all measurements were scaled accordingly. Imaging measurements were done by switching L_5 for another plano-convex lens of $f = 10$ cm, imposing unity magnification. The camera is an Indium-Gallium-Arsenide (InGaAs) infrared red charge-coupled device (CCD) camera (Bobcat 320 Gig-E). The camera is placed on the translation stage to measure the beam spot size along the direction of propagation.

121

5.4 Measured transmittance of four devices. CR1 and CR2 show side peaks due to multiple resonances based on integer-valued multiples of $\lambda/4$ layer thickness. Devices MS1 and MS2 show one single resonance peak due to layer thickness based on gradient descent. Designs were simulated using the TMM centred at $\lambda_{\text{device}} = 1550$ nm. Fabrication intolerances push the actual central wavelengths λ_m to different locations, where $\lambda_{m,\text{CR1}} \approx 1547$ nm, $\lambda_{m,\text{CR2}} \approx 1531$ nm, $\lambda_{m,\text{MS1}} \approx 1562$ nm, and $\lambda_{m,\text{MS2}} \approx 1566$ nm. Devices were fabricated on top of 3 mm thick fused silica, with an anti-reflective coating on the films to minimize stress and maximize transmission. The lowest transmittance was measured to be approximately 25% at the peak of device MS2. Transmittance peaks correspond to regions of spatial compression, where the magnitude of spatial compression governs the device's resonance bandwidth and angular range [2].

122

5.5	<p>Experimentally measured transverse walk-off for glass (blue curve), SP+glass (red curve), and the SP alone (green curve). The result is shown for the device CR2, at an input wavelength of $\lambda = 1532.905$ nm, corresponding to the left peak seen in Fig. 5.2(d). The red curve, associated with an $11.51 \mu\text{m}$ thick SP on top of a 3 mm thick glass, shows no transverse walk-off over an approximately two-degree interval. The red curve shows that the effect of the small SP cancels the walk-off of a large piece of glass.</p>	124
5.6	<p>Experimentally measured transverse walk-off for all devices. Curves show transverse walk-off as a function of angle over a region larger than the SP region of four devices in (a) and different peaks of CR2 in (b). (a) The SP region of $\theta = \pm 1^\circ$ for devices CR2, and MS2, $\theta = \pm 3.5^\circ$ for CR1, and $\theta = \pm 10^\circ$ for devices CR2. Fitting the devices over their respective SP region, maximum compression factors of $R = 176$, $R = 42$, $R = 30$, and $R = 3.4$ are found for the central resonance peaks of devices MS2, CR2, MS1, and CR1, respectively. (b) Angular dependence of the transverse walk-off for the central position of each resonance peak for CR2. The left and right peaks show larger spatial compression than the central, resulting in compression factors of $R_l = 96$, $R_c = 42$, and $R_r = 49$. Simulated transverse walk-off curves are plotted in solid lines, showing good agreement with the experiment. Further study is needed to understand the compression factor scaling with observed side peaks.</p>	125
5.7	<p>Experimentally measured and simulated wavelength dependence of devices. (a) The performance of CR2, with the three maximum compression factors, observed to be $R_l = 96 \pm 2$, $R_c = 41.9 \pm 0.6$, and $R_r = 48.6 \pm 1.4$, corresponding to the left, central, and right peaks, respectively. Bandwidths of the peaks are found to be $\Delta\lambda_l = 143 \pm 4$ pm, $\Delta\lambda_c = 282 \pm 6$ pm, and $\Delta\lambda_r = 147 \pm 5$ pm. (b) The performance of MS2, reaching a maximum value of $R = 176 \pm 14$, with a bandwidth of $\Delta\lambda = 55 \pm 7$ pm. (c) The performance of MS1, reaching a maximum value of $R = 30 \pm 3$, with a bandwidth of $\Delta\lambda = 2.8 \pm 0.3$ nm. Experimentally measured compression factors (red) match the simulated results (blue) well for three devices.</p>	126

- 5.8 **Focal retraction and imaging of an SP.** The beam waist evolution is plotted against the z -position for (a) free space, (b) SP on top of glass, and (c) glass, highlighting the focus points of each. Extracting the beam waists and their positions, we plot the beam waist evolution in (d) for each case (a)-(c), as well as the predicted SP beam waist evolution (cyan). The focal retraction produced by the SP is denoted F_{sp} , from which we plot the predicted SP effect using the free space evolution shifted by F_{sp} . The corresponding images of the measured beam waist are plotted in (e), showing the focus points of each corresponding case. The top row of images is for free space, the middle row is SP on glass, and the bottom row is glass. 128
- 5.9 **The Strehl ratio of design MS2 and transverse beam profiles for CR2 and MS2.** The Strehl ratio plotted over the SP region of $\theta = \pm 1^\circ$ and over the resonance peak in wavelength in (a). Strehl ratio reached a minimum of $S = 0.86$, above the diffraction-limited threshold of 0.8. (b) and (c) show the transverse beam profile for the peak positions of devices CR2 and MS2 at normal incidence, respectively. The transverse beam profile of CR2 is unaffected, while MS2 shows some distortions in the beam profile. The distortions are likely due to thermal fluctuations that locally change the resonance response. 129
- 5.10 **Transverse walk-off spectral and angular response for CR2.** The transverse walk-off is shown for device CR2, highlighting the three resonance peaks resulting from four unit cells. The values Δx and R shown here are not scaled by the magnification and are, therefore, $M = 1.48$ larger than the value measured at the SP. The 3D representation highlights local changes in Δx , possibly due to fabrication intolerances. The spectral response corresponds to the measured linewidth in the compression factor in Fig. 5.7(a). 131

5.11 **Transverse walk-off spectral and angular response for MS2.** The transverse walk-off is shown for device MS2, highlighting one narrow resonance peak. The values Δx and R shown here are not scaled by the magnification and are, therefore, $M = 1.48$ larger than the value measured at the SP. The 3D representation highlights local changes in Δx , possibly due to fabrication intolerances. However, the design of MS2 has local changes in the phase response as a function of angle, and these are reflected in the transverse walk-off, as expected accordingly to $\Delta x \propto \frac{d\phi}{d\theta}$. The compression factor is measured as a global value over the working range of angles of the device. For a given angle, however, the value of R may be larger or smaller than the global R value. As the value is a global measure, the spectral response corresponds approximately to the measured linewidth in the compression factor in Fig. 5.7(b). 132

List of Publications

Papers

1. **R. Hogan**, A. Safari, G. Marccuci, B. Braverman, R. W. Boyd, "Beam deflection and negative drag in a moving nonlinear medium," *Optica*, 54 (10) 544-551 (2023).
2. **R. Hogan**, G. Marccuci, A. Safari, A. N. Black, B. Braverman, J. Upham, R. W. Boyd, "Modelling nonlinear propagation effects on beam deflection and negative drag," (in preparation).
3. **R. Hogan**, Y. Mamchur, D. Hutama, G. Carlow, B. T. Sullivan, O. Reshef, J. Lundeen, R. W. Boyd, "High-Compression Multilayer Stack-Based Spaceplates," (in preparation).

Conference Proceedings

1. **R. Hogan**, J. Upham, M. Z. Alam, A. Haché, R. W. Boyd, "Tuning the Dielectric Constant Zero Crossing of Vanadium Dioxide (VO₂)," 2019 Photonics North (PN), 1-2
2. O. Reshef, M. S. Bin-Alam, N. A. Chaitanya, T. Stolt, **R. Hogan**, M. Karimi, M. Z. Alam, G. Carlow, B. T. Sullivan, I. De Leon, JM Ménard, M. J. Huttunen, K. Dolgal-eva, R. W. Boyd, "Nonlinear plasmonic metasurfaces using multiresonant surface lattice resonances," 2020 Conference on Lasers and Electro-Optics (CLEO), 1-2

Chapter 1

Introduction

1.1 Motivation of Slow Light

In this thesis, the effects of slow light are studied in two different major concepts: photon drag, and spaceplates. The first application of slow light is applied to the photon drag effect [3], which is significantly enhanced when using a slow light medium. We use the large group index seen in ruby at 473 nm to try and observe negative photon drag [4]. However, due to Kramers-Kronig relations, the delayed response is due to a strong nonlinear response, particularly nonlinear refraction [5]. Nonetheless, we will provide theory and experiment to develop a thorough understanding of how nonlinear dispersion and nonlinear refraction play a key role in the propagation of beams through slow light media.

The second application utilizes slow light by tuning the group delay within a spaceplate, a direct result of the group velocity [6], which allows for a longer light-matter interaction, therefore, accumulating enough phase to mimic free space propagation [7–12]. A spaceplate is a device that replaces the space needed for an image to focus, and one can play with resonance effects and the optical properties of the material such that the input wave acquires enough phase to retract the focus [1, 13]. It has been shown that spaceplates are also considered slow-light angular media [14]. The focus of the latter half of this thesis, Chapters 4 and 5, provides a theoretical and experimental study of spaceplates, particularly comprised of thin film multilayer stacks. In structuring materials properly to have specific resonant conditions, the group index can be manipulated within that structure, enabling the large spatial compression of modern optical systems through the spaceplate effect.

Slow light is indeed a useful phenomenon in both linear and nonlinear optics. The scope of this thesis will be to exploit the utility of slow light and study fundamental concepts, as well as provide insight into an enticing technological advancement toward miniaturizing optical systems [15]. Furthermore, this thesis can serve as a stepping stone to understanding the link between slow light enhancement on optical effects and nonlinear refraction. Indeed, the two processes have commonalities and are touched on in other research areas. One field that could benefit from a fundamental understanding of the link between slow light and nonlinear refraction is epsilon-near-zero materials, in some cases now coined as time-varying media [16–18]. Time-varying media is a new way of describing a fundamental concept of slow light media, and the present thesis will provide some insight into this fundamental concept in the context of the dynamics observed in a rotating ruby rod, the focus of Chapters 2 and 3.

To understand the application of slow light overall in each of these platforms, we will build an understanding of wave propagation and the various effects that manipulate the trajectories that light can take. Therefore, we will begin the current chapter by introducing the wave equation derived from Maxwell’s equations and exploring general wave theory. We will then elaborate on linear and nonlinear propagation through wave equations and the nonlinear Schrödinger equation. From these equations, we will come to appreciate and comprehend the components that manipulate wave propagation, such as nonlinear refraction or dispersion. Moreover, we will elaborate on dispersion and its relation to slow and fast light and slow- and fast-light-enhanced optical processes.

1.2 Wave Theory

The study of light-matter interaction is a rich field in physics that spans many different phenomena, from linear to nonlinear optics. Light is an electromagnetic (EM) wave with spatially and temporally varying electric and magnetic fields. In vacuum, these fields travel at the speed of light, c , which is governed by the frequency, ω , and wave vector, k , of the light, such that $c = \omega/k$. The wave vector is inversely proportional to the wavelength of the input light, λ , such that $k = 2\pi/\lambda$, and the frequency is inversely proportional to its period T , where $\omega = 2\pi/T$. Using these wave properties, we can give the description of a monochromatic plane wave written as

$$\tilde{E} = \tilde{E}_o e^{-i(\vec{k}\cdot\vec{r}-\omega t)}, \quad (1.1)$$

where \tilde{E}_o is the amplitude of the wave, r is a vector comprised of Cartesian coordinates (x, y, z) such that $\vec{r} = x\hat{x} + y\hat{y} + z\hat{z}$, and the wave vector in 3D is $\vec{k} = k_x\hat{x} + k_y\hat{y} + k_z\hat{z}$.

Plane waves are used since any wave can be written as a superposition of plane waves. It is important to note that this field will interact with materials and respect Maxwell's equations.

1.2.1 Maxwell's Equations

Firstly, we consider how the behaviour of the electric field and the magnetic field is modified when considering a material response. Assuming that the fields have spatial and temporal variation, we write Maxwell's equations in the form presented by Boyd [19]

$$\nabla \cdot \tilde{D} = \rho, \quad (1.2)$$

$$\nabla \times \tilde{E} = \frac{-\partial \tilde{B}}{\partial t}, \quad (1.3)$$

$$\nabla \cdot \tilde{B} = 0, \quad (1.4)$$

$$\nabla \times \tilde{H} = -\frac{\partial \tilde{D}}{\partial t} + \tilde{J}, \quad (1.5)$$

where H is the magnetic field

$$\tilde{H} = \mu_0 \tilde{B} - \tilde{M}, \quad (1.6)$$

and \tilde{D} is the electric displacement

$$\tilde{D} = \epsilon_0 \tilde{E} + \tilde{P}, \quad (1.7)$$

where \tilde{P} is the linear polarization that arises in a material, and \tilde{M} is the magnetization field. We will assume no free charge, $\rho = 0$, no current density, $\tilde{J} = 0$, and there is no magnetization field, $\tilde{M} = 0$. The other undefined variables are ϵ_0 , the dielectric permittivity, and μ_0 , the magnetic permeability. These constants change based on whether they are in vacuum or in a material. In this case, we must introduce the dielectric permittivity in a material, $\epsilon = \epsilon_r \epsilon_0$, and the magnetic permeability in a material $\mu = \mu_r \mu_0$, where ϵ_r and μ_r are the relative permittivity and permeability of a given material, respectively. We know that the speed of an EM wave travelling in a vacuum is c , and this can be written as $c = \frac{1}{\sqrt{\epsilon_0 \mu_0}}$. By simple inspection, we can see that the speed of the EM wave will change when in a material, particularly $c \rightarrow v = \frac{1}{\sqrt{\epsilon \mu}}$. We introduce an important quantity in optics, $n = \sqrt{\epsilon \mu}$, known as the refractive index. One point to note is that in optical frequencies, μ is taken to be unity, and therefore $n = \sqrt{\epsilon}$. The refractive index will play a key role in the wave properties and, therefore, the propagation of waves. We will now derive the wave equation using Maxwell's equations that will be used to describe the propagation of light in a medium with a given refractive index, n .

1.2.2 Wave Equation: Linear to Nonlinear

Linear

Taking inspiration from Boyd [19], let us first take the curl of Eq. (1.3)

$$\nabla \times (\nabla \times \tilde{E}) = \nabla \times \left(-\frac{\partial \tilde{B}}{\partial t} \right) = -\frac{\partial}{\partial t} (\nabla \times \tilde{B}). \quad (1.8)$$

Assuming no current density, i.e. $\vec{J} = 0$, we can substitute Eq. (1.5) into Eq. (1.8) to find

$$\nabla \times (\nabla \times \tilde{E}) = -\mu_0 \frac{\partial}{\partial t} \frac{\partial \tilde{D}}{\partial t} = -\mu_0 \frac{\partial^2 \tilde{D}}{\partial t^2}. \quad (1.9)$$

Substituting the expression for the electric displacement, \tilde{D} in Eq. (1.7), we find

$$\nabla \times (\nabla \times \tilde{E}) = -\mu_0 \frac{\partial^2 (\epsilon_0 \tilde{E} + \tilde{P})}{\partial t^2}. \quad (1.10)$$

Regarding the right-hand side, vector identities state that $\nabla \times (\nabla \times \tilde{E}) = -\nabla^2 \tilde{E} - \nabla(\nabla \cdot \tilde{E})$. However, according to Eq. (1.2), $\nabla \cdot \tilde{E} = 0$, therefore, we find the wave equation

$$\nabla^2 \tilde{E} - \frac{1}{c^2} \frac{\partial^2 \tilde{E}}{\partial t^2} = -\frac{1}{\epsilon_0 c^2} \frac{\partial^2 \tilde{P}}{\partial t^2}. \quad (1.11)$$

Here, we can see that polarization is a driving term for the equation. Polarization is important in the scope of driving the wave equation and opens the idea of nonlinear driving terms to the wave equation. The material properties become dependent on the input field, \tilde{E} , and therefore change the driving force in the equation.

Before reaching the nonlinear expansion, we must make assumptions about the material. Let us first assume that the medium we are studying is linear, homogeneous, and isotropic. Therefore, the response to the input electric field scales linearly with the field, the material itself is the same in all directions, and the refractive index in all directions is the same. Assuming these parameters, we can write the polarization as

$$\tilde{P} = \epsilon_0 \chi \tilde{E}. \quad (1.12)$$

Here, we have introduced χ , which is the electric susceptibility, an optical property of the material (as opposed to a fundamental constant). This provides a more direct link to the

material response rather than the polarization. If we consider the electric displacement, substitute Eq. (1.12) into Eq. (1.7), we find

$$\tilde{D} = \epsilon_0 \tilde{E} + \epsilon_0 \chi \tilde{E} = \epsilon_0(1 + \chi) \tilde{E} = \epsilon \tilde{E}. \quad (1.13)$$

Therefore, the permittivity within a material, ϵ , is related the electric susceptibility χ by the relationship

$$\epsilon = 1 + \chi. \quad (1.14)$$

Up to this point, we have considered the permittivity as scalar; however, certain materials can have anisotropy that causes a directional response of the permittivity. Therefore, it is important to note that, in general, the permittivity and permeability are considered as tensors.

Nonlinear

The electric susceptibility is important to determine how strongly a material will respond to an input EM wave. Light from a laser may be sufficient to induce changes in the material response. With increasing laser power, the electric fields interacting with the material become large enough to induce nonlinear changes in the material response. The increase in power changes the polarization driving term and can be represented by taking a power expansion of the polarization with respect to the electric field. Expanding Eq. (1.12) in terms of the electric field, we find

$$\begin{aligned} \tilde{P}(t) &= \epsilon_0(\chi^{(1)} \tilde{E}(t) + \chi^{(2)} \tilde{E}(t)^2 + \chi^{(3)} \tilde{E}(t)^3 + \dots) \\ &= \tilde{P}^{(1)}(t) + \tilde{P}^{(2)}(t) + \tilde{P}^{(3)}(t) + \dots, \end{aligned} \quad (1.15)$$

where $\chi^{(1)}$ represents the linear susceptibility, and $\chi^{(2)}$, $\chi^{(3)}$ and onwards represent the nonlinear susceptibility. By inspection, it can be seen that $\tilde{P}^{(1)}(t) = \epsilon_0(\chi^{(1)} \tilde{E}(t)$, $\tilde{P}^{(2)}(t) = \epsilon_0(\chi^{(2)} \tilde{E}(t)^2$, $\tilde{P}^{(3)}(t) = \epsilon_0(\chi^{(3)} \tilde{E}(t)^3$, etc. However, the terms are usually grouped into a linear polarization term, $\tilde{P}^{(1)}(t)$ and a nonlinear polarization term $\tilde{P}^{NL}(t)$ comprising $\tilde{P}^{(m)}(t)$, where $m = 2, 3, 4$, etc. Therefore, we can write

$$\tilde{P} = \tilde{P}^{(1)}(t) + \tilde{P}^{NL}(t). \quad (1.16)$$

We have used \tilde{P} to describe a complex scalar quantity; however, all calculations can be generalized to vector quantities.

With Eq. (1.16), it allows us to transform the wave equation in Eq. (1.11) to a nonlinear representation. Using Eqs. (1.7) and (1.16), we can rewrite the wave equation to a nonlinear wave equation as

$$\nabla^2 \tilde{E} - \frac{1}{c^2} \frac{\partial^2 \tilde{D}}{\partial t^2} = -\frac{1}{\epsilon_0 c^2} \frac{\partial^2 \tilde{P}^{NL}}{\partial t^2}, \quad (1.17)$$

where the driving term is now completely driven by the nonlinear components of the polarization, \tilde{P}^{NL} , and the linear component is incorporated in \tilde{D} , where $\tilde{D} = \epsilon \tilde{E} + \tilde{P}^{(1)}(t)$.

Given the nonlinear wave equation, we can start considering how light can generate nonlinear polarization and how light travels based on the different linear and nonlinear components. When considering nonlinear processes, multiple frequencies can interact with one another and generate new frequencies. The frequency of light also affects another critical property, dispersion. Dispersion is a measure of how the wave vector changes with the frequency. Depending on the material's optical properties, these frequencies can be resonant or non-resonant and lead to interesting optical effects.

As we saw in Eq. (1.15), the polarization includes nonlinear components scaling with the electric field. However, it is essential to note that not all materials support all nonlinearities. In general, materials are classified into two groups: centrosymmetric and non-centrosymmetric. Centrosymmetry states that a material is invariant under inversion, which means that the medium will be symmetric and allow only odd-order nonlinear terms. In the case of non-centrosymmetry, the material properties will change under inversion, and the symmetry is broken, allowing even-order nonlinear polarization terms.

There are many different ways in which frequencies can mix that generate nonlinear polarization terms when considering the lowest-order nonlinear optical responses. $\chi^{(2)}$ materials can be used for nonlinear optical processes like second harmonic generation [20, 21], spontaneous parametric down-conversion [22, 23], and optical rectification [24, 25]. $\chi^{(3)}$ materials, however, have many more processes that can occur like third harmonic generation [26, 27], the Kerr effect [28, 29], or four-wave mixing [30, 31]. The nonlinear response is due to the frequency mixing resulting from proper phase-matching and a sufficiently strong EM wave, such as a laser beam. For now, we will consider a plane wave that interacts with a material that has the form

$$\tilde{E}(x, y, z) = \tilde{E}_0(x, y, z) e^{-i(kz - \omega t)}. \quad (1.18)$$

We will return to discuss the implications of a transverse profile later in Section 1.3.

1.3 Nonlinear Refraction

When considering nonlinear polarization, one optical effect of interest is nonlinear refraction [19, 32, 33], a third-order nonlinearity. Under sufficiently intense illumination, the refractive index of a material can have a nonlinear component large enough to alter the linear refractive index. For a third-order nonlinearity, the nonlinear polarization scales with the electric field squared. For most materials, we can assume that the magnetic permeability is close to 1. Therefore, we find the refractive index to be

$$n = \sqrt{\epsilon} = \sqrt{1 + \chi}. \quad (1.19)$$

Here, χ represents the total electric susceptibility with linear and nonlinear components. In general, the permittivity can be expanded, like that of the polarization, in terms of the electric field where

$$\epsilon = 1 + \sum_{n=1}^{\infty} \chi^{(n)} E^{n-1} = 1 + \chi^{(1)} + \chi^{(2)} \tilde{E} + \chi^{(3)} \tilde{E}^2 + \dots \quad (1.20)$$

Assuming this form, we can see that the refractive index will contain nonlinear corrections that scale with the electric susceptibility and field. Suppose we have a centrosymmetric medium and keep only odd-order terms in the susceptibility. Therefore, the dielectric permittivity simplifies to

$$\epsilon = 1 + \chi^{(1)} + \chi^{(3)} \tilde{E}^2 + \chi^{(5)} \tilde{E}^4 + \dots \quad (1.21)$$

We will consider only the first-order nonlinear correction to ϵ . The form of ϵ is based on a perturbative approach where each correction makes a smaller and smaller contribution to the linear effect. However, the higher-order terms must be considered in the case of very intense beams [34] or highly nonlinear materials [35]. In some cases, like in the case of epsilon-near-zero materials such as Indium-Tin-Oxide (ITO) [36], the perturbative expansion no longer holds, nonlinear components can be larger than linear, and one has to take a non-perturbative approach [37]. This effect is a result of the optical Kerr effect. The refractive index of a material can have an intensity dependence when the illuminating light is intense and changes the beam properties as it propagates. In the case of the ruby crystal in the following chapter, we observe a large optical Kerr effect, and therefore, we should spend time discussing what happens to the refractive index in the presence of a strong electric field. However, we will just consider the case of sufficiently intense lasers, but still in the regime that we can take the perturbative expansion of the permittivity. Therefore, we find that

$$\epsilon = 1 + \chi^{(1)} + \chi^{(3)} \tilde{E}^2. \quad (1.22)$$

Substituting Eq. (1.22) into Eq. (1.19), we find

$$n = \sqrt{\epsilon} = \sqrt{1 + \chi^{(1)} + 3\chi^{(3)}\tilde{E}^2}. \quad (1.23)$$

Let us assume that the nonlinear contribution perturbs the refractive index by Δn , such as $n \rightarrow n + \Delta n$. Assuming $1 + \chi^{(1)} \gg \chi^{(3)}\tilde{E}^2$, we find that

$$n + \Delta n = 1 + \chi^{(1)} + 3\frac{\chi^{(3)}\tilde{E}^2}{2}. \quad (1.24)$$

Therefore, by inspection, we find that

$$\Delta n \approx 3\frac{\chi^{(3)}\tilde{E}^2}{2}. \quad (1.25)$$

Often, nonlinear refraction is represented by a nonlinear refractive index, n_2 , multiplied by the input intensity, I , such that

$$\Delta n = n_2 I. \quad (1.26)$$

The input intensity is related to the square of the electric field, where

$$I = 2n_0\epsilon_0 c\tilde{E}^2, \quad (1.27)$$

and substituting the expression for I into Eq. (1.26), equating Eqs. (1.26) and (1.25), we find the nonlinear refractive index to be

$$n_2 = \frac{3\chi^{(3)}}{4n_0\epsilon_0 c}, \quad (1.28)$$

where the factor of 3 arises from the degeneracy of the frequency components.

When a laser beam has a spatial structure, the intensity distribution will cause a different amount of nonlinear contribution to the refractive index. Typically, lasers have a Gaussian beam profile. The transverse structure of a Gaussian beam takes the form

$$E(x, y, z) = A(x, y, z)e^{-((x-x_0)^2+(y-y_0)^2)/w(z)^2}, \quad (1.29)$$

where $A(x, y, z)$ is a slowly varying envelope function, x_0 and y_0 are the coordinates of the central position of the beam, and $w(z)$ is the beam waist that follows a hyperbolic evolution along z . The beam waist of a Gaussian beam is written

$$w(z) = w_0(1 + (z/z_R)^2)^{1/2}, \quad (1.30)$$

where z is the propagation distance, w_0 is the beam waist at $z = 0$, and z_R is the Rayleigh range, defined as

$$z_R = \pi w_0^2 / \lambda. \quad (1.31)$$

With spatial structure, the singular wave vector describing a plane wave is no longer sufficient to describe the nonlinear interaction, and therefore, we must consider phase matching. Phase-matching is crucial for more efficient interactions from a laser with the material in question [38–40]. In general, phase-matching dictates momentum conservation and, therefore, involves an analysis of the wave vectors that describe the interaction. The phase matching can be maximized by aligning the material to enhance the targeted nonlinear response. Phase matching becomes complicated when there is a beam structure that invites multiple wave vectors, and laser beams have Gaussian characteristics and a profile that has many wave vectors.

The distribution of intensity follows the square of the transverse Gaussian profile. The intensity is highest at the centre of the profile and, therefore, would induce the largest nonlinear refraction that perturbs that linear index. In the case of a positive nonlinear refractive index $n_2 > 0$ and a beam with the spatial structure, the beam can create an index pattern in the material that acts as a lens [41, 42] and causes the high-intensity parts to focus the beam. Self-focusing necessitates a positive nonlinear refractive index, while $n_2 < 0$ is self-defocusing [43, 44]. If n_2 is sufficiently large, the beam can undergo processes like filamentation [45, 46] where a beam will break up into many parts of the same critical power, or self-channel [47] where the beam propagates with a fixed waist then starts to diffract. Another exciting condition is when nonlinear refraction is balanced with nonlinear dispersion, causing solitons to form [48–50].

When considering different nonlinear processes, the timescale of their interactions can also play an important role. Nonlinear refraction is often considered nearly instantaneous [51, 52] when a Kerr-type nonlinearity is present. However, in some cases, nonlinear refraction can be associated with sluggish response, and due to Kramers-Kronig relations, the group index n_g is also affected [5, 53]. The importance of Kramers-Kronig relations will be discussed further in Section 1.6.1 of this chapter. Dispersion has increased relevance when considering nonlinear optical responses like nonlinear refraction.

The beam parameters, like the distribution of wave vectors in the beam, can also play a key role in linear optical systems. In Chapters 4 and 5, we study spaceplates that are dependent on the angular spread of the beam and, therefore, the wave vectors. Lenses can focus a beam, which changes the angular spread of the beam and sets the numerical aperture at its focus point. This is crucial to the performance of the spaceplate, which is limited to a certain numerical aperture. However, if the beam is focused to fit in this range

of angles, the focus can be retracted, which is a key interesting feature of a spaceplate. The wave vectors will acquire different amounts of phase after propagating through the spaceplate, which ultimately shifts the focus backward. This is controlled by the group delay in the material, which can be explained by the material dispersion. Therefore, we will develop an understanding of dispersion, starting with how dispersion relates to wave properties, particularly the phase and group velocity.

1.4 Dispersion

1.4.1 Wave Properties

The phase velocity describes how fast the wave moves through a medium. Since a medium can be described by refractive index, and light moves at speed c , the phase velocity is written as

$$v_p = \frac{c}{n}. \quad (1.32)$$

The phase velocity describes the local variation of the wave as it propagates. The group velocity, however, describes the envelope of this wave, and it can be written as

$$v_g = \frac{c}{n_g}. \quad (1.33)$$

Both of these quantities can be written in terms of the frequency and wave vector, which are important in describing the dispersion. Moreover, the speed of the group can be used to enhance or manipulate light-matter interaction, which is known as slow or fast light. Given that $\omega = kc/n$, substituting this expression into Eq. (1.32) gives $v_p = \omega/k$. The group velocity captures the envelope, which looks at the variation and is therefore described by the derivative of the phase velocity,

$$v_g = \frac{d\omega}{dk}. \quad (1.34)$$

From here, we determine an expression for the group index as a function of wavelength.

$$v_g = \frac{d\omega}{dk} = \frac{d\omega}{d\lambda} \left(\frac{dk}{d\lambda} \right)^{-1} = \frac{d}{d\lambda} (-2\pi\lambda^2\omega). \quad (1.35)$$

Substituting the expression $\omega = kc/n$ into Eq. (1.35), we find the group velocity to be

$$v_g = \frac{c}{1 - \frac{\lambda}{n} \frac{dn}{d\lambda}}, \quad (1.36)$$

where $n_g = n - \lambda \frac{dn}{d\lambda}$. Similarly, these equations can be written in terms of the frequency where the phase and group velocities are

$$v_p = \frac{c}{n(\omega)}, \quad (1.37)$$

and

$$v_g = \frac{c}{1 + \frac{\omega}{n} \frac{dn}{d\omega}}. \quad (1.38)$$

and the group index is found to be $n_g = n + \omega \frac{dn}{d\omega}$.

Now that we understand the fundamental wave properties that are used to describe light propagation, we will investigate how a material response can be used to manipulate and control the propagation. Therefore, we will spend time understanding dispersion and how it affects nonlinear propagation.

Not only is dispersion important in compensating nonlinear optical response, but it also plays a key role when considering slow or fast light media. We find slow or fast light regimes when the group index is large with respect to the phase index n_0 . Regarding the velocities, the group velocity is much slower than the phase velocity. Sometimes, the group index can also be smaller than the phase index or even negative, considering the fast light regime. A proper way of stating these regimes is saying the group velocity of an EM wave is subluminal or superluminal [54–56], which means that the group travels faster or slower than the speed of light. These phenomena can happen when the material response changes rapidly with frequency or wavelength. Group velocities that are subluminal or superluminal can result from nonlinearities, but some materials are naturally very dispersive [57]. It is important to note, however, that the phase velocity can also be considered as superluminal or subluminal, but not bounded by the speed of light [58]. We now look at how we describe dispersion and how higher-order corrections to dispersion can affect wave propagation. Slow and fast light are higher-order terms in the dispersion, which bring relevance to higher-order corrections.

Depending on the frequency of input light, the material response will vary. The wave vector is written as $k = 2\pi/\lambda$, but it can be equivalently written as $k = \omega/c$. If we take a Taylor expansion of the wave vector as a function of frequency ω , we will find higher-order dispersion terms about a resonance frequency ω_0 . The Taylor expansion of the wave vector

results in

$$\begin{aligned}
k &= k_0 + \sum_{n=1}^{\infty} \frac{k_n}{n!} (\omega - \omega_0)^n = k_0 \sum_{n=1}^{\infty} \frac{1}{n!} \left(\frac{d^n k}{d\omega^n} \right)_{\omega_0} (\omega - \omega_0)^n \\
&= k_0 + \frac{k_1}{1!} (\omega - \omega_0) + \frac{k_2}{2!} (\omega - \omega_0)^2 + \frac{k_3}{3!} (\omega - \omega_0)^3 + \dots \\
&= k_0 + \left(\frac{dk}{d\omega} \right)_{\omega_0} (\omega - \omega_0) + 1/2 \left(\frac{d^2 k}{d\omega^2} \right)_{\omega_0} (\omega - \omega_0)^2 + 1/6 \left(\frac{d^3 k}{d\omega^3} \right)_{\omega_0} (\omega - \omega_0)^3 + \dots
\end{aligned} \tag{1.39}$$

Upon expanding k , we find that the coefficients of k_1 , k_2 , etc. represent physical quantities that describe the propagating wave. We find $k_1 = \left(\frac{dk}{d\omega} \right)_{\omega_0}$, which is the inverse of the group velocity. Therefore, the coefficient for k_2 is the inverse derivative of group velocity, formally known as group velocity dispersion (GVD) [19, 59]

$$\text{GVD} = k_2 = (dv_g/d\omega)_{\omega_0}^{-1}. \tag{1.40}$$

Going one step further into the expansion, we find k_3 which is group delay dispersion (GDD) [19, 59], or in other words, the spectral variation of the group delay,

$$\text{GDD} = k_3 = (d\text{GVD}/d\omega)_{\omega_0}^{-1}. \tag{1.41}$$

For this thesis, we only need to consider the effects of dispersion up to GVD. However, higher-order dispersion terms can become significant in highly nonlinear systems with a large dispersion. Upon propagation, all orders of dispersion, except the first order, shape the pulse. The modification of the pulse is also dependent on the sign, which changes how the frequency is modulated with the wave vector. Therefore, it is essential to note regions of positive (normal) and negative (anomalous) dispersion [4, 60]. In other words, the wave sees normal (anomalous) dispersion with an increase (decrease) in refractive index with an increase in wavelength.

In optics, normal or anomalous dispersion can balance out nonlinear effects and lead to the formation of solitons, or EM waves, that propagate for long distances without distortion of the beam shape [49]. Solitons form when there is a balance between GVD and nonlinear refraction. Often, this balancing is based on the lengths needed for each interaction. Following the derivation of Boyd [19], we find the nonlinear length associated with nonlinear refraction as

$$L_{NL} = \frac{1}{(\omega_0/c)n_2 I}. \tag{1.42}$$

When L_{NL} is equal to the dispersion length, L_{dis} , defined as,

$$L_{dis} = T^2|k_2|, \quad (1.43)$$

where T is the time duration of a pulse, we can find the condition of solitons or self-channelling [61]. Therefore, we will spend some time deriving the nonlinear Schrödinger equation that considers nonlinear refraction and dispersion to understand the dynamics of a given system.

1.5 Nonlinear Schrödinger Equation

We can derive the nonlinear Schrödinger equation from the wave equation. We want to develop the nonlinear Schrödinger equation to be able to model nonlinear light propagation, as in the following chapter, where we model the light propagation through a rotating rub rod. Thus, we will derive the nonlinear Schrödinger equation to develop a basic understanding. Thus, let us consider an electric field that describes a pulse of the form

$$\tilde{E}(z, t) = \tilde{A}(z, t)e^{ik_0z - i\omega_0t} + c.c., \quad (1.44)$$

where $\tilde{A}(z, t)$ is a pulse envelope function, and *c.c.* is a complex conjugate of the field. In the remainder of this derivation, $k_0 = n_{lin}(\omega_0)\omega_0/c$, and the pulse propagates through a dispersive, nonlinear medium.

To arrive at the nonlinear Schrödinger equation, we can relate the time and frequency of the field \tilde{E} using a Fourier transform

$$\tilde{E}(z, t) = \int_{-\infty}^{\infty} \tilde{E}(z, \omega)e^{-i\omega t}d\omega/2\pi, \quad (1.45)$$

and similarly for \tilde{D} and \tilde{A} . We also must consider that the permittivity depends on the frequency such that

$$\tilde{D}(z, \omega) = \epsilon_0\epsilon(\omega)\tilde{E}(z, \omega). \quad (1.46)$$

Assuming we only have variation along the longitudinal direction, i.e. along propagation and substituting Eqs. (1.45) and (1.46) into Eq. (1.11), we find

$$\frac{d^2\tilde{E}(z, \omega)}{dz^2} - \frac{\epsilon(\omega)\omega^2}{c^2}\frac{\partial^2\tilde{E}}{\partial\omega^2} = 0. \quad (1.47)$$

We only take the resonant term (i.e. $\omega - \omega_0$ rather than anti-resonant $\omega + \omega_0$, where ω_0 is resonant frequency) as in [19], and assuming the slowly varying envelope approximation for \tilde{A} , i.e.

$$\left| \frac{\partial^2 \tilde{A}}{\partial z^2} \right| \ll \left| 2k_0 \frac{\partial \tilde{A}}{\partial z} \right|, \quad (1.48)$$

we find a simplified expression for the wave equation

$$2ik_0 \frac{d\tilde{A}}{dz} + (k^2 - k_0^2)\tilde{A} = 0. \quad (1.49)$$

Rearranging Eq. (1.49) and assuming that k and k_0 only differ by a small fraction, we find

$$\frac{d\tilde{A}(z, \omega - \omega_0)}{dz} - i(k - k_0)\tilde{A}(z, \omega - \omega_0) = 0. \quad (1.50)$$

The field \tilde{A} will have both a resonant ($\omega - \omega_0$) and an anti-resonant ($\omega + \omega_0$) term as a result of the complex conjugate. However, we only take the resonant term into consideration in the nonlinear interaction as the anti-resonant term does not interact strongly [19].

The wave vector can be Taylor expanded to include higher-order dispersion terms as well as a nonlinear contribution due to nonlinear refraction such that

$$k - k_0 = \Delta k_{NL} + k_1(\omega - \omega_0) + \frac{k_2}{2}(\omega - \omega_0)^2 + \dots, \quad (1.51)$$

where $\Delta k_{NL} = \Delta n_{NL}\omega_0/c = n_2 I \omega_0/c$. We can substitute Eq. (1.51) into Eq. (1.50) to find

$$\frac{d\tilde{A}(z, \omega - \omega_0)}{dz} - i\Delta k_{NL}\tilde{A}(z, \omega - \omega_0) + ik_1(\omega - \omega_0)\tilde{A}(z, \omega - \omega_0) + \frac{ik_2}{2}(\omega - \omega_0)^2\tilde{A}(z, \omega - \omega_0) = 0. \quad (1.52)$$

It is important to note that if we take a Fourier transform of Eq. (1.52), we can find a temporal evolution of the wave equation

$$\frac{\partial \tilde{A}}{\partial z} - i\Delta k_{NL}\tilde{A}(z, \omega - \omega_0) + ik_1 \frac{\partial \tilde{A}}{\partial t} + \frac{ik_2}{2} \frac{\partial^2 \tilde{A}}{\partial t^2} = 0. \quad (1.53)$$

Then, if we make the substitution that $\tau = t - z/v_g$, we can find a simplified version of the equation that accounts for the envelope

$$\frac{d\tilde{A}_s}{dz} + ik_2/2 \frac{\partial^2 \tilde{A}}{\partial \tau^2} - i\Delta k_{NL}\tilde{A}(z, \omega - \omega_0) = 0, \quad (1.54)$$

where $\Delta k_{NL} = n_2 I \omega_0 / c = 2n_0 \epsilon_0 n_2 \omega_0 |\tilde{A}_s|^2 = \gamma |\tilde{A}_s|^2$ is the nonlinearity, k_2 represents the nonlinear dispersion, and \tilde{A}_s refers to the optical field in retarded time. We can write the final form of this equation as

$$\frac{d\tilde{A}_s}{dz} + \frac{ik_2}{2} \frac{\partial^2 \tilde{A}_s}{\partial \tau^2} = i\gamma |\tilde{A}_s|^2 \tilde{A}_s, \quad (1.55)$$

which is otherwise known as the nonlinear Schrödinger equation. This form can capture the dynamics upon propagation, and we will use it to model our rotating ruby rod using the specific optical properties associated with that system, as in Chapter 2, which covers our theoretical work [62]. This model will then be tested experimentally in our work in Chapter 3 [5].

1.6 Slow Light and its Applications

Dispersion is related to the spectral response of the refractive index. Typically, the group index and the phase index are approximately the same value, but large group indices are possible if the refractive index rapidly changes over the frequency or wavelength. This behaviour is usually associated with a resonance feature in absorption [63]. These sorts of resonance features happen when a certain symmetry in materials or certain atomic features allow the energy states of the electrons to absorb photons more preferably [64, 65]. When a photon is absorbed, electrons are moved to excited states and decay at different rates depending on the material. The energy levels are highly discretized for atomic vapours, allowing for highly resonant features, like sodium [61] or rubidium vapor [63, 65]. Due to the selection rules of the electrons and the orbitals that they can exist in, the electronic states accessible within an atomic vapour can be very narrow, on the order of kHz [66, 67]. The allowed states can vary depending on the material platform. For solids, the material is rigid and can allow a variety of different energies as the energy is discretized into bands with a wide variety of allowed photonic transitions [68–70], and the shape of these bands depends on the constituent atoms and their place within the material. Doped transparent oxides like rubies were initially used in the first optical masers [71], but indeed are now seen as interesting solid-state materials because they are very similar to an atomic vapor [72, 73]. The crystalline structure can be transparent to certain wavelength regions. Still, the crystal is doped with a much heavier atom, chromium, Cr^{3+} , in the case of ruby and sapphire. Both materials host these heavier atoms within a transparent solid of Al_2O_3 but show very different optical properties. The Cr^{3+} lodged within the structure are similar to that of the atomic vapour, with multiple ions floating around; however, the ions are more localized

and have to obey strict rules regarding the crystalline structure of materials. The crystal structure will also affect how light is absorbed. Thus, it is worthwhile to talk about how absorption is defined.

In most of the discussion up to this point, we have defined the refractive index as a real-valued quantity. The refractive can have an imaginary component that quantifies how much light is absorbed. Looking at the representation of the refractive index with the dielectric permittivity, we can write a complex refractive index as

$$n = \sqrt{\epsilon_r + i\epsilon_i}, \quad (1.56)$$

where ϵ_r refers to the real part of the permittivity (rather than relative permittivity) and ϵ_i is the imaginary part of the permittivity. Let us suppose that the complex refractive index also consists of a real and imaginary part, such that

$$n = n_0 + ik, \quad (1.57)$$

where n_0 is the real part of the refractive index, and k is the imaginary part. Using some algebra, we can relate the real and imaginary parts of the dielectric permittivity to n and k , where

$$\epsilon_r = n^2 - k^2, \quad (1.58)$$

and

$$\epsilon_i = 2nk. \quad (1.59)$$

Each of these quantities will have a very different response depending on the input wavelength. We can use the imaginary part of the refractive index to find the absorption. The absorption, denoted α is written as

$$\alpha = 4\pi k/\lambda. \quad (1.60)$$

Typically, the resonant features seen in absorption have a Lorentzian lineshape [74]. Around a resonance position, the refractive index should change. Depending on how narrow this lineshape is, a large group index could be possible, inviting an excellent spot to talk about Kramers-Kronig relations.

1.6.1 Kramers-Kronig Relations

Kramers-Kronig relations describe that a complex physical quantity written in terms of a real and imaginary part will be linked spectrally [75, 76]. In particular, the Lorentzian

lineshape seen in absorption leads to a swing in the refractive index and, therefore, a scaled swing in the group index. If we consider the complex refractive index, for example, we can relate the real and imaginary parts using Kramers Kronig relations

$$\text{Re}[n(\omega)] = 1/\pi \int_{-\infty}^{\infty} \frac{\text{Im}[n(\omega')]d\omega'}{\omega - \omega'}, \quad (1.61)$$

and

$$\text{Im}[n(\omega)] = -1/\pi \int_{-\infty}^{\infty} \frac{\text{Re}[n(\omega')]d\omega'}{\omega - \omega'}, \quad (1.62)$$

where $k = \text{Im}[n]$ and $n_0 = \text{Re}[n]$, and ω' is the frequency that we are integrating over. Kramers Kronig relations allow switching from real to imaginary parts of any complex and serve as a useful tool in optics. Kramers Kronig relations, although they do not work well with nonlinear optics [77, 78], can relate to the ideas of delayed responses when the nonlinear response is large. The Kramers-Kronig relations only work well in nonlinear optics if the input and output fields can be treated as linear interactions, like harmonic generation where the frequency is always one or integer multiples of ω that participate in the interaction. Indeed, the time scale of nonlinear interactions can affect other optical processes and cause delays similar to slow light. Therefore, we must address the idea of slow light and how it plays a role in nonlinear optics.

1.6.2 Slow-Light Media

For a laser beam, we know that the phase velocity and group velocity affect how it travels. The phase velocity describes the local variations of the field, and the group velocity describes the field's envelope. The group velocity and phase velocity are not bounded by the speed of light, and in some cases, the group carries information [79]. Only the leading edge of the pulse is bounded by the speed of light [80]. Group velocities can also be subluminal or superluminal, like that of the phase velocity. Slow light is usually referred to as the case of subluminal speeds, where the group travels much slower than wave oscillations. In some cases, the group can be slowed so much that the light stops [81–83]. For the interest of this thesis, group velocities of interest are slow (fast if the sign of the group index is negative) but not zero.

Slow (fast) light is quite versatile in its ability to aid optical processes, most evidently by aiding light-matter interaction. In general, optical processes need a certain distance of which to build up appreciable magnitude. As discussed by Miller [84], optics need thickness. Indeed, optical processes must take place over a certain spatial range, but slow

or fast light provides a different degree of freedom or tuning knob which can, in some cases, dramatically increase light-matter interaction. Increasing light-matter interaction in this fashion can also help avoid parasitic effects of absorption associated with large spatial propagation. This is crucial in platforms like waveguides where the amount of light lost per unit length is a critical parameter to determine the usability of a device [85]. For the scope of this thesis, we will look at free space optics and enhancing or manipulating their response with the utilization of slow (or fast) light. In this case, we can look for certain material platforms that can exhibit slow (fast) light and the associated optical process that enables it.

1.6.3 Optical Effects for the Creation of Slow-Light

Material platforms like rubidium [66] and ruby exhibit specific optical processes that allow sharp absorption features that give rise to large group indices as a result of Kramers-Kronig relations, on the order of $n_g \approx 10^6$. Figure 1.1 shows the absorption, refractive index, and group index as a function of the frequency. The typical absorption feature is Lorentzian, and if we use Kramers-Kronig relations, we can find the corresponding refractive index. Since the group index is related to the rate of change of the refractive index with respect to the frequency, we can look at the slope to find the group index. Figure 1.1 shows two regions of interest for the group index, particularly when $n_g > 0$ and $n_g < 0$, corresponding to normal and anomalous dispersion, respectively.

These regions are considered normal and anomalous and can be regarded as fast and slow light regimes. We can enhance other optical effects in these regions by having a longer interaction time. The magnitude of the slow or fast light effect depends on the type of optical effect used to obtain it. For the case of rubidium vapour, electromagnetically induced transparency [86, 87] can produce a group index of $n_g = 10^5$, and ruby, through coherent population oscillation (CPO) [70, 88], can reach group indices of $n_g = 10^6$ for 514.5 nm light and $n_g = -1.17 \times 10^6$ for 473 nm light. CPO consists of an intense field and a weak detuned field that illuminates the crystal simultaneously, creating a small transparency window in the absorption spectrum that leads to a rapid change of the refractive index and thus the group index [88]. Regarding $n_g \approx -10^6$, although the group velocity is small in magnitude and therefore travels slowly, this regime is considered as fast light. Fast light happens when there is anomalous drag present in the system or when $n_g < n_0$. Fast light can describe two situations: The group will reach the end of a system faster than the oscillations of the phase, or the group will seemingly begin at the back end of a system and travel backward, against the propagation direction of energy flow [89]. Going against

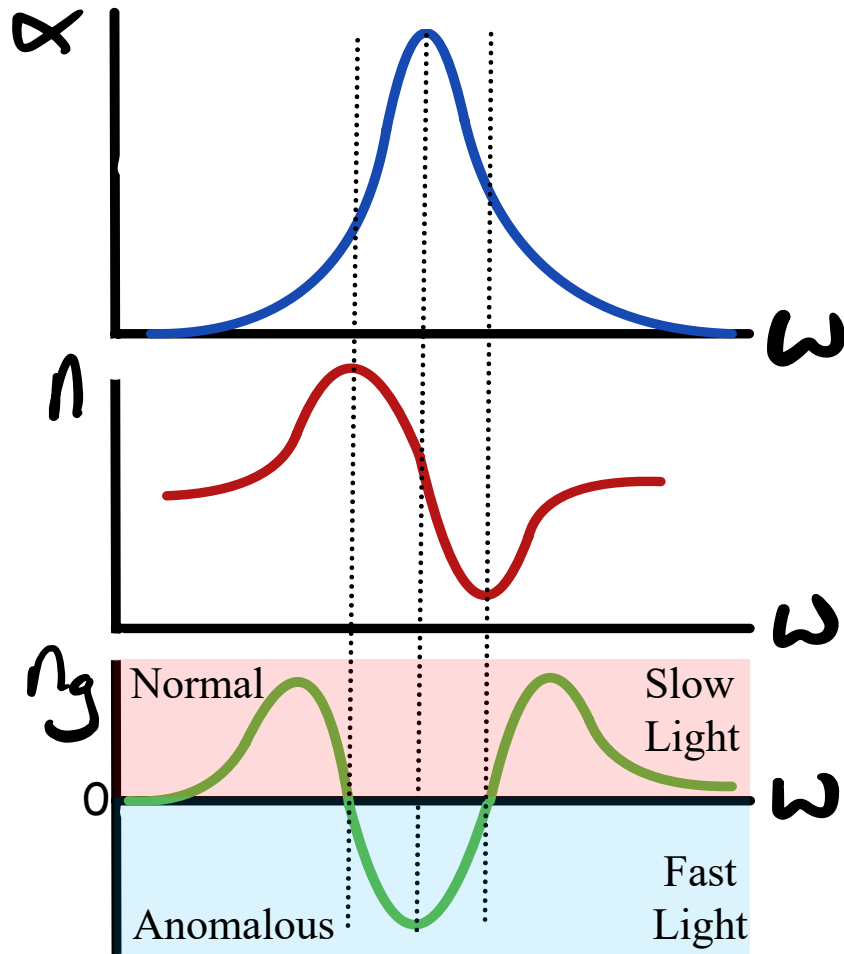


Figure 1.1: **Schematic of the spectral response of the absorption α , the refractive index n , and the group index n_g .** By Kramers-Kronig, the Lorentzian lineshape in the absorption spectrum gives the swing in the refractive index. This variation in the refractive index will give a non-zero slope and, therefore, a variation in the group index. The region in red for the group index shows a region of normal dispersion and slow light behaviour. The blue region, on the other hand, shows anomalous dispersion and a fast-light effect. These slow and fast light regions can enhance the light-matter interaction in specific spectral regions.

energy flow seems to break causality, but this would only happen if the phase velocity behaved like the group velocity.

1.7 Thesis Outline

The subsequent chapters will focus on the theoretical and experimental investigation of two main topics, the photon drag effect and nonlinear deflection, and the development and testing of multilayer stack-based spaceplates.

In Chapter 2, we model the nonlinear propagation of light through a rotating ruby rod using Nonlinear Schrödinger equations based on the work of Hogan et al. [62]. The response of the medium is captured in a dielectric tensor that incorporates rotation, birefringence, and thermal nonlinearity. We also incorporate a nonlinear group index that captures the slow-light effect in the crystal. This group index was found to have a rotation speed- and intensity-dependence that can change the beam's trajectory through the crystal. These effects are incorporated into coupled Nonlinear Schrödinger equations from which the transverse trajectories and transverse shift are extracted. The trajectories of each beam are investigated, as well as the electric field evolution in space and time.

In Chapter 3, we experimentally measure the transverse trajectories and transverse shift at the output of the ruby rod, based on the work of Hogan et al. [5]. We observe that the centre of intensity of the sometimes overlapping two beams trace figure-eight trajectories in the transverse plane at the crystal output. The average position is then experimentally calculated for each trajectory to map out the transverse shift as a function of input intensity and rotation speed. The dependence of the output angle is also calculated, showing the dependencies on rotation speed and intensity. To understand the output angle, the transverse shift is also measured at other positions past the output. A Townes profile was also observed, and the strength of this nonlinear refraction was quantified.

In Chapter 4, we investigate four different spaceplate designs based on thin film multilayer stacks, according to the work of Hogan et al. [2]. The spaceplates are each designed by either a gradient descent optimization method or by optimizations of a multiple coupled resonator model. The four devices are characterized using the Transfer Matrix Method to extract the transmission phase and transmittance dependencies on the input angle and wavelength. The transmission phase as a function of angle can then be used to calculate the transverse walk-off, from which we extract the compression factor as a function of wavelength. Due to the nature of the coupled resonator structure, multiple resonances are found. A brief theoretical investigation of the resonance positions and bandwidth is also proposed.

In Chapter 5, we experimentally measure the transverse walk-off of each spaceplate discussed in Chapter 4 and extract the compression factor as a function of wavelength, according to the work of Hogan et al. [2]. The full dependency of the transverse walk-off

and angle is shown for each device type, and the characterization of beam quality is also measured and discussed. These experimental values are compared to simulations showing good agreement. Focal shifts of the imaging plane are also measured to show the viability and functionality of the spaceplate.

Chapter 2

Photon Drag Theory and Nonlinear Propagation

In the present chapter, as per the results of Hogan et al. [62], we will develop an understanding of photon drag and light propagation through a rotating, anisotropic, birefringent medium with a thermal nonlinear response and a nonlinear group index. The complexities of the system will be modelled and simulated using coupled nonlinear Schrödinger equations that represent two beams that propagate through the medium. The evolution of the fields through the crystal in space and time will be investigated. Furthermore, the weighted average position of the intensity of the two beams will be used to track the dynamics in the transverse plane. The average position of these trajectories can then be used to extract the amount of transverse shift at the output facet of the medium.

2.1 Background

First predicted by Fresnel [90], and later experimentally proved by Fizeau [91], the propagation of light in a medium in motion is subject to the photon drag effect. Depending on the direction of medium motion relative to the optical path, light drag causes a longitudinal or transverse shift in the beam, leading to a shift in the beam along or perpendicular to the path of propagation, respectively. This effect has been studied in various media, including those with large group indices [92–95]. Since the photon drag effect scales with group index (n_g), one can use fast or slow light to manipulate and even significantly enhance the shifts induced upon the beam [3, 88]. The mechanism of interest to realize a large

group index is coherent population oscillation (CPO) [3, 88] in ruby with $n_g \approx 10^6$, which allows for a much larger shift in the beam position when in motion. Appreciable speeds are also necessary to produce a measurable optical beam shift. In the case of a transverse shift, fast-speed medium translation is often practically difficult. Reaching large, constant speeds is more viable with rotation, so it is used instead. The speeds achieved by rotation serve twofold, as the rotation speed should match the lifetime of the atomic excitations in the case of CPO, and the drag effect scales linearly with speed, so it should also be considered. The tangential component of the rotation, provided far from the center of rotation, is almost completely translational. Therefore, a beam can be dragged at significant speeds. However, rotation requires additional considerations, such as a rotating reference frame and birefringence in the case of a ruby rod. Therefore, modelling light propagation in such a system must account for the rate of rotation, the birefringence, the group index, and the impact of each on any nonlinear optical or thermal response.

To date, the photon drag effect has been modelled as a linear effect [3, 88, 90, 91, 96]. To more accurately model the dynamics of such a system, like the one in our experimental work [5], one must distinctly consider the contributions of instantaneous versus non-instantaneous regimes in a nonlinear context and how this affects the group index and, ultimately, the photon drag effect. This states that when considering the nonlinear response of thermal origin versus optical origin, the interaction's timescale will affect the beam's trajectories depending on how fast the medium moves. Thermal nonlinearities are non-instantaneous, and optical nonlinearity is often instantaneous. However, the optical nonlinearity still has an associated timescale before the effect has impinged on the system, usually associated with the lifetime of an excited state, as in the case of CPO [88]. For CPO, the dielectric tensor that describes the systems has a non-trivial frequency derivative that leads to distorted figure-eight-like trajectories in the transverse plane of the beam. The rotation and nonlinear components will drastically modify this dielectric tensor in time, changing the dynamics measured at the crystal output face. Therefore, one must incorporate the rotation and nonlinear response to the dielectric tensor to accurately model the system's dynamics, affecting the group velocity and the transverse shift measured at the crystal output.

Here, we model the dynamics of transverse photon drag in a rotating ruby rod experiencing CPO, accounting for its uniaxial birefringence and its non-instantaneous self-focusing nonlinearity. This modelling effort draws from our experimental work on such a system presented in our paper [5], which we will talk about in the following chapter. Furthermore, this modelling demonstrates that the contribution of the linear response of the photon drag effect is negligible compared to the nonlinear contribution based on n_g^{NL} . We will also show that n_g^{NL} depends on rotation speed, which is needed to match the simulations well with

experimentally measured values.

Using a primarily general theory that describes the interaction of linearly polarized light with a birefringent medium and considering rotation, nonlinear refraction, and the nonlinear photon drag effect, we develop nonlinear Schrödinger equations for the ordinary (o) and extraordinary (e) beams that fully describe the dynamics of the system. Our model matches the linear and nonlinear dynamics of the system in the transverse plane, following the rotary motion of the medium. This model can be applied to our experimental work [5], as well as to the propagation of light in a rotating, nonlinear medium [97], and has implications for applications in beam-steering [98], mode-sorting [99, 100] as the trajectory of the light is tracked, and the transverse shift at the output is controllable based on input intensity and rotation speed. Furthermore, detecting sensitivities to polarization imperfection could be possible as they dictate a certain transverse trajectory. The beam trajectory through the birefringent ruby rod is highly sensitive to the input beam polarization, the rotation speed, and any nonlinear refraction. Furthermore, this work could lead to investigations on the stability of complex electric field structures [99, 100] with respect to whether a beam will filament or solitons [101–104] by tuning the dispersion and nonlinear response of the medium.

This chapter focuses on creating a model to predict the beam path trajectory and evolution through a rapidly rotating, birefringent medium that can experience Kerr and thermal nonlinearities. This is also considered for cases such as non-normal incident beam angle, which is often the case in experiments. Furthermore, the angle dependence is affected by the birefringence tilt relative to the axis of rotation and index gradients. All of these components will modify the transverse trajectories at the crystal output fact and the transverse shifts. Therefore, we will begin by introducing the photon drag effect and how it is extended to the nonlinear regime and incorporated into the nonlinear Schrödinger equation.

2.2 Photon Drag Theory

2.2.1 Linear Drag

As light travels through a moving medium, the momentum of the medium is transferred to the light, producing light drag. The effect is more subtle, resulting from different momentum components having different phase shifts (in analogy to different frequencies having a different phase producing a group velocity). This movement can be either along the

propagation direction, producing an optical phase shift and longitudinal drag [105], or perpendicular to propagation, inducing transverse drag of the light [96]. From the derivation of Carusotto et al. [96], we consider monochromatic, collimated light that interacts with an isotropic, lossless, dispersive, linear medium in motion with constant speed, v , to find an expression for the transverse shift due to photon drag.

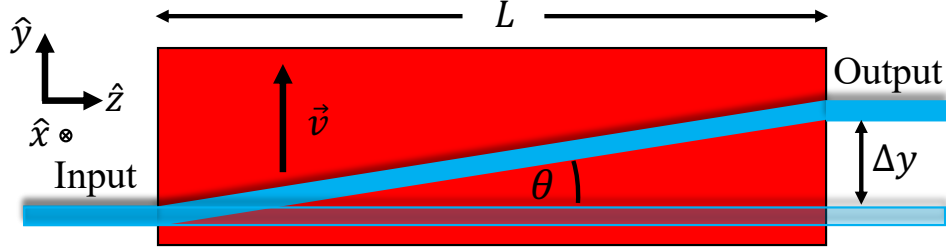


Figure 2.1: **Schematic of the linear, transverse photon drag effect.** A beam of light passing through an isotropic, lossless medium of length L , moving transversely with speed v , gets laterally shifted by Δy due to a small angle deviation, θ .

Due to the motion of the medium, the beam is deflected from its original direction of propagation. We suppose this transverse deflection is a small angle deviation, θ . We find the angle θ as a function of phase index n_0 , and the group index n_g [96]

$$\tan \theta = \frac{v}{c} \left(n_g - \frac{1}{n_0} \right), \quad (2.1)$$

where v is the medium speed, and c is the speed of light. We can find the amount of transverse shift Δy in terms of the medium length L , replacing $\tan(\theta) = y/L$ to find

$$\Delta y = \frac{vL}{c} \left(n_g - \frac{1}{n_0} \right). \quad (2.2)$$

The transverse shift is a measurable quantity that is often the measure of the magnitude of the photon drag effect. Knowing that group index is $n_g = n_0 + \omega_0 \left(\frac{dn_0}{d\omega} \right)_{\omega_0}$, and the phase index is $n_0 = \sqrt{\epsilon} = \sqrt{\epsilon_r + i\epsilon_i} \approx \sqrt{\epsilon_r}$ (assuming a lossless medium), we find

$$\Delta y = \frac{vL}{c} \left[\left(\epsilon_r(\omega_0) + \frac{\omega_0}{2\sqrt{\epsilon_r(\omega_0)}} \left(\frac{d\epsilon_r}{d\omega} \right)_{\omega_0} \right) - \left(\frac{1}{\sqrt{\epsilon_r(\omega_0)}} \right) \right]. \quad (2.3)$$

We will now consider how the assumption of a linear system no longer holds for an intense laser beam and the associated implications.

2.2.2 Nonlinear Drag

In the presence of an intense laser beam, certain media can exhibit large group indices ($|n_g| \approx 10^6$ [4, 88]), therefore extending the linear photon drag effect to nonlinear. Therefore, we must consider the lowest order correction to the indices n_0 and n_g . The correction takes the form $\Delta n = n_2 I$, arising from an instantaneous Kerr-type nonlinearity, where n_2 is the nonlinear refractive index, and I is the input beam intensity. Therefore, the phase and group indices become

$$\begin{aligned} n_0^{NL} &= n_0 + n_2 I, \\ n_g^{NL} &= n_g^0 + n_2^g I, \end{aligned} \quad (2.4)$$

where n_g^0 is the linear group index, n_2^g is the nonlinear group index

$$n_2^g = \left(n_2 + \omega_0 \left(\frac{dn_2}{d\omega} \right)_{\omega_0} \right), \quad (2.5)$$

and n_g^{NL} represents the nonlinear change of the group index due to a Kerr-like nonlinear response. Substituting the nonlinear group index, we find the transverse shift due to nonlinear photon drag

$$\Delta y_{NL} = L \tan(\theta_{NL}) = \frac{Lv}{c} \left(n_g^{NL} + \frac{1}{n_0} \right). \quad (2.6)$$

We note that $\theta_{NL} = \theta \pm \Delta\theta$, depending on the sign of nonlinear response of the medium, where $\Delta\theta$ is the nonlinear correction to linear output angle.

In the presence of slow light media, we can approximate $|n_g^{NL}| \gg n_0$, and therefore find the transverse shift as

$$\Delta y_{NL} \approx \frac{Lv}{c} n_g^{NL}, \quad (2.7)$$

which is positive for normal ($n_g^{NL} > 0$) dispersion [88] or negative in an anomalous ($n_g^{NL} < 0$) dispersion regime [4, 60].

In Sec. 2.4.3, we will elaborate further on the effect of medium speed on n_g^{NL} . When considering the speed dependence, the nonlinearity is treated as approximately instantaneous; however, the nonlinearity is indeed non-instantaneous. We see that medium speed is also important in the photon drag effect regarding the magnitude of the shift observed. The nonlinear photon drag effect can be tuned using medium speed, creating a range of transverse shifts.

So far, the discussion has focused on the purely linear motion of an isotropic medium. It is easier to achieve considerable transverse speeds using rotational motion in practice. Therefore, we will use rotation, but we will also have to account for added complexity arising when illuminating a rotating system.

2.3 Media in Rotation

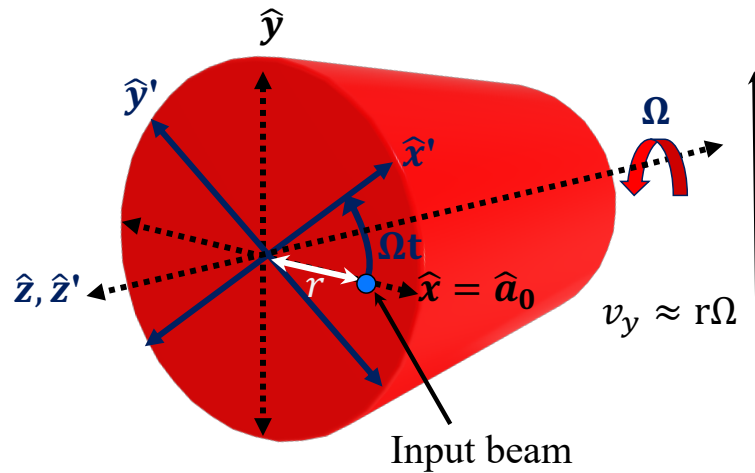


Figure 2.2: **A laser beam incident on a rotating medium far from the center of rotation.** Far from the center, the beam experiences the tangential component of the velocity in the direction according to the sign of the angular velocity, Ω , that rotates about the z -axis. Two frames of reference are also shown. The lab frame is shown in (x, y, z) and the crystal frame is (x', y', z') .

We have shown the nonlinear transverse shift scales with the group index, but our model requires high, uniform speeds ($v \approx 1$ m/s) to predict measurable shifts. Using rotation to achieve large constant speeds over translational motion is experimentally favourable. Therefore, we consider a rotating medium with a beam far from the centre of rotation, that is $r > w_0$, where r is the radius from the centre of the medium to the beam centre and w_0 is the beam waist, such that the beam experiences only the tangential component of the rotation speed, representing approximately translational motion, seen in Fig. 2.2.

Accounting for rotation and taking the speed to be $v = r\Omega$, we can then substitute into Eq. (2.7) and find the nonlinear photon drag effect as

$$\Delta y_{NL} \approx \frac{Lr\Omega}{c} n_g^{NL}, \quad (2.8)$$

where Ω is the rotation speed of the medium. Therefore, to maximize the nonlinear photon drag effect, we need a medium that rotates easily about the transverse plane and a medium with dispersion that creates a large group index to achieve large transverse shifts. An example of such a medium is a ruby rod which has significant dispersion [106], has been used to investigate slow and fast light experiments [3, 70, 94, 107–110], and has a measurable nonlinear effect like Kerr or others [107, 111–113]. However, it is not an isotropic medium. Therefore, our model must incorporate the different refractive indices along the ordinary and extraordinary axes of its crystal structure. Motivated by this example, we will incorporate a rotating reference frame for a birefringent, nonlinear material into our model.

2.3.1 Rotation and Anisotropy

Consider a solid, birefringent rod rotating about the z -axis with a constant rotation speed Ω , as shown in Fig. 2.2. We wish to describe how incoming collimated, monochromatic light interacts with this medium by utilizing a vector wave equation derived from Maxwell's equations

$$\mathbf{k} \times (\mathbf{k} \times \mathbf{E}) + \frac{\omega^2}{c^2} \epsilon \mathbf{E} = \mathbf{0}. \quad (2.9)$$

To adequately describe the system, we must define the vector quantities in two reference frames: the lab frame, (x, y, z) , and the rotating crystal frame (x', y', z') . The two reference frames are used because light propagation is broken into parts using the Split-Step Fourier Method, and each propagator must take care of its respective reference frame.

In the lab reference frame, the orthonormal basis of unit vectors is $\hat{\mathbf{x}}, \hat{\mathbf{y}}, \hat{\mathbf{z}}$. Furthermore, the crystal rotates with constant angular velocity $\boldsymbol{\Omega}$, and away from the center of rotation, the crystal moves with tangential velocity $\mathbf{v} = \boldsymbol{\Omega} \times \mathbf{r}$, where $\mathbf{r} = x\hat{\mathbf{x}} + y\hat{\mathbf{y}} + z\hat{\mathbf{z}}$. The crystal reference frame is written as another orthonormal basis $\hat{\mathbf{x}}', \hat{\mathbf{y}}', \hat{\mathbf{z}}'$, however we take $\hat{\mathbf{x}} = \hat{\mathbf{a}}_0$, where $\hat{\mathbf{a}}_0$ is the crystal optic axis [114], as shown in Fig. 2.2. The crystal frame is accessed by applying a rotation matrix to the lab frame and vice versa. In an ideal case, the crystal basis is exactly aligned with the crystal axes, but we must account for circumstances where they are not perfectly aligned. Therefore, we suppose the system has a slight tilt angle,

γ , that rotates the xz plane, tilting into the crystal, as seen in Fig. 2.3. We will consider $\gamma \neq 0$; however, we highlight some simplifications when $\gamma = 0$.

Perfect Crystal Alignment $\gamma = 0$

Let us consider a change of basis matrix \mathbf{C} to incorporate the rotating reference frame that interchanges between lab to a crystal frame

$$\mathbf{C} = \begin{pmatrix} \cos(\Omega t) & -\sin(\Omega t) & 0 \\ \sin(\Omega t) & \cos(\Omega t) & 0 \\ 0 & 0 & 1 \end{pmatrix} = \mathbf{R}_{\mathbf{z}}(\Omega t), \quad (2.10)$$

where $\mathbf{R}_{\mathbf{z}}(\Omega t)$ is the rotation matrix about the z -axis, Ω is the rotation speed, and t is time. To obtain the orthonormal basis in the crystal frame, we apply \mathbf{C} to the column vector $(\hat{\mathbf{x}}, \hat{\mathbf{y}}, \hat{\mathbf{z}})$ resulting in the crystal orthonormal basis set

$$\begin{aligned} \hat{\mathbf{x}}' &= \cos(\Omega t)\hat{\mathbf{x}} + \sin(\Omega t)\hat{\mathbf{y}}, \\ \hat{\mathbf{y}}' &= -\sin(\Omega t)\hat{\mathbf{x}} + \cos(\Omega t)\hat{\mathbf{y}}, \\ \hat{\mathbf{z}}' &= \hat{\mathbf{z}}, \end{aligned} \quad (2.11)$$

as sketched in Fig. 2.2.

One must apply an inverse matrix, \mathbf{C}^{-1} , from crystal to lab frame. Neglecting terms $O[(\delta n)^2]$, where $\delta n = n_o - n_e$ (e.g. $\delta n \approx 0.008$ for a ruby rod), one obtains the corresponding dielectric tensor in the lab frame

$$\epsilon(\Omega t) = \mathbf{C}\epsilon'\mathbf{C}^{-1} = \epsilon' + \epsilon''(\Omega t). \quad (2.12)$$

where

$$\epsilon' = \epsilon_0 \begin{pmatrix} n_e^2 & 0 & 0 \\ 0 & n_o^2 & 0 \\ 0 & 0 & n_o^2 \end{pmatrix}. \quad (2.13)$$

and

$$\epsilon''(\Omega t) = 2\epsilon_0 n_o \delta n \begin{pmatrix} \sin^2(\Omega t) & -\frac{1}{2}\sin(2\Omega t) & 0 \\ -\frac{1}{2}\sin(2\Omega t) & -\sin^2(\Omega t) & 0 \\ 0 & 0 & 0 \end{pmatrix}. \quad (2.14)$$

Imperfect Crystal Alignment $\gamma \neq 0$

A slightly misaligned crystal induces a further rotation by γ considered to be between the optic axis, $\hat{\mathbf{a}}_0$, and the xy plane. We again set the optic axis to be along the unit vector \hat{x} such that $\hat{\mathbf{x}}' = \hat{\mathbf{a}}_0$. The other units vectors $\hat{\mathbf{y}}', \hat{\mathbf{z}}'$ are set according to $\hat{\mathbf{x}}'$, and the crystal frame orthonormal basis becomes

$$\begin{aligned}\hat{\mathbf{x}}' &= \cos(\gamma) \cos(\Omega t) \hat{\mathbf{x}} + \cos(\gamma) \sin(\Omega t) \hat{\mathbf{y}} + \sin(\gamma) \hat{\mathbf{z}}, \\ \hat{\mathbf{y}}' &= -\sin(\Omega t) \hat{\mathbf{x}} + \cos(\Omega t) \hat{\mathbf{y}}, \\ \hat{\mathbf{z}}' &= \sin(\gamma) \cos(\Omega t) \hat{\mathbf{x}} + \sin(\gamma) \sin(\Omega t) \hat{\mathbf{y}} + \cos(\gamma) \hat{\mathbf{z}}.\end{aligned}\tag{2.15}$$

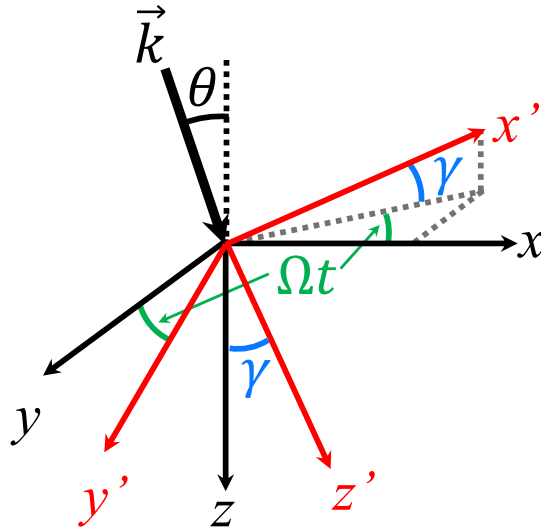


Figure 2.3: **Schematic of two different frames of reference.** The reference frames are laboratory (x, y, z) and crystal (x', y', z') . The wave vector comes in at an angle θ in the xz plane. The reference frames become tilted by Ωt , where Ω is the rotation speed, and t , time, and γ , the crystal orientation with respect to the optic axis. Ωt shifts the coordinates in xy plane, and γ in xz plane.

Incorporating the tilt angle into the change of basis matrix \mathbf{C} , we find

$$\begin{aligned}\mathbf{C} &= \mathbf{R}_y(-\gamma) \mathbf{R}_z(\Omega t) \\ &= \begin{pmatrix} \cos(\gamma) \cos(\Omega t) & \cos(\gamma) \sin(\Omega t) & \sin(\gamma) \\ -\sin(\Omega t) & \cos(\Omega t) & 0 \\ -\sin(\gamma) \cos(\Omega t) & -\sin(\gamma) \sin(\Omega t) & \cos(\gamma) \end{pmatrix},\end{aligned}\tag{2.16}$$

which is comprised of the rotation matrix about the z -axis $\mathbf{R}_z(\Omega t)$ and $\mathbf{R}_y(-\gamma)$, the matrix representing the tilt angle, γ , applied along the y direction. If $\gamma = 0$, we only find a rotation about the z -axis, $\mathbf{R}_z(\Omega t)$. A schematic of how the two matrices rotate the system is depicted in Fig. 2.3.

Returning to lab frame, we apply \mathbf{C}^{-1} to the dielectric tensor, neglect terms $O[(\delta n)^2]$, and find

$$\epsilon(\gamma, \Omega t) = \mathbf{C}\epsilon'\mathbf{C}^{-1} = \epsilon' + \epsilon''(\gamma, \Omega t). \quad (2.17)$$

We must consider the crystal symmetry when switching reference frames and its effect on the dielectric tensor. Incoming light in the crystal frame will see the ordinary (n_o) and extraordinary (n_e) refractive indices. Assuming the optical axis is perpendicular to the axis of rotation, the dielectric tensor is therefore [114]

$$\epsilon' = \epsilon_0 \begin{pmatrix} n_e^2 & 0 & 0 \\ 0 & n_o^2 & 0 \\ 0 & 0 & n_o^2 \end{pmatrix}. \quad (2.18)$$

Assuming $\delta n = n_o - n_e \ll 1$ (i.e. for a uniaxial ruby rod, $\delta n = -0.008$), we find $\epsilon''(\gamma, \Omega t)$

$$\begin{aligned} \epsilon''(\gamma, \Omega t) &= (2\epsilon_0\delta n \cos(\gamma)^2) \begin{pmatrix} \sin(\Omega t)^2 + \sec(\gamma)^2 - 1 & -\sin(2\Omega t)/2 & \cos(\Omega t) \tan(\gamma) \\ -\sin(2\Omega t)/2 & \sin(\Omega t)^2 & \sin(\Omega t) \tan(\gamma) \\ -\cos(\Omega t) \tan(\gamma) & -\sin(\Omega t) \tan(\gamma) & \tan(\gamma)^2 \end{pmatrix} \\ &\xrightarrow{\gamma=0} 2\epsilon_0 n_o \delta n \begin{pmatrix} \sin^2(\Omega t) & -\frac{1}{2} \sin(2\Omega t) & 0 \\ -\frac{1}{2} \sin(2\Omega t) & -\sin^2(\Omega t) & 0 \\ 0 & 0 & 0 \end{pmatrix}. \end{aligned} \quad (2.19)$$

One needs the permittivity tensor and the fields interacting with the crystal to understand light propagation through the medium. So far, we have described the dielectric permittivity, including birefringence, tilt angle, and medium rotation, but one still needs to consider how these quantities affect the fields.

2.3.2 Electric Fields in Rotating Media

Consider a monochromatic field propagating through a linear medium $\mathbf{E} = \mathbf{E}_0 e^{i(\mathbf{k}\cdot\mathbf{r} - \omega t)}$ under the hypothesis of weak birefringence ($\delta n \ll 1$) and $v \ll c$ (for which $\frac{\partial^2}{\partial t^2} \epsilon \mathbf{E} \simeq \epsilon \frac{\partial^2}{\partial t^2} \mathbf{E}$). That is to say, the speed of the medium does not create a time-varying permittivity over the time the light spends in the medium. This is under the assumption that the medium

is short enough such that the time it takes light to propagate through it is negligible compared to all other time scales.

We aim to solve the vector wave equation in Eq. (2.9) in the lab frame as a linear system of variables E_x, E_y, E_z , the electric field coordinates, satisfying $\mathbf{A} \cdot \mathbf{E} = \mathbf{0}$, where $\mathbf{A} = \mathbf{k}^2 - \frac{\omega^2}{c^2}\epsilon$. Non-trivial solutions of $\mathbf{A} \cdot \mathbf{E}$ are only found if the determinant of the coefficient matrix is non-null (i.e. $\mathbf{k}^2 - \frac{\omega^2}{c^2}\epsilon \neq 0$). We solve this equation using the dielectric tensor in Eq. 2.17 as in Sec. 2.3.1 and the associated monochromatic field \mathbf{E} for a rotating birefringent medium.

Perfect Crystal Alignment $\gamma = 0$

We suppose that our initial wave vector \mathbf{k} comes in at an angle θ between the optic axis and the z -axis, where at time $t = 0$, $\hat{\mathbf{x}} = \hat{\mathbf{x}}' = \hat{\mathbf{a}}_0$ (See Fig. 2.2). Neglecting all the terms $O[(n_o^2 - n_e^2)^2]$ in $\mathbf{A} \cdot \mathbf{E}$ and supposing that the crystal perfectly aligned case ($\gamma = 0$), the conditions for which the wave vector coordinates k_x, k_z ($k_y = 0$) resolve non-trivial solutions in the lab frame are

$$\frac{k_x^2}{n_{e,2}^2} + \frac{k_z^2}{n_{e,2}^2} = \frac{\omega^2}{c^2}, \quad (2.20)$$

$$\frac{k_x^2}{n_o^2} + \frac{k_z^2}{n_{e,1}^2} = \frac{\omega^2}{c^2}, \quad (2.21)$$

where

$$\begin{aligned} n_{e,1}(\Omega t) &= n_e + \delta n \sin^2(\Omega t), \\ n_{e,2}(\Omega t) &= n_o - \delta n \sin^2(\Omega t). \end{aligned} \quad (2.22)$$

The quantities $n_{e,1}$ and $n_{e,2}$ represent the new refractive indices along x, y , respectively. Indeed, while in the crystal, the refractive indices ellipsoid reads

$$\frac{(x')^2}{n_e^2} + \frac{(y')^2}{n_o^2} + \frac{(z')^2}{n_o^2} = 1, \quad (2.23)$$

and in the lab frame, its expression is

$$\frac{x^2}{n_{e,1}^2} + \frac{y^2}{n_{e,2}^2} + \frac{z^2}{n_o^2} = 1, \quad (2.24)$$

as sketched in Fig. 2.4. We will now look at how the beams propagate through the crystal following the newfound refractive indices.

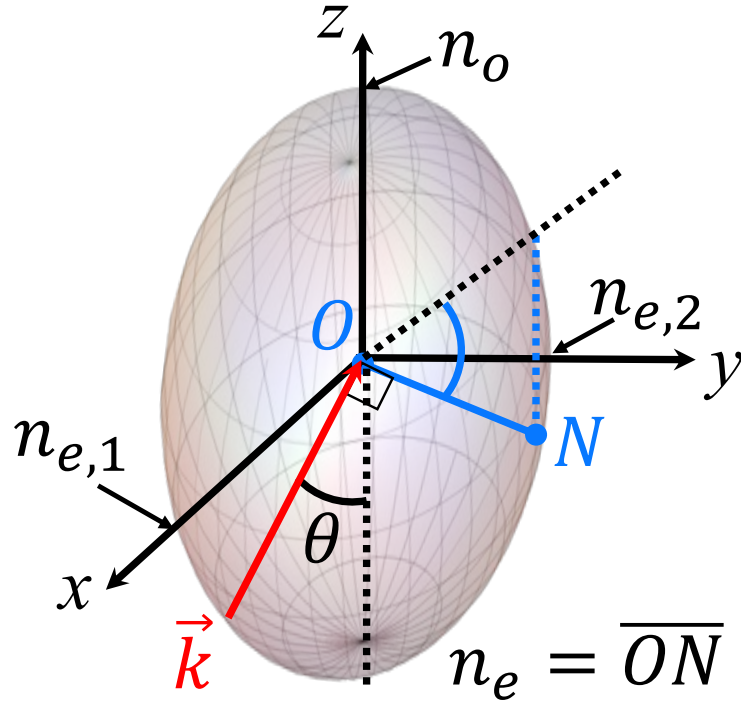


Figure 2.4: **The refractive index ellipsoid in the lab's frame.** Four refractive indices are labeled on the ellipsoid, n_o as a projection onto the z -axis, n_e , which is equal to the length from O to N , defined as \overline{ON} , and $n_{e,1}$ and $n_{e,2}$ defined in Eq. (2.22). The point N is on the edge of the index ellipsoid such that \overline{ON} is perpendicular to \vec{k} , and therefore corresponds to the point at which the refractive index is n_e .

Figure 2.5 shows a schematic of two beams that propagate through the crystal. The two beams are a result of the birefringence and have specific dynamics when considering linearly polarized light illuminating the rotating crystal. Even if the crystal is uniaxial, the rotation in the lab frame results in a biaxial-like crystal with time-dependent birefringence. That is to say, at certain instances in time, only one beam is seen due to a lack of birefringence, like in a biaxial crystal. However, in some cases, it is also possible to see one beam in a uniaxial crystal. This inherent birefringence, or lack thereof, causes the incoming linearly polarized light to interchange between beams, where o- and e-beams reach their maximum and zero intensity each quarter turn of the crystal. Ultimately, predicting the exit position, exit angle, and relative intensity will be necessary to compare to experiments. Also, looking at the centre of intensity (COI) of these beams allows for a better method to compare to our

experiment [62] as seen in Chapter 3. Since the o- and e-beams become large and hard to distinguish in the experiment after propagation of the full crystal length, the COI is preferred. In fact, the trajectory that is traced out following the COI is a figure-eight. The figure-eight serves as a good marker to understand how much they distort or shift due to the nonlinear contributions, which is simulated using the theory in this chapter and matches well with the experimental measurements in Chapter 3. For the simulations, however, the COI is generated and investigated by looking at both the o- and e-beam propagation independently, an advantage over the experiment, and then the two individual trajectories can be tracked together to create the COI trajectories.

Another key aspect is how the light interacts with the air-crystal and crystal-air interfaces. Assuming that the light illuminates at some angle of incidence θ like in Fig. 2.5, the new ordinary and extraordinary refractive indices in the lab frame are

$$n_o(\Omega t) = n_{e,2}(\Omega t), \quad (2.25)$$

$$n_e(\Omega t, \theta) = \left[\frac{\cos^2(\theta)}{n_{e,1}^2(\Omega t)} + \frac{\sin^2(\theta)}{n_o^2} \right]^{-\frac{1}{2}}. \quad (2.26)$$

Once the light sees the birefringence, two angles α and β emerge within the crystal, shown in Fig. 2.5. A small deviation in angle θ can change the transverse trajectories at the output due to a different set of indices. Using standard algebra and modified Snell's law [114],

$$\alpha(\Omega t, \theta) = \arcsin \left(\frac{n_{\text{air}}}{n_o(\Omega t)} \sin(\theta) \right), \quad (2.27)$$

$$\beta(\Omega t, \theta) = \arcsin \left(\frac{n_{\text{air}}}{n_e(\Omega t, \theta)} \sin(\theta) \right) - \alpha(\Omega t, \theta). \quad (2.28)$$

Upon propagation, the o-beam shifts transversely by a distance d' , found as the tangent of the angle α multiplied by the crystal length L

$$d'(\Omega t, \theta) = L \tan [\alpha(\Omega t, \theta)], \quad (2.29)$$

Similarly, we can find the distance between o- and e-beams d using Eqs. (2.27), (2.28) and (2.29)

$$d(\Omega t, \theta) = L \tan [\alpha(\Omega t, \theta) + \beta(\Omega t, \theta)] - d', \quad (2.30)$$

defined as the distance between the o- and e-beam in the xy plane. It is important to know the distance between the two beams as the distance can change due to nonlinear interactions when the intensity becomes large.

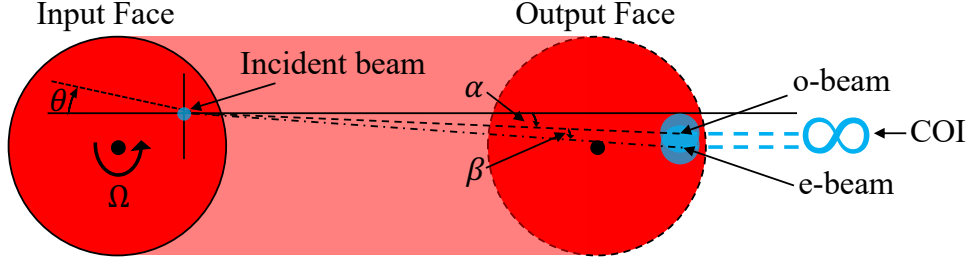


Figure 2.5: **Transverse movement of the ordinary (o) and the extraordinary (e) beam upon rotation and the walk-off angle β .** The o-beam propagates straight through the crystal, while the e-beam revolves around it in a circular pattern. Also depicted schematically is the centre of intensity (COI) of their intensities, tracing out figure-eight-like patterns for the linear dynamics of the system.

With the full description of the wave vectors in the case of a linear, rotating birefringent medium, we can describe the respective fields and how they will propagate within the crystal measuring in the lab frame. The sum of two fields describes the full field, the o- and e-fields, with spatially varying functions $A(x, y, z)$ and $B(x, y, z)$ as

$$\begin{aligned} \mathbf{E}(x, y, z, t, \Omega, \gamma) = & \hat{\mathbf{E}}_o(\Omega t, \theta)A(x, y, z)e^{i[\mathbf{k}_o(\Omega t, \theta) \cdot \mathbf{r} - \omega t]} \\ & + \hat{\mathbf{E}}_e(\Omega t, \theta)B(x, y, z)e^{i[\mathbf{k}_e(\Omega t, \theta) \cdot \mathbf{r} - \omega t]}, \end{aligned} \quad (2.31)$$

where $\hat{\mathbf{E}}_o = \hat{\mathbf{x}}'$, $\hat{\mathbf{E}}_e = \hat{\mathbf{y}}'$, and $\hat{\mathbf{x}}'$, $\hat{\mathbf{y}}'$ are defined in Eq. (2.15).

In most cases, the input optical beam is taken to be normal incidence. Alignment can justify $\theta = 0$, but a crystal can be cut in a non-optimal direction with respect to the easiest axis of rotation. Therefore, due to the crystal-cut optical axes, we consider the beam at normal incidence but imperfectly aligned ($\gamma \neq 0$). However, the simulation allows small angles in both γ and θ .

Imperfect Crystal Alignment $\gamma \neq 0$

Assuming normal incidence and non-zero tilt-angle, we find the electric field for linearly polarized light interacting with the medium as

$$\begin{aligned} \mathbf{E}(x, y, z, t, \Omega, \gamma) = & \hat{\mathbf{E}}_o(\Omega t, \gamma)A(x, y, z)e^{i[\mathbf{k}_o(\Omega t, \gamma) \cdot \mathbf{r} - \omega t]} \\ & + \hat{\mathbf{E}}_e(\Omega t, \gamma)B(x, y, z)e^{i[\mathbf{k}_e(\Omega t, \gamma) \cdot \mathbf{r} - \omega t]}. \end{aligned} \quad (2.32)$$

where $\hat{\mathbf{E}}_o = \hat{\mathbf{x}}'$, $\hat{\mathbf{E}}_e = \hat{\mathbf{y}}'$, and $\hat{\mathbf{x}}'$, $\hat{\mathbf{y}}'$ are defined in Eq. (2.15).

Due to linearly polarized light interacting with a rotating birefringent medium, we observe interesting linear dynamics in transverse trajectories at the output. The crystal is aligned such that, in the linear regime, the o-beam passes straight through, and the e-beam rotates around the o-beam at a rate of Ω . The behaviour of these trajectories to the rotation speed in linear and nonlinear regimes is discussed further in Sec. 2.6.3. Experimentally, the COI is more easily measured, so we simulate and produce COI trajectories looking for figure-eight-like trajectories [5] as seen in the experiment. The figure-eight shape arises from tracking intensity that reaches a maximum and minimum over each 90-degree interval between the o- and e-beams. COI is plotted in both simulation and experiment later in the discussion; however, the two beam positions can be tracked independently through simulation.

Applying Eq. (2.9) to the newly found fields of Eq. (2.32), we again search for non-trivial solutions of the system $\mathbf{A} * \mathbf{E} = \mathbf{0}$

$$\mathbf{A} = \begin{pmatrix} -k_z^2 + \frac{\omega^2}{c^2} \epsilon_{11} & \frac{\omega^2}{c^2} \epsilon_{12} & k_x k_z + \frac{\omega^2}{c^2} \epsilon_{13} \\ \frac{\omega^2}{c^2} \epsilon_{21} & k_x^2 - k_z^2 + \frac{\omega^2}{c^2} \epsilon_{22} & \frac{\omega^2}{c^2} \epsilon_{23} \\ k_x k_z + \frac{\omega^2}{c^2} \epsilon_{31} & \frac{\omega^2}{c^2} \epsilon_{32} & -k_x^2 + \frac{\omega^2}{c^2} \epsilon_{33} \end{pmatrix}. \quad (2.33)$$

We solve the determinant to find refractive indices in the crystal frame as $n_i = \sqrt{\epsilon_{ii}}$, that is

$$\begin{aligned} n_1 &= n_{e,1} + \delta n \cos^2(\gamma) [\sin^2(\Omega t) + \tan^2(\gamma)], \\ n_2 &= n_{e,2} - \delta n \cos^2(\gamma) \sin^2(\Omega t), \\ n_3 &\simeq n_o - \delta n \sin^2(\gamma). \end{aligned} \quad (2.34)$$

One can then write the index ellipsoid in the lab frame as

$$\frac{x'^2}{n_1^2} + \frac{y'^2}{n_2^2} + \frac{z'^2}{n_3^2} = 1, \quad (2.35)$$

where in the limit of the tilt angle going to zero, i.e. $\gamma = 0$, one recovers Eq. (2.24). In the simulation, we chose a value of $\gamma = \pi/1800 = 0.1$ degrees. We will now model how the new refractive indices' presence will alter the beam's propagation in the crystal.

We model the propagation of light starting from the vector wave equation to derive a nonlinear Schrödinger equation (NLSE) for the o- and e-beam by substituting the electric field from Eq. (2.32) and eigenvalue solutions for the wave vectors in Eq. (2.33). We assume

$\nabla \cdot \mathbf{E} \simeq 0$, $v \ll c$ and weak birefringence to obtain two NLSEs for the o- and e-beams

$$\begin{aligned}
& - \hat{\mathbf{E}}_o \nabla^2 [A e^{i(\mathbf{k}_o \cdot \mathbf{r} - \omega t)}] - \hat{\mathbf{E}}_e \nabla^2 [B e^{i(\mathbf{k}_e \cdot \mathbf{r} - \omega t)}] \\
& + \frac{1}{\epsilon_0 c^2} \frac{\partial^2}{\partial t^2} \left[\epsilon \hat{\mathbf{E}}_o A e^{i(\mathbf{k}_o \cdot \mathbf{r} - \omega t)} + \epsilon \hat{\mathbf{E}}_e B e^{i(\mathbf{k}_e \cdot \mathbf{r} - \omega t)} \right] = \mathbf{0}.
\end{aligned} \tag{2.36}$$

Being that $\hat{\mathbf{E}}_o = (E_{ox}, E_{oy}, E_{oz})$ and $\hat{\mathbf{E}}_e = (E_{ex}, E_{ey}, E_{ez})$ are orthogonal, we can separate the o- and e- beams into two distinct coupled NLSEs

$$\begin{aligned}
& \nabla^2 (A e^{i\mathbf{k}_o \cdot \mathbf{r}}) + \frac{\omega^2}{\epsilon_0 c^2} \hat{\mathbf{E}}_o \cdot \epsilon \hat{\mathbf{E}}_o A e^{i\mathbf{k}_o \cdot \mathbf{r}} \\
& \quad + \frac{\omega^2}{\epsilon_0 c^2} \hat{\mathbf{E}}_o \cdot \epsilon \hat{\mathbf{E}}_e B e^{i\mathbf{k}_e \cdot \mathbf{r}} = 0, \\
& \nabla^2 [B e^{i\mathbf{k}_e \cdot \mathbf{r}}] + \frac{\omega^2}{\epsilon_0 c^2} \hat{\mathbf{E}}_e \cdot \epsilon \hat{\mathbf{E}}_o A e^{i\mathbf{k}_o \cdot \mathbf{r}} \\
& \quad + \frac{\omega^2}{\epsilon_0 c^2} \hat{\mathbf{E}}_e \cdot \epsilon \hat{\mathbf{E}}_e B e^{i\mathbf{k}_e \cdot \mathbf{r}} = 0.
\end{aligned} \tag{2.37}$$

Evaluating $\nabla^2 [A e^{i\mathbf{k}_o \cdot \mathbf{r}}]$ and $\nabla^2 [B e^{i\mathbf{k}_e \cdot \mathbf{r}}]$, and applying the slowly varying envelope approximation, we obtain

$$\begin{aligned}
& 2i\mathbf{k}_o \cdot \nabla A + \nabla_{\perp}^2 A + \left(\frac{\omega^2}{\epsilon_0 c^2} \hat{\mathbf{E}}_o \cdot \epsilon \hat{\mathbf{E}}_o - \mathbf{k}_o^2 \right) A = 0, \\
& 2i\mathbf{k}_e \cdot \nabla B + \nabla_{\perp}^2 B + \left(\frac{\omega^2}{\epsilon_0 c^2} \hat{\mathbf{E}}_e \cdot \epsilon \hat{\mathbf{E}}_e - \mathbf{k}_e^2 \right) B = 0,
\end{aligned} \tag{2.38}$$

where $\nabla_{\perp}^2 = \frac{\partial^2}{\partial x^2} + \frac{\partial^2}{\partial y^2}$ is the transverse Laplacian, and $\mathbf{k}_{o,e}^2(\Omega t, \theta) = \frac{n_{o,e}^2(\Omega t, \theta)\omega^2}{c^2}$ are the wave vectors with refractive indices defined as in Eqs. (2.25), (2.26).

Suppose that dispersion is large such that the phase and group indices are significantly different. As a result, the group indices can be written as

$$\begin{aligned}
& n_o \rightarrow n_o^g = n_o + \omega_0 \left(\frac{\partial n_o}{\partial \omega} \right)_{\omega_0}, \\
& n_e \rightarrow n_e^g = n_e + \omega_0 \left(\frac{\partial n_e}{\partial \omega} \right)_{\omega_0},
\end{aligned} \tag{2.39}$$

where $n_{o,e}^g$ are the group refractive indices for the o- and e-beams, respectively.

2.3.3 Nonlinear Group Index Contributions to NLSE

Everything up to this point has been considered linear; however, the large dispersion results from a nonlinear contribution, a key feature of this work. We write this response as

$$n_{g_{o,e}} \rightarrow n_{g_{o,e}}^{\text{eff}} \approx n_{o,e}^g + \frac{1}{2}n_2^g I_{o,e}. \quad (2.40)$$

Here, we have introduced a nonlinear contribution to the group index, n_2^g , being the nonlinear group index, and $I_{o,e}$ are the intensities for both the o- and e-beams, respectively. It is important to note that we assume that both beams see the same magnitude of the nonlinear contribution of self-focusing. However, the magnitude will change based on the intensity that varies between the o- and e-beams as the crystal rotates. The implications of this intensity dependence, as well as rotation speed dependence of the group index, will be further discussed in Sec. 2.4.1. We can define an effective refractive index for the o- and e-beams

$$\begin{aligned} n_o^{\text{eff}^2} &= n_o + \omega_0 \left(\frac{dn_o}{d\omega} \right)_{\omega_0} + \frac{n_2^g |A|^2}{2}, \\ n_e^{\text{eff}^2} &= n_e + \omega_0 \left(\frac{dn_e}{d\omega} \right)_{\omega_0} + \frac{n_2^g |B|^2}{2}. \end{aligned} \quad (2.41)$$

We must also apply a Lorentz transformation, Δk , to be in a moving reference frame,

$$\Delta k = -\frac{\omega^2 \Omega x_0}{c}. \quad (2.42)$$

Applying the transform and substitutions for the effective refractive indices, our transverse beam profile becomes

$$\begin{aligned} A &= a \exp \left(i \frac{(n_o^{\text{eff}^2} - n_o^2)}{2k_o^2 c^2} \Delta \vec{k}'_o \cdot \hat{r} \right), \\ B &= b \exp \left(i \frac{(n_e^{\text{eff}^2} - n_e^2 \cos(\gamma)^2)}{2k_e^2 \cos(\gamma)^2 c^2} \Delta \vec{k}'_e \cdot \hat{r} \right). \end{aligned} \quad (2.43)$$

Substituting the fields into the two generalized coupled NLSEs, we arrive at

$$\begin{aligned}
\partial_z a &= \frac{i}{2k_o} \nabla_{\perp}^2 a - \frac{k_o}{n_o} \Delta n_{NL} a - \frac{\omega^2 (n_o^{\text{eff}2} - n_o^2) \Delta k}{2k_o^2 c^2} \partial_y a, \\
\partial_z b &= \frac{i}{2k_e \cos(\gamma)^2} \nabla_{\perp}^2 b + \frac{k_e}{n_e \cos(\gamma)^2} \Delta n_{NL} b \\
&\quad + 2 \tan(\gamma) (\cos(\Omega t) \partial_x b + \sin(\Omega t) \partial_y b) + 2 \frac{\omega^2 (n_e^{\text{eff}2} - n_e^2) \Delta k}{2k_e^2 \cos(\gamma)^4 c^2} \partial_y b.
\end{aligned} \tag{2.44}$$

We have introduced a nonlinear index gradient caused by nonlinear refraction, $\Delta n_{NL}(I)$, where I is the beam intensity. This contribution becomes relevant with intense illumination, further discussed in Sec. 2.4.3. In general, the component $\Delta n_{NL}(I)$ can contribute to the system, but the nonlinear contributions that are large enough to affect the nonlinear Schrödinger equations are only Kerr nonlinearities. Assuming monochromatic light, weak birefringence ($\delta n \ll 1$) and $v \ll c$, the coupled nonlinear Schrödinger equations become

$$\begin{aligned}
\partial_z a &= \frac{i}{2k_o} \nabla_{\perp}^2 a - \frac{ik_o}{n_o} \Delta n_{NL} a - \frac{n_g^{NL}}{c} \partial_y a, \\
\partial_z b &= \frac{i}{2k_e \cos(\gamma)^2} \nabla_{\perp}^2 b + \frac{ik_e}{n_e \cos(\gamma)^2} \Delta n_{NL} b + 2 \tan(\gamma) (\cos(\Omega t) \partial_x b + \sin(\Omega t) \partial_y b) + \frac{n_g^{NL}}{c} \partial_y b.
\end{aligned} \tag{2.45}$$

We simulate these two NLSEs and show the results of nonlinear propagation through the 2 cm long rotating birefringent ruby rod to extract the transverse trajectories of the COI of the two beams and the amount of transverse shift at the output face of the crystal in Sec. 2.6.4. The thermal nonlinear response of Δn_{NL} is important when the timescales of interactions are long (i.e., non-instantaneous), and the nonlocal response is strong. However, the simulations show that these effects are small in comparison to the nonlinear response of the group index. That being said, a discussion on the thermal response is included in Sec. 2.4.3. Therefore, we will now discuss the effects of the nonlinear group index.

2.4 Influence of Nonlinear Group Index

2.4.1 Definition of the Nonlinear Group Index of the COI

Starting from the general definition, we have the group refractive indices for the o- and e-beams as

$$n_{o,e}^g = n_{o,e} + \left(\omega \frac{\partial n_{o,e}}{\partial \omega} \right)_{\omega_o}. \quad (2.46)$$

We can represent the individual dependencies on the rotation speed and input intensities of the group indices for the o- and e-beams by utilizing the Lorentz transformation in Eq. (2.42) to find

$$\begin{aligned} n_o^g &= n_o + \frac{\left(n_o^{\text{eff}^2} - n_o^2 + n_o^g n_2^g I_a \right)}{2n_o^3} \frac{\Omega x_0}{c}, \\ n_e^g &= n_e + \frac{\left(n_e^{\text{eff}^2} - n_e^2 + n_e^g n_2^g I_b \right)}{2n_e^3 \cos(\gamma)^4} \frac{\Omega x_0}{c}, \end{aligned} \quad (2.47)$$

where

$$\begin{aligned} I_a &\simeq |(-h) \sin(\Omega t) + v \cos(\Omega t)|^2 I_0, \\ I_b &\simeq |h \cos(\Omega t) + v \sin(\Omega t)|^2 I_0. \end{aligned} \quad (2.48)$$

These intensities are the individual intensities of the o- and e-beams, respectively. The variables h and v represent the input polarization in the lab frame, whether H - and V -linear polarization. We have made a correction to the lowest order to the ordinary and extraordinary refractive indices that $n_o^{\text{eff}} \approx n_o^g + \frac{1}{2} n_2^g I_a$ and $n_e^{\text{eff}} \approx n_e^g + \frac{1}{2} n_2^g I_b$. We can define a collective n_g^{NL} that describes the COI of these two beams as

$$n_g^{NL} = n_g^0 + n_2^g I, \quad (2.49)$$

where $I = I_a + I_b$ and we approximate $n_g^0 = (n_o^g + n_e^g)/2$ due to weak birefringence, and $n_2^g I \gg n_g^0$.

2.4.2 Rotation Speed and Intensity Dependence of Nonlinear Group Index

We have shown in great detail that the o- and e-beams depend on the intensity and the rotation speed for their respective $n_{o,e}^g$. However, the transverse shift observed in the

experiment is a result of their collective effect. The collective nonlinear group index n_g^{NL} is rotation speed and intensity-dependent, that is

$$n_g^{NL} := n_g^{NL}(\Omega, I_0), \quad (2.50)$$

which controls the magnitude of the nonlinear photon drag effect.

One can draw an analogy to transverse self-steepening [115]. In a self-steepened pulse, the group velocity of the region near the peak of the pulse, corresponding to its maximum intensity, will travel faster than the wings. This effect is often considered along the propagation direction, but one can also consider the transverse equivalent. In the transverse case, since the medium is moving, the maximum index gradient, whether of thermal or optical origin, is located at the place of maximum intensity. If the medium is rotating, the maximum intensity moves and therefore beam deflects off of the moving index gradient, changing the beam shape similar to that of a self-steepened pulse. This lateral shift in the beam depends on the rotation speed's magnitude and direction, which controls the magnitude of the index gradient.

Our model has considered an instantaneous nonlinearity, which is the case for Kerr nonlinearities. That is, however, a simplification of the system in question. The rotation speed represents the non-instantaneous nature of the nonlinearity. The rotation describes a temporal-like response, where the rate at which the heat dissipates within the crystal is governed by the sampling time the rotation speed dictates. Fast timescales can act and locally affect the beam when considering slow speeds. On the other hand, fast speeds see the effects of more long-lived effects on an integer multiple of a full rotation of the crystal due to the fact that the heat doesn't fully dissipate over a full rotation. In the following two sections, we will describe how the thermal and optical nonlinear response contribute to the index gradient that controls the magnitude of the n_g^{NL} and the amount of transverse shift experienced by the optical beam upon propagation for a non-instantaneous, nonlinear response.

Thermal Contribution

When considering slower rotation speeds, the thermal nonlinear response contributes most of the nonlinear response of the n_g^{NL} as the time scale of the interaction can locally affect the beam, typically on the order of several hundred microseconds [116]. To understand how the thermal nonlinear response impinges upon the crystal, a depiction of the heat deposition and distribution of the crystal is shown in Fig. 2.6. Sufficiently slow speeds keep the index gradient created by the input beam relatively constant in magnitude. That

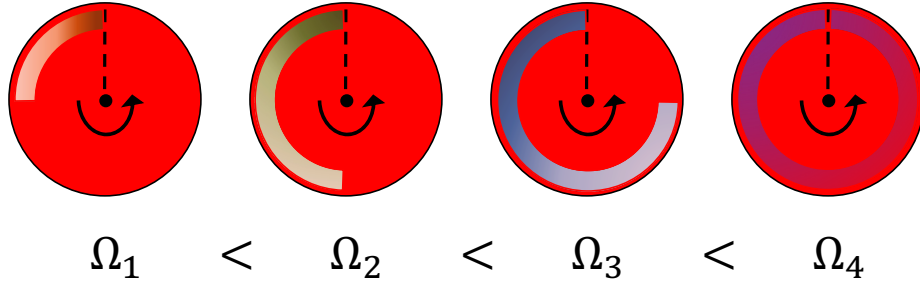


Figure 2.6: **Schematic optical beam distributing heat over a rotating ruby rod crystal face.** The heat distribution circles about the crystal cause an index gradient with varying magnitude depending on speed. The heat reaches different distances depending on the rotation speed until it reaches fully around the crystal, producing a smaller magnitude of index gradients at higher rotation speeds. The distribution can also reach a steady-state-like response where the heat is equally distributed.

is to say, the movement causes an index gradient that does not change in time as quickly. The transverse shift due to the index gradient steadily increases with rotation speeds up to characteristic speed, Ω_c . After this threshold, the beam sees less build-up of a moving index gradient upon rotation and experiences less transverse shift. Both the thermal and optical nonlinear response contribute to the size of the index gradient; however, both effects take place over different timescales and, therefore, different rotation speeds. Here, we observe a diminishing contribution from the thermal nonlinear response with increasing rotation speed, or even a steady-state response like in the case of Ω_4 in Fig. 2.6.

The characteristic speed is related to the timescale of the interaction. For example, if the timescale of the interaction is $\tau_c = 3$ ms, then the characteristic rotation speed in deg/s would be $\Omega_c = (2\pi\tau_c)^{-1} \approx 60$ deg/s. For a characteristic rotation speed of $\Omega_c = 100$ deg/s, as is the case for our ruby rod [5], the time scale is $\tau_c = 1.6$ ms. Above a characteristic speed, Ω_c , the nonlinearity becomes predominantly optical in nature.

The optical effect also occurs at slow speeds but with a smaller magnitude. The time scale of the optical nonlinear response acts strongly when the rotation speed matches the rotation time for an integer multiple of rotations. The exponential decay at slow speeds has a relatively constant index gradient. At higher speeds, the beam samples only some of the index gradient by the thermal nonlinear response. The maximum group index gradient is represented as

$$\Delta n_{\max}^g(t) = n_2^g I_0 e^{-(t-t_0)/\tau_c}, \quad (2.51)$$

where I_0 is the input intensity, τ_c is a characteristic decay time of the nonlinear process, and t_0 is an offset time. We rewrite Eq. (2.51) as a function of the rotation speed, $(t - t_0)/\tau_c = (\Omega - \Omega_0)/\Omega_c$, where Ω_c is a characteristic rotation speed, and Ω_0 is an offset rotation speed. This expression relates the temporal dynamics to the rotation speed such that we write n_g^{NL} ,

$$n_g^{NL} = n_g^0 + n_2^g I = n_g^0 + n_2^g I_0 e^{-(\Omega - \Omega_0)/\Omega_c}. \quad (2.52)$$

The n_g^{NL} in the form of Eq. (2.52) shows the general case when considering the system dynamics. For $\Omega < \Omega_c$, the nonlinear response is predominantly thermal, denoted $\Omega_f = (2\pi\tau_f)^{-1}$, where $\tau_f \approx 200 \mu\text{s}$ [116] is a typical thermal timescale. The thermal contribution to the n_g^{NL} is therefore

$$n_g^{NL} = n_g^0 + n_{2,\text{therm}}^g I_0, \quad (2.53)$$

where $n_{2,\text{therm}}^g$ is the thermal nonlinear group index,

$$n_{2,\text{therm}} = -\alpha_f n_2^g e^{-(\Omega - \Omega_0)/\Omega_f}, \quad (2.54)$$

and α_f is a phenomenological scaling factor.

For $\Omega > \Omega_c$, other nonlinear responses take over, denoted $\Omega_s = (2\pi\tau_s)^{-1}$. Some optical processes depend on the lifetime of the excited state of an atom, which can be on the order of $\tau_s = 3 \sim 5 \text{ ms}$ [88] that fit into this region. If the effect was only a thermal nonlinear process, the shift would progressively approach zero with higher rotation speeds.

Optical Contribution

In order to facilitate the explanation of the optical contributions, we'll begin using experimental parameters here. We input a Gaussian beam profile in the xy plane with a beam waist of $10 \mu\text{m}$ at a position $x_0 = 0.8R$, where R is the radius ($R = 0.35 \text{ cm}$) and L is the length ($L = 2 \text{ cm}$) of the crystal, respectively. In the regime of $\Omega > \Omega_c$, n_g^{NL} is the optical nonlinear response of CPO, giving rise to large group indices [88]. Similarly, we write the optical response of n_g^{NL}

$$n_g^{NL} = n_g^0 + n_{2,\text{opt}}^g I_0, \quad (2.55)$$

where the optical nonlinear group index takes the form

$$n_{2,\text{opt}} = \alpha_s n_2^g e^{-(\Omega - \Omega_0)/\Omega_s}, \quad (2.56)$$

where α_s is a scaling constant. We note the sign of the nonlinear contribution is now positive. Certain systems exhibit a large negative group index $n_g \approx -10^6$ [4], and the

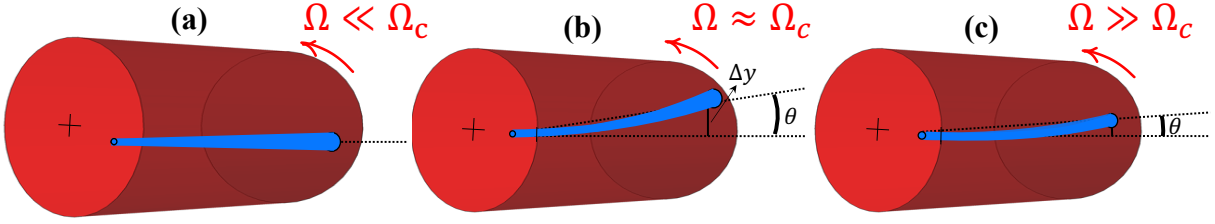


Figure 2.7: **Schematic of curved trajectory induced by a moving index gradient created by the nonlinear refraction.** (a) shows the trajectory at very slow speeds, (b) shows the largest transverse shift around $\Omega = \Omega_c$, and (c) shows a smaller transverse shift at high speeds.

value was set to be $n_2^g I_0 = -1.1 \times 10^6$. The coexistence of the two nonlinear processes results in a purely positive transverse shift at the output of the crystal. $n_2^g I_0$, however, can be set to any value depending on the system at hand.

Since the system impinges an index gradient that moves with the medium, the trajectory can be curved, contributing to the overall transverse shift. An example of a curved trajectory is shown in Fig. 2.7, which conveys the idea of a non-zero output angle at the end of the medium. It is crucial to measure this output angle to distinguish if nonlinear deflection has also contributed to the transverse shift. The photon drag effect generally exits the crystal parallel to the input beam. However, we stress that although the beam exits at an angle that is not parallel, it propagates in a straight line from that output angle, as expected in free space.

Intensity (W/cm ²)	Speed Range (deg/s)	Variable	Value
6.4×10^4	5~100	$(n_g^0/n_2^g I_0)/\alpha_f/\Omega_f$	166/1.4/21
6.4×10^4	100~9000	$(n_g^0/n_2^g I_0)/\alpha_s/\Omega_s$	11/151/576
3.3×10^5	5~100	$(n_g^0/n_2^g I_0)/\alpha_f/\Omega_f$	617/80/49
3.3×10^5	100~9000	$(n_g^0/n_2^g I_0)/\alpha_s/\Omega_s$	51/486/1190

Table 2.1: **Results of the phenomenological fit for the n_g^{NL} .** Fit variables for the expressions in Eq. (2.59) in the nonlinear ($P = 100$ mW, $I = 3.3 \times 10^4$ W/cm²) and highly nonlinear ($P = 520$ mW, $I = 6.4 \times 10^5$ W/cm²) regimes for low-to-mid speeds ($\Omega = 5 \sim 100$ deg/s) and mid-to-high speeds ($\Omega = 100 \sim 9000$ deg/s) are shown.

Coexistence of Nonlinear Optical Responses on Nonlinear Group Index

Since the n_g^{NL} depends on both the optical and thermal nonlinear responses, one can write the full n_g^{NL} as

$$n_g^{NL} = n_g^0 + n_{2,\text{opt}}^g I_o + n_{2,\text{therm}}^g I_o. \quad (2.57)$$

Expanding this form using Eqs. (2.53, 2.55), we can rewrite n_g^{NL}

$$n_g^{NL} = n_g^0 + n_2^g I_o \left(\alpha_s e^{-(\Omega-\Omega_0)/\Omega_s} - \alpha_f e^{-(\Omega-\Omega_0)/\Omega_f} \right). \quad (2.58)$$

The nonlinear group index is $n_2^g I_o = 0.11 \times 10^7 \text{m}^2/\text{W}$, and fit constants α_s and α_f are taken to be 0.97 and 0.94, respectively. Equation (2.58), however, is a simplified, compact form of n_g^{NL} . These values are found by comparing them to our experiment in Chapter 3. The behaviour of n_g^{NL} is piece-wise about a characteristic speed Ω_c , which captures the dynamics above and below Ω_c . We use the piece-wise form for n_g^{NL} in our simulations written as

$$n_g^{NL} = n_2^g I_o \times \begin{cases} (n_g^0/n_2^g I_o) - \alpha_f \exp\left(-\frac{\Omega-\Omega_c}{\Omega_f}\right) & \Omega \leq \Omega_c \\ (n_g^0/n_2^g I_o) + \alpha_s \exp\left(-\frac{\Omega-\Omega_c}{\Omega_s}\right) & \Omega \geq \Omega_c. \end{cases} \quad (2.59)$$

Fit values for the piece-wise function are summarized in Table 2.1. Offsets are described by $a_{1,2}$, amplitudes $b_{1,2}$, and characteristic speeds $c_{1,2}$ for thermal and optical nonlinear response. All constants are strictly positive and retrieved for low-to-mid (5~100 deg/s) and mid-to-high (100~9000 deg/s) rotation speeds.

With complete knowledge of the system and the dynamics of n_g^{NL} , nonlinear propagation of the two coupled NLSEs is simulated using the Split-Step Fourier Method (SSFM) to extract the amount of transverse shift as well as the transverse trajectories at the crystal output. The results of the simulated NLSEs are discussed in the following section. Furthermore, the details of how the simulations are performed are described in Sec. 2.5.

2.4.3 Thermal Nonlinear Response

Although the index gradient impinged by a thermal nonlinearity does not contribute strongly to the amount of transverse shift, analyzing the effect is worth noting. Let's consider intense illumination impinged on media with nonlinear refraction, creating an index gradient modifying the dielectric tensor. Therefore, for first-order correction in the crystal frame, the dielectric permittivity is

$$\epsilon' \longrightarrow \epsilon' + \Delta\epsilon'_{NL}, \quad (2.60)$$

where $\Delta\epsilon'_{NL}$ is written as

$$\Delta\epsilon'_{NL} = 2\epsilon_0\Delta n'_{NL} \begin{pmatrix} n_e & 0 & 0 \\ 0 & n_o & 0 \\ 0 & 0 & n_o \end{pmatrix}. \quad (2.61)$$

The index gradient created by nonlinear refraction is also affected by the rotation of the medium and tilt angle γ , where

$$\Delta n'_{NL} \rightarrow \Delta n'_{NL}(\Omega t, \gamma). \quad (2.62)$$

In thermal media [117], the index gradient due to thermal nonlinear response is

$$\Delta n'_{NL} = \left(\frac{\partial n}{\partial T} \right)_0 \Delta T(\mathbf{r}'), \quad (2.63)$$

where $\left(\frac{\partial n}{\partial T} \right)_0$ is the medium's thermo-optic coefficient at thermal equilibrium (steady-state response) and $\Delta T(\mathbf{r}')$ is the temperature variation about the point $\mathbf{r}' = (x', y', z')$. $\Delta T(\mathbf{r}')$ for a stationary medium is governed by the 3D heat equation

$$(\partial_{x'}^2 + \partial_{y'}^2 + \partial_{z'}^2) \Delta T(\mathbf{r}') = -\gamma |\mathbf{E}'(\mathbf{r}')|^2, \quad (2.64)$$

with $\gamma_l = (L_{loss}\rho_0 c_P D_T)^{-1}$, where L_{loss} is the loss characteristic length, ρ_0 the material density, c_P the specific heat at constant pressure, and D_T is the thermal diffusivity. The solution can be written in terms of a Green function $G(\mathbf{r}')$, which depends only on the sample geometry and the boundary conditions and expresses the nonlocality of the nonlinear effect

$$\Delta T(\mathbf{r}') = \iiint d\tilde{\mathbf{r}}' G'(\mathbf{r}' - \tilde{\mathbf{r}}') |\mathbf{E}'(\tilde{\mathbf{r}}')|^2. \quad (2.65)$$

Around the neighborhood of the medium's midpoint, i.e. $z_0 = L/2$, in the longitudinal parabolic approximation of characteristic width $L_{nloc} = \sqrt{\frac{|n_2|}{\gamma_l \left| \frac{\partial n}{\partial T} \right|_0}} \propto \sqrt{L_{loss}}$ [117], n_2 the nonlinear refractive index, L_{loss} is the characteristic loss length, Eq. (2.65) reads

$$\Delta T_{\perp}(\mathbf{r}_{\perp}') = \iint d\tilde{\mathbf{r}}'_{\perp} G'_{\perp}(\mathbf{r}_{\perp}' - \tilde{\mathbf{r}}'_{\perp}) I'_{\perp}(\tilde{\mathbf{r}}'_{\perp}), \quad (2.66)$$

with $I'_{\perp}(\mathbf{r}_{\perp}') = \frac{1}{L} \int dz' I'(\mathbf{r}_{\perp}', z')$, $I'(\mathbf{r}') = |\mathbf{E}'(\mathbf{r}')|^2 = |\mathbf{E}(\mathbf{r})|^2 = I(\mathbf{r})$, and $\mathbf{r}_{\perp}' = (x', y')$. Assuming absorption is low ($L \ll L_{loss}$), we find $\Delta T(\mathbf{r}') \sim \Delta T_{\perp}(\mathbf{r}_{\perp}')$ and $\partial_{z'} I'(\mathbf{r}') \sim 0$. As a result, the index gradient impinged on the crystal by the thermal nonlinear response is

$$\Delta n'_{NL}(\mathbf{r}_{\perp}') = n_2 \iint d\tilde{\mathbf{r}}'_{\perp} K'(\mathbf{r}_{\perp}' - \tilde{\mathbf{r}}'_{\perp}) I'(\tilde{\mathbf{r}}'_{\perp}) - n_{o,e}, \quad (2.67)$$

Variable	Functionality
K_γ	Thermal Kernel Function
$\left(\frac{\partial n}{\partial T}\right)_0$	Thermo-optic coefficient
$\Delta T(\mathbf{r}')$	Temperature Variation
L_{loss}	Characteristic Loss Length
ρ_0	Material Density
c_P	Specific Heat at Constant Pressure
D_T	Thermal Diffusivity
$G(\mathbf{r}')$	Green's Function
L_{nloc}	Nonlocal Length
t_N	Non-instantaneous timescale

Table 2.2: **Summary of the relevant variables used to calculate the index gradient Δn_{NL} due to a thermal nonlinearity.** The definition of the variables is used to clarify the function of each variable within the derivative.

with $n_2 K'(\mathbf{r}_\perp) = \left(\frac{\partial n}{\partial T}\right)_0 G'_\perp(\mathbf{r}'_\perp)$. The index gradient is now written as

$$\Delta n_{NL}(x, y, \Omega t, \gamma) = n_2 \iint d\tilde{x}d\tilde{y} K_\gamma(\Delta x, \Delta y, \Omega t) I(\tilde{x}, \tilde{y}) - n_{o,e}, \quad (2.68)$$

where K_γ is the nonlinear nonlocal kernel function affected by the weak birefringence, written as

$$K_\gamma(x, y, \Omega t, \gamma) = K'[\cos(\gamma)(\cos(\Omega t)x + \sin(\Omega t)y), -\sin(\Omega t)x + \cos(\Omega t)y]. \quad (2.69)$$

Understanding the importance of the kernel function further requires a definition in Fourier space, as the NLSE adds the nonlinear response as a phase term. Therefore, the kernel function in Fourier space is

$$K_\gamma(k_x, k_y, \Omega t, \gamma) = \frac{1}{2\pi [(k'_x)^2 + (k'_y)^2] \left[1 + L_{nloc}^2 \left(1 - \exp\left(-\frac{t}{\tau_N}\right)\right)\right]}, \quad (2.70)$$

where L_{nloc} is the nonlocal length, τ_N is the non-instantaneous timescale, and k'_x and k'_y are the x and y wave vectors in the crystal reference frame. The nonlocality does not play a huge role but scales the non-instantaneous response. The non-instantaneous part

only plays a role when the timescales of the interactions are long-lived, on the order of seconds or more. A summary of the variables and their functionality can be found in Table 2.2. With all relevant variables, we can define how the dielectric permittivity is affected by an index gradient. Therefore in the lab frame, we write the dielectric tensor with all perturbative terms under the assumption of weak birefringence

$$\epsilon = \epsilon' + \epsilon''(\gamma, \Omega t) + \Delta\epsilon'_{NL}(x, y, \Omega t, \gamma). \quad (2.71)$$

2.5 Simulation Methods

We apply the SSFM to simulate nonlinear propagation through the rotating ruby rod of length L . We input a Gaussian beam profile in the xy plane focused to a position far from the centre of rotation.

2.5.1 Linear and Nonlinear Propagators

The NLSEs in Eq.(2.45) are propagated with the usual formalism of a linear propagator \hat{D} and a nonlinear propagator \hat{N} . We can represent the NLSEs in the SSFM formalism as

$$\begin{aligned} \partial_z a &= (\hat{D}_o + \hat{N}_o)a, \\ \partial_z b &= (\hat{D}_e + \hat{N}_e)a, \end{aligned} \quad (2.72)$$

where the linear propagators are defined as

$$\begin{aligned} \hat{D}_o &= \frac{i}{2k_o} \nabla_{\perp}^2 - \frac{n_g^{NL}}{c} \partial_y, \\ \hat{D}_e &= \frac{i}{2k_e \cos(\gamma)^2} \nabla_{\perp}^2 + \frac{n_g^{NL}}{c} \partial_y + 2 \tan(\gamma) (\cos(\Omega t) \partial_x + \sin(\Omega t) \partial_y), \end{aligned} \quad (2.73)$$

and the nonlinear propagators are defined as

$$\begin{aligned} \hat{N}_o &= \frac{ik_o}{n_o} \Delta n_{NL}, \\ \hat{N}_e &= \frac{ik_e}{n_e \cos(\gamma)^2} \Delta n_{NL}. \end{aligned} \quad (2.74)$$

The fields a and b represent the o- and e- fields, respectively. We can interchange between real space (a and b) and Fourier space (\hat{a} and \hat{b}) using a Fourier Transform (FT), or vice versa with the inverse FT, that is

$$\begin{aligned} a(x, y, z) &= \frac{1}{2\pi} \iint_{\mathbb{R}^2} dk_x dk_y \hat{a}(k_x, k_y, z) e^{-i(k_x x + k_y y)}, \\ \hat{a}(k_x, k_y, z) &= \frac{1}{2\pi} \iint_{\mathbb{R}^2} dx dy a(x, y, z) e^{i(k_x x + k_y y)}. \end{aligned} \quad (2.75)$$

where b and \hat{b} are written in a similar fashion.

We apply the linear propagators in Fourier space between the points z and $z + h$, that is

$$\begin{aligned} \exp\left(\frac{h}{2}\hat{D}_o\right) &= \exp\left(\frac{-ih}{2}\left[\frac{-1}{2k_o}(k_x^2 + k_y^2) - i\frac{n_g^{NL}}{c}k_y\right]\right), \\ \exp\left(\frac{h}{2}\hat{D}_e\right) &= \exp\left(\frac{-ih}{2}\left[\frac{-1}{2k_e \cos(\gamma)^2}(k_x^2 + k_y^2) - i\frac{n_g^{NL}}{c}k_y + 2\tan(\gamma)(\cos(\Omega t)k_x + \sin(\Omega t)k_y)\right]\right). \end{aligned} \quad (2.76)$$

The linear step is then applied by taking the inverse FT of the product of the linear propagator in Fourier space and the FT of the field

$$\begin{aligned} K_{1n} &= hf(x_n, y_n), \\ K_{2n} &= hf\left(x_n + \frac{1}{2}h, y_n + \frac{1}{2}K_{1n}\right), \\ y_{n+1} &= y_n + K_{2n} + O(h^3). \end{aligned} \quad (2.77)$$

We then will apply the nonlinear propagators assuming the boundary conditions $y' = f(x, y)$ and $y(x_o) = y_o$. At the n^{th} step, we have

$$\begin{aligned} a &= \text{IFT}\left[\exp\left(\frac{h}{2}\hat{D}_o\right)\text{FT}[a]\right], \\ b &= \text{IFT}\left[\exp\left(\frac{h}{2}\hat{D}_e\right)\text{FT}[b]\right]. \end{aligned} \quad (2.78)$$

Recall that Δn_{NL} is dependent on both fields, that is $\Delta n_{NL} := \Delta n_{NL}(|a|^2 + |b|^2)$. Therefore, the nonlinear propagators are functions of both a and b . We apply the propa-

gators in the following manner

$$\begin{aligned}
A_{1n} &= h\hat{N}_o(a_n, b_n) a_n, \\
B_{1n} &= h\hat{N}_e(a_n, b_n) b_n, \\
A_{2n} &= h\hat{N}_o\left(a_n + \frac{1}{2}A_{1n}, b_n + \frac{1}{2}B_{1n}\right) \left(a_n + \frac{1}{2}A_{1n}\right), \\
B_{2n} &= h\hat{N}_e\left(a_n + \frac{1}{2}A_{1n}, b_n + \frac{1}{2}B_{1n}\right) \left(b_n + \frac{1}{2}B_{1n}\right), \\
a_{n+1} &= a_n + A_{2n} \\
b_{n+1} &= b_n + B_{2n}.
\end{aligned} \tag{2.79}$$

Once we have applied these propagators over the entire length of the crystal, one can take the centre of intensity of the two beams and track the transverse trajectories at the crystal's output facet. Furthermore, we can take the average, weighted by the intensities, of these trajectories to extract the transverse shift, which is controlled by the rotation speed input intensity.

This section has allowed us to break up light propagation into linear and nonlinear propagators, and this can capture the effects of the dynamics. With this, we can simulate the transverse trajectories and extract the transverse shifts to match to experiment seen in the following chapter.

2.6 Simulation Results

2.6.1 Fields along Propagation in Space and Time

The field is calculated frame by frame in time for a given z -position. Therefore, we can look at how the beam looks in the linear, nonlinear and highly nonlinear regime for a given speed at different z -positions to understand its evolution in space and time. The beam impinges at normal incidence, with a slight tilt angle, $\gamma = \pi/1800$.

Although the positions of the o- and e-beams can be tracked, looking at the electric field distribution is also often beneficial. Figure 2.8 shows the evolution of the beam along z , rotation in time for three input powers $P = 0.2$ mW, $P = 100$ mW, and $P = 520$ mW at a rotation speed of $\Omega = 100$ deg/s. This speed was chosen to show the effects of both nonlinear responses resulting from optical and thermal origin. We examine the overlapped

o- and e-beam fields along z at three positions $z = L/3$, $z = 2L/3$, and $z = L$, where $L = 2$ cm. Figure 2.8(a) shows the beam size increases along propagation direction z and how the beam rotates in time t in a linear regime; while Fig. 2.8(b) and (c) show nonlinear and highly nonlinear regimes. For a fixed time $t = 0.90$ s, the beam transverse profile increases in size along z due to the beam diverging. The beam also moves further out in x - and y -directions with an increase in power. In the highly nonlinear case, the transverse profile leaves a shadow-like beam behind. This shadow is a gradient impinged by the beam that disappears over thermal time scales of a few hundred microseconds. Another point to note about the transverse profile is that the beam is not structured, but takes on a structured look, likely due to the interference of the two beams overlaid on top of one another in the transverse plane. There is indeed no modal structure considered for the beams that are propagating through the crystal.

For a fixed z -position in Fig. 2.8, the advancement in time shows the beam rotating about the transverse plane. Tracking the beam movement is much more easily followed if the centre of intensity (COI) is taken. The COI is the weighted average of the intensity of the two beams by considering the relative weighting for a given point in time and space. If one follows the COI, a figure-eight would be traced out for the case in the linear regimes. The nonlinear and highly nonlinear regimes contain more complicated dynamics and show transverse shifting and distortions to the figure-eight-like patterns discussed in Sec. 2.6.3.

In the linear regime ($P = 0.2$ mW), the medium rotation speed has little to no effect on the beam trajectories and beam path. The beam paths will vary significantly with rotation speed when considering the nonlinear and highly nonlinear regimes. Both optical and thermal nonlinearities contribute to the dynamics and change the amount of transverse shifting as well as how much a beam trajectory is distorted. At fast speeds, for example, thermal nonlinear effects are essentially averaged out, while for slower speeds, the timescale can act on the beam more locally and cause larger distortions. The optical nonlinear effect is considered at faster speeds and affects the beam trajectories based on how well it affects the same region over an integer multiple of rotation. Therefore, investigating different speeds and input powers gives a much better understanding of the dynamics happening within the system, as well as the crystal output.

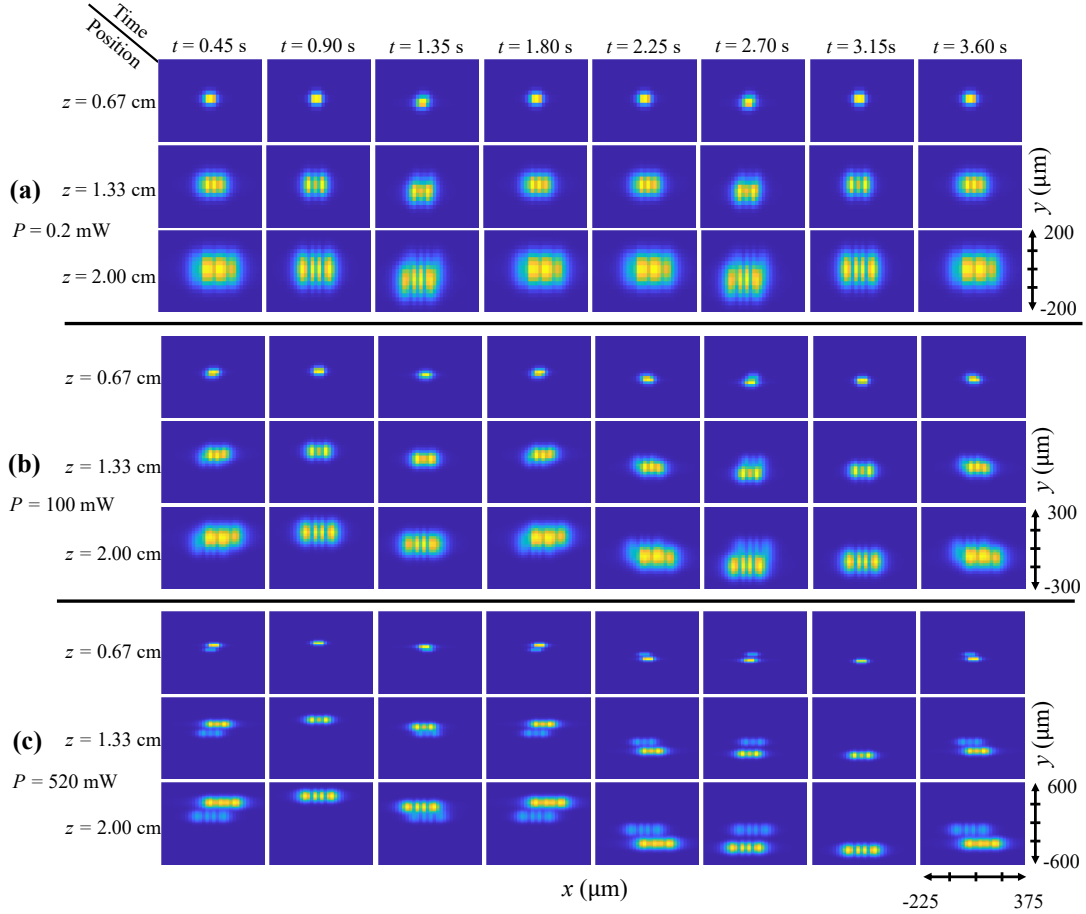


Figure 2.8: **Numerical results for propagation and rotation effects on the electric field distribution.** The total electric field of the o- and e-beams is plotted for three z -positions, $z = L/3$ cm, $z = 2L/3$, and $z = L$, where $L = 2$ cm, and over eight different frames along the rotation in time for a rotation speed of $\Omega = 100$ deg/s for three regimes: **(a)** Linear ($P = 0.2$ mW), **(b)** Nonlinear ($P = 100$ mW) and **(c)** Highly Nonlinear ($P = 520$ mW). Nonlinear effects can be observed leaving imprinted beams when the input power is sufficiently high $P > 100$ mW. The field trajectories widen with increasing power due to the nonlinear deflection as a result of the nonlinear group index. For a given z , the time evolution shows beam rotation in the xy plane. Field structure is complicated for the o- and e-beams overlapped, and therefore, the centre of intensity is favourable to track the dynamics, seen in Fig. 2.10. For a given t , the field evolution increases in size and moves more in the xy plane with higher powers. The field value is maximum in the yellow regions and zero in the dark blue. The faint beam seen in the highly nonlinear regime is an index gradient imprinted on the crystal.

Furthermore, the beam is shifted significantly more with increasing power as expected with the increasing nonlinear deflection due to photon-drag. We have plotted only for a rotation speed of $\Omega = 100$ deg/s; however, it can be seen that if the rotation speed is slow, the imprinted beams could cause deflection as expected from the thermal nonlinear response. On the other hand, high speeds would allow integer multiples of one complete rotation to experience the nonlinear optical effects as the time scales are longer. The discretization of time and z -position can be much finer to see the temporal dynamics due to the rotation speed, especially when considering the nonlinear regimes where the group index contains intensity and rotation speed-dependent terms.

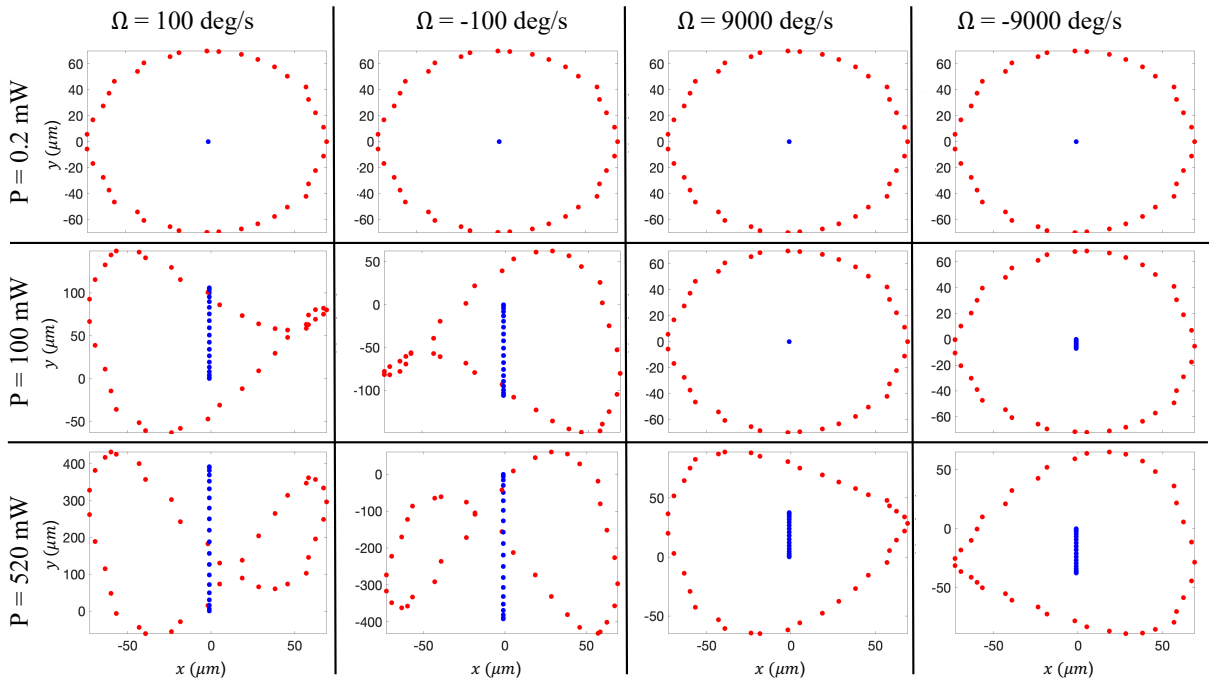


Figure 2.9: **Simulated transverse trajectories of the o- (blue) and e- (red) beams for three input powers at positive/negative low/high rotation speeds.** Linear regime shows no transverse shift drag in either beam for different speeds, while nonlinear and highly nonlinear regimes show increasing shifts for a given speed. The amount of shift is seen more clearly in the o-beam movement. At the same time, the e-beam shows deviations from a circular trajectory, which is due to the nonlinear response of the system. Opposite speeds show opposing translations of each beam.

2.6.2 Birefringence and the Associated Trajectories

Due to birefringence, we know that tracing the COI in transverse trajectories creates figure-eight-like patterns. Tracking the o- and e-beam trajectories is necessary to produce these figure-eights in simulations. Figure 2.9 shows the trajectories of the o-beam in blue and the e-beam in red for three input powers in the low and high-speed regimes. The o-beam shows a transverse shift with increasing power, while the e-beam revolving around starts to cross and form a twisted pattern in the nonlinear regimes. It is important to note that opposite speeds show opposing translations of each beam. An interesting point to note is that the amount of transverse shift is visualized by the o-beam very well, but the e-beam shift is less pronounced since it rotates about the o-beam. It can also be seen here that at high speeds, the trajectory of the e-beam does not drastically deviate from a circle, and therefore, the expected COI trajectory will have a resemblance to the linear regime. However, as discussed, we will still see a transverse shift, which is reflected in the extent to which the o-beam moves about the y -direction.

2.6.3 Trajectories of the COI

The COI is useful as it tracks the motion of both o- and e-beams, and it is often difficult to distinguish them in experiments. Therefore, the simulation utilizes this technique to understand the dynamics that are captured from both beams and will be matched to the experiment in Chapter 3. The relative intensities of the o- and e-beams will go through maxima and minima upon rotation, so the COI is a preferred method of analysis.

Taking the COI, we can see that the linear dynamics trace out a figure eight, and the twisting of the e-beam trajectories creates the twisting seen in the nonlinear regimes. If the intensity varies from o-beam to e-beam and the e-beam revolves around the o-beam, this results in a figure-eight pattern. This results from the thermal and optical nonlinear response the crystal impinges on the light as it passes through the crystal, resulting in distorted patterns. The trajectory patterns get distorted and transversely shift relative to one another based on the nonlinear photon drag effect. Incorporating the birefringence, dispersion, and nonlinear response, we have observed that simulations produce transverse trajectories that display key features of the linear and nonlinear dynamics of the system, seen in Fig. 2.10. The COI for three rotation speeds of $\Omega = 10, 100, \text{ and } 9000 \text{ deg/s}$ corresponds to i), ii) and iii), respectively. More specific conditions for the simulations are compared to the experiment in Chapter 3, showing good agreement.

The transverse shift for experimentally measured data points, phenomenological fits, and simulated curves due to the nonlinear deflection as a result of the nonlinear group

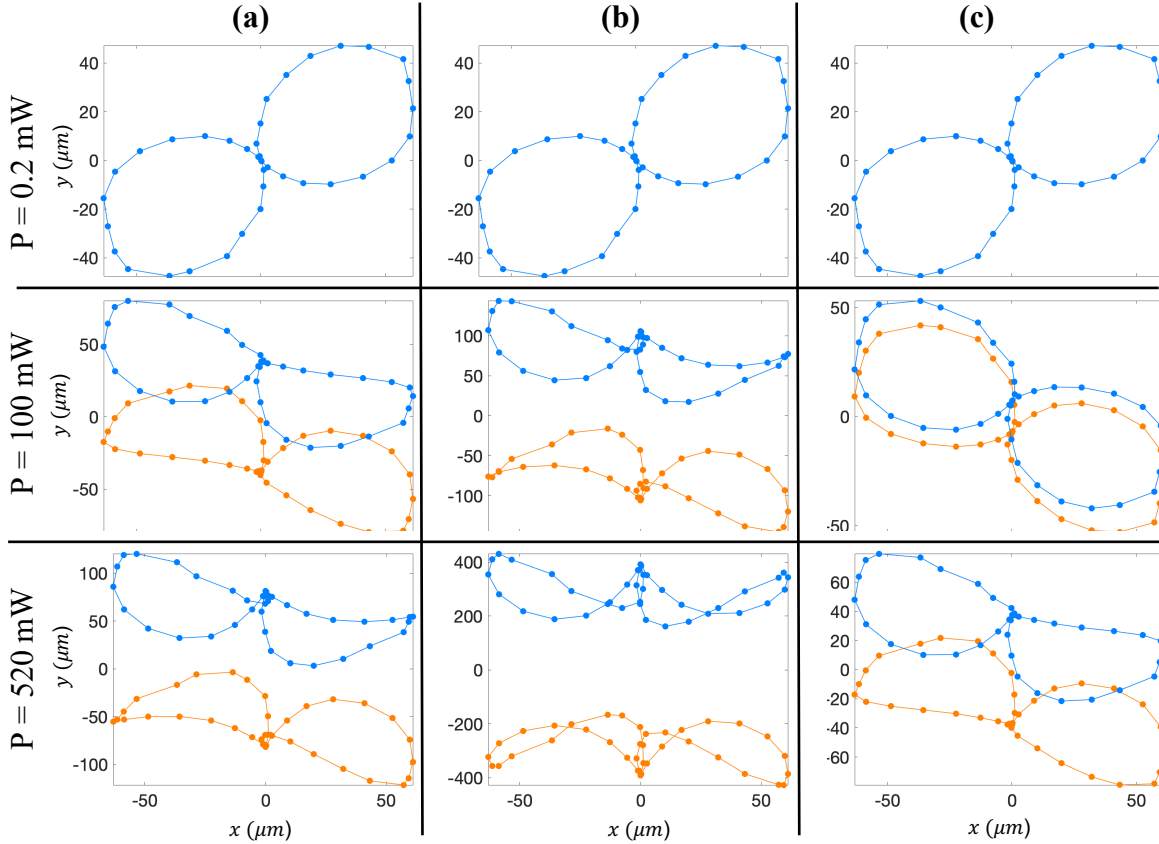


Figure 2.10: **Transverse trajectories for three input powers and three input speeds (a) $\Omega = \pm 10$ deg/s, (b) $\Omega = \pm 100$ deg/s, and (c) $\Omega = \pm 9000$ deg/s.** Simulated curves for the linear ($P = 0.2$ mW) regime show a figure-eight-like trajectory for the COI, while nonlinear ($P = 100$ mW) and highly nonlinear ($P = 520$ mW) regimes show deviations from a figure-eight, as well as transverse shifting along y . Blue and orange curves correspond to positive and negative rotation speeds, respectively.

index. The COI trajectories drift apart for positive and negative speeds, where taking the average positions of these trajectories gives the transverse shift as a function of rotation speed and input intensity, as seen in Fig. 2.11. The fits plotted in dashed lines are based on a slow and fast characteristic rotation speed following the exponential decay is also shown following the experimental data points. These fits are incorporated into the group index that modifies the dispersive terms within the nonlinear Schrödinger equations. The

fit function, described by the continuous function in Eq. (3.3), suggests the characteristic rotation speed to be $\Omega_c = 100$ deg/s. However, we incorporate the piece-wise function into the NLSE to better describe the dynamics in the respective rotation speed ranges. The simulation results for rotation speeds spanning 1~9000 deg/s show excellent agreement with experimental data.

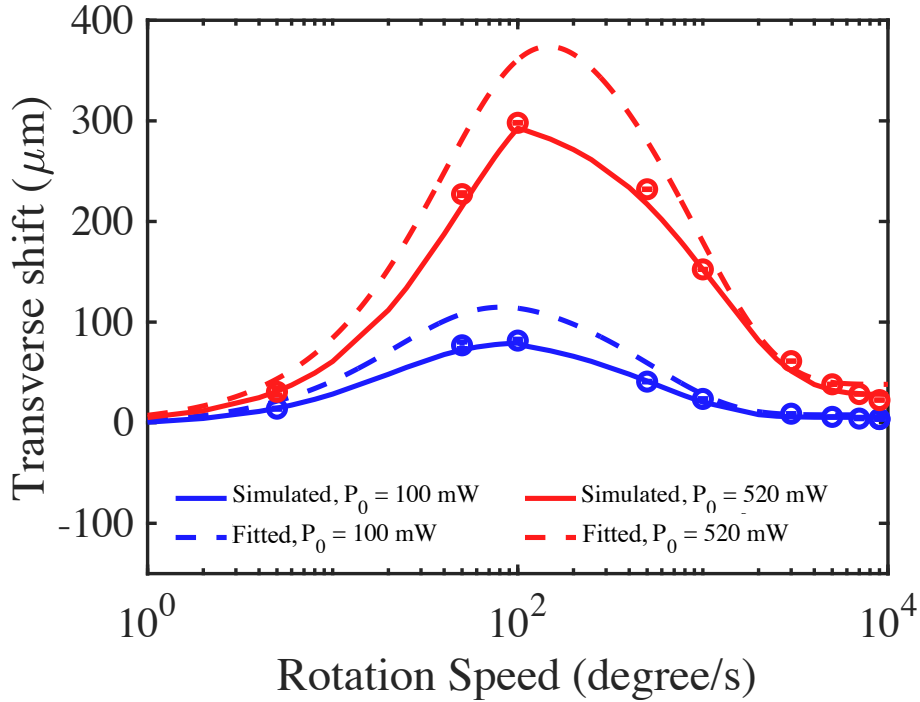


Figure 2.11: **The transverse shift in the nonlinear and highly nonlinear regime for various rotation speeds.** The distribution shows a log-normal-like distribution about $\Omega = 100$ deg/s. The phenomenological fit (dashed lines) suggests a peak closer to $\Omega = 150$ deg/s, while the simulation values suggest $\Omega = 100$ deg/s. About the peak rotation speed, considered as some characteristic rotation speed of the system, the amount of shift drops exponentially. The exponential behaviour is comprised of both optical and thermal nonlinear response and is modelled using the nonlinear group index discussed in Sec. 2.4.2. Several points are highlighted along the curve for comparison of the amount of drag when considering different input powers. These shifts are taken as half the difference between positive and negative rotation speeds.

2.6.4 Transverse Shifts at the Crystal Output

Often, a saturable medium response is associated with a logarithmic dependence of the power, but certain wavelengths show that ruby exhibits reverse saturable absorption [4], which has an exponential dependence on the power. Indeed, this further supports the exponential nature of the group index found in Eq. (2.59). The characteristic timescales associated with the fit of the n_g^{NL} like that in Eq. (3.3) will change based on input power and rotation speed. The fast timescale, τ_f , follows a thermal dissipation timescale that changes based on the beam intensity. That is to say, this timescale will increase with lower intensities, or lower powers, due to Newton's law of cooling [118]. This states that a body heated from thermal equilibrium will dissipate heat from the system as a decaying exponential with different rates based on the thermal gradient impinged on the system. As such, the larger the thermal gradient, the faster the thermal dissipation rate and relates to the scaling of n_g^{NL} . High intensities will decay faster and thus diminish the value of the group index at a much faster rate. This can be seen as a smaller average phase shift for a more intense beam than a less intense one; thus, the group index will be smaller in magnitude.

On the other hand, the optical timescale also plays a key role in n_g^{NL} . Excited atoms in ruby will decay from an excited state to the ground state within $\tau_s = 3 \sim 5$ ms. The more photons available for the system to absorb, the faster the transition can reach an inverse saturated response and decay back to the ground state. In the case of an input power of $P = 520$ mW, $\tau_s \approx 3.5$ ms, but if the power is decreased to 100 mW, the time increases to $\tau_s \approx 6$ ms. This difference in timescale can be attributed to the effect of reverse saturable absorption [4], and similar to the thermal nonlinear response, higher intensity is associated with fast decay rates.

2.7 Summary

In the present chapter, we have implemented an SSFM code that uses NLSEs to simulate light propagation through a rotating, birefringent material while carefully accounting for the impact of optical and thermal nonlinearities on both the refractive index and group index, particularly accounting for their gradients across the propagating beam.

We believe that these are the necessary elements to account for to properly predict beam propagation through such a medium that can also predict the beam propagation as a function of rotation rate and input intensity while also allowing for experimental

deviations of the beam incident angle and the orientation of the medium's refractive index ellipsoid relative to the axis of rotation (or direction of translational motion).

If experimental results match well with the predictions of this model, it would encourage us to believe that we have a robust model that describes beam propagation under translational drag while accounting for the interplay of several complex but experimentally significant phenomena.

While first and foremost, a predictive model to test our fundamental understanding of strong light-matter interaction in slow/fast light media, a working model could also be necessary if the nonlinear optical circumstances of slow/fast light are to be properly implemented in aerospace guidance systems [119].

In the following chapter, based on the work by Hogan et al. [5], we will test our model by measuring the transverse trajectories and transverse shifts at the output of the crystal in linear and nonlinear regimes. We will also quantify the strength of the nonlinear refraction in the system and measure the effect of nonlinear deflection from the index gradient created by the nonlinear refraction by measuring the output angle. The propagation of the beam after the crystal will also be measured to gain an understanding of how the beams propagate through the nonlinear medium by extrapolation. We will see that slow light indeed enhances and manipulates the beam propagation, leading to larger, more easily measurable transverse shifts and exotic transverse trajectories.

Chapter 3

Photon Drag, Nonlinear Deflection, and Nonlinear Refraction

In the previous chapter, we simulated the dynamics of a rotating ruby rod using coupled Nonlinear Schrodinger equations (NLSE), including rotation, birefringence, thermal and optical nonlinear response, and a nonlinear group index. The NLSEs were used to produce transverse trajectories at the output of the crystal, as well as study the transverse shift as a function of rotation speed and input power.

In the present chapter, we experimentally measure the transverse shift and transverse trajectories at the output of a rotating ruby crystal, as presented in the work of Hogan et al. [5]. We then compare the simulated results of our theory to the experiment, showing good agreement. The transverse trajectories are also measured at two positions past the crystal to investigate the output angle. Evidence of the nonlinear refraction is investigated in the context of a Townes profile formation.

3.1 Background

Recall that the transverse shift a beam experiences, Δy , traversing a medium of length L moving with a transverse speed, v is written,

$$\Delta y = \frac{v}{c} \left(n_g - \frac{1}{n_\phi} \right) L, \quad (3.1)$$

depicted schematically in Fig. 3.1(a).

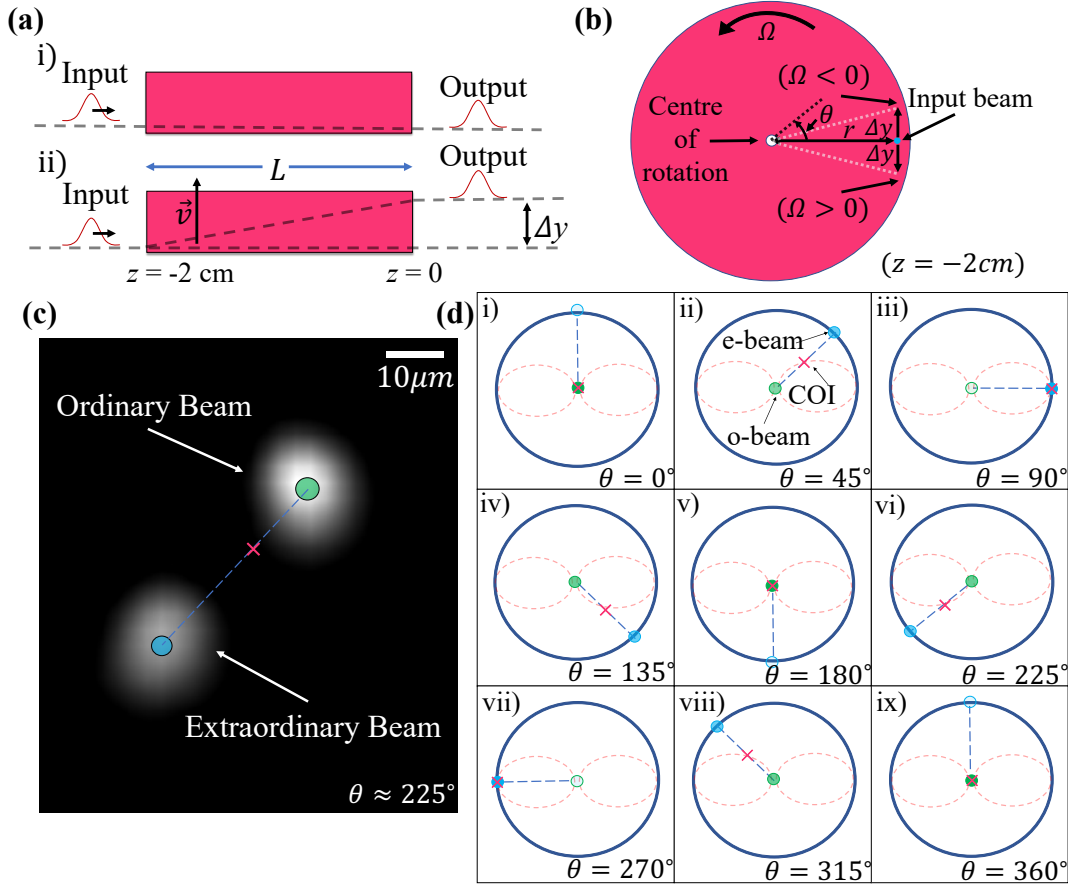


Figure 3.1: **Schematics of the dynamics in the system.** (a) A schematic showing laser beam propagation in i) a stationary medium versus ii) a moving medium which exhibits a transverse shift of Δy . For simplicity of illustration, we show the laser beams as pulses. (b) The edge of a rotary ruby rod is used to achieve an approximately linear motion in the $-y$ ($+y$) direction when the crystal rotates clockwise (counterclockwise). (c) A single frame imaged at the input face of the crystal ($z = -2$ cm) that shows the o- and e-beams propagated through the 2-cm-long ruby crystal. (d) A diagram showing the trajectories of o- and e-beams at different crystal orientations highlighting each beam's intensity change at 45-degree intervals. The red "x" shows the centre of intensity (COI) position for different crystal orientations, highlighting the emergence of a figure-eight-like pattern. In contrast, o- and e-beams are shown by green and blue dots, respectively, with varying transparency to signify their relative intensities.

Light propagation in a medium of length L is sketched for two cases: i) a stationary medium and ii) a medium moving transversely at speed v . The rotational equivalent is shown in Fig. 3.1(b), which highlights transverse shifts for positive and negative rotation speeds, which are approximately translational movements when far from the centre of rotation. When the group index is large compared to the phase index, i.e. $n_g \approx -10^6$ ruby at 473 nm [4], the transverse shift is simplified to

$$\Delta y \approx n_g L \left(\frac{r\Omega}{c} \right), \quad (3.2)$$

where Ω is the medium's rotational speed and the medium radius, r . Using the large negative group, one can expect a large negative transverse shift. This is a direct utilization of slow (fast in the case of negative group indices) light, which results from coherent population oscillations. We seek to experimentally measure the fast-light enhanced transverse shift due to the large group index this optical effect creates. We also seek to measure the transverse trajectories, which follow the dynamics of the two beams shown in Fig. 3.1(c). At the output, these beams are large and overlap, and therefore, another analysis method must be used: the centre of intensity (COI). The COI, as discussed in the previous chapter, takes the relatively weighted intensity of the two beams and then follows a trajectory as the e-beam revolves around the o-beam, which as spatially separated by walk-off due to crystal alignment. Figure 3.1(d) shows a figure-eight trajectory for the linear regime, which is a result of the o- and e-beam reaching maximum and minimum intensity on each quarter turn depicted by green and blue dots and its respective filling of colour. The COI is shown as a red "x". We will experimentally measure these transverse trajectories, as well as the transverse shifts at the crystal output and two other positions for various rotation speeds and input intensities, to see how the dynamics evolve. We will then compare to simulations from the previous chapter.

As we will come to find out based on the modelling of the system from Chapter 2, the ruby will exhibit a large nonlinear refractive index that causes a beam to deflect, and therefore, the transverse shift will be affected by nonlinear deflection. We will also find that the trajectories distort and shift from one another based on these nonlinear thermal and optical responses. It is clear that due to the simultaneous presence of birefringence, an intensity-dependent photon-drag, and strong nonlinearity, ruby is an interesting platform rich in physics with lots of potential applicability and could lead to experiments in beam steering [97, 120], polarization detection [99, 100], image rotation [3, 121], and velocimetry [122].

3.2 Methodology

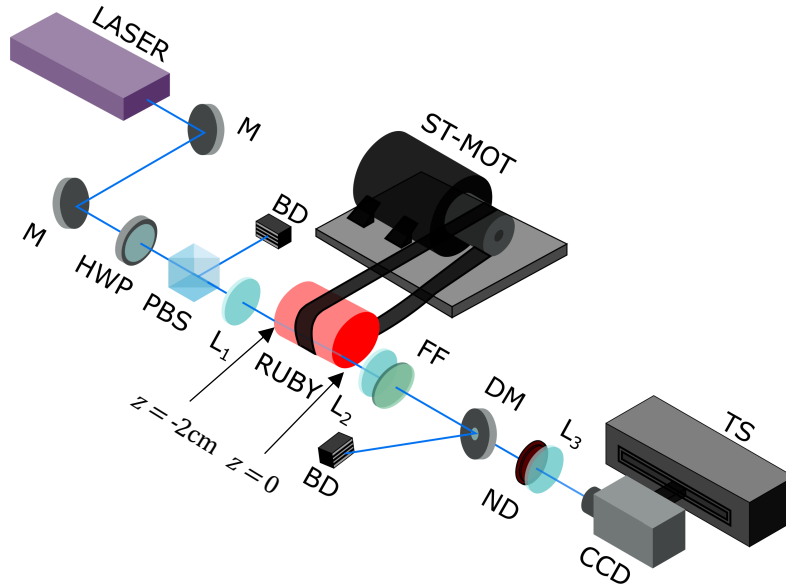


Figure 3.2: **Experimental setup for measurement of transverse shifts.** A 520 mW continuous-wave laser beam at 473 nm is focused using a 100 mm focal length plano-convex lens L_1 to a spot size of $20 \mu\text{m}$ onto the input face of a rotating ruby rod. The rod spins around its axis, driven by a stepper motor. The laser beam at the output of the crystal is imaged onto a CCD camera with unity magnification using a 4-f system consisting of two lenses L_2 and L_3 of focal length $f = 150$ mm. The CCD camera captures the beam, with a frame rate of 1000 fps, as the stepper motor is rotated at various speeds. An ND filter is placed between the dielectric mirror and lens L_2 for nonlinear measurements and between L_1 and the ruby for linear measurements. The CCD camera images at different z -positions using a translation stage. Measurements are taken at $z = 0$, $z = 0.762$ cm, and $z = 1.524$ cm to measure the transverse shift, as well as the output angle of the beam as it exits the crystal. Input beam power was controlled by a half-wave plate and a polarizing beam-splitter before the ruby crystal. (M: Mirror, HWP: Half-wave plate, PBS: Polarizing beam-splitter, BD: Beam dump, L_1 : Plano-convex lens [$f = 100$ mm], L_2 : Plano-convex lens [$f = 150$ mm], L_3 : Plano-convex lens [$f = 150$ mm], FF: Fluorescence filter, DM: Dielectric mirror, ND: Neutral density filter [O.D. 1], and a CCD: Charge-coupled device.)

As shown in Fig. 3.2, the laser source used in the experiment is a continuous-wave (CW) diode-pumped solid-state laser operating at 473 nm with an output power of 520 mW. The

power of the laser is controlled using a half-wave plate and polarizing-beam splitter. We use a 2-cm-long ruby rod, 9 mm in diameter, with a Cr^{3+} doping concentration of 5%. We focus the laser beam onto the input face of the crystal far from the centre of rotation ($r = 0.35$ cm). The ruby was mounted in a hollow spindle whose rotation was controlled by a stepper motor and belt. The fluorescence filter FF (high transmission near 473 nm) minimizes fluorescence. The dielectric mirror DM is used as a neutral density filter with low absorption to limit the beam intensity for high-power tests while minimizing image distortions due to aberrations induced by thermal nonlinearities in a standard neutral density filter. The crystal output face was then imaged using a 4-f lens system relaying onto a charged-coupled device (CCD) camera.

Linearly polarized light illuminating a rotating birefringent medium sees two refractive indices upon propagation, $n_o = 1.770$ and $n_e = 1.762$. Due to the difference in refractive index, the two beams (o- and e-beams) will propagate separated by an angle of $\gamma_b \approx n_o - n_e = 8$ mrad, regardless of nonlinearity or photon drag. Maximum and minimum relative beam intensities are reached each quarter turn of the crystal (i.e., every 90°). The beam input is aligned such that, regardless of crystal orientation, the o-beam propagates directly through the crystal, while the e-beam revolves around the o-beam as modelled in Chapter 2. For analysis, the COI is taken to track the beam’s combined transverse trajectory.

3.3 Results

3.3.1 COI Trajectories

We measure the COI at the output facet of the rod ($z = 0$) for three input powers of 0.2 mW, 100 mW, and 520 mW and various rotational speeds of $\Omega = \pm 50, \pm 100, \pm 1000$, and ± 9000 deg/s in clockwise (negative) and counterclockwise (positive) directions. Figure 3.3 shows the COI trajectories in the linear regime (i.e. a laser power of 0.2 mW). The experimentally measured COI trajectories are shown in Fig. 3.3(a) and are compared to the simulations in Fig. 3.3(b) using the theory from Chapter 2, showing good agreement. The curves match the tilt of the figure-eights, as well as the movement the beam experiences about the xy plane. The amount of transverse shift is negligible for all rotation speeds since the group index is on the order of unity. The dynamics are captured in the simulation using the birefringence and rotation in the linear regime. The discrepancy at the center of the curves between the experiment and simulation is a result of polarization impurity. Due to the limited extinction ratio of a polarizing beam splitter, light that is passed

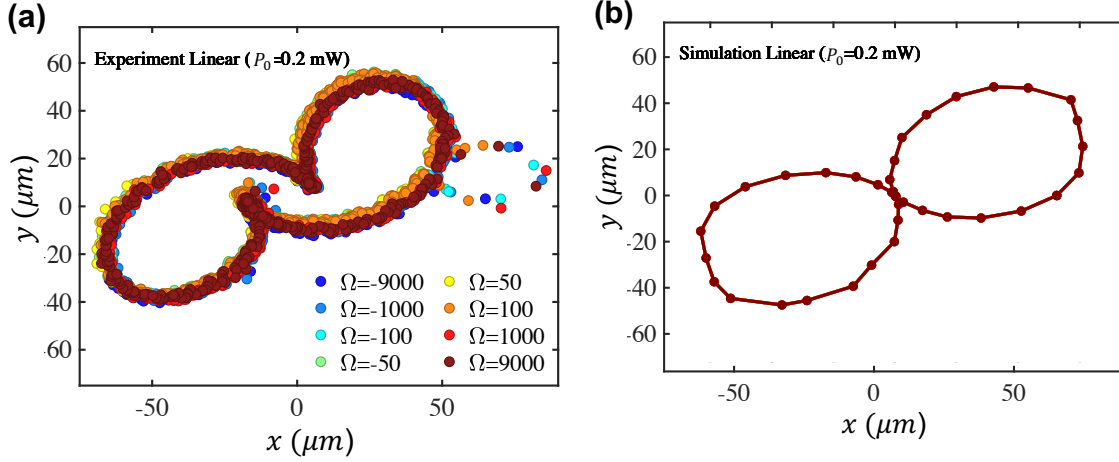


Figure 3.3: **(a) Measured COI trajectories in linear ($P_0 = 0.2$ mW) regime. (b) Simulated COI trajectories in the linear regime.** Legend of different rotation rates (deg/s) applies to **(a)** and **(b)**. Looking into the beam, (counter) clockwise rotation speeds are (negative) positive. No significant shift is observed in y for trajectories at different speeds because the group index and the nonlinear refraction are negligible.

through contains a mix of H - and V -polarization, and in the linear regime, each polarization component is comparable in magnitude. Therefore, the beam does not fully go to zero at each quarter turn of the crystal, and therefore, the beam would be slightly displaced from zero. The simulations in 3.3(a), however, assume a perfectly linear polarized light beam in H -polarization. The overall shape of the transverse trajectories is observed to be figure-eight-like trajectories for all speeds, but no transverse shift is measured. This is expected as the group index is on the order of unity in the linear regime, and therefore, no transverse drag is expected.

Figure 3.4 shows the experimentally measured COI trajectories in **(a)** and simulated COI trajectories in **(b)** in the nonlinear regime (i.e. laser power of 100 mW). At low speeds ($\Omega \leq 100$ deg/s), the o- and e-beams are coupled due to the intensity and overlap of the beams. Each beam creates an index gradient for one another, causing significant variation in the traces of the COI upon rotation. The nonlinear refraction of each beam is affected by the intensity, which alternates between the o- and e-beam as the medium rotates. Therefore each beam is pulled toward another when the intensity is high and is modelled as coupled in our simulations since the intensity is written as $I = I_o + I_e$, where $I_{o,e}$ represents the intensity of each beam. At high speeds, the deviations from a figure-eight-like pattern begin to resemble linear dynamics as seen in Fig. 3.3, but

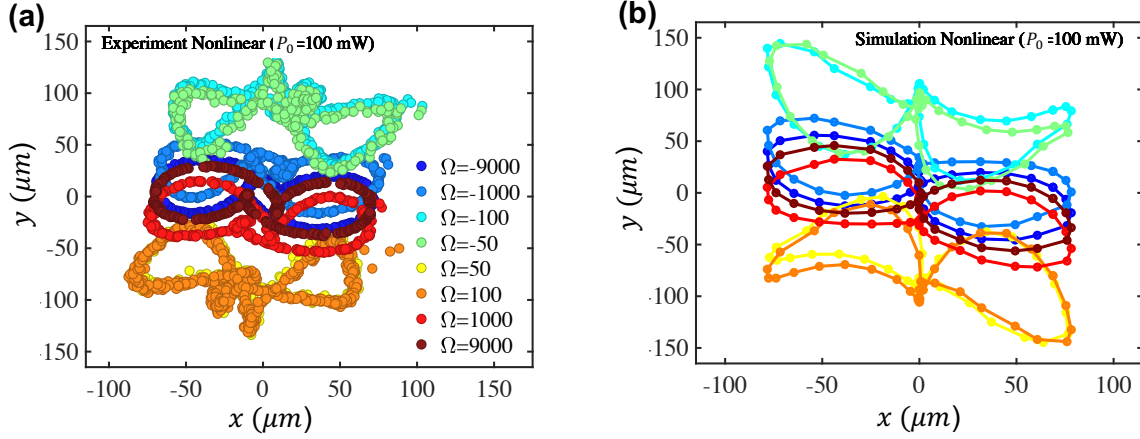


Figure 3.4: (a) Measured COI trajectories in nonlinear ($P_0 = 100$ mW) regime. (b) Simulated COI trajectories in the nonlinear regime. Legend of different rotation rates (deg/s) applies to (a) and (b). Trajectories at low speeds are distorted due to the index gradient formed by each beam at its respective max intensity. The gradient diminishes at high speeds, and thus, the figure eights are recovered but transversely shifted from one another based on the nonlinear deflection for a given rotation speed.

a measurable transverse shift is observed between trajectories associated with different rotation speeds. The amount of transverse shifting the COI experiences matches well between the experiment and simulation, where the maximum transverse shift is about $\Delta y = 120 \mu\text{m}$, for a rotation speed of $\Omega = 100$ deg/s. The transverse shift of the COI due to birefringent walk-off is approximately zero since it follows the weighted position of both beams. As seen in Chapter 2, both the thermal and optical nonlinear responses contribute to the group index at different rotation speed regions. Our modelling of the response of the nonlinear group index to rotation speed and intensity incorporated into the NLSE from Chapter 2 matches the amount of transverse shift well. The interplay of thermal and optical nonlinear response is reflected in the rotation speed such that the transverse shift reflects the relative contributions of each nonlinear response at high rotation speeds. No distortions are observed on the trajectories as a result of the diminishing contribution of thermal nonlinear response but a remaining response from the optical nonlinearity. However, when the beam intensity is very intense, the index gradient will be larger and, therefore, cause more significant distortions that extend to higher rotation speeds, as in Fig. 3.5.

Figure 3.5 shows more drastic deviations from a figure-eight pattern in the highly

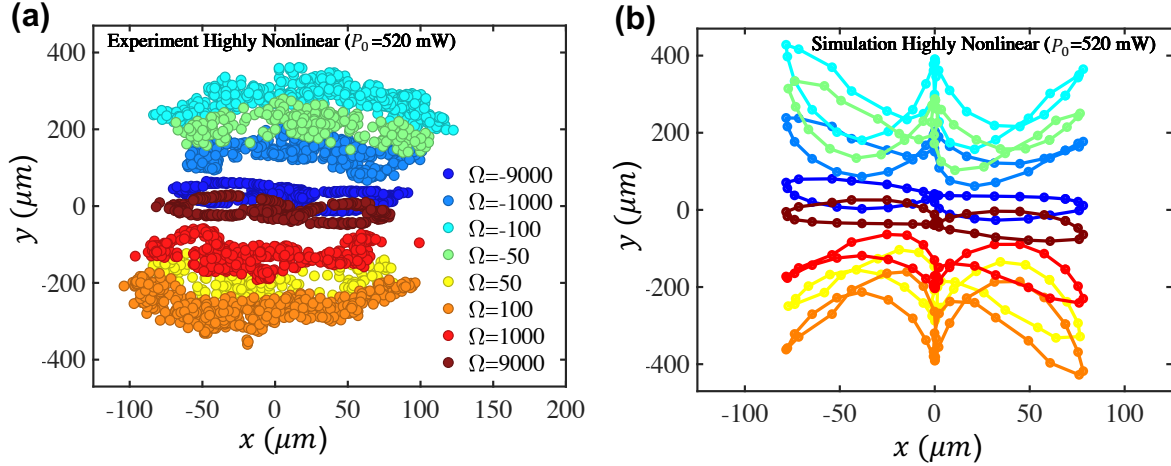


Figure 3.5: **Experimentally measured (a) and simulated (b) COI trajectories in the nonlinear regime (input laser power of 520 mW) for different rotational speeds (Ω) in units of deg/s.** At low speeds, trajectories are significantly distorted and have similar paths to the 100 mW results but with more distortion due to stronger nonlinear coupling between the beams. At high speeds, the coupling between the beams is weaker due to the finite response time of the medium. For slow speeds, $\Omega \leq 100$ deg/s, the trajectories are very noisy, and no discernable pattern is easily observed. This behaviour is mainly due to the thermal gradient impressed on the crystal by the intense illumination, and therefore, the transverse beam shape is drastically modified.

nonlinear regime ($P_0 = 520$ mW), where trajectories are noisier. Experimentally measured points are shown in Fig. 3.5(a), and simulated points in Fig. 3.5(b). As for the case of $P_0 = 100$ mW, the figure-eight pattern is recovered, but only at very high speeds, i.e. $\Omega \geq 9000$ deg/s. This noise is likely due to a large thermal effect that locally affects the beam frame by frame. With lower speeds, the figure-eight-like trajectories knot near the center due to a larger index gradient created by the o- or e-beam. The amount of transverse shifting the COI experiences matches well between the experiment and simulation for given rotation speeds. The maximum transverse shift from zero y -position to the center point of a trajectory is about $\Delta y = 300$ μm , for a rotation speed of $\Omega = 100$ deg/s. For rotation speeds around $\Omega = 1000$ deg/s, the curves resemble the patterns observed in Fig. 3.4 for rotation speeds of $\Omega = 50 - 100$ degs/s. This supports that the effects of the index gradient are much larger and, therefore, do not wash out as quickly with faster rotation speeds.

In all cases of linear ($P_0 = 0.2$ mW), nonlinear ($P_0 = 100$ mW) and highly nonlinear regimes ($P_0 = 520$ mW), simulations are compared, showing good agreement in the shape

of the trajectories and magnitudes of transverse shift. A noticeable discrepancy between the experiment and simulations is that near the centre of the figure-eight, they do not close due to the imperfect H -polarization caused by the optical elements. Moreover, if the crystal faces are slightly non-parallel, the output angle of the light could be manipulated depending on the crystal orientation and the birefringence effects.

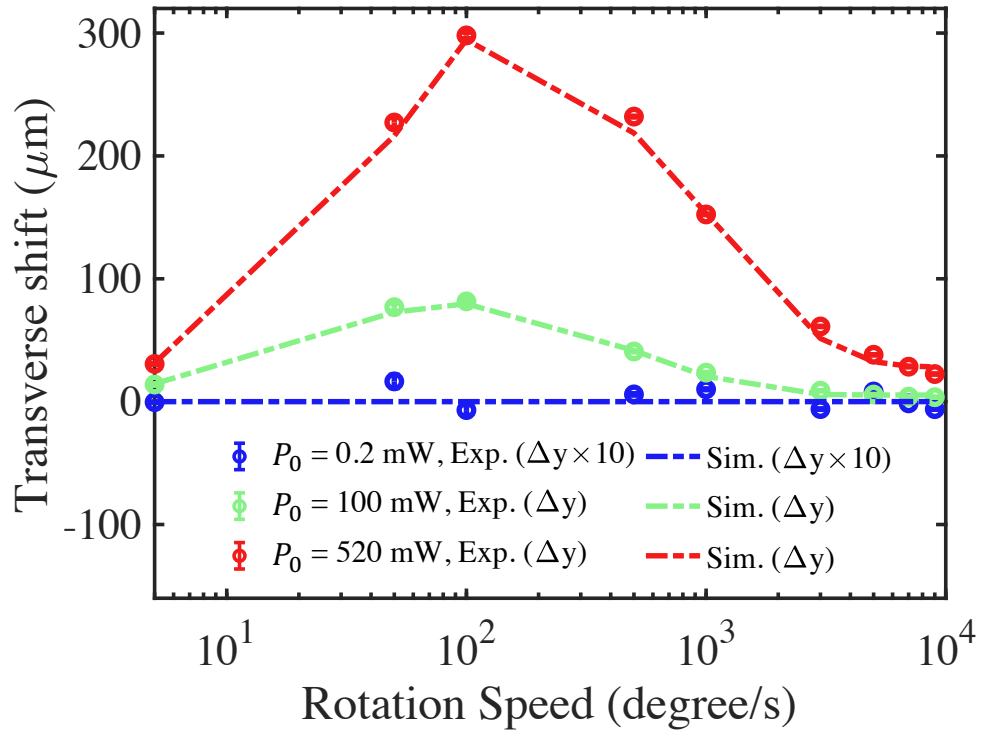


Figure 3.6: **Experimental and simulated amount of shift in the beam’s transverse position at the end of the crystal for 0.2 mW, 100 mW, and 520 mW input beam laser power.** The measured shift for the linear regime (i.e., $P_0 = 0.2$ mW) for both experiment and simulations is multiplied by a factor of 10, showing no discernible deviation from zero shift. The magnitude of the transverse shift is shown against the magnitude of the rotation speed. This shift is calculated between the position with no rotation, i.e. $\Omega = 0$ deg/s, and the respective transversely shifted position. Simulations are plotted using dotted lines in green and red for the nonlinear and highly nonlinear regimes for better comparison to experimental data. The fits were based on a phenomenological exponential function in Eq. (3.2). The fit is not a perfect match due to the simulated nonlinear response of the material acting on the beams upon propagation through the crystal.

In the nonlinear regimes $P_0 > 100$ mW, the input polarization component of H -polarization would become large compared to the V -component, and so the argument can change slightly. The reason the curves do not close could be attributed to the rotational movement approximated as translational movement along the y -direction. The beam is not infinitely far from the centre of rotation and, therefore, could be dragged along the x -direction as well. The amount of transverse shift is mainly witnessed in the y -direction, however, so we will extract the transverse shift in y , looking at the dependency on rotation speed and intensity.

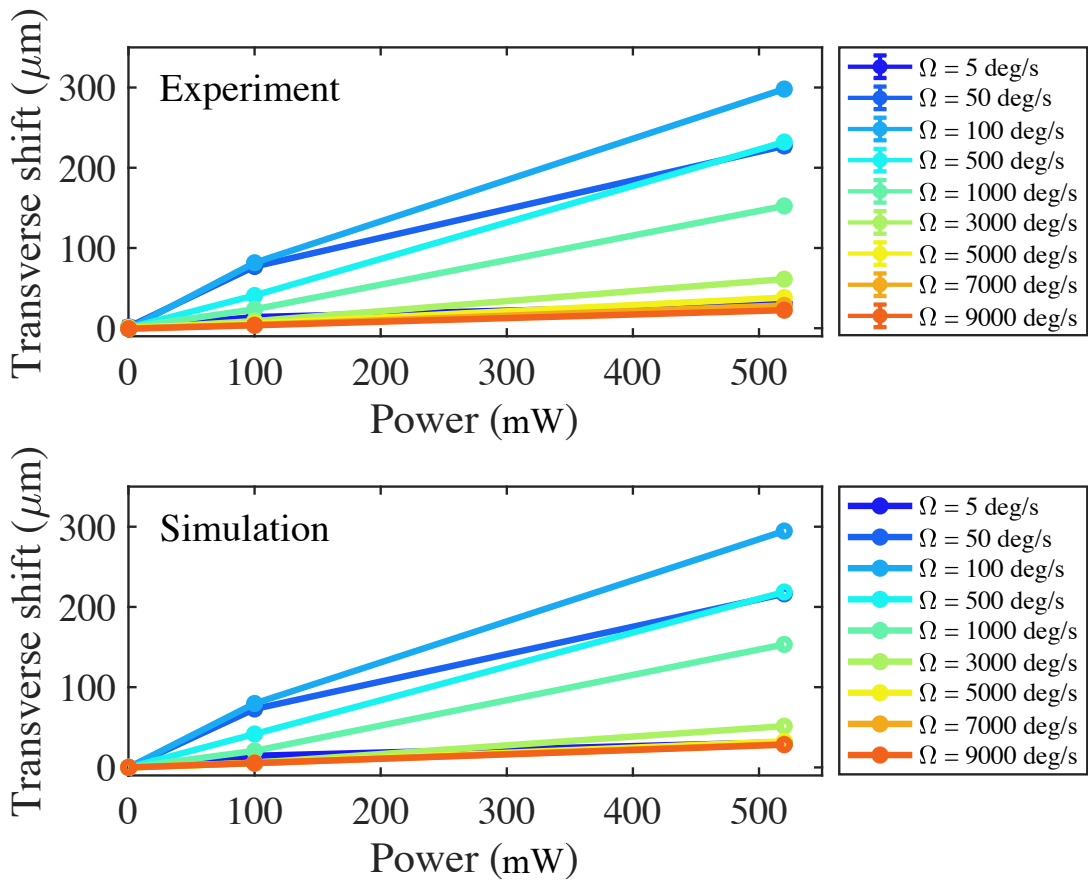


Figure 3.7: **Power dependence of experimental and simulated transverse shifts.** The evolution of the transverse shift with power for various rotation speeds is shown for both experiment and simulation.

We extract the average position of these COI trajectories over an integer number of full rotations, and the results are plotted in Fig. 3.6. Here, we see the rotation speed

dependence of the extracted transverse shift at $z = 0$ (crystal's output face) for linear ($P_0 = 0.2$ mW), nonlinear ($P_0 = 100$ mW), and highly nonlinear ($P_0 = 520$ mW) regimes. The transverse shifts appear to only show trends in the nonlinear and highly nonlinear regime taking shape similar to that of a log-normal function centred around $\Omega = 100$ deg/s.

Another representation of the amount of drag can be shown to highlight the effect of the power or intensity on the amount of transverse shift. Figure 3.7 shows the amount of drag for various rotation speeds for three input powers, which form an approximately linear dependence on the input power. These plots agree and more directly show how the maximum transverse shift is bounded by some characteristic speed near $\Omega_c = 100$ deg/s.

We note that the transverse spatial shift can, in principle, comprise photon-drag and nonlinear deflection. While the photon drag predicts transverse shifts of the beam at the output parallel to the input beam, the nonlinear deflection deflects the output beam at an angle with respect to the input. We measure the transverse shifts at $z = 0$ and two other locations after the crystal to find the output angle. It is important to note that we cannot subtract out the deflection to get the true shift due to the photon-drag effect. However, we model the deflection as a nonlinear group index, which is a result of the moving index gradient created by the nonlinear refraction. This index gradient changes in the trajectory inside the crystal by nonlinear deflection cannot be imaged. As expected from nonlinear deflection, this angle is non-zero and intensity- and rotation-speed-dependent (Fig. 3.9).

3.3.2 Transverse Shift

The magnitude of the nonlinear deflection is proportional to the magnitude of the nonlinear group index, controlled by the intensity and rotation speed. As discussed in Chapter 2, the rotation speed changes the conditions for how quickly the heat dissipates through the crystal and, thus, the magnitude of the index gradient. Sufficiently slow speeds seed an index gradient that stays relatively constant in magnitude upon rotation and leads to an increased transverse shift. The time scale typically needed to deflect the beam is always very short (i.e. $2\text{cm}/(c/n_g)$); however, once the maximum amount of transverse shift is met, i.e. $\Omega \approx 100$ deg/s, the crystal starts rotating faster than the timescale needed to form the index gradient. Increasing rotation speed sets that the beam sees less index gradient and thus less transverse shift. The curve associated with transverse shift versus rotation speed, seen in Fig. 3.6, is comprised of two decaying exponentials centred about $\Omega = 100$ deg/s that gives rise to an asymmetric distribution. The index gradient decays slower for slow speeds and faster for higher speeds.

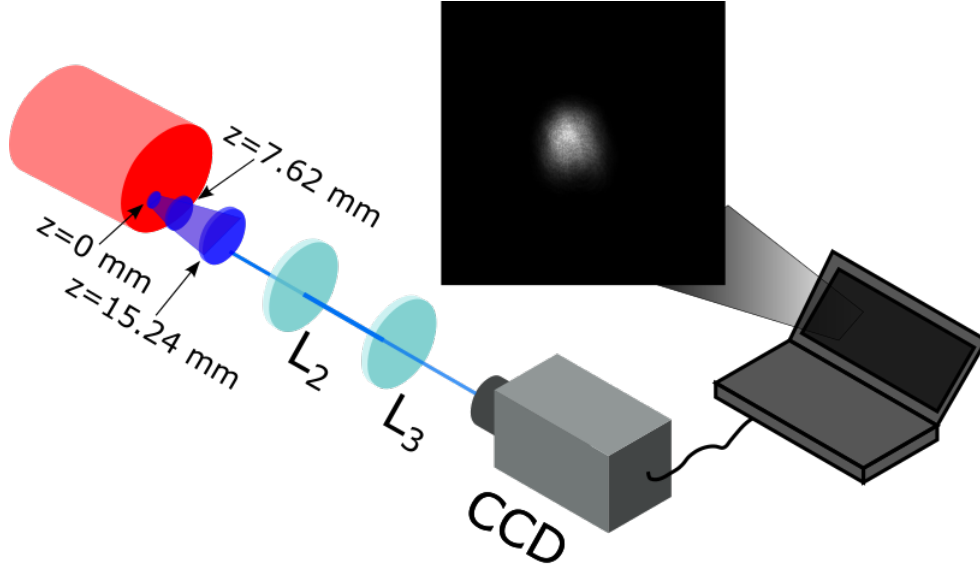


Figure 3.8: **Schematic showing the three positions imaged by translating a CCD fast camera.** With a frame rate of 1000 frames/s, we measure three positions moving away from the output face of the crystal by using a 4-f system of lenses 2 and 3. A single frame of a video of the beam at the output face (i.e. $z = 0$ mm) is shown in the inset of which the COI is taken to show the movement of the COI and the amount the beam is dragged over many frames. The frame shows a single large beam encompassing the o- and e-beams. The two beams expand significantly upon propagation through 2 cm in the ruby crystal, so they are no longer distinguishable on the camera.

A phenomenological fit for the transverse shift was created using the experimental data in Fig. 3.6 with the form of a decaying exponential, as discussed in Chapter 2. Recall that the nonlinear group index is a time-averaged response for a given speed and can be broken up into a fast and slow contribution, like in Eq. 2.56, written as

$$n_g^{\text{eff}} = n_g^0 + n_2^g I_o \left(\frac{1}{f_s} e^{-\Omega/\Omega_s} - f_f e^{-\Omega/\Omega_f} \right), \quad (3.3)$$

Ω_s and Ω_f are slow and fast inverse time scales, where $\Omega_{s,f} = 1/(2\pi\tau_{s,f})$ and the timescales are $\tau_s = 3.5$ ms, and $\tau_f = 175$ μ s, respectively. The slow (optical) timescale is on the order of the excited ion lifetime, typically 3 to 5 ms [3], and the fast (thermal) timescale on the order of thermal diffusion ($\approx 200\mu$ s) [116]. This averaged response modifies the magnitude of the nonlinear group index, representing an approximate non-instantaneous response alleviating computational expense as done in the simulations in Chapter 2. This

is a good approximation, as the results are shown in Figs. 3.3, 3.4, and 3.5 show good agreement amongst the trajectories and the transverse shift.

The input face of the crystal could be measured by moving the camera closer to the crystal, measuring a seemingly negative drag effect, i.e. a beam shifted in the opposite direction to crystal motion. However, this measurement would extrapolate the output beam onto the crystal input face due to a large output angle. We can look at the evolution of the beam as it propagates after the crystal to see how this extrapolation could be realized.

3.3.3 Transverse Shift at Different Longitudinal Positions

The transverse shift is also measured at two other positions other than the crystal output face, depicted in Fig. 3.8. The CCD can image at different points using a translation stage with a range of ± 2.54 cm from $z = 0$. A set of measurements was taken at each z -position, consisting of three powers, $P_0 = 0.2$ mW, $P_0 = 100$ mW, and $P_0 = 520$ mW for rotation speeds between 1~9000 deg/s was measured at three z -positions and is plotted in Fig. 3.10. The transverse shift grows along the direction of propagation. The spacing between curves is non-uniform for different rotation speeds is a clear indicator that the nonlinear response of the medium changes the output angle, discussed later in Sec. 3.3.3. The transverse shift is plotted in Fig. 3.10 for powers of $P_0 = 100$ and $P_0 = 520$ mW. We exclude the linear regime $P_0 = 0.2$ mW since it is on the order of the system noise. One can see that in the limits of high or low rotation speed, the amount of transverse shift is roughly equal in magnitude. It is only in the region mid-range of speeds where the spacing is very non-uniform. For a given rotation speed, the difference in transverse shift over the distance propagated in z can give the output angle. The angle is directly calculated

$$\theta_L = \arctan\left(\frac{\Delta y}{\Delta z}\right). \quad (3.4)$$

The results of the output angle are shown in Fig. 3.9. A schematic of the points is shown in Fig. 3.9(a), and the output angle is calculated for various rotation speeds and input powers.

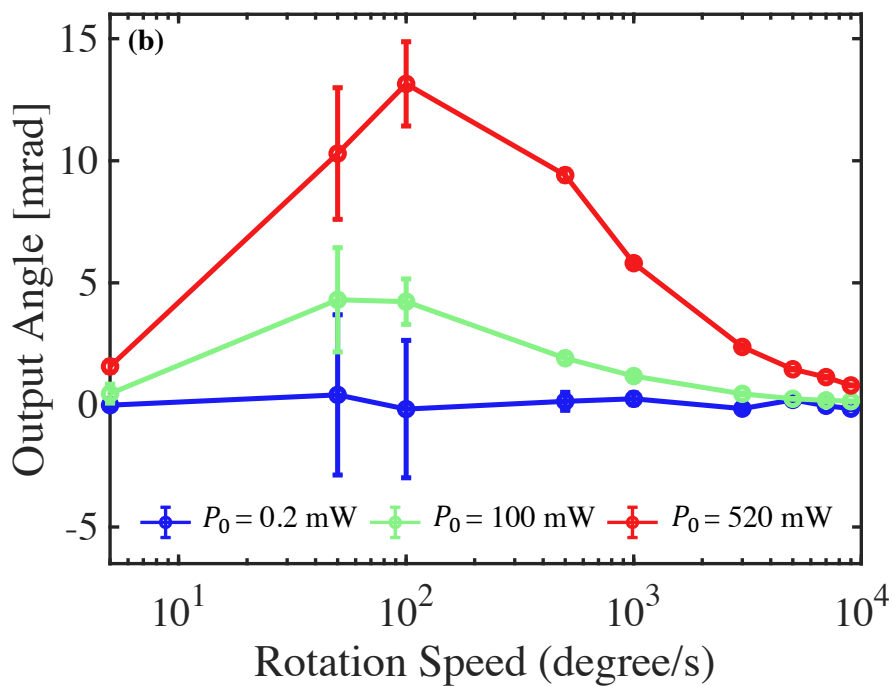
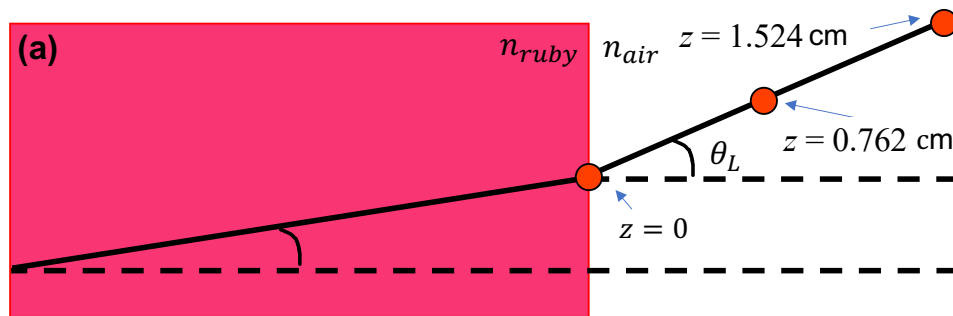


Figure 3.9: **Measurement of the output angle versus input power and rotation speed.** (a) a schematic showing the output beam's angle after leaving the crystal. The nonlinear response of the crystal changes the angle at the interface of the crystal output face and, therefore, changes the propagation pathway. (b) The output angle and its uncertainty are calculated from the beams' transverse positions measured at three points along the z -axis ($z = 0$, $z = 0.762$ cm, and $z = 1.524$ cm). The output angle increases as the laser's power increases, as expected from nonlinear deflection.

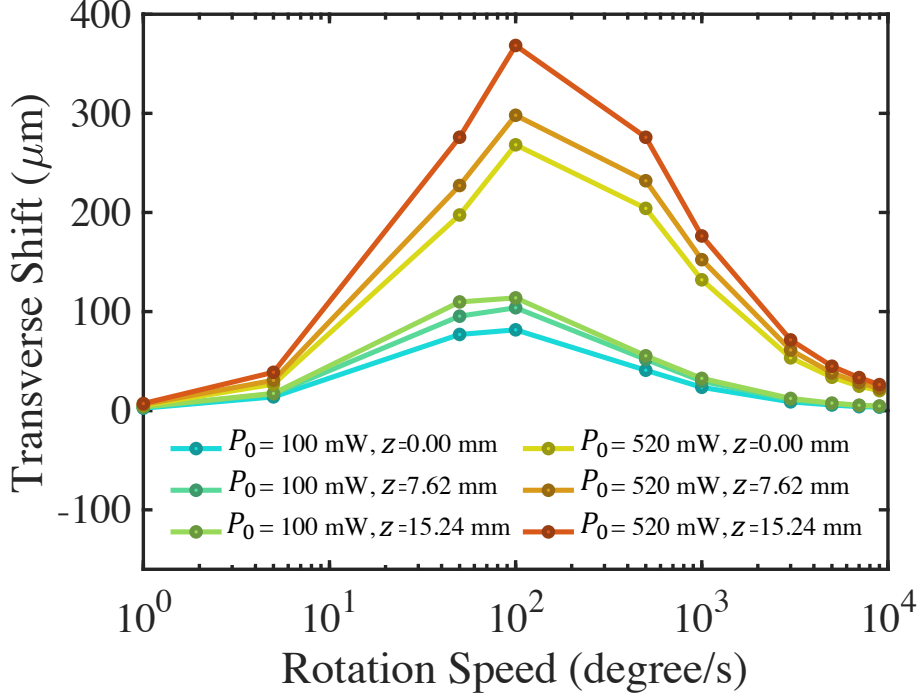


Figure 3.10: **Experimentally measured transverse shift in nonlinear ($P_0 = 100$ mW), and highly nonlinear ($P_0 = 520$ mW) regimes at different z -positions.** Measurements were taken at $z = 0, 7.62$ mm, and 15.24 mm to calculate the output angle. The transverse shift approaches $\Delta y = 10 \sim 15 \mu\text{m}$ for an input power $P_0 = 100$ mW, and $\Delta y = 60 \mu\text{m}$ for $P_0 = 520$ mW. The curve takes shape similar to a log-normal distribution, but is modelled as the sum of two decaying exponentials with different decay rates centred around a rotation speed of $\Omega = 100$ deg/s.

One can calculate the output angle seen prior using the values for the transverse shifts as Δy and the difference between the z -positions along propagation Δz , as seen in Fig. 3.10. The output angle is therefore tuned by the rotation speed and the beam's intensity since $\Delta y := \Delta y(\Omega, I)$. As such, this can be useful in applications where the position and angle need to be controlled. Therefore, we can look at how the beam propagates along z after the crystal is controlled by the rotation speed and intensity. Since we expect no shift in the linear regime, we will only focus on the nonlinear and highly nonlinear regimes to examine the amount of transverse shift along z .

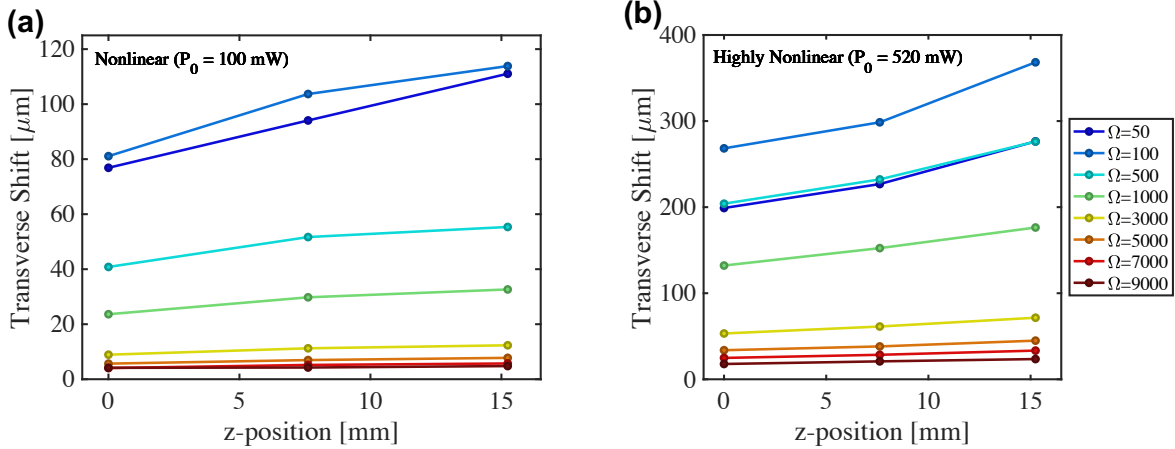


Figure 3.11: **Extrapolation of transverse shift for input laser powers of $P_0 = 100$ mW, and $P_0 = 520$ mW.** Evolution of the amount of transverse drag at three points, including the crystal output face, and two positions hereafter, as shown in Fig. 3.8. The extrapolation of these points in the highly nonlinear regime ($P_0 = 520$ mW) also shows a linear dependence on the transverse shift as the propagation distance increases, consistent with a straight-line propagation of the COI. The difference from the nonlinear regime is the magnitude of the slopes is much larger due to a larger nonlinear response in the system for input powers of 520 mW. One could extrapolate these curves as a linear regression back to the crystal input face $z = -20$ mm and see that the value does not reach zero. It is clear in the range of speeds from $\Omega = 50 \sim 1000$ deg/s, where the value would be non-zero at the crystal input face, and thus a nonlinear trajectory is suspected.

Here, we plot the transverse shift versus z -position to gain insight into the propagation after the crystal. This also aids in understanding the propagation throughout the crystal where imaging is ambiguous due to the nonlinear response in the measurements. One could extrapolate the function to the crystal input face $z = -20$ mm and see the trajectory along z . For the case of $\Omega = 100$ deg/s, linear regression shows a non-zero value at the crystal input face, showing evidence that the beam propagation is deviating from a straight-line and could be curved based on the nonlinear response of the system. Figure 3.11(a) and 3.11(b) show the measured transverse shift values along the z -direction. The progression of these beams should follow a linear regression as the drag is calculated taking an average position of the COI trajectories, which follows a straight line. Instead, as stated before, taking a linear regression gives non-zero values for certain rotation speeds. Thus, the trajectory of the beam along z could be curved or deflected due to a moving index gradient via nonlinear refraction. The linear regression in Fig. 3.11 is also consistent with the COI

travelling in a straight line. The magnitudes of the output angle are much larger due to the larger nonlinear response within the crystal. Although the curves slightly deviate from straight lines, this can be attributed to the measurement error in our system.

3.3.4 Fitting Function for Effective Group Index

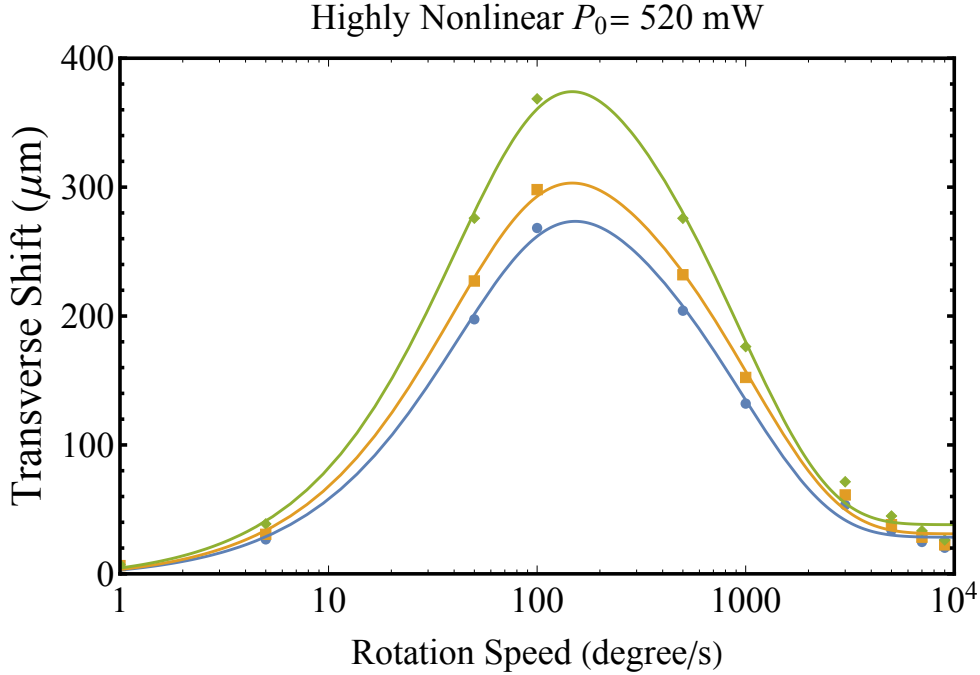


Figure 3.12: **A continuous fitting function consisting of the sum of two exponentials.** The transverse shift is plotted for the highly nonlinear regime $P_0 = 520$ mW for three positions along z : $z = 0$ (blue), $z = 7.62$ mm (yellow), and $z = 15.24$ mm (green). Similar behaviour can be seen in the case of an input power of $P_0 = 100$ mW with transverse shifts of smaller magnitude. The form of the fitting function is $f(\Omega) = a - be^{-\Omega/c} + de^{-\Omega/f}$, where a , b , c , d , and f are fitting constants. One can see that the maximum drag should be closer to $\Omega_c \approx 150$ deg/s, while discrete points in Fig. 3.11 suggest 100 deg/s. It is clear that the two exponentials indeed fit the discrete points from low to high rotation speeds and provide strong evidence that the transverse shift scales with a sum of exponentials.

We create a continuous fitting function consisting of the sum of two exponentials and an offset constant to fit the transverse shift. The transverse shift is plotted in Fig. 3.12 for the

Position (mm)	Fitting Parameters				
	a	b	c	d	f
0	28.4	334	46.3	302	959
7.52	31.0	362	42.7	326	1052
15.24	38.1	456	44.7	412.8	937

Table 3.1: **Results of the fitting parameters are shown for the highly nonlinear regime.** a, b, c, d, f, g and h for the effective group index in the highly nonlinear ($P_0 = 520$ mW) regime for all rotation speeds ($\Omega = 1 \sim 9000$ deg/s). We fit a continuous function consisting of two exponentials and a constant offset of the form: $f(\Omega) = a - be^{-\Omega/c} + de^{-\Omega/f}$.

highly nonlinear regime $P_0 = 520$ mW for three positions along z : $z = 0$ in blue, $z = 7.62$ mm in yellow, and $z = 15.24$ mm in green. Plots for the nonlinear regime ($P_0 = 100$ mW) are not shown here but follow similar behaviour of smaller magnitude. The form of the fitting function is $f(\Omega) = a - be^{-\Omega/c} + de^{-\Omega/f}$, where a, b, c, d , and f are fitting constants. When creating a continuous function, one can see that the maximum drag should be closer to $\Omega_c \approx 150$ deg/s, rather than the discrete points that suggest 100 deg/s. It is clear that the two exponentials indeed fit the discrete points taken at low to high rotation speeds and provide strong evidence that the transverse shift scales exponentially. Table 3.1 shows the fit parameters for each position along z for an input power of 520 mW. The behaviour follows two exponentials with an offset constant value that fits well with our data. This is then used along with the simulation parameters to understand the full system and the nonlinear propagation within and after the crystal. The fitting function acts on a higher-order component of the generalized nonlinear Schrodinger equation seen in the main text, manipulating the effective group index.

The speed regimes highlight different interaction timescales of the nonlinear response. Both optical and thermal processes are relevant; however, thermal processes dominate at slow speeds and optical at high speeds. Since the timescale of thermal processes is on the order of several hundred microseconds [116], this would have a greater effect locally with slower rotation speeds. However, we examine the effects over a complete cycle, and therefore, high rotation speeds are affected more by optical timescales, which in our case are on the order of 3~5 ms.

We model the temporal dynamics in these two regimes using a phenomenological fit consisting of two decaying exponentials discussed later in this chapter. We take an analogy to spatial self-steepening [50, 123]. The beam is shifted due to the group index, and therefore, the group velocity which is intensity and rotation speed dependent. This rota-

tion speed dependence, therefore samples the dynamics representing a non-instantaneous temporal response of the system.

This behaviour could be considered an effective time-varying response. Time-varying media often rely on highly nonlinear materials, such as epsilon-near-zero (ENZ) materials [16], that change the refractive index in time [18, 124], inviting optical effects like non-reciprocity [125, 126]. The strong nonlinear optical response of ruby could perhaps exhibit non-reciprocity due to an effective time-varying effect, but further work needs to be done. The magnitude of the index gradient induced by nonlinear refraction ($\Delta n = 3 \times 10^{-3}$) is estimated and discussed in Sec. 3.3.3., as well as its use in the formation of a Townes profile in the steady-state when observing a stationary medium case.

3.3.5 Townes Profile and Calculation of Nonlinear Refractive Index

Intense linearly polarized light in a rotating birefringent medium causes o- and e-beams to both experience nonlinear refraction as the maximum intensity continuously moves between them, creating a moving index gradient. The gradient leads to nonlinear coupling between the beams. The local index variation pulls one beam toward the other with the higher refractive index, locally distorting the figure-eight-like COI trajectory. The magnitude of the distortions is dictated by the rotation speed, where the speed controls the amount of time that the beam imprints an index gradient on the crystal. The maximum strength of beam coupling is observed at low speeds when the beams have sufficient time to imprint the maximum nonlinear index. On the contrary, higher rotation speeds imprint less gradient, blurring the effect of nonlinear refraction, and non-distorted figure-eight-like trajectories are recovered. Quantification of the nonlinear refraction and the size of the index gradient is useful to understand how it can manipulate the beam trajectory. The effects of nonlinear refraction are interesting for both the cases of a moving medium and also in the stationary case to understand the timescale of the interaction.

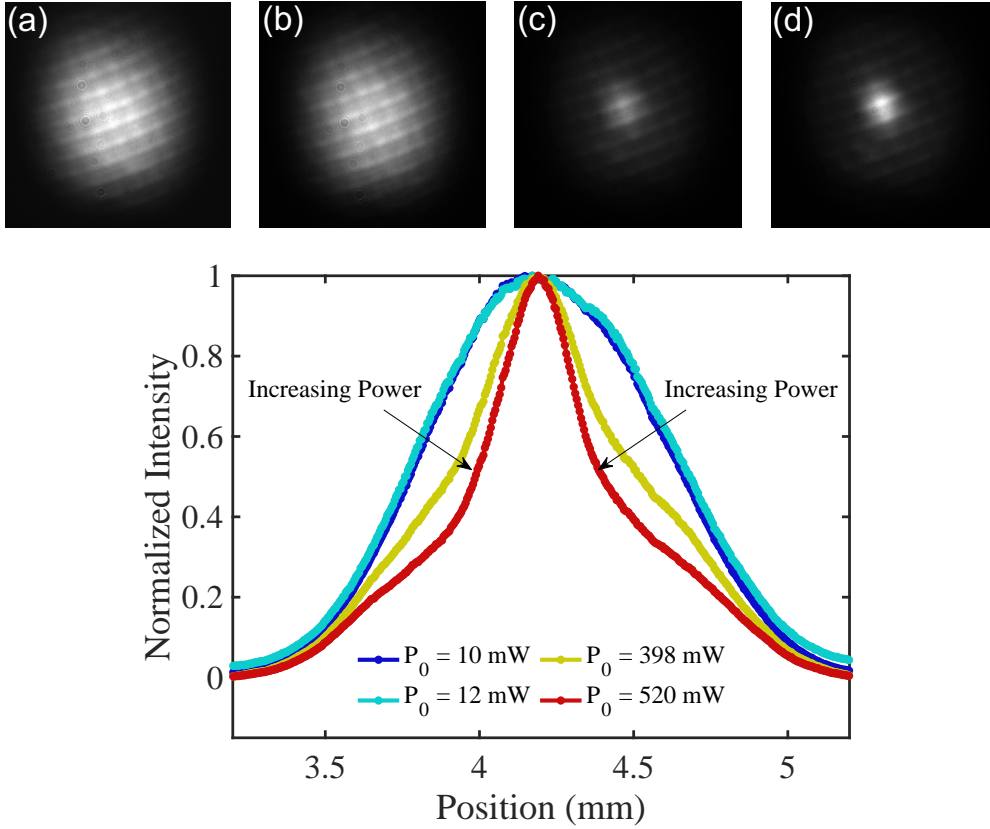


Figure 3.13: **The effect of input beam power on beam shape in a stationary medium for a beam waist of 3 mm.** Four powers are shown (a) $P_0 = 10$ mW, (b) $P_0 = 12$ mW, (c) $P_0 = 398$ mW, and (d) $P_0 = 520$ mW, where the blue ($P_0 = 10$ mW) and cyan ($P_0 = 12$ mW) curves do not meet the threshold power to show nonlinear refraction and thus self-focusing. Increasing laser power causes the input beam to self-interact and self-focus, creating a spatial soliton. This solitonic behaviour is seen in the yellow ($P_0 = 398$ mW) and red ($P_0 = 520$ mW) curves, which are significantly more intense and show a change to the beam's transverse profile. One can see that moderate intensity ($P_0 = 398$ mW) shows slightly less self-focusing than the red curve ($P_0 = 520$ mW). The red curve approaches a stable solitonic-type solution known as the Townes Profile. The tapering and stabilization of the beam waist for a Gaussian beam due to a self-focusing nonlinearity is a well-known characteristic of spatial solitons. The Townes profile observation here indicates a considerably large nonlinear index in the system at an input wavelength of $\lambda_0 = 473$ nm. A lens does not focus the beam in this case and is the straight output of the laser with a beam diameter of 3 mm. Townes profile formation with CW lasers is uncommon as most soliton solutions are formed using pulsed lasers that need sufficiently long propagation distances to stabilize.

Although the system is considered instantaneous in this work, it is interesting to study the system's time response and ability to reach a steady state. When the ruby crystal is stationary, i.e. $\Omega = 0$ deg/s, the system's time response can stabilize and reach a steady state where interesting solutions to wave propagation are possible. A self-focusing nonlinearity was observed in a stationary version of this experiment, and thus, nonlinear refraction contributes to the transverse shifting of the beam due to nonlinear deflection. The index gradient impinged on the crystal would move with the rotation of the crystal, causing the beam to follow in the direction of a higher index. The magnitude of this gradient is

$$\Delta n \approx n_2 \frac{2P}{\pi w_o^2} = (10^{-12} m^2/W) \frac{2 \times (520 \times 10^{-3} W)}{\pi (10^{-5} m)^2} = 3.3 \times 10^{-3}, \quad (3.5)$$

where $n_2 \approx 10^{-12} m^2/W$ is the nonlinear refractive index, P is the power, and w_o is the beam waist. The value of n_2 is not known at 473 nm; however, the value was measured at 514.5 nm and used in this calculation as an order of magnitude estimation [107]. Figure 3.13 shows evidence of forming a well-known soliton solution, the Townes Profile. This supports the fact that our system has a self-focusing nonlinearity, and further studies are needed to quantify the value of $n_2(\lambda = 473\text{nm})$ and fit the Townes profile.

Figure 3.13 suggests that nonlinear refraction is strong enough to match the amount of diffraction in the system and stabilize. The stabilization results in a steady-state solution. The beam waist used here was much bigger than that used in the transverse drag experimental data, and thus, the timescale to reach equilibrium is much longer. Here, the change in the waist should be equivalent to the change in the index due to the nonlinear refraction. Further work is needed to measure these values, but it is clear that the self-focusing length scale is on the order of the diffraction length scale. Furthermore, the non-instantaneous response of the system will be the subject of a further study to understand how the timescale can affect the amount of transverse shift.

Furthermore, once the beam reaches a steady state, the transverse beam profile reaches the form of the Townes profile. Since the system uses a continuous-wave laser passing through a 2 cm long solid-state ruby rod, forming a soliton is interesting as most solitons are created using pulsed lasers that propagate over several metres. Moreover, it would be interesting to see if solitons are also subject to drag and can propagate without breaking up.

3.4 Summary

In this chapter, we have experimentally demonstrated and compared with simulation with good agreement that a 2 cm long rotating ruby crystal illuminated with 473 nm light produces large transverse shifts and creates interesting transverse trajectories at the crystal output. In rotating saturable media with self-focusing nonlinear refraction, one must measure the output angle to understand if nonlinear deflection is present in the system. Even if the medium presents large negative group indices, nonlinear deflection can dominate over negative drag when nonlinear refraction is large and positive. The maximum transverse shift is found to be $\Delta y = +300 \mu\text{m}$, and the maximum angular shift is found to be $\theta = 13$ mrad at the output face of the crystal ($z = 0$). Since the position of the transverse profile of the beam is controllable by the rotation speed of the crystal and input intensity of the beam, one can imagine applications in beam-steering and image rotation, velocimetry, as well as understanding the resilience of the state of polarization to the motion of the medium. Due to slow-light enhancement, the scale of beam control is much larger, leading to better integration into optical applications.

This closes the research topic of nonlinear optics in a rotating medium. In the following chapters, we explore the effects of slow light in another concept, spaceplates.

Chapter 4

Theory and Design of Multilayer Stack-Based Spaceplates

In the two previous chapters, the manipulation of beam propagation was studied in a slow media, particularly in the context of a rotating ruby rod, through simulation and experiment. The transverse shifts observed were enhanced by the slow light effects and were measured alongside the transverse trajectories of the centre of intensity at the crystal output facet. Experimental measurements and simulation were found to match the dynamics of the system well and allowed for an in-depth understanding of a complex rotating system that could be used in a variety of optical applications.

In the present chapter, based on the work of Hogan et al. [2], we investigate a new platform that uses the principles of slow light to achieve different functionality than the previous chapters. The new platform in this chapter consists of devices known as spaceplates that replace space in an optical system. Space is replaced by carefully designing structures that impose transverse shifts while conserving the angle of the input beam, and the imaging plane, or beam focus, is therefore moved closer. By tailoring the phase response in these devices as per the group delay, one can achieve a response dependent on slow light that can be used to create devices that can help modern imaging systems. As in the case of the rotating ruby rod, manipulating beam propagation by means of elongating the response in time leads to optical functionality useful in any optical system.

4.1 Background

Spaceplates (SPs) are devices that can mimic the effects of propagation through free space, replacing the needed space with a much smaller device, and they do so by replicating the transfer function of free space. SPs can be very useful in creating much thinner optics like flat optics [15, 127, 128] but show promise in any optical system requiring long free space propagation distances. Many different avenues can achieve this concept, whether it be low-index materials submerged in an environment of a higher index or uniaxial crystals [1], photonic crystals [129], multiple lens systems [130], and the focus of this chapter, thin film multilayer stacks [13]. We will go into more detail on these designs later in the chapter, but each follows a basic theory that describes their functionality. We will discuss the parameters that characterize an SP, like the compression factor (R), numerical aperture (NA), and bandwidth ($\Delta\lambda$), and we will use the Transfer Matrix Method (TMM) to develop their basic theory.

4.1.1 Basic Theory of Spaceplates

The compression factor is a figure of merit assigned to devices that replace space in an optical system, which characterizes how well it can compress space. If we consider a certain distance of propagation in free space as the effective distance we wish to represent, denoted d_{eff} , we can relate it to the actual thickness of the device we are using, d as in Fig. 4.1.

The ratio of these two distances gives the compression factor [1] written as

$$R = d_{\text{eff}}/d. \quad (4.1)$$

Therefore, we see that if $d < d_{\text{eff}}$, $R > 1$, which is the condition for which we see spatial compression and devices can be termed as SPs. For the other regimes, $R = 1$ is the case of free space propagation, and $R < 1$ represents the majority of optics when the optical path length in the material represents a longer propagation distance than in free space.

Consider inserting an SP in the path of a focusing beam. If $R > 1$, the beam would focus earlier than in the free space case, while $R < 1$ would push the focus forward. The focal shift is due to a transverse shift of the beam, particularly the transverse walk-off, Δx , shown in Fig. 4.1. The amount of shift is calculated based on the phase the device accumulates upon propagation and will be discussed and quantified later in this chapter. However, a key point to note is that the phase response is tailored such that the angle is conserved upon propagation through an SP, unlike for a lens, which conserves position.

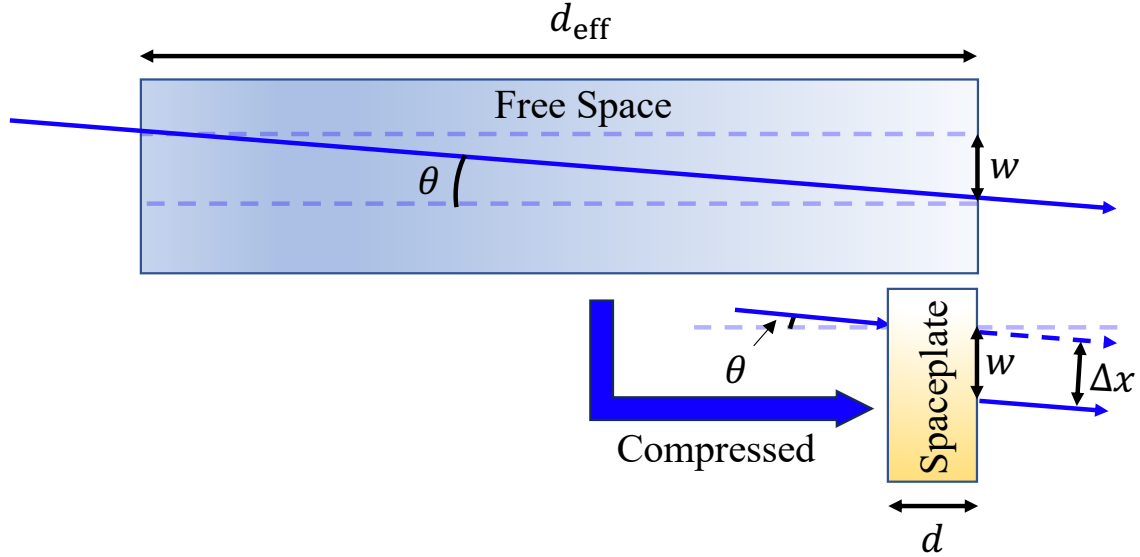


Figure 4.1: **A schematic of how an SP device of thickness d acts as an effective distance of free space propagation, d_{eff} .** The distance w represents the lateral shift over a certain distance propagated in free space where the angle of the input ray, θ , is conserved for both free space and the SP. The distance between an apparent ray, in dashed lines, and the actual ray is the transverse walk-off, Δx .

If we consider a plane wave normally incident on a lens, the lens will locally affect the beam on a position-by-position basis and manipulate the angle such that all rays will converge to a point. The lens performs a unitary process, a local operation on the input light that conserves spatial position upon propagation of the optic. An SP also performs a unitary operation on the input beam but acts nonlocally [131]. An SP acts on the wave vectors such that the angle is conserved, but the spatial position is not. In general, SPs and lenses can be considered complementary optics in terms of local (position-dependent) and nonlocal (wave-vector-dependent) phase response. Both optics will affect the focus, but the key difference for an SP is the mechanism by which the SP shifts the focus closer to the device, conserving the angle and transversely shifting the beam. We have made it clear that the phase response is important in understanding lenses and SPs in the scope of their phase response to input light. Therefore, we will take time to understand the associated phases and how the response is considered local or nonlocal.

4.1.2 Lens Phase vs. Spaceplate Phase

Lenses are widely used optics in almost every optical application. In the geometric optics picture, a lens takes all input rays and converges them to a point. This operation is done by imprinting a position-dependent phase, a local-phase response. This phase response has the form

$$\phi(x, y) = k\sqrt{f^2 - x^2 - y^2}, \quad (4.2)$$

where f is the focal length, and x and y represent the transverse position in Cartesian coordinates. This states that if we situated the origin at the center of the lens, therefore setting $x = y = 0$, the amount of phase accumulated is $\phi = kf$. As such, if the beam is located at any other point on the lens, the light ray will experience a different amount of phase that will change the angle and cause all rays to converge to a point at the point f only if an object is placed at infinity, according to Lens maker's equation [132]

$$\frac{1}{f} = \frac{1}{s_o} + \frac{1}{s_i}. \quad (4.3)$$

Here, s_o refers to the object distance, and when set to infinity, the image forms at $s_i = f$, known as the image distance.

In the case of an SP, the phase response is considered nonlocal. The phase response is considered nonlocal in that the phase acts on the wave vectors, conserving the angle but changing the output position once the light has traversed the optic. The nonlocal phase response of an SP [1] is written as

$$\phi_{SP}(k_x, k_y, d_{\text{eff}}) = k_z d_{\text{eff}} = d_{\text{eff}} \sqrt{|\vec{k}|^2 - k_x^2 - k_y^2}, \quad (4.4)$$

where \vec{k} describes the wave vector with components in x , y , and z . Acting on the wave vectors, the phase accumulated upon propagation can impinge a transverse shift in a ray position, like in Fig. 4.1. This behaviour is best discussed as a group delay imposed on the input light based on a difference in the group velocities of different light components. This topic will be discussed further in Sec. 4.5.

4.1.3 Types of Spaceplates

Although not many experimental studies have demonstrated spatial compression, it has been theoretically studied in depth [14, 128, 129]. As mentioned, one approach uses a low-index material surrounded by a higher-index material. This was inspired by using epsilon-near-zero (ENZ) materials, which have a refractive index approach zero, leading to things

like enhancement of the nonlinear refractive index [36], or use in easing phase-matching conditions [133]. However, regarding SPs, the low-index ENZ material allows for spatial compression by surrounding the medium with a higher-index material [1]. The resulting compression factor is quantified by the index contrast of the two materials. Therefore, the closer to zero the refractive index can reach, the compression factor could be infinite in theory. However, in reality, the compression factor achievable is closer to $R = 1.48$, where

$$R = n_2/n_1. \quad (4.5)$$

and n_1 is the ENZ index, and n_2 is the surrounding medium index.

It has also been experimentally demonstrated that a uniaxial crystal is aligned along its optical axis with the input light, the light will also experience spatial compression. This was also shown using a uniaxial crystal [1], where a similar concept is applied. However, it is important to note that both the uniaxial crystal method and the low-index SP method are limited by the constituent materials and, therefore, cannot lead to large compression factors due to the material index contrast. Moreover, in both cases, the polarization of light can affect the device's performance, making the application of such devices more difficult. Furthermore, the size of the system is quite large and would not allow for the miniaturization of modern imaging systems.

Another avenue was using photonic crystals to produce spatial compression [129]. This mechanism relies on the strategic placement of the guided mode in the photonic crystal, which is placed between two dielectric stacks such that the light experiences spatial compression. The periodic nature of the photonic crystal can be exploited to help achieve the SP effect. The photonic crystal creates a Fano-resonance, and the phase rapidly changes near this resonance. Using the guided resonance, the band dispersion is quadratic in phase, which can be used to match the SP phase. This method is less dependent and is more focused on utilizing resonances rather than straight material parameters, resulting in larger compression factors; however, realizing such SPs seems difficult in practice.

The fourth avenue that achieves spatial compression is using a three-lens setup [130]. The conditions of the two external lenses are the same focal length, f_2 , and the third lens located at the focus of the other two has a focal length, f_1 , less than the others, resulting in a compression factor of

$$R = \frac{f_2}{2f_1} - 1. \quad (4.6)$$

The condition that $R > 1$ is only if the outer lens $f_2 > 4f_1$. Placing a lens in the Fourier plane of a 4-f system, in the paraxial approximation, inputs a phase like an SP, where the condition above must be met to match the quadratic term of the phase. Indeed,

lenses complement SPs but do not provide the same base functionality. The 3-lens system, however, indeed behaves as an SP and has experimentally shown modest compression factors of $R = 15.6$ and is polarization insensitive. However, the space needed to match these conditions is costly for a miniaturized optical system. On the other hand, if long-scale spatial compression is needed, the system size multiplied by the compression factor can serve as a great tool to alleviate long propagation distances in free space. A few disadvantages are that the outside lens must be large to ensure that no aberrations impinge on the input light, and the NA is very limited (NA=0.017). Moreover, moving a large system like this would be cumbersome.

The final proposed platform uses multilayer stacks. Many variations of this platform can serve to produce spatial compression; however, some perform better than others. One considers a Fabry-Perot (FP) cavity coupled by a quarter wave layer [13]. All other layers are set to integer value multiples of a quarter wave, except the cavity of length $\lambda/2$. The basic design consists of alternating layers of low and high refractive indices and has the form $[L, H, 2L, H]^n$, where L represents the low index layer, H represents the high index layer, and n is the number of unit cells. As more unit cells are added to the structure, the compression will moderately increase, reaching a value of $R = 5 \sim 6$ over a large NA and wavelength range. Often, a device's NA and bandwidth can become limited when reaching large compression factors [14]. In this thesis, we will present two different approaches to multilayer stacks that increase the compression factor significantly. Two design philosophies will be discussed later when considering high-performing multilayer stack-based SPs with a more limited angular range and bandwidth but much larger compression factors. The NA and bandwidth trade-offs will also be discussed later in this chapter.

4.2 Transfer Matrix Method

TMM is a useful tool for characterizing the optical properties of thin films or multilayer stacks [134–136]. TMM allows for easy analysis of multiple layers by considering two types of matrices that describe all interactions between input light and the full structure. TMM comprises two matrices that describe the interaction of input light with an interface, known as the T-matrix, and the propagation of light through a layer with a refractive, n , referred to as the P-matrix, which describes the phase accumulated on propagation. The resulting matrix, M , that describes a thin film multilayer structure can predict the reflection and transmission phase, the transmittance, reflectance, and other properties that are key to understanding the expected performance of a device. Moreover, since the phase of an SP must be tailored to mimic the transfer function of free space, the results of TMM can be

used to match the correct conditions for a multilayer stack such that it indeed behaves as an SP.

Since the multilayer stacks are built of many different materials, their response will vary based on input polarization. Therefore, it is important to note that when considering suitable materials to create an SP, the response can be tailored based on the response due to the input polarization of the light. The simplest case is p -polarized or s -polarized light, which relates to how the electric field is oriented with respect to a surface. A way to represent the polarization is using a plane containing unit vectors along incident, reflected (transmitted), and normal to the surface. P -polarization will be parallel to the plane, and s -polarization will be perpendicular. The s - and p -fields will interact with a surface differently and lead to different responses, particularly when deviating away from normal incidence. The interaction at the interface can be defined by a matrix, T , comprised of the fields before and after the interface.

Let us suppose that we are at the boundary of two materials with refractive indices, n_1 and n_2 , respectively, and medium 2 has a finite thickness d . In this case, let us build up the interface and phase matrices, T and P , to describe the full interaction of input light at an angle, $\theta_i \neq 0$ passing through a material of thickness d and refractive index n_2 .

First, we should consider the simplest case of light at an interface described by Snell's Law [137], where

$$n_1 \sin(\theta_i) = n_2 \sin(\theta_t) = n_1 \sin(\theta_r), \quad (4.7)$$

and θ_i is the angle of incidence, θ_t is the transmitted angle, and θ_r is the reflected angle. Since the reflected light is in the same medium, we find that $\theta_i = \theta_r$, as seen in Fig. 4.2.

Considering the fields, if we have input light interact with the surface with a field amplitude E_i , a reflected field amplitude E_r , and a transmitted field amplitude E_t , we can start to define quantities known as the Fresnel coefficients [132]. These coefficients will be useful in developing the interface matrix toward the total matrix from TMM, describing the full interaction of the input light with the material.

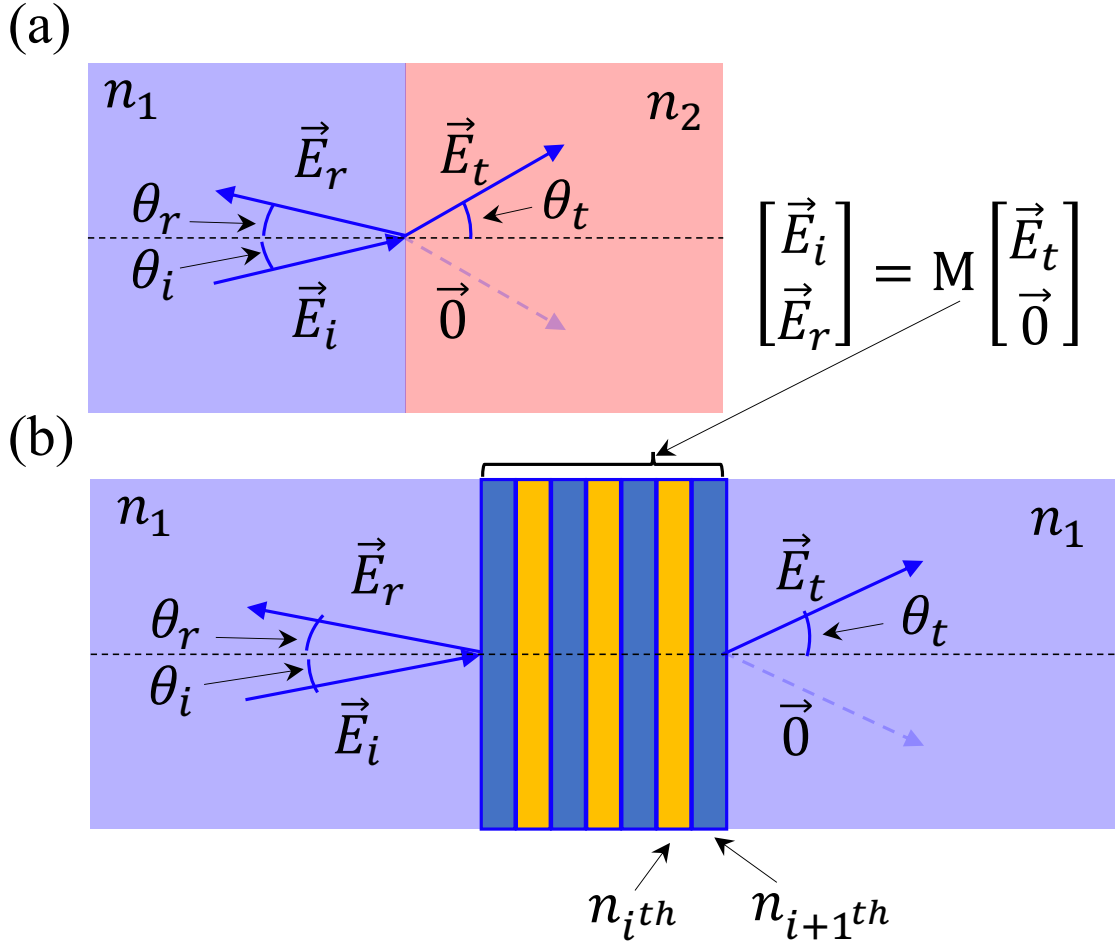


Figure 4.2: **Schematics of the incident, reflected and transmitted fields for (a) a single interface and (b) a multilayer stack interface.** An incident field \vec{E}_i interacts with a surface at an angle θ_i for the normal, and creates a reflected field \vec{E}_r , at angle $\theta_r = \theta_i$, and a transmitted field \vec{E}_t , at an angle θ_t . For a single interface of infinitely thin thickness, the interaction is governed by Snell's Law in Eq. (4.7) relating the refractive indices n_1 and n_2 and the angles θ_i , θ_r , and θ_t . The fields are related by Fresnel coefficients, discussed in Eqs. (4.8)- (4.11). For a multilayer stack, the stack is described by a matrix, M , calculated using TMM to relate the inward and outward fields discussed in more detail later in the chapter. Propagation and interface matrices can be defined in between layers i and $i + 1$, which will be used to calculate the full matrix M of the device.

4.2.1 Interface Matrix

Generally, the interface matrix is written using coefficients r_s , r_p , t_s , and t_p , referred to as Fresnel coefficients. These coefficients represent how the input light is reflected and transmitted based on the angle of incidence of the input light and the refractive index of each material in question.

Fresnel Coefficients

Fresnel coefficients represent the ratios of the electric fields when considering an interface. Supposing that we impinge light at an angle θ_i , and the transmitted angle is θ_t , we can define the reflection Fresnel coefficients for p - and s -polarized light as

$$r_p = \left(\frac{E_r}{E_i} \right)_p = \frac{n_2 \cos(\theta_i) - n_1 \cos(\theta_t)}{n_1 \cos(\theta_i) + n_2 \cos(\theta_t)} = \frac{n_2 \cos(\theta_i) - n_1 \sqrt{1 - \left(\frac{n_1}{n_2} \sin(\theta_i) \right)^2}}{n_1 \sqrt{1 - \left(\frac{n_1}{n_2} \sin(\theta_i) \right)^2} + n_2 \cos(\theta_i)}, \quad (4.8)$$

and

$$r_s = \left(\frac{E_r}{E_i} \right)_s = \frac{n_1 \cos(\theta_i) - n_2 \cos(\theta_t)}{n_1 \cos(\theta_i) + n_2 \cos(\theta_t)} = \frac{n_1 \cos(\theta_i) - n_2 \sqrt{1 - \left(\frac{n_1}{n_2} \sin(\theta_i) \right)^2}}{n_1 \cos(\theta_i) + n_2 \sqrt{1 - \left(\frac{n_1}{n_2} \sin(\theta_i) \right)^2}}. \quad (4.9)$$

Furthermore, we can define the transmission Fresnel coefficient using the transmitted and incident field amplitude ratios. The transmission

$$t_p = \left(\frac{E_t}{E_i} \right)_p = \frac{n_1 \cos(\theta_i)}{n_1 \cos(\theta_t) + n_2 \cos(\theta_i)} = \frac{n_1 \cos(\theta_i)}{n_1 \sqrt{1 - \left(\frac{n_1}{n_2} \sin(\theta_i) \right)^2} + n_2 \cos(\theta_i)}, \quad (4.10)$$

and

$$t_s = \left(\frac{E_t}{E_i} \right)_s = \frac{2n_1 \cos(\theta_i)}{n_1 \cos(\theta_i) + n_2 \cos(\theta_t)} = \frac{2n_1 \cos(\theta_i)}{n_1 \cos(\theta_i) + n_2 \sqrt{1 - \left(\frac{n_1}{n_2} \sin(\theta_i) \right)^2}}. \quad (4.11)$$

These constituent Fresnel coefficients describe what happens with light at an interface but are more closely related to energy transfer at the interface. When light interacts with a

surface, we expect to have energy conservation, as well as momentum conservation. This discussion will focus on energy conservation related to relevant physical quantities that describe the system. Using the reflection Fresnel coefficients, we can define the reflectance, R , which describes the total energy reflected at an interface. Similarly, we can define the transmittance, T , which describes the total energy transmitted at an interface. When considering a lossless medium, we know that $T + R = 1$ is based on energy conservation [132]. This can be generalized to include absorption (A) of the medium, diffusion (D), and other properties, which can have more or less weight depending on the material and the response to a given wavelength. If we include the other effects, the energy conservation would look like $A + D + R + T = 1$ [138]. In general, this type of light-matter interaction is always considered a conservation law. However, some cases are not conservative, typically when work is applied to the system, and energy is lost by heat. However, this is out of the scope of this thesis and will not be elaborated on further. Instead, we will represent the transmittance and reflectance as functions of the Fresnel coefficients.

The reflectance writes as

$$R_s = |r_s|^2, \quad (4.12)$$

and

$$R_p = |r_p|^2. \quad (4.13)$$

The absolute value is taken since the Fresnel coefficients can be complex as a result of the refractive index.

Considering the simplest case, one would expect the transmittance to be just $T = 1 - R$; however, the impedance mismatch, or otherwise stated wave vector mismatch, must also be considered. The transmittance, therefore, is written as

$$T_s = \frac{n_2 \cos(\theta_t)}{n_1 \cos(\theta_i)} |t_s|^2, \quad (4.14)$$

and

$$T_p = \frac{n_2 \cos(\theta_t)}{n_1 \cos(\theta_i)} |t_p|^2. \quad (4.15)$$

Now, with the full description of the transmittance, the energy conservation relationship is conserved for $T + R = 1$.

Although this is a complete overview of one interface, optical systems have finite thicknesses and often comprise multiple layers with many interfaces. Therefore, we should first represent the interface matrix using Fresnel coefficients before moving on to the phase matrix upon propagation.

Supposing that we have multiple layers of materials, where each layer can be represented as the i -th layer, $i = 0, 1, 2, 3, \dots$, and each interface, represented by i is located between the i -th and $(i + 1)$ -th layer, as in Fig. 4.2, we can write

$$T_i = \frac{1}{t_i} \begin{bmatrix} 1 & r_i \\ r_i & 1 \end{bmatrix}. \quad (4.16)$$

The T -matrix can simply represent the interaction for s - or p -polarized light by substituting the Fresnel coefficients. We will return to how this matrix is incorporated into the whole picture of a multilayer system later. For now, we will consider the matrix that describes light propagation through a medium, the P -matrix.

4.2.2 Propagation Matrix

Suppose input light impinges the system at an angle θ_i and passes through a layer, picking up a certain amount of phase over the layer thickness. If we assume we have multiple layers, where the i -th layer has a thickness d_i and refractive index n_i , we can describe the phase accumulated on propagation as

$$\delta_i = \frac{2\pi}{\lambda} n_i d_i \cos(\theta_i), \quad (4.17)$$

where λ is the wavelength of the input light. We can see that the amount of phase depends on various parameters. Therefore, if we want to control the amount of phase accumulated upon propagation in the SP, we must consider the input angle, the layer thicknesses, and the spectral response based on the input wavelength. This phase is applied to the input wave as an exponential of the form $e^{-i\delta}$. Using this form, we write the P -matrix as

$$P = \begin{bmatrix} e^{i\delta_i} & 0 \\ 0 & e^{-i\delta_i} \end{bmatrix}. \quad (4.18)$$

Now that we have both the T - and P -matrices, we can build up the full matrix that describes the light-matter interaction in a multilayer stack.

The full matrix, as described by TMM, goes in order from the last interaction to the first, such that we have

$$M = T_1 P_1 T_2 P_2 \dots T_n = \begin{bmatrix} M_{11} & M_{12} \\ M_{21} & M_{22} \end{bmatrix}. \quad (4.19)$$

The components $M_{i,j}$, where $i, j = 1, 2$ are useful in calculating specific system parameters. If we want the effective Fresnel coefficients t and r , we can use the constituents of the M -matrix. Using the M_{11} element, we have that

$$t = \frac{1}{M_{11}}. \quad (4.20)$$

Similarly, for the effective reflection Fresnel coefficient, we can write

$$r = \frac{M_{21}}{M_{11}}. \quad (4.21)$$

To find the overall transmittance of the structure, we can make a similar approach to the case of one layer, where

$$T = \frac{k_{out}}{k_{in}} |t|^2, \quad (4.22)$$

and

$$R = |r|^2. \quad (4.23)$$

Since the layers incorporate the angular response and wavelength dependence of the input light, both T and R are functions of the angle of incidence and input wavelength. This is incredibly valuable as we can investigate the spectral response to resonant features and look at the allowed angles when a structure becomes more complex. Moreover, since the polarization affects the Fresnel coefficients, and one can write subscripts s or p for the given polarization, T and R are also calculated for the respective polarization. The remaining quantity that is important to understand and be able to manipulate is the total phase of propagation. In this case, we can use the argument of t and r to find the transmitted light's total phase and the reflected light's total phase to match it to the SP phase, which we will talk about later. Therefore, the total transmission and reflection phases of the structure are

$$\phi_t(\theta, \lambda) = \arg(t(\theta, \lambda)), \quad (4.24)$$

and

$$\phi_r(\theta, \lambda) = \arg(r(\theta, \lambda)). \quad (4.25)$$

Here, we have dropped the subscript i where θ represents the angle of incidence defined at the beginning of a structure for simplicity of writing. Now, through TMM, we can characterize the transmittance, reflectance, and their associated phase for a multilayer structure of an arbitrary amount of layers. We will now discuss the specific designs used for the SPs, the ideal phase that we wish to match the device phase, and the philosophies that go into the design process. Moreover, we will look at the spectral response outside the design region to see the possibilities of achieving spatial compression in other spectral windows, even when designing for a targeted wavelength.

4.3 Device Design

Using TMM targets a more specific subset of SPs, specifically multilayer stack-based SPs, which are the focus of this chapter and the next. However, TMM can still describe any system that can be broken down into interfaces and propagation layers. Regardless of the type of SP, we can describe the phase needed from an SP according to a few key parameters.

4.3.1 Ideal Spaceplate Phase

As mentioned before, an SP is supposed to mimic free space propagation. The SP phase, therefore, must match accordingly. We will consider the free space phase as the ideal case, and so the ideal SP phase is written [1]

$$\phi_{SP} = -\frac{2\pi}{\lambda} n_{BG} d_{\text{eff}} \cos(\theta), \quad (4.26)$$

where n_{BG} is the background index referring to air and, therefore, can be set to equal to one. We write the effective distance in this description of the ideal SP, as this is what we wish to mimic using an SP. We know that $d_{\text{eff}} = Rd$, thus we can write the SP phase as

$$\phi_{SP} = -R \frac{2\pi}{\lambda} d \cos(\theta). \quad (4.27)$$

We can then fit the total transmission phase ϕ_t to the device and extract the value of the compression factor, R , over a certain angular range. An example of the total phase for a device is shown in Fig. 4.3 for both p - and s -polarization.

There are several jumps in the phase, but the most important section is the first rapid change of the phase near normal incidence. Another thing to note is that the phase starts from zero rather than a value. This is due to a subtraction of a global phase term. If the $\cos(\theta)$ term in the phase is Taylor expanded with respect to θ , the global phase does not have any dependence on the angle. Only higher-order terms in the Taylor expansion with respect to the angle can contribute to matching the transmission phase to an ideal SP phase. Since the phase is related to $\cos(\theta)$, we look for fitting based on the quadratic term in the expansion of the cosine. The initial term merely moves the two curves to another position and, therefore, does not affect the fitting of the SP phase to the device phase. That being said, we must fit the SP to this region to accurately measure the compression factor of the device. For this chapter, we will be able to extract the compression factor using solely the phase calculated from TMM and fit it to an ideal spaceplate phase. However,

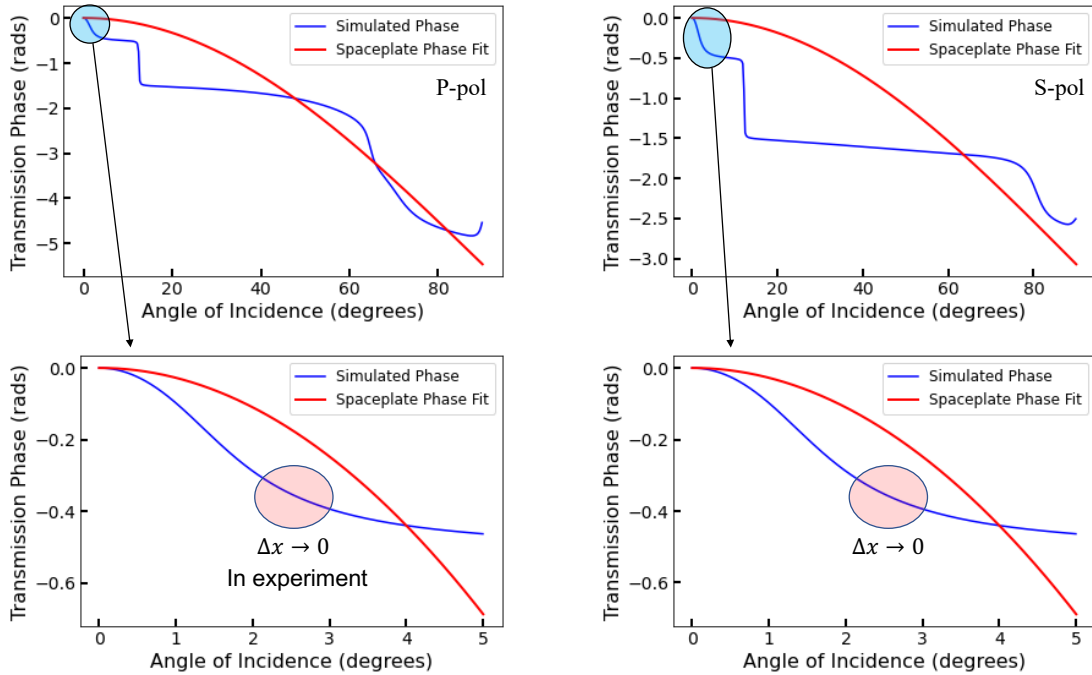


Figure 4.3: **Fitting an ideal SP phase to the transmission phase of a device.** Phase is shown over the full angular range of $\theta = 0 \sim 90^\circ$ and a smaller region $\theta = 0 \sim 5^\circ$ for both s - and p -polarization. The smaller angular range allows for a better fit to the device's phase and, therefore, provides a correct quantification of the compression factor for this given device.

in practice, as in Chapter 5, it is more preferential to measure the transverse walk-off and extract the compression factor from it. Therefore, we will present how one can calculate the transverse walk-off, Δx , from the phase using the derivative of the phase as a function of angle.

Given that an SP conserves angle, we should restrict our attention/fits to the region where the slope of the transverse walk-off, determined by the derivative of the phase, is nearly constant near small angles. If we zoom in, as in the case of the two lower panels of Fig. 4.3, we can see that the phase starts to plateau around $\theta = 2.5^\circ$, where we denote $\Delta x \rightarrow 0$ in the experiment. Δx refers to the transverse walk-off, a good measure of the device's compression factor, as seen in Fig. 4.4. The true measure of the transverse walk-off consists of a tilted SP and measuring the shift Δx_{sp} . We will show how to extract R from Δx_{sp} shortly; however, it must be said that the fit now should consider the region

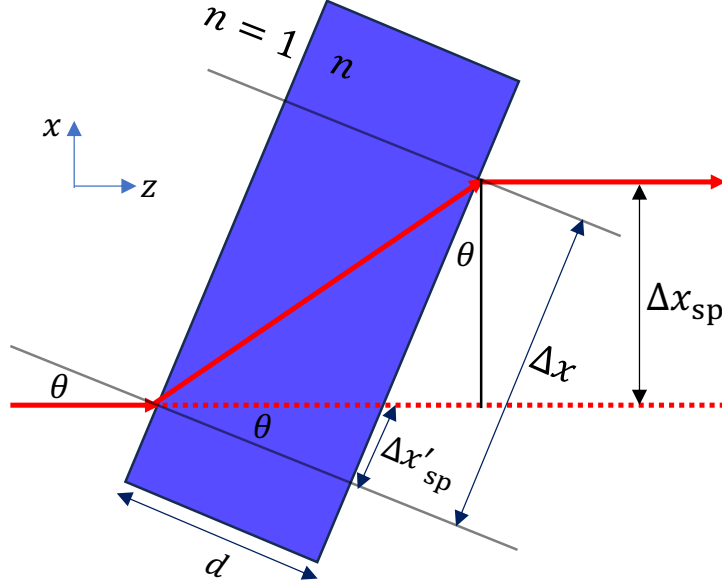


Figure 4.4: **A schematic of the transverse walk-off for a given incident angle θ .** The measured transverse walk-off Δx_{sp} comprises components of the addition of the apparent walk-off, Δx and the SP walk-off, $\Delta x'_{sp}$ [1].

associated with half of the angular range at which $\Delta x_{sp} \rightarrow 0$. This region refers to the range of angles where the angle is conserved, and the effect can be deemed as an SP. To accurately determine the R of a given device, the transmission phase must be fit to the region where the angle is conserved or otherwise stated, where the transverse walk-off has a linear dependence on the angle. We relate the transverse walk-off to the phase by its derivative [11], that is,

$$\Delta x = \frac{\partial \phi_t}{\partial k_x} = \frac{1}{k \cos(\theta)} \frac{\partial \phi_t}{\partial \theta}, \quad (4.28)$$

where k_x represents the x -component, or otherwise written $k_x = k \cos(\theta)$. This supposes that the spaceplate is tilted by θ rather than the input beam tilted from normal. Let us also suppose that ϕ_t can be written as the wave vector component in the xz plane projected onto the z -axis. In that case, $\phi_t = k_x d = kd \cos(\theta)$. Therefore, we find the transverse walk-off to be

$$\Delta x = \frac{1}{k \cos(\theta)} (kd \sin(\theta)) = d \tan(\theta). \quad (4.29)$$

This transverse walk-off represents the walk-off for any optic in consideration. However, we wish to determine the transverse walk-off for an SP. The ideal phase for an SP is given

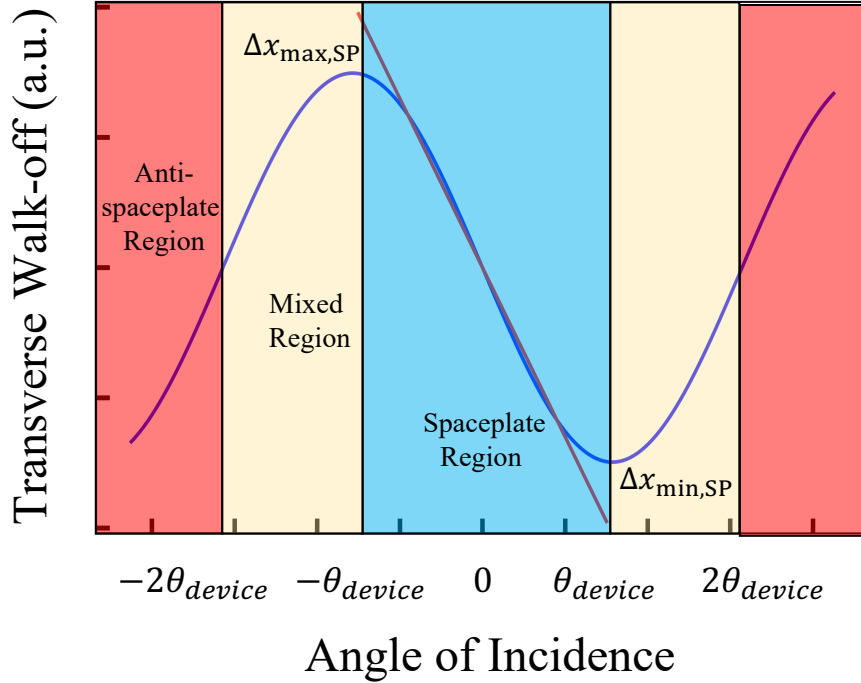


Figure 4.5: **A schematic of the evolution of the transverse walk-off for an SP.** Spatial compression is witnessed in the blue region, denoted SP region. The device's NA, $\pm\theta_{\text{device}}$, is set based on the region between where the slope of the transverse walk-off goes to zero. $\Delta x_{\text{max/min}}$ show the maximum and minimum transverse walk-off measured within the SP region. The yellow regions show a region where R starts to decrease from its maximum value until the device reaches a zone where it is no longer spatially compressing but acting larger than its given size, indicated in red. This region is usually seen after $\pm 2\theta_{\text{device}}$.

by Eq. (4.27), and if we derive the walk-off for an SP, we find

$$\Delta x'_{SP} = -d_{\text{eff}} \tan(\theta) = -Rd \tan(\theta). \quad (4.30)$$

However, as presented by Reshef [1], this does not completely describe the transverse shift. Therefore, the component of this shift is taken by adding the apparent and SP walk-off and taking the component along x , i.e. multiplying by $\cos(\theta)$ to find the actual transverse walk-off given by

$$\Delta x_{SP} = (\Delta x'_{SP} + \Delta x) \cos(\theta) = -(R - 1)d \sin(\theta). \quad (4.31)$$

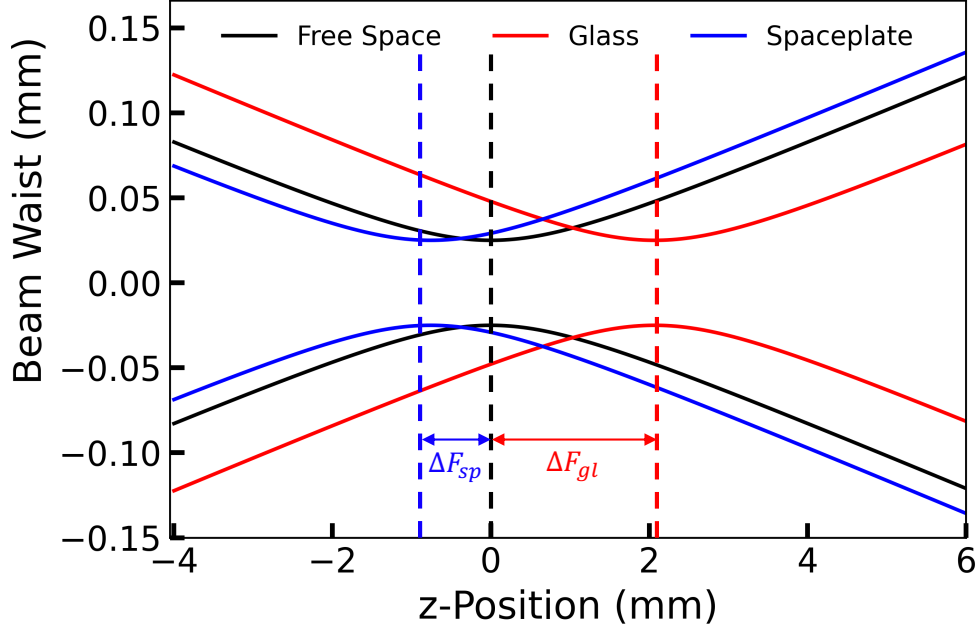


Figure 4.6: **Schematic representation of a Gaussian beam waist evolution for three cases for a beam with a waist $w_0 = 10 \mu\text{m}$.** The beam waist evolution of free space is plotted in black, and the waist is situated at $z = 0$. The evolution of beam waist for a 3 mm thick piece of glass is shown in red and for a $10 \mu\text{m}$ thick SP ($R = 80$) in blue. These two cases for a piece of glass and an SP highlight the focal advance and retraction, respectively. The advance in focus is denoted as ΔF_{gl} , and the focal retraction is denoted ΔF_{sp} .

as seen in Fig. 4.4.

This relationship for the transverse walk-off will be used extensively in Chapter 5 to extract the compression factor of the devices to measure their spectral response and operating angular ranges. A schematic of the behaviour of the transverse walk-off as a function of angle is shown in Fig. 4.5. We can see that the slope of the transverse walk-off at small angles is negative, as expected for an SP.

The focal shift is another metric that can be used to understand the SP effect. The

focal shift [11] can be represented similarly using the transmission phase, taking the form

$$\Delta F = k \frac{\partial^2 \phi_t}{\partial k_x^2} = \frac{1}{k \cos^2(\theta)} \left(-\tan(\theta) \frac{\partial \phi_t}{\partial \theta} + \frac{\partial^2 \phi_t}{\partial \theta^2} \right). \quad (4.32)$$

Assuming the same phase $\phi_t = kd \cos(\theta)$, we find the focal shift of a regular optic to be

$$\Delta F = d \sec^2(\theta). \quad (4.33)$$

Similarly, for an SP, the focal shift would be

$$\Delta F'_{SP} = -d_{\text{eff}} \sec^2(\theta). \quad (4.34)$$

Using the same logic to calculate the real focal shift, we find

$$\Delta F_{SP} = (\Delta F + \Delta F'_{SP}) \cos(\theta) = (d - d_{\text{eff}}) \sec(\theta). \quad (4.35)$$

Assuming the small angle approximation, we find the focal shift due to an SP to be

$$\Delta F_{SP} \approx d - d_{\text{eff}} \quad (4.36)$$

Therefore, this is in accordance with our original claim that the focal shift is $\Delta F_{SP} = d - d_{\text{eff}} < 0$, and therefore a focal retraction as expected for an SP. A schematic depicting this shift is shown in Fig. 4.6, highlights the focal shift of glass advancing the focus by an amount ΔF_{gl} , and the SP focal shift ΔF_{SP} , both with respect to the focus position in free space.

4.4 Characterization of Spaceplates

4.4.1 Design Philosophies

The focus of this chapter is to design and characterize multilayer stack-based SPs; however, there are different approaches one can take to develop a high-performance SP. We have taken two different philosophies to create four distinct SPs. Two are inspired by the design process of Chen et al. [13] but adapted differently. The other designs were created by an algorithm using gradient descent by Pagé et al. [139]. These designs have thicknesses that are not determined by the input wavelength, that is, some fraction of the wavelength, but are chosen based on the optimization to have a global effect leading to large compression factors. In both cases, we will discuss the implications of each design, their characterization, and other resonant features away from the design wavelength.

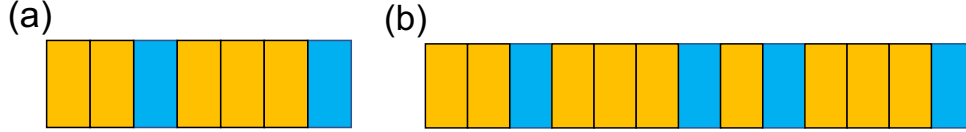


Figure 4.7: **Unit cells of two SP devices using a coupled resonator approach.** The unit cell in (a) is repeated four times, resulting in three peaks in the wavelength dependence of the transmittance for device CR1. The unit cell in (b) is repeated eight times, resulting in seven peaks in the wavelength dependence of the transmittance for device CR2. The resonance peaks result from interference of multiple cavities formed in the device, and the amount of peaks is governed by $n - 1$ unit cells. $n_H > n_L$, where n_H are the blue layers, and n_L are the orange layers.

Coupled Resonator Approach

The first approach is referred to as a coupled resonator approach. The basic design proposed by Monticone consists of three core components: a coupling layer, two mirrors, and an FP cavity [13]. Each of these layers must obey the condition of integer multiples of a quarter wave. This design was further elaborated on by manipulating the length of the cavity, coupling layer, as well as the structure of the mirror within the device. Two designs in Fig. 4.7 follow this coupled resonator approach. The low-index layer is indicated in orange, and the high-index layers are in blue. The coupling layer is set to a length of $\lambda/2$, the mirrors are $\lambda/4$ in length, and the FP cavity is $3\lambda/4$ in length. Together, these components make up a unit cell replicated many times to create the entire SP. The unit cell associated with the design in Fig. 4.7(a) is repeated eight times. The resonant wavelength of the device would be at

$$\lambda_{\text{res}} = 2L_c, \quad (4.37)$$

where L_c is the length of the Fabry Perot cavity. In this case, $\lambda_{\text{res}} = 1.5\lambda$. However, when another unit cell is added, the coupling layer then becomes the cavity between two mirror-like sections of the device of form

$$2L/[H, 3L, H][2L][H, 3L, H], \quad (4.38)$$

and so on for more unit cells. If two adjacent layers are the same, they effectively do not add phase to the input wave, except for the placement of the cavity. Therefore, the structure can be simplified to

$$[H, L, H][2L][H, L, H]. \quad (4.39)$$

Therefore, this would give a resonant wavelength at the target wavelength $\lambda_{\text{res}} = \lambda$. As more unit cells are added, the cavities will interfere with one another, and resonance positions will appear. Resonances will appear at constructive positions for an even number of unit cells and destructive positions for an odd number, with the number of resonant peaks corresponding to $n - 1$, and n is the number of unit cells. This also holds for the design seen in Fig. 4.7(b). However, the simplified design is more complex. The design for two unit cells is

$$2L/[H, 3L, H, L, H, 3L, H][2L][H, 3L, H, L, H, 3L, H]. \quad (4.40)$$

We can simplify this structure to be

$$[H, L, H, L, H, L, H][2L][H, L, H, L, H, L, H]. \quad (4.41)$$

As we can see from the structure, the simplified version creates a long Bragg mirror [140] on either side of an FP cavity that supports a resonant wavelength of λ .

As we add more unit cells, the interference effect between these cavities is also seen. The interference of many unit cells also allows for sharp resonant features that significantly increase the compression factor for these devices. In the case of Fig. 4.7(b), the unit cell is repeated four times.

Gradient Descent

The next two designs were built using an algorithm to optimize the layer thickness. The optimization was calculated to maximize the compression factor for a given angular range. Since there is no overall periodic structure, the device imposes more effective resonance associated with large compression factors.

Figure 4.8(a) is a design with 17 layers that creates a larger working angular range (larger NA) ($\theta \pm 10^\circ$) with a moderate compression factor ($R = 18$), while Fig. 4.8(b) is a much larger compression factor ($R = 238$), but a more limited angular range ($\theta = \pm 1^\circ$). The refractive indices of the low- and high-index layers are silica and silicon at $\lambda = 1.55 \mu\text{m}$, resulting in $n_L = 1.458$ and $n_H = 3.196$.

The nomenclature that is chosen for the four devices is CR1 and CR2 for the ‘‘Coupled Resonator’’ devices in Fig. 4.7(a) and (b), respectively, and MS1 and MS2 for the ‘‘Multilayer Stack Gradient Descent’’ devices in Fig. 4.8(a) and (b), respectively. We will now apply TMM to each of these four devices to quantify the compression factor for each device and understand the operating angular ranges and bandwidth.

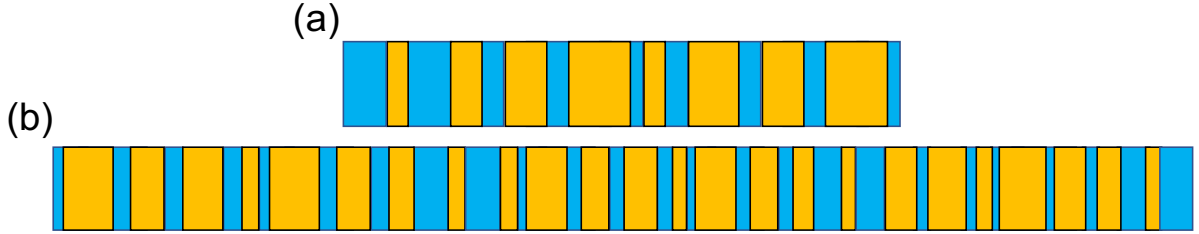


Figure 4.8: **Unit cells of two SP devices using gradient descent.** (a) shows a design (MS1) with a moderate angular range ($\theta \pm 10^\circ$), and a modest compression factor ($R = 18$), while (b) shows a design (MS2) with a small angular range ($\theta = \pm 1^\circ$) and a large compression factor ($R = 238$).

4.4.2 TMM Characterization of Devices

As stated previously, TMM is a powerful tool for modelling the interaction of light with a multilayer structure. The phase and transmittance can be extracted to understand each given device's angular and spectral response. In the simulations, the designs were targeted for an input wavelength of $\lambda = 1.55 \mu\text{m}$; however, due to fabrication imperfections, the central wavelength was shifted in simulation to match the response better. The telecommunication wavelength of $1.55 \mu\text{m}$ was chosen based on a large index contrast of usable materials when considering the fabrication and a low loss for the constituent materials at this wavelength. Silicon and silica are also very robust and resistant to oxidation. In an ideal world, the SPs would be manufactured without a base substrate; however, since the structure is on the order of a few wavelengths, from approximately $d = 2.5 \sim 14 \mu\text{m}$, the feasibility of a free-floating SP is experimentally limited. However, the simulations are done solely for an SP. Although the materials have a small amount of absorption, the TMM is calculated based on only the real part of the refractive index. The transmission would drop if absorption were included, but the other parameters are left unaffected.

The first device, CR1, has an angular range of $\theta = 3.5^\circ$, with a compression factor of $R = 3.48$. Figure 4.9 shows the TMM results of the simulation of CR1. The transmission phase is shown in Fig. 4.9(a) over two times the operating angular range of the device. This angular range corresponds to the point that the transverse walk-off should return to zero. Figure 4.9(b) shows a transmittance that remains relatively constant over the working angular, but the area of interest corresponds to spectral peaks seen in Fig. 4.9(c). Since there are eight unit cells, the device should show seven resonant peaks in the transmittance spectrum. Indeed, the device has seven peaks, but only five are shown to highlight the peaks near the design wavelength. Comparing the resonance peaks in transmittance, the

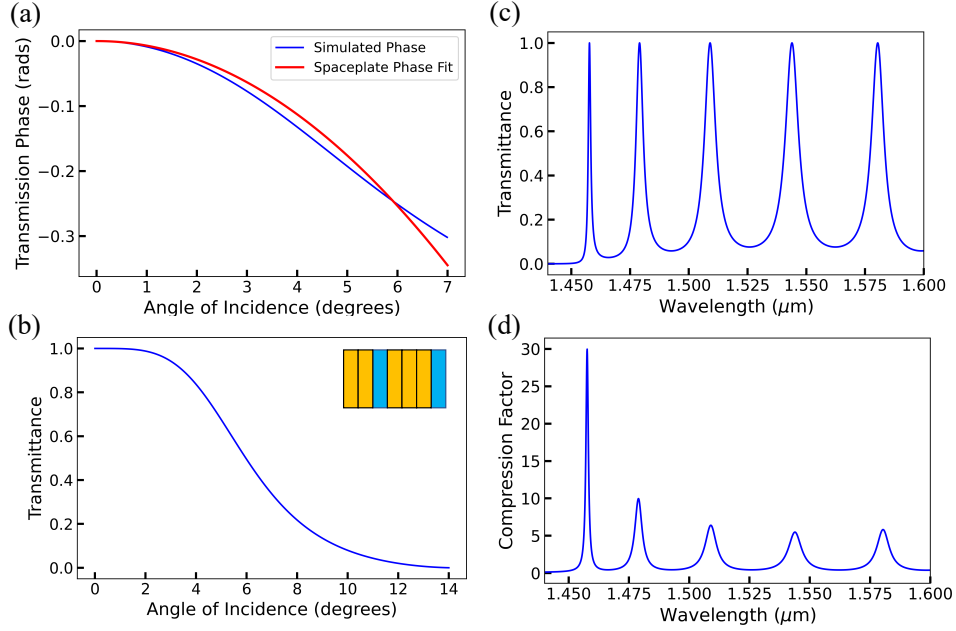


Figure 4.9: **An example of the simulated characterization methods for an SP (CR1) is shown.** (a) shows transmission phase calculated from TMM is plotted in blue and fitted to an ideal SP phase (See. Eq. (4.27)). The device is fit over $\theta = 3.5^\circ$; however, the fit is shown for twice that range. (b) shows the transmittance as a function of angle. The inset in the plot shows the device that is characterized, showing one unit cell comprised of varying layer thicknesses and alternating low/high index. (c) shows the transmittance as a function of wavelength, where five resonance peaks are shown. The unit cell in b) is repeated eight times, resulting in seven peaks in the wavelength dependence of the transmittance; however, only five are shown near the operating range of the laser. The resonance peaks result from coupling because the cavity is formed in the device, and the amount of peaks is governed by $n - 1$ unit cells. (d) shows the corresponding compression factor as a function of wavelength.

compression factor dependence on the wavelength matches well. As the peaks move further from the design wavelength, the other peaks further away show larger compression factors and more narrow bandwidths. The increase in a compression factor is an interference effect; however, the theory that describes this is unclear. More work is needed to understand the scaling of the compression factor and the narrowing of the bandwidth; however, we will take some time to discuss this idea.

The side peaks result from the interference of unit cells with one another. Considering two unit cells, the resonance wavelength shows a certain resonance peak. If we continue to increase to four unit cells, there are new conditions to consider. Four unit cells create three FP cavities that can interact with one another. If there are an odd number of FP cavities, the original resonant wavelength will always be λ_c . Although the sole FP cavity creates the central peak, the sideband peak positions can also be determined using the free spectral range (FSR) calculation for an FP cavity [132, 141]. The FSR is calculated as

$$\Delta\lambda = \frac{\lambda^2}{2n_{\text{eff}}L \cos(\theta)}, \quad (4.42)$$

where λ is the input wavelength, n_{eff} is the effective refractive index of the medium, L is the length of the FP cavity, and θ is the deflection angle. In this case, we will take the angle to be approximately zero. We can find an approximate value for the effective refractive index by a weighted average of the indices in the structure. Let us consider CR1 as an example, with eight unit cells, and define the new FP cavity, its length, and the effective refractive index. This can be done by looking at two unit cells. When considering two unit cells, the structure looks like

$$2L//[H, 3L, H][2L][H, 3L, H] \rightarrow 2L//[H, [3L, H, 2L, H, 3L], H], \quad (4.43)$$

where now the FP cavity is $[3L, H, 2L, H, 3L]$ surround by two high-index mirrors. The effective refractive index would be

$$n_{\text{eff}} = \frac{N_L}{N_{\text{tot}}}n_L + \frac{N_H}{N_{\text{tot}}}n_H, \quad (4.44)$$

where N_L and N_H refer to the number of low or high index layers, respectively. Using the CR1 structure, the effective index is $n_{\text{eff}, \text{CR1}} = 1.95$. To figure out the cavity length, we must consider that each of these layers has a thickness

$$d_i = \frac{\lambda}{4n_i}. \quad (4.45)$$

Thus the total thickness of the FP cavity would be

$$L_{\text{tot}} = (3 + 2 + 3) \left(\frac{\lambda}{4n_L} \right) + 2 \left(\frac{\lambda}{4n_H} \right). \quad (4.46)$$

Substituting the proper values, we find that $L_{\text{tot}} = 2.37 \mu\text{m}$. Now, using $L = L_{\text{tot}}$, and the calculated n_{eff} , we find the FSR of CR2 to be

$$\Delta\lambda_{\text{CR1}} = \frac{1.55^2 \mu\text{m}^2}{2 * (2.37 \mu\text{m}) * 1.95} = .346 \mu\text{m} = 346 \text{ nm}. \quad (4.47)$$

Looking at Fig. 4.9, this FSR calculation matches the spacing of the resonances well. However, calculating the effective refractive index is an estimate and may slightly change the results. Moreover, the spacing could also increase if a very small angle is introduced.

This idea was pushed further to the design CR2, which follows the same philosophy but a more complex structure. Here, a larger compression factor comes with a more stringent angular range. The compression factor predicted for the device is $R = 66.6$, and the angular range is $\theta = \pm 1^\circ$. However, the characterization methods of the device still follow the same procedure as CR1. Figure 4.10 shows the full characterization of CR2, where Fig. 4.10(a) shows the transmission phase over $\theta = 2^\circ$ and relatively constant transmittance over the operating range of the device in Fig. 4.10(b). The transmittance spectrum is shown in Fig. 4.10. Fig. 4.10(c), with three resonant peaks due to four unit cells. Moreover, the compression factor peak positions in Fig. 4.10(d) match well with the resonance peak positions in Fig. 4.10(c).

The spacing can be calculated in a similar fashion. However, the effective index of the medium will change, as well as the FP cavity length. Let us take a look at the 2 unit cell case for CR2. Two unit cells would look like

$$\begin{aligned} & 2L/[H, 3L, H, L, H, 3L, H][2L][H, 3L, H, L, H, 3L, H] \\ \rightarrow & 2L/[H, [3L, H, L, H, 3L, H, 2L, H, 3L, H, L, H, 3L], H]. \end{aligned} \quad (4.48)$$

This configuration based on the methods used in the previous calculation would yield $L_{tot} = 4.99 \mu\text{m}$, and an effective index of $n_{\text{eff}} = 1.99$. Using these values, the FSR for CR2 is found to be

$$\Delta\lambda_{CR2} = \frac{1.55^2 \mu\text{m}}{2 * (4.99 \mu\text{m}) * 1.99} = .120 \mu\text{m} = 120 \text{ nm}. \quad (4.49)$$

The remaining two designs were designed based on gradient descent [139]. These designs show only one resonant peak near the design wavelength. This is likely due to an effective resonant effect over the whole structure rather than cavities and interference between cavities like that in CR1 and CR2. Figure 4.11 shows the results of a 17-layer SP based on gradient descent. Although the optimization was done by Pagé [139], the designs can be simulated through TMM to look at the transmission phase and transmittance. The goal of MS1 was to create a device with a modest compression factor with a larger angular range. The device has shown the largest angular range out of any other device while holding a larger R than the CR1 design.

MS1 was designed to have a compression factor of $R = 18$ and an angular range of $\theta = \pm 10^\circ$. The sidebands of CR1 do reach slightly higher R values but are out of the range of the working laser readily available to test in the experiment. Although the transmittance

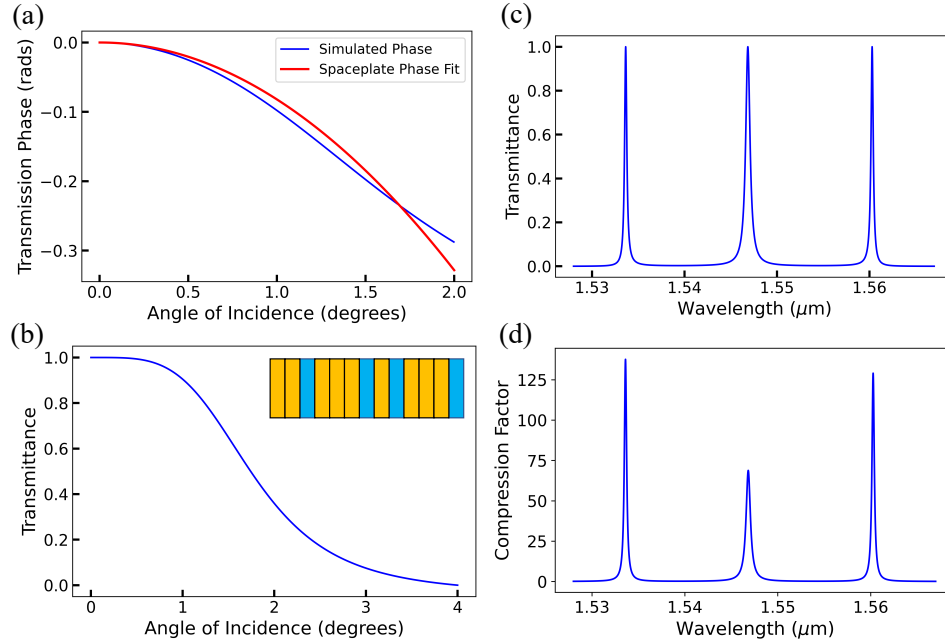


Figure 4.10: An example of the simulated characterization methods for an SP (CR2) is shown. (a) shows the transmission phase calculated from TMM plotted in blue and fitted to an ideal SP phase. The operating angular range of the device is $\theta = \pm 1^\circ$. (b) shows the transmittance as a function of angle. The inset in the plot shows the device that is characterized, showing one unit cell comprised of varying layer thicknesses and alternating low/high index. (c) shows the transmittance as a function of wavelength, where three resonance peaks are shown. The unit cell in (b) is repeated four times, resulting in three peaks in the wavelength dependence of the transmittance. The resonance peaks result from coupling because the cavity is formed in the device, and the amount of peaks is governed by $n - 1$ unit cells. (d) shows the corresponding compression factor as a function of wavelength. The resonant features are more narrow due to a large compression factor.

seems low, as seen in Fig. 4.11(b), it is not zero and still shows transmitted light. This device has much higher transmittance at higher angles of incidence but still rapidly drops at the working angular range of the device. Figure 4.11(c) and (d) show the transmittance and compression factor as a function of wavelength, showing a much larger bandwidth than those seen in the coupled resonator approach.

Moreover, the design was optimized to have a compression factor of 18, but the TMM results predict a value much higher. The reasoning is that the compression factor fits

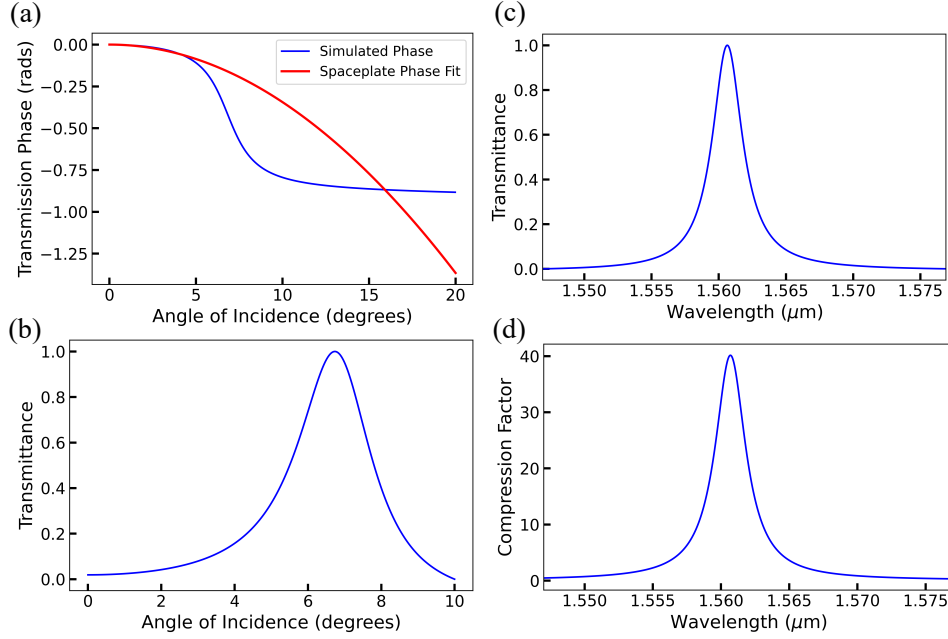


Figure 4.11: **An example of the simulated characterization methods for an SP (MS1) is shown.** (a) shows the transmission phase, TMM in blue, and the ideal SP phase in red. The device is fit over $\theta = 10^\circ$. (b) shows the transmittance as a function of angle. (c) shows the transmittance as a function of wavelength, where one peak with a much larger bandwidth is shown, compared to the central peak of CR1 and CR2. (d) shows the corresponding compression factor as a function of wavelength. The maximum compression factor was found to be $R = 40$, roughly two times the size of the predicted R by gradient descent.

the phase calculated from TMM rather than by gradient descent, which could provide a compression factor more closely related to the compression factor expected near normal incidence rather than the full angular range of the device. This device serves the purpose that larger compression factors are still attainable with large bandwidth and NA, but the devices have to be optimized carefully to find such conditions. However, if the goal is to have large spatial compression without worrying about a large angular range, MS2 is a much higher-performing design.

Figure 4.12 shows the results of a 49-layer SP based on gradient descent. MS2 has a significantly higher compression factor of $R = 238$ but a much more narrow bandwidth and angular range. The operating angular range is $\theta = \pm 1^\circ$, as seen in Fig. 4.12(a). The

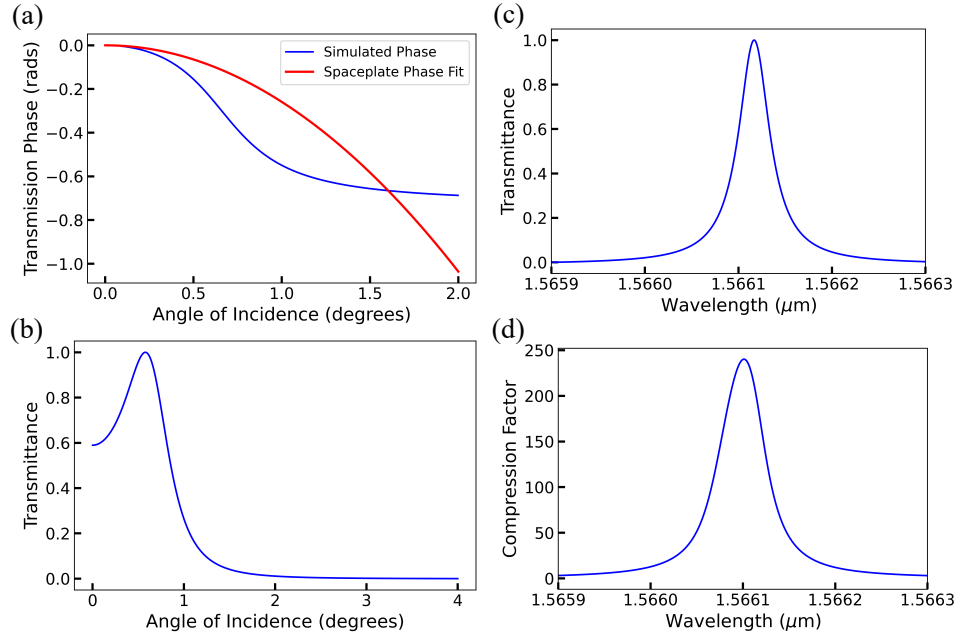


Figure 4.12: **An example of the simulated characterization methods for an SP (MS2) is shown.** (a) shows the transmission phase, TMM in blue, and the ideal SP phase in red. The device is fit over $\theta = 1^\circ$. (b) shows the transmittance as a function of angle. (c) shows the transmittance as a function of wavelength, where one peak with a more narrow bandwidth is shown, compared to CR1 and CR2. (d) shows the corresponding compression factor as a function of wavelength. The maximum compression factor was $R = 238$, matching the predicted R by gradient descent.

transmittance again reaches a maximum at a non-zero angle. However, the transmittance near normal incidence is higher, as seen in Fig. 4.12(b). Figure 4.12(c) and (d) show the transmittance and compression factor with a very narrow resonant peak. This device, however, fits much better regarding the results of the optimization methods of gradient descent and the results of TMM.

Although all these devices were designed to work near $\lambda = 1.55 \mu\text{m}$, the multilayer stack structure supports other resonances in different sections of the EM spectrum. Therefore, we will take some time to show interesting features outside the proposed design wavelength.

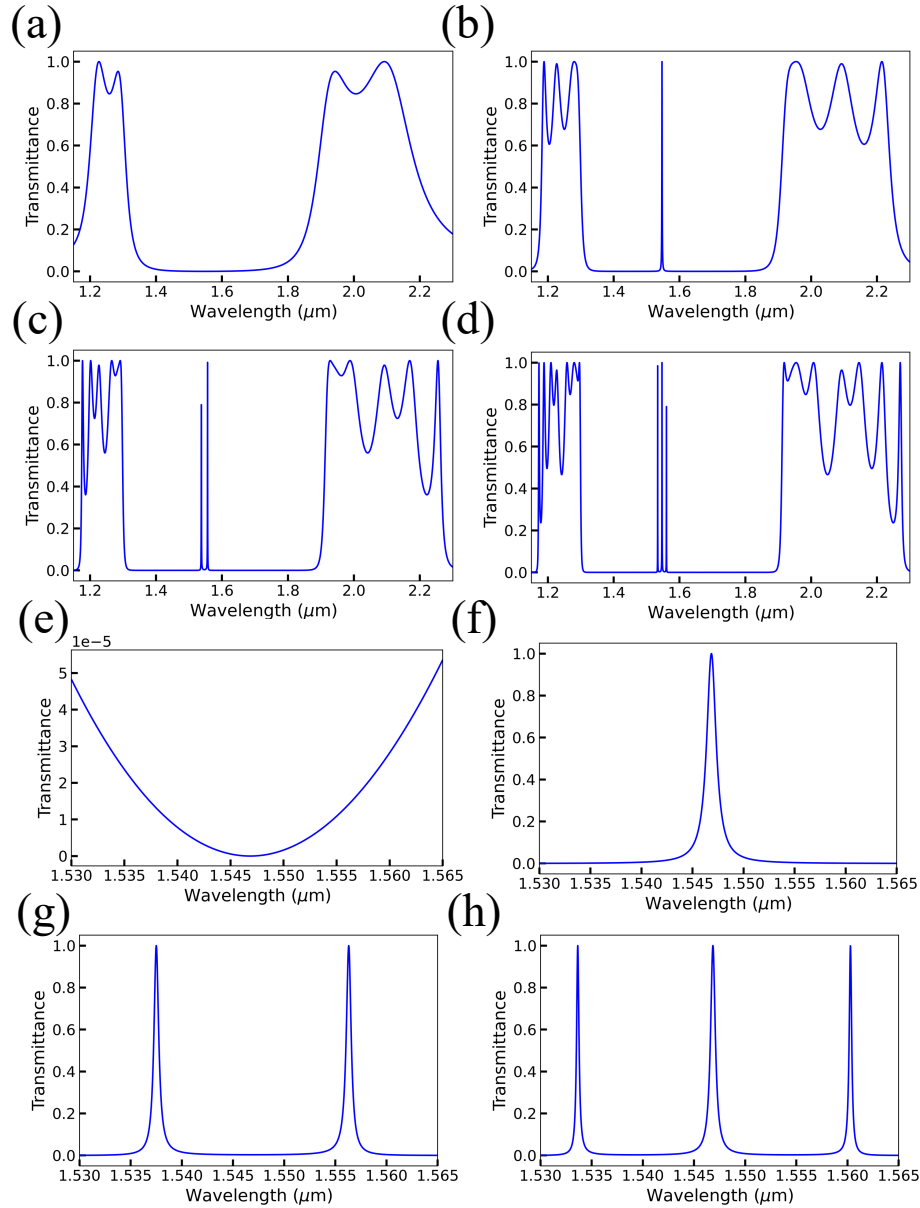


Figure 4.13: **Spectral behaviour when changing the number of unit cells for CR2.** (a)-(d) shows a long range spectral response of CR2 with increasing amount of unit cells from $n = 1$, to $n = 4$. (e)-(h) show only the region near the design wavelength of $\lambda = 1.55 \mu\text{m}$ with an increasing amount of unit cells according to (a) through (d). Peaks present resonance locations according to constructive and destructive interference positions, with the number of peaks determined by $n - 1$ unit cells.

4.4.3 Spectral Response of Devices

Since the coupled resonator designs follow layer thickness as integer multiples of a quarter wave, it is clear that other harmonics of the design wavelength should be supported as well. Let us assume the dispersion is relatively flat for the two constituent materials over a large wavelength range. In reality, dispersion could play a role; however, this investigation is to demonstrate that a device could work elsewhere than expected. CR2 was designed with four unit cells, but the resonant features change depending on the number of unit cells.

As explained before, the amount of peaks near the design wavelength goes at $n - 1$ resonances for n unit cells in Fig. 4.13(a) through (d), the amount of unit cells is incrementally increased from $n = 1$ to $n = 4$. In the region of the $\lambda = 1.55 \mu\text{m}$, the resonances increase as $n - 1$. To stress the idea of the originally Fabry Perot cavity length of $3\lambda/4$, a resonance is seen at 1.5λ in Fig. 4.13(a), corresponding to one unit cell. Figure 4.13(e) through (h) show the zoomed-in response around the design wavelength of CR2. However, one can see that other resonant features are also present as a result of interference of unit cells with lengths of $3\lambda/4$ and $3\lambda/2$. A similar behaviour can be expected in the compression factor but is not shown here. Moreover, CR1 would also have similar behaviour, but the compression factors are lower and add no extra value to the discussion. Therefore, it is understood that one can design multiple resonance structures that work over many different regions, which is more valuable when considering an application to modern-day imaging systems.

Perhaps a more interesting case is regarding the two designs based on gradient descent. Since the structure does not follow a rule of quarter wave thicknesses but thicknesses governed by an optimization method, one may think that other regions over the EM spectrum would not show interesting features. The design is less regular because the layers are not periodically repeated, but any repetition would have exhibited similar effects. However, regardless of repetition, the characteristics of the single resonance feature observed at the design wavelength of $\lambda = 1.55 \mu\text{m}$, like the bandwidth, are reflected in other spectral regions, as in Fig. 4.14.

The devices have an effective dependence on the input wavelength and show resonances at lower and higher wavelength regions. Understanding the positions is likely linked to harmonic positions but for an effective wavelength λ_{eff} , again assuming dispersion is flat. Figure 4.14 shows the proposed design wavelength in Fig. 4.14(a) and (c) for designs MS2 and MS1, respectively, and other resonant features for the devices in Fig. 4.14(b) and (d). The resonant features of MS2 are reflected with very narrow features in Fig. 4.14(b). At the same time, the features in higher and lower wavelengths for MS1 reflect the larger NA and bandwidth of the design wavelength in 4.14(d). Overall, the devices also show

promise in other regions of wavelengths, making them a much more appealing device to applications.

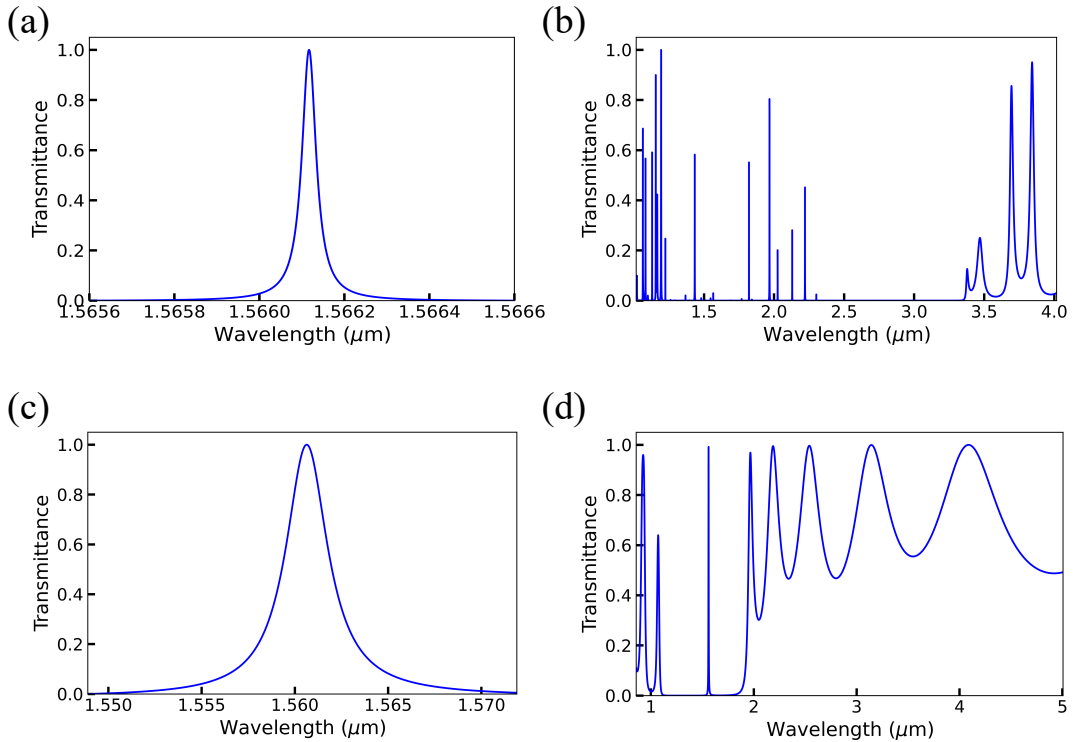


Figure 4.14: **Transmittance for devices MS2 and MS1 are plotted around their design wavelengths and over a larger range. (a) shows the design range of MS2, while (b) shows an extended range with rich, resonant features in lower and higher wavelengths. (c) shows the design range of MS1, while (d) also shows an extended range with rich, resonant features in lower and higher wavelengths, but features are much more narrow than MS1. This reflects the sharp feature seen around the design wavelength.**

These devices have multiple resonant features in transmittance that correspond to points of spatial compression. These resonant features are associated with areas where the phase rapidly changes, impacting how the input light propagates through the material. The implications of sharp features and how they contribute to the group index were discussed in Chapter 1. Therefore, there is merit in discussing how the resonant features of these devices are related to the idea of slow light. Although it was assumed that the dispersion was flat when considering the design of the devices, a key component of SPs is

to imprint a phase equal to that of free space propagation by acting on the wave vectors. Therefore, the dispersion around the features could be flatter and can be discussed as an effective group delay to the light propagating through. As such, we will spend some time discussing the SP effect and its relation to group velocity and dispersion.

4.5 Group Velocity and Group Delay in Spaceplates

The theory behind how the SP is related to group velocity was discussed by Shastri et al. [14]. They showed that the group velocity along the transverse direction, assuming 1D, along x , is manipulated when trying to mimic free space propagation using SPs. If the SP is supposed to change the input light to conserve angle but replace space by imprinting a phase of free space propagation, it is clear that this phase is conserved in another variable. The group delay, and therefore large group index, delays the light long enough to travel a distance in the transverse plane to mimic free space. These types of actions are, of course, limited by physical parameters such as the NA and bandwidth of the devices. All of these constraints must go into a calculation of the group delay to understand how large compression factors can be.

Following the derivation by Shastri et al. [14], let us first suppose the beam is moved by an amount ΔL_x in the transverse plane. This distance is written as

$$\Delta L_x = (d_{\text{eff}} - d) \tan(\alpha), \quad (4.50)$$

where α is the angle with respect to the normal of the surface. The transverse shift L_x can be written as the product of a transverse group velocity v_{gx} and a total time delay τ such that

$$L_x = v_{gx}\tau. \quad (4.51)$$

If we wish to find the difference ΔL_x related to these variables, we need a reference position from which the beam enters, denoted x_0 . Therefore, the beam will be shifted by L_x away from x_0 upon propagation of the device of length d . Another way of writing this is

$$\Delta L_x = (x, z) - (x_0, 0) = (x_0 + L_x, d) - (x_0, 0). \quad (4.52)$$

This invites the use of the group velocity and time delay and takes the form

$$\Delta L_x = v_{gx}\tau - v_{gx}^0\tau^0 = c \sin(\alpha)\tau, \quad (4.53)$$

The initial group velocity is the component of the speed of light along x and set equal to c , assuming the light is in the air before entering the material. The other parameter τ^0

represents the delay as if the wave were to travel the same distance through the background, in this case, air, with the form

$$\tau^0 = \frac{d}{c \cos(\alpha)} = \frac{dn_b}{c_0 \cos(\alpha)}, \quad (4.54)$$

where n_b is in the case of a background refractive index, not in the air.

Here, it is clear that spatial compression is enhanced in two ways. The first is increasing the transverse group velocity, which is limited by an upper bound of the speed of light or by increasing the total time delay with respect to the background. Generally, materials' transverse group velocity decreases, so specific conditions must be met to increase the SP effect. They can also be manipulated for the time delays but pose an interesting point. Time delays τ and τ^0 show importance as their difference limits the bandwidth of the device. The larger the total time delay in the device, the larger the spatial compression experienced, but more narrow bandwidths. This is linked to the delay-bandwidth product, which is conserved. It is the excess time delay that limits the bandwidth, and therefore, it should be stated that the excess time is written as

$$\Delta T = \tau - \tau^0 = \frac{\Delta L_x + (\sin(\alpha) - v_{gx}/c)d \sec(\alpha)}{v_g x}. \quad (4.55)$$

This value should be non-zero and positive to see an SP effect. Using this expression, we can find how the bandwidth is limited regarding the group velocity and the dependence on the NA. It can be seen that the effects of slow light manipulate these devices and, therefore, must be treated carefully.

If we assume that an SP has a maximum angular range α_m , the corresponding transverse shift would be $\Delta L_m = (d_{\text{eff}} - d) \tan(\alpha_m)$. We know that the compression factor $R = d_{\text{eff}}/d$. Furthermore, we can introduce the concept of numerical aperture, defined as

$$NA = n_b \sin(\alpha_m). \quad (4.56)$$

Substituting the compression factor and NA into the excess time delay in Eq. (4.55), we find

$$\Delta T = \frac{d(R \cdot NA/n_b - v_{gx}/c)}{v_g x \sqrt{1 - (NA/n_b)^2}}. \quad (4.57)$$

Formally, the delay-bandwidth product is conserved and follows the relationship

$$\Delta T \Delta \omega \leq \kappa, \quad (4.58)$$

where κ is described by the properties of the structure as a whole. If we want to find the bandwidth of the resonance, consider the central angular frequency ω_c , or corresponding central wavelength λ_c ; the bandwidth of the resonance is written as

$$\Delta\omega = \frac{1}{2\pi} \frac{\kappa\omega_c}{d/\lambda_c} \frac{\sqrt{1 - (NA/n_b)^2} v_{gx}/c}{(R \cdot NA/n_b - v_{gx}/c)}. \quad (4.59)$$

Any excess time delay that is zero or positive up to ΔT will produce an SP effect, but the values are limited based on this value. We can see here that higher-order dispersion directly affects the bandwidth, relating to the group delay. However, it can be written more simply in terms of the transverse group velocity. We can also see that the slow-light effects also affect the NA. Therefore, understanding the dispersion of the materials is crucial in both linear and nonlinear optical systems.

4.6 Summary

In this chapter, we presented four different multilayer stack-based SP designs based on two different design philosophies, coupled resonators, and optimization by gradient descent. We used TMM to calculate the transmission phase as a function angle and wavelength for each device and extract the dependency of the wavelength on the compression factor. We then developed a basic theory to predict the resonance positions, spacing, and bandwidth of the devices.

The coupled resonator approach provided a new avenue to create multi-resonant designs useful for various optical applications, such as an all-optical resonance tuning device or spatial compression of frequency combs. The utility that multilayer stacks could also be relevant to the field of flat optics. The capability of simulating a multilayer stack-based spaceplate's performance using TMM shows it is a fundamental building block of optical design. When integrated with metalenses, SPs show promise to play a key role in creating ultrathin optical systems and will be easily integrated due to their ultrathin size.

In the following chapter, we will experimentally test these devices to realize their performance. The devices' transverse walk-off will be measured and used to extract the compression factor as a function of wavelength. Moreover, the transverse walk-off will allow us to understand the numerical aperture of the device, as well as the bandwidth when looking at the response of compression factor versus wavelength. The capability of using the devices for imaging will also be tested by measuring the focal shifts of the imaging plane. Characterization of the beam quality will also be investigated.

Chapter 5

Experimental Observation of Spatial Compression using Multilayer Stack-Based Spaceplates

In the previous chapter, four spaceplate (SP) designs using multilayer stacks were proposed based on two design philosophies: coupled resonators and gradient descent. These four designs were characterized using the Transfer Matrix Method (TMM) to extract the simulated transmittance and transmission phase dependencies on the wavelength and angle. The transmission phase was then used to investigate the compression factor as a function of wavelength matching the resonance positions of the transmittance spectra. A brief theory was discussed to predict resonance positions and spacing of resonances for the case of coupled resonator SP.

The current chapter, based on the work of Hogan et al. [2], aims to experimentally test the devices studied in Chapter 4 to see the extent of their performance by quantifying their respective compression factors. The transverse walk-off of the four devices is measured and then used to extract the compression factor as a function of wavelength. The transverse walk-off versus angle and compression factor versus wavelength reveal two important quantities: the numerical aperture of the device and the bandwidth, respectively. The viability of its performance is also tested by relaying an image through the SP to show focal retraction. The beam profile is also studied as certain high finesse features in resonant structures can affect the beam quality. With a full depiction of their functionality and the compactness of their design, multilayer stack-based SPs show promise in realizing much smaller modern-day imaging systems, and therefore, we will spend some time motivating them.

5.1 Background

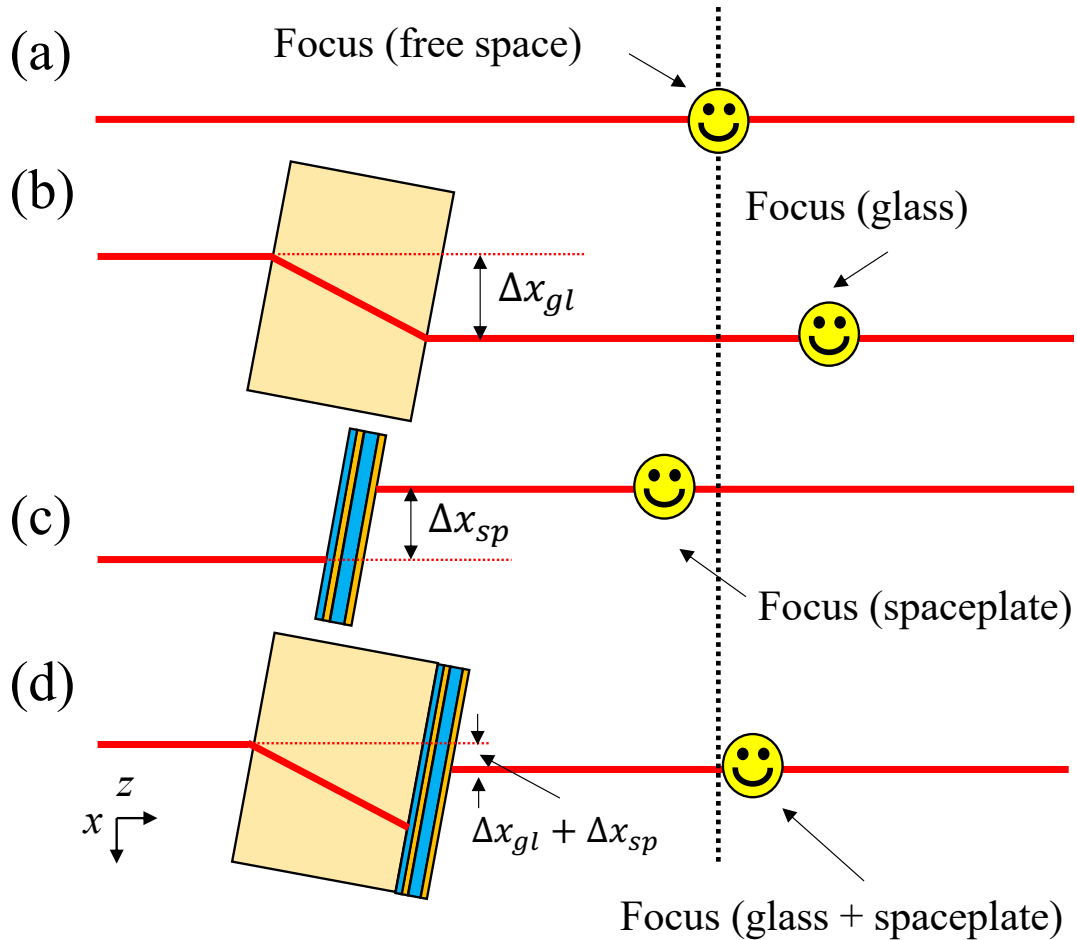


Figure 5.1: **Schematic of beam propagation for three different cases.** A different focal plane is shown in the case of a beam propagating (a) in free space, (b) through a tilted 3-mm long piece of glass, (c) through a tilted 10- μm multilayer stack based SP, and (d) the combined tilted system comprised of the glass and the SP. With respect to the imaging plane of free space, the glass advances the focus and positively shifts the beam to a different transverse position. The focus retracts in the case of the SP, and the beam negatively shifts in the transverse plane. The combined system shows that a 10 μm SP can undo the effects of the glass slide, leading to an unaffected beam.

The growing demand for the miniaturization of optical devices is often limited by the distance needed for an image to come into focus and any operations, like defocusing, hereafter. Several works have utilized meta-lens [142–145] and other optical elements to control the position of the focal plane and then attempts to push towards the realization of flat optics [15, 127, 146–148]. To achieve flat optics, one must be able to mimic the action of standard optics in a spatially compact way. This can be done if the phase of the incoming light field can be fully controlled. As described by Chen et al. [149], the transverse phase of the light field can be controlled by manipulating the electric field on a position-by-position basis. As discussed in Chapter 4, a position-dependent phase response is said to be a local response. While a metalens locally influences the wave vector angle through its position-dependent response, an SP nonlocally influences the transverse position through its angle-dependent response. To realize an ultrathin flat optical system, both a meta-lens and an SP would be required.

In recent years, theoretical studies have examined SPs to understand the physical limits of compressing space [13, 14, 129]. However, an experimental demonstration of those limits is still pending. As we saw in Chapter 4, Reshef et al. [1] tested two prototypical SP designs and showed that using low-index media or uniaxial crystals can achieve spatial compression. The devices exhibit modest spatial compression, but the material index contrast of the constituents limits their performance. However, another design was proposed consisting of alternating high and low indices that show promise of much larger spatial compression. This idea was analyzed theoretically by Chen et al. [13], Pagé et al. [139], as well as Shastri et al. [14] who have shown larger compression factors at the cost of numerical aperture (NA) and device bandwidth. Photonic SPs [129] also exhibit moderate spatial compression and angular range but again suffer from limitations imposed by the optical properties of the materials. The idea of an SP is inspired by earlier works of optical filters that examine the lateral and longitudinal shifts using the group delay as a characteristic metric [7–12]. Although these studies show lateral and longitudinal shifts, the SP effect is not discussed in these works. The SP effect does diminish the amount of space required in optical systems but still needs some space to operate properly in an optical system [84].

As discussed in Chapter 4, it is possible to quantify the performance of these devices in terms of a metric known as the compression factor, R , defined as $R = d_{eff}/d$, where d_{eff} is the effective distance, and d is the device thickness. We can determine the compression factor in one of two ways: 1) by observing a focal shift along propagation ΔF , which moves the focal plane closer to the object, or 2) by observing the transverse walk-off $\Delta x(\theta)$, which shifts the beam transversely as a function of input angle in the opposite direction of the tilt. Figure 5.1(a)-(d) shows the focus advancement/retraction and the transverse walk-off for three different cases, namely a glass slide, an SP, and the two together. Here, we show

pictorially how the effect of a 10 μm SP with a compression factor of $R = 150$ can nearly cancel the effect of a 3 mm glass slide. If we place an SP in an optical system such as a modern camera, we can shrink the imaging system by 3 mm and enable a much more compact system.

5.2 Methodology

5.2.1 Design and Characterization

Recall that for an ideal SP, the transverse walk-off takes the form

$$\Delta x(\theta) = - (R - 1) d \sin(\theta), \quad (5.1)$$

where θ is the angle of incidence. Fitting this expression over small angles allows us to extract R , which is proportional to the slope. However, calculating the transverse walk-off directly from the phase can estimate what to expect from a device.

From Chapter 4, we used TMM to extract the transmittance and phase response of the device as a function of the angle of incidence and input wavelength to simulate the expected response of the compression factor. Figure 5.2 shows the general protocols for characterizing a given device, in this case, CR2. From the dependence of the angle on the phase, one can deduce the angular range of which the device shows spatial compression. Figure 5.2(a) shows the simulated phase as a function of angle in blue and the ideal SP phase in red. The highlighted region in blue in Fig. 5.2(a) shows the range at which the simulated phase is fit to an ideal SP phase. The blue region dictates the operating angular range of the device, which we call the SP region.

We fabricated four devices based on multilayer stacks following the designs in Chapter 4. Two devices were created, inspired by the Fabry-Perot SP proposed by Chen et al. [149] using multiples of integer value quarter-wave thicknesses. One device (CR1) showed moderate spatial compression but a larger angular range and, consequently, a larger bandwidth. Another device (CR2) had much larger spatial compression but a limited angular range and bandwidth. Two other devices, MS1 and MS2, will be tested where MS1 showed moderate spatial compression, sizeable angular range, and MS2, large spatial compression, limited angular range. Devices were all designed to thicknesses of approximately 12 μm or less, except MS1, which was about four times smaller. These devices were fabricated and grown on fused silica of thicknesses $d = 3.03$ mm for CR2, MS1, and MS2, and $d = 2.84$ mm for CR1. Alternating high and low indices comprise silicon ($n_H = 3.196$ at 1550 nm)

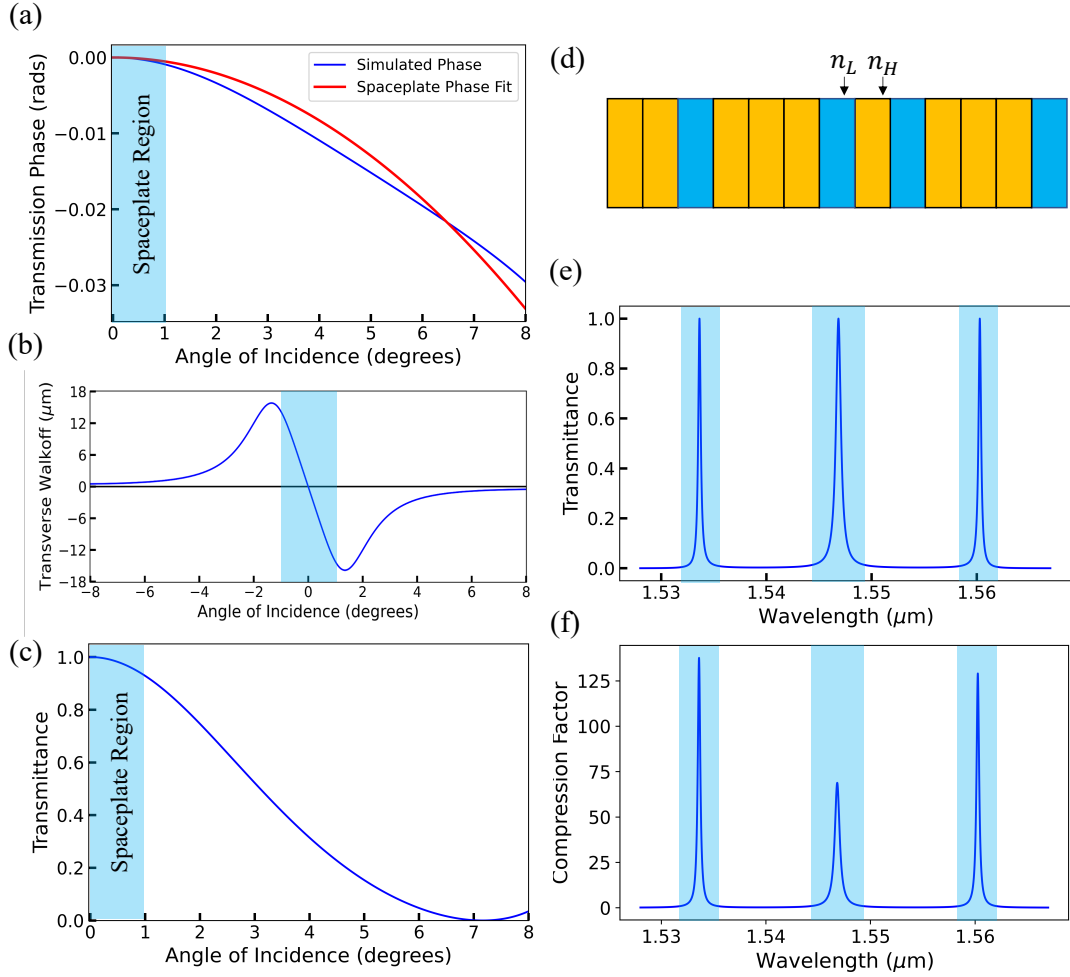


Figure 5.2: **Characterization methods for an SP.** (a) Transmission phase calculated from TMM is plotted in blue and fitted to an ideal SP phase in red. The device is fit over the SP region shown in light blue. (b) Transverse walk-off is calculated from the derivative of the phase in (a). (c) Transmittance as a function of angle is plotted and maximized over the SP region. (d) The corresponding SP multilayer stack unit cell is shown with low (n_L) and high (n_H) refractive indices layers quarter-wave thickness. The device consists of a unit cell repeated four times, creating a coupled resonator-like response with sharp resonances that exhibit larger compression factors. (e) Transmittance as a function of wavelength is plotted, showing three resonance peaks. The number of peaks follows $n - 1$ unit cells. (f) The corresponding compression factor is shown calculated from (b) for various wavelengths.

Device	Unit cell configuration	# of unit cells	Device Length (μm)	Effective device length (μm)	Compression Factor	Angular Range ($^\circ$)
CR1	[2L,H,3L,H]	8	12.57	43.76	3.368	3.5
CR2	[2L,H,3L,H,L,H,3L,H]	4	11.51	767	43.0	1
MS1	Gradient Descent	17*	2.48	44.7	18.0	10
MS2	Gradient Descent	49*	13.42	3196	238.2	1

Table 5.1: **Device parameters for four devices:** CR1 and CR2 comprise integer-valued multiples of quarter-waves for low and high index layers represented as L and H , respectively, and two other devices of an alternating index, with thicknesses determined by gradient descent. The number of unit cells indicates the repetition count of the unit cell. The compression factor denotes the effective to the real device length ratio. The number of layers is indicated with a star for the gradient descent devices. The device’s angular range is also displayed. Note that all devices are quoted for p -polarized light, although s -polarized light exhibits comparable performance in a limited angular range of $\theta_{\text{device}} \leq 10^\circ$.

and silica ($n_L = 1.458$ at 1550 nm), respectively. An anti-reflective coating was placed on the device to minimize reflection and counteract any curvature of the sample due to the stress of the films after growth. The device parameters are summarized in Table 5.1.

Characteristics like the angular and wavelength dependence of the transmittance are necessary to investigate to understand the feasibility of an SP. The wavelength dependence directly links with the structure and order of the layers, so we pictorially show an example of a unit cell for device CR2 in Fig. 5.2(d). Figure 5.2(e) shows the transmittance spectrum for CR2. However, due to fabrication intolerances, the device is centred on $\lambda_{\text{device}} = 1.54685 \mu\text{m}$ rather than 1.550 μm . The compression factor is extracted for each wavelength so to show the spectral response, and this result is plotted in Fig. 5.2(f). As expected from the compression factor as a function of wavelength, the peak positions match with the transmittance in Fig. 5.2(e). Both the bandwidth and resonance positions are in great agreement with those seen in transmittance. The highlighted regions in Fig. 5.2(e) and 5.2(f) show regions of which the compression factor is larger than unity.

Another characterization method for the compression factor is measuring how much the device shifts the focus, i.e., how close the imaging plane is to the object. We show that these devices significantly increase performance compared to the previous experiments [1, 130]. Therefore, multilayer stack-based SPs are key in modern technologies requiring miniaturized imaging systems pushing toward ultrathin monolithic devices. We will now show

the performance of said devices to show their viability and performance. We will now discuss how we experimentally test these devices for their angular range and wavelength dependence, showing trade-offs of spatial compression versus NA and bandwidth.

5.2.2 Experimental Setup

We use a 1.6 mW tunable laser, from 1525 nm to 1630 nm with a resolution of 0.1 picometers, to measure the compression factor of four different SP devices. We couple the laser to a fibre collimator that outputs a collimated beam with a diameter of ~ 7 mm. We then use two *c*-coated plano-convex lenses L_1 and L_2 , with focal lengths $f_1 = 5$ cm and $f_2 = 25$ cm, respectively, to minify the beam by a ratio of $M = -f_1/f_2$, where M is the magnification. We then pass the beam through a quarter-wave plate (QWP) to set a known input polarization state and through a half-wave plate (HWP) and a polarizing beam-splitter (PBS) to control the power. Another set of QWP and HWP is used after the PBS to control the polarization input into the SP, whether it be *s*-polarized, *p*-polarized, right- or left-circularly polarized. We set the input to *p*-polarization, and then the beam is focused onto the sample using a third lens L_3 with focal length $f_3 = 25$ cm. The spot size of the beam is found to be $2w_0 = 310 \mu\text{m}$. The beam size is tuned to be focused to an angular range smaller than the device’s designed angular range, where the angular range is $\theta_{\text{half}} = 0.2^\circ$.

The SP is placed at the focus on a mount that is connected to a rotation stage controlled by a K-cube, as shown in 5.3. The SP is rotated about normal incidence within the device angular range to measure the transverse walk-off. The beam is then re-collimated using another lens L_4 with focal length $f_4 = 10$ cm placed a focal length away from the sample, creating a $4f$ system. Another $4f$ system is created, placing a fifth lens L_5 , of focus length $f_5 = 15$ cm, at a distance $z = f_4 + f_5$ away from L_4 . The beam is focused onto an Indium-Gallium-Arsenide (InGaAs) infrared red charge-coupled device (CCD) camera (Bobcat 320 Gig-E). The CCD camera is placed on a translation stage to image the device in the imaging plane (Fourier plane), allowing measurement of the focal shifted image plane due to an SP. All data were corrected to account for a magnification of $M = 1.48$ due to the $4f$ system of L_5 and L_4 , which increased the transverse walk-off measured at the camera. Imaging measurements in Fig. 5.8, discussed in Sec. 5.3.3, were done by replacing lens L_4 and L_5 with two lenses with focal lengths of $f = 10$ cm, and therefore unity magnification.

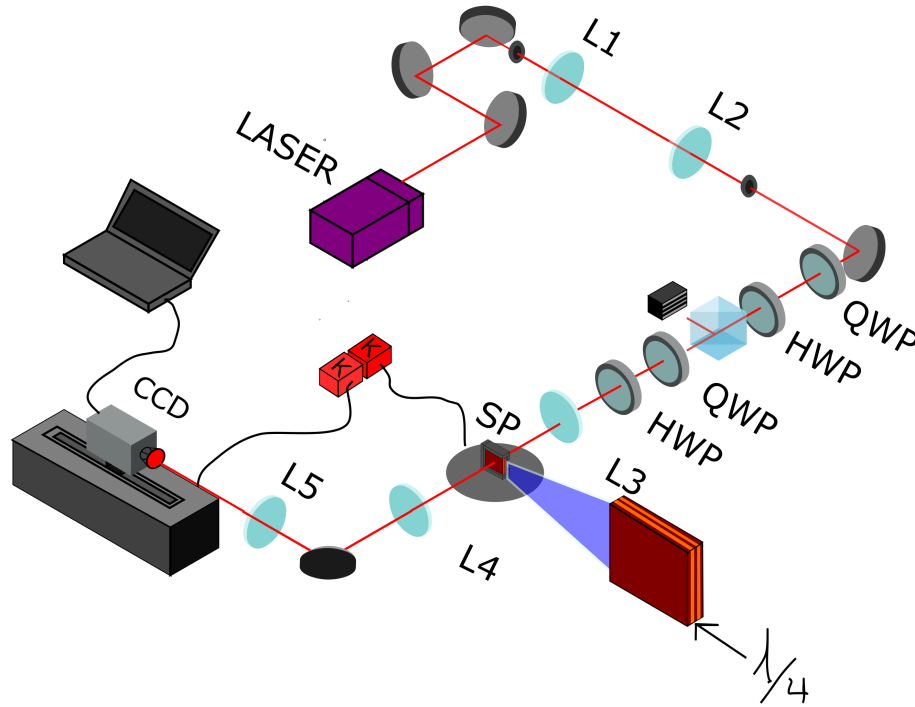


Figure 5.3: **Experimental setup to measure transverse walk-off and focal shifts.**

A 1.6 mW continuous-wave tunable laser at 1550 nm with a spot size of 7 mm is minified by a factor of five by a telescope consisting of two plano-convex lenses L_1 ($f = 25$ cm), and L_2 ($f = 5$ cm). The beam is then sent through a quarter wave plate (QWP) to set the input polarization, followed by a half-wave plate (HWP) and polarizing beam-splitter (PBS) to control the power. The beam is then sent through another QWP, and HWP, set such that p -polarization illuminates the sample. The QWP and HWP can have p - and s -polarization and circular polarization if needed. The beam is then focused by a plano-convex lens L_3 ($f = 25$ cm) down to a spot size of approximately $2w_0 = 310 \mu\text{m}$, with a half angle divergence of $\theta_{\text{half}} = 0.2^\circ$. At the focus, an SP is placed on a rotation mount controlled by a K-cube to measure the transverse walk-off as a function of the angle. The beam is then recollimated by another plano-convex lens L_4 ($f = 10$ cm) and refocused using a plano-convex lens L_5 ($f = 15$ cm) to be imaged on a camera situated on a translation stage with 2.54 cm range of motion, controlled by another k-cube. The imposed magnification was calibrated to be $M = 1.48$, and all measurements were scaled accordingly. Imaging measurements were done by switching L_5 for another plano-convex lens of $f = 10$ cm, imposing unity magnification. The camera is an Indium-Gallium-Arsenide (InGaAs) infrared red charge-coupled device (CCD) camera (Bobcat 320 Gig-E). The camera is placed on the translation stage to measure the beam spot size along the direction of propagation.

5.2.3 Measured Transmittance

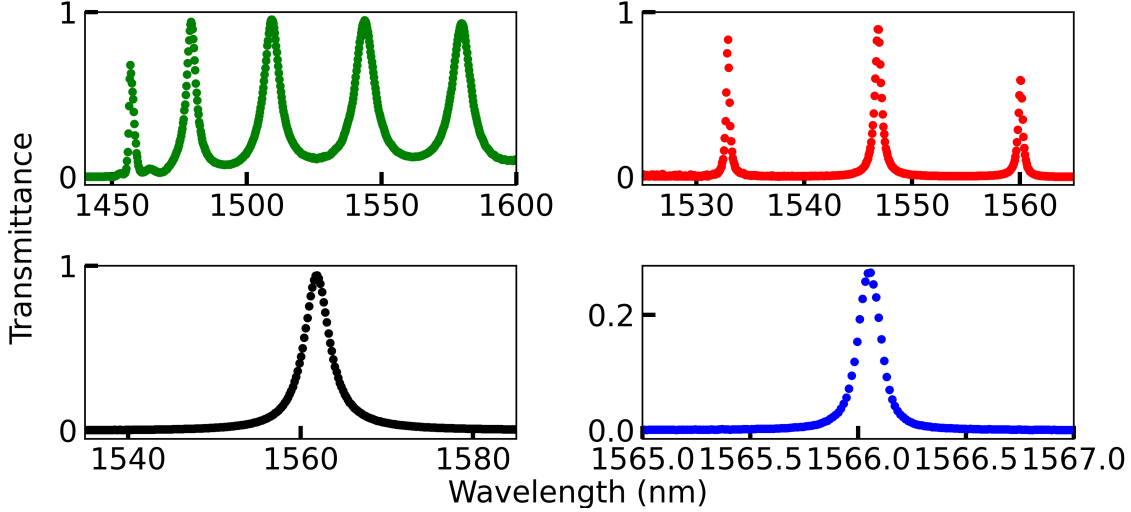


Figure 5.4: **Measured transmittance of four devices.** CR1 and CR2 show side peaks due to multiple resonances based on integer-valued multiples of $\lambda/4$ layer thickness. Devices MS1 and MS2 show one single resonance peak due to layer thickness based on gradient descent. Designs were simulated using the TMM centred at $\lambda_{\text{device}} = 1550$ nm. Fabrication intolerances push the actual central wavelengths λ_m to different locations, where $\lambda_{m,\text{CR1}} \approx 1547$ nm, $\lambda_{m,\text{CR2}} \approx 1531$ nm, $\lambda_{m,\text{MS1}} \approx 1562$ nm, and $\lambda_{m,\text{MS2}} \approx 1566$ nm. Devices were fabricated on top of 3 mm thick fused silica, with an anti-reflective coating on the films to minimize stress and maximize transmission. The lowest transmittance was measured to be approximately 25% at the peak of device MS2. Transmittance peaks correspond to regions of spatial compression, where the magnitude of spatial compression governs the device’s resonance bandwidth and angular range [2].

With most optical elements, high transmittance is important to realize imaging applications. As such, we use TMM to plot the transmittance of the device CR2 as a function of angle, showing high transmittance over the SP region in Fig. 5.2(c). This angular response is plotted for a particular wavelength; however, it is important to note that devices CR1 and CR2 were designed with a quarter-wave condition at $\lambda_{\text{device}} = 1550$ nm. Therefore, the transmittance should also be sensitive to the input wavelength. The measured transmittance of each device is shown in Fig. 5.4. Fabrication intolerances push the actual central wavelengths λ_m to different locations, where $\lambda_{m,\text{CR1}} \approx 1547$ nm, $\lambda_{m,\text{CR2}} \approx 1531$ nm,

$\lambda_{m,MS1} \approx 1562$ nm, and $\lambda_{m,MS2} \approx 1567$ nm. Devices were fabricated on top of 3 mm thick fused silica, with an anti-reflective coating on the films to minimize stress and maximize transmission. The lowest transmittance was measured to be approximately 25% at the peak of device MS2.

Device transmittance was measured for each of the four devices at normal incidence, shown in Fig. 5.3. CR1 and CR2 show multiple sideband peaks centred around their central working wavelength. These sideband peaks result from the quarter-wave thicknesses, representing other resonant wavelengths within these devices. Devices were designed to maximize transmittance, with the lowest transmittance at approximately $T = 0.25$ for MS2. The central wavelength is designed for $\lambda_{\text{device}} = 1550$ nm; however, due to fabrication intolerances, peaks are slightly shifted from the proposed design. The device designs aim to achieve maximum spatial compression near the transmission peaks. The bandwidth seen in the simulation and measured is directly proportional to the bandwidth of the device compression factor.

5.3 Results and Discussion

5.3.1 Angular Dependence of Transverse Walk-off

Often with these devices, it is beneficial to measure the transverse walk-off to extract the compression factor of a given device. Figure 5.5 shows the measured transverse walk-off for a 3 mm thick piece of glass (in blue), an 11.51 μm thick SP (CR2) on top of a 3 mm thick glass (in red), and the 11.51 μm thick SP (CR2) only (in green). The transverse walk-off for the SP alone is calculated by taking the difference of the walk-off measured for SP on glass and the walk-off for glass. The effective distance of the 11.51 μm thick SP completely undoes the effect of a 3 mm piece of glass over an angular range of about 1.5° .

The transverse walk-off serves as a good indicator of the device's performance. Therefore, we experimentally measured the transverse walk-off as a function of the incident angle for four different devices. The designed devices were found to work experimentally within the angular range of $\theta = \pm 1^\circ$ for devices CR2 and MS2, $\theta = \pm 3.5^\circ$ for CR1, and $\theta = \pm 10^\circ$ for MS1.

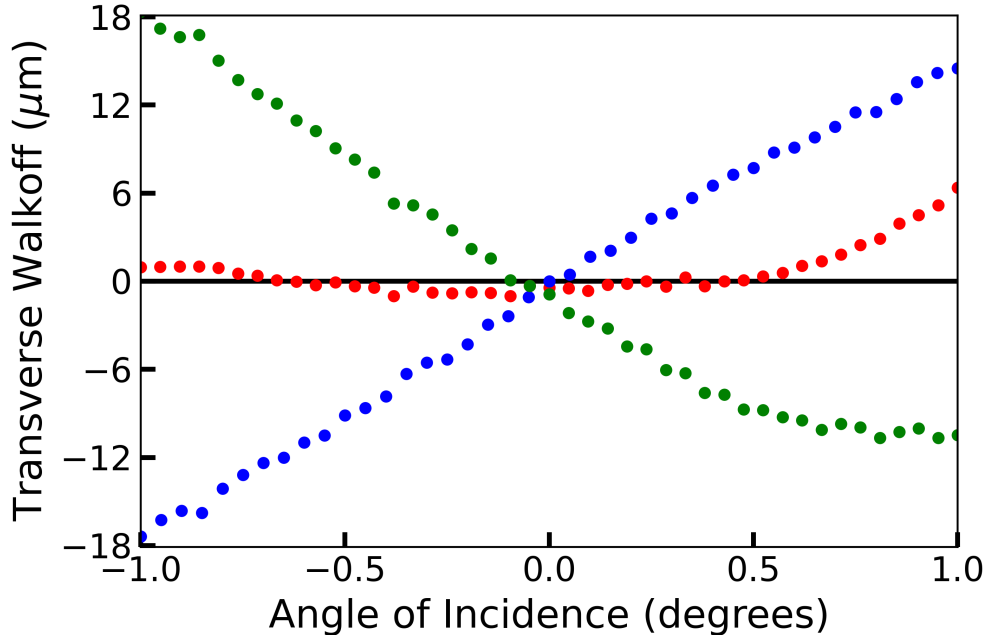


Figure 5.5: Experimentally measured transverse walk-off for glass (blue curve), SP+glass (red curve), and the SP alone (green curve). The result is shown for the device CR2, at an input wavelength of $\lambda = 1532.905$ nm, corresponding to the left peak seen in Fig. 5.2(d). The red curve, associated with an $11.51 \mu\text{m}$ thick SP on top of a 3 mm thick glass, shows no transverse walk-off over an approximately two-degree interval. The red curve shows that the effect of the small SP cancels the walk-off of a large piece of glass.

Figure 5.6(a) shows the angular response of four devices at the peak position in transmittance, where the highlighted zones show the operating range of the device, or SP region, in which the SP effect was designed. A larger negative slope in the transverse walk-off corresponds to a larger compression factor. Figure 5.6(b) shows the angular response of the transverse walk-off for the central position of each of the three resonances measured in the transmittance spectra of CR2, as shown in Fig. 5.4. Side peaks show roughly a factor of two enhancement in the measured compression factor. The physical origin of enhancing the side peaks' compression factor will be studied in future works.

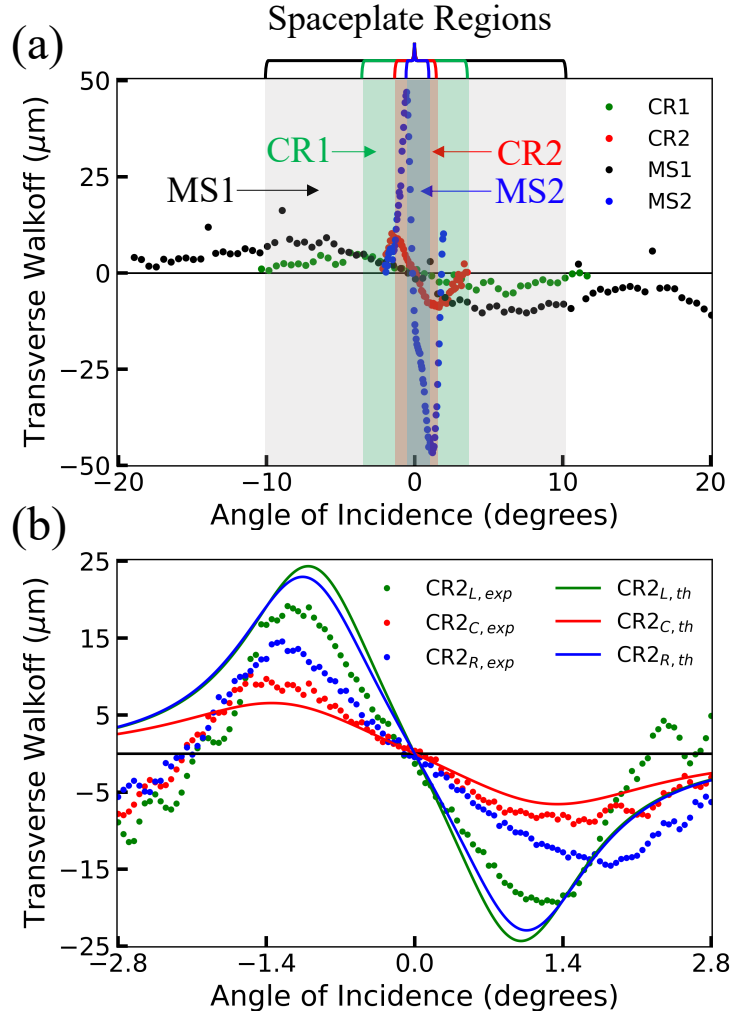


Figure 5.6: **Experimentally measured transverse walk-off for all devices.** Curves show transverse walk-off as a function of angle over a region larger than the SP region of four devices in (a) and different peaks of CR2 in (b). (a) The SP region of $\theta = \pm 1^\circ$ for devices CR2, and MS2, $\theta = \pm 3.5^\circ$ for CR1, and $\theta = \pm 10^\circ$ for devices CR2. Fitting the devices over their respective SP region, maximum compression factors of $R = 176$, $R = 42$, $R = 30$, and $R = 3.4$ are found for the central resonance peaks of devices MS2, CR2, MS1, and CR1, respectively. (b) Angular dependence of the transverse walk-off for the central position of each resonance peak for CR2. The left and right peaks show larger spatial compression than the central, resulting in compression factors of $R_l = 96$, $R_c = 42$, and $R_r = 49$. Simulated transverse walk-off curves are plotted in solid lines, showing good agreement with the experiment. Further study is needed to understand the compression factor scaling with observed side peaks.

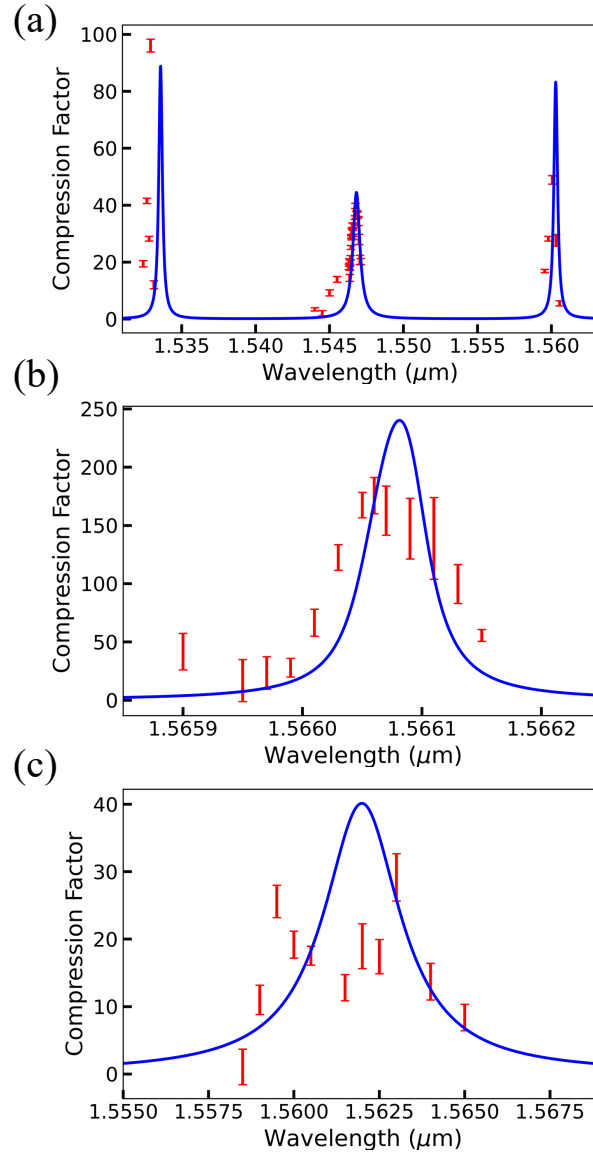


Figure 5.7: **Experimentally measured and simulated wavelength dependence of devices.** (a) The performance of CR2, with the three maximum compression factors, observed to be $R_l = 96 \pm 2$, $R_c = 41.9 \pm 0.6$, and $R_r = 48.6 \pm 1.4$, corresponding to the left, central, and right peaks, respectively. Bandwidths of the peaks are found to be $\Delta\lambda_l = 143 \pm 4$ pm, $\Delta\lambda_c = 282 \pm 6$ pm, and $\Delta\lambda_r = 147 \pm 5$ pm. (b) The performance of MS2, reaching a maximum value of $R = 176 \pm 14$, with a bandwidth of $\Delta\lambda = 55 \pm 7$ pm. (c) The performance of MS1, reaching a maximum value of $R = 30 \pm 3$, with a bandwidth of $\Delta\lambda = 2.8 \pm 0.3$ nm. Experimentally measured compression factors (red) match the simulated results (blue) well for three devices.

5.3.2 Wavelength Dependence of Compression Factor

Since the devices are sensitive to the input wavelength, the amount of transverse walk-off can vary. The transmittance curve correlates to the device's bandwidth, and therefore, the four devices were measured over the resonant wavelengths. We measured the transverse walk-off over the input angle for several input wavelengths and extracted the corresponding compression factor as a function of wavelength. Figure 5.7 shows the wavelength dependence of the top three performing devices, CR2, MS2, and MS1. The experimentally measured points in red are compared to the simulated response plotted in blue, showing good agreement. Furthermore, as predicted by the transmittance curves, the simulated and experimentally measured compression factors of the devices correspond to the predicted resonance positions.

Figure 5.7(a) shows the wavelength response of CR2 containing three resonances. The three maximum compression factors measured for CR2 were $R_l = 96 \pm 2$, $R_c = 41.9 \pm 0.6$, and $R_r = 48.6 \pm 1.4$, corresponding to the left, central, and right peaks, respectively. At the cost of bandwidth, larger compression factors can be achieved. As a result, we found the bandwidths of the three resonances to be $\Delta\lambda_l = 143 \pm 4$ pm, $\Delta\lambda_c = 282 \pm 6$ pm and $\Delta\lambda_r = 147 \pm 5$ pm.

Figure 5.7(b) shows the spectral response of the compression factor for MS2, reaching a maximum compression factor of $R_c = 176 \pm 14$ with a bandwidth of $\Delta\lambda_r = 55 \pm 7$ pm. Similarly, if a larger bandwidth is needed, the compression is smaller in magnitude but extends over a larger wavelength range. The performance of MS1, with a maximum compression factor of $R_c = 30 \pm 3$, with a bandwidth of $\Delta\lambda = 2.8 \pm 0.3$ nm is shown in Fig. 5.7(c).

5.3.3 Focal Retraction and Imaging

One of the interesting functionalities of an SP is to observe a focal retraction of the imaging plane. A focal retraction would mean negative focal shifts of the image plane rather than advancing the focus with most other optics. Figure 5.8(a)-(c) displays the measured beam waists upon propagation along z for free space, SP on glass, and glass, respectively. Experimentally measured points show the beam waists as functions of the z -position, and the solid line indicates the fitted beam waist.

Figure 5.8(d) shows the fitted beam waist evolution of the three cases in (a)-(c) and a predicted beam waist evolution for a free-standing SP. That is, the free space beam waist evolution shifted by an amount ΔF_{sp} calculated by the difference in the focus of glass

and SP on glass. Moreover, an image was propagated through the system, shown in Fig. 5.8(e), highlighting the colour-coded focal positions of the glass, free space, and SP on glass, corresponding to the top, middle and bottom rows, respectively.

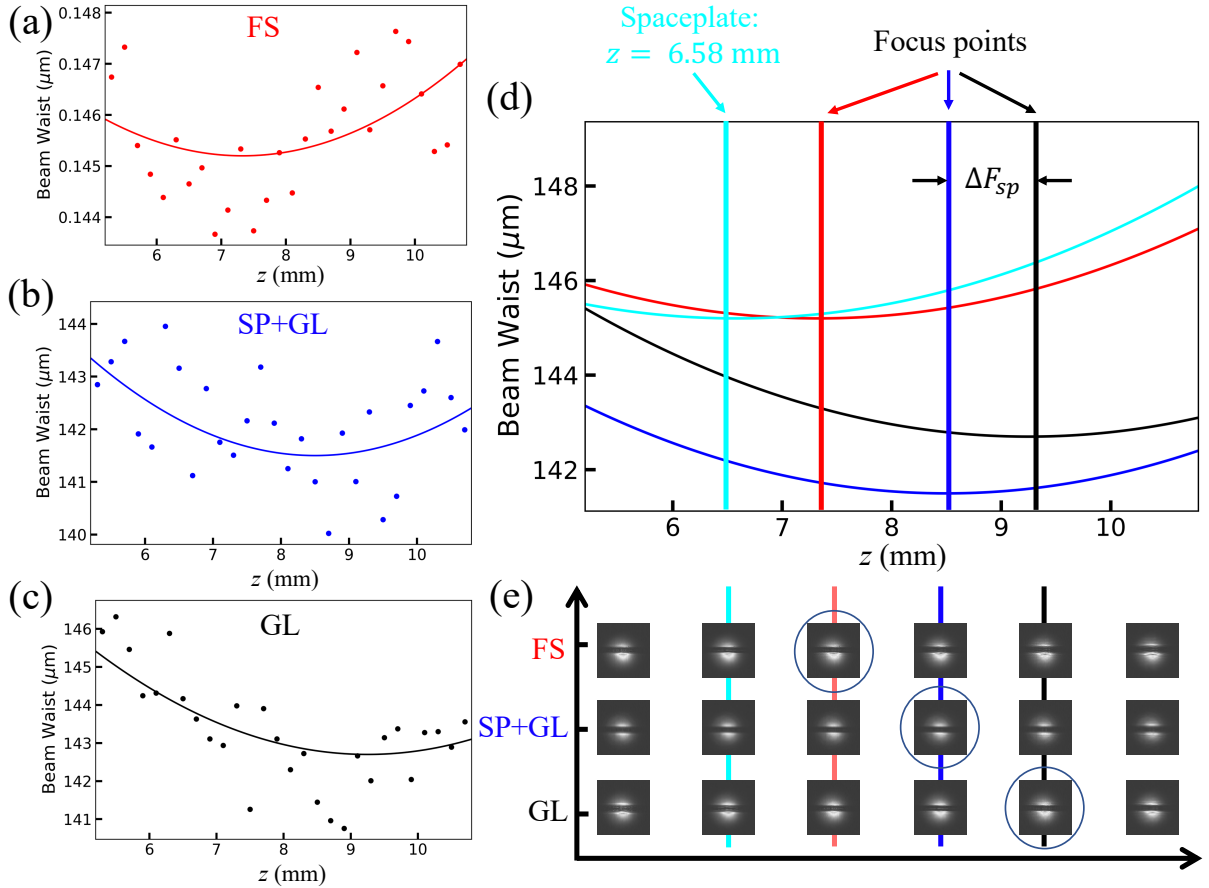


Figure 5.8: **Focal retraction and imaging of an SP.** The beam waist evolution is plotted against the z -position for (a) free space, (b) SP on top of glass, and (c) glass, highlighting the focus points of each. Extracting the beam waists and their positions, we plot the beam waist evolution in (d) for each case (a)-(c), as well as the predicted SP beam waist evolution (cyan). The focal retraction produced by the SP is denoted F_{sp} , from which we plot the predicted SP effect using the free space evolution shifted by F_{sp} . The corresponding images of the measured beam waist are plotted in (e), showing the focus points of each corresponding case. The top row of images is for free space, the middle row is SP on glass, and the bottom row is glass.

Beam Shape Analysis

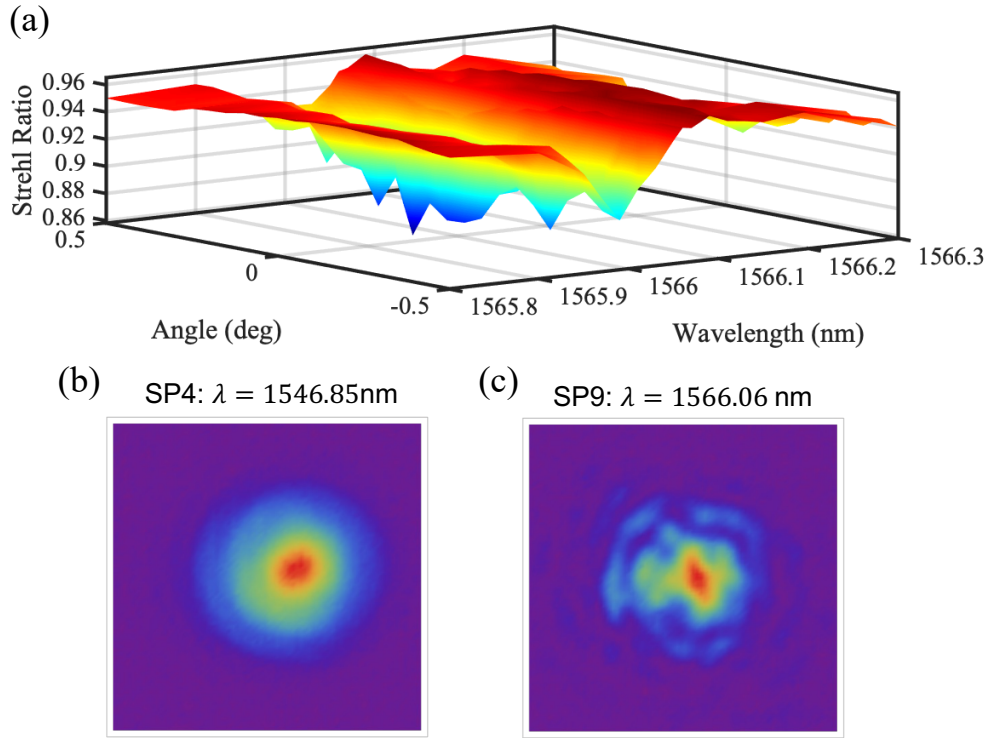


Figure 5.9: **The Strehl ratio of design MS2 and transverse beam profiles for CR2 and MS2.** The Strehl ratio plotted over the SP region of $\theta = \pm 1^\circ$ and over the resonance peak in wavelength in (a). Strehl ratio reached a minimum of $S = 0.86$, above the diffraction-limited threshold of 0.8. (b) and (c) show the transverse beam profile for the peak positions of devices CR2 and MS2 at normal incidence, respectively. The transverse beam profile of CR2 is unaffected, while MS2 shows some distortions in the beam profile. The distortions are likely due to thermal fluctuations that locally change the resonance response.

When an SP exhibits significant compression, the transverse profile of the beam is slightly modified from its original Gaussian profile. The difference in shape is characterized by the Strehl ratio. Since the devices are measured over various angles and wavelengths, the Strehl ratio will also show dependence on these parameters. Figure 5.9 plots the Strehl ratio of our highest performing SP, MS2, over the SP region of $\pm 1^\circ$, and the resonance observed in experimentally measured transmittance in Fig. 5.3.

The Strehl ratio is a metric used to quantify the quality of a beam by examining the residuals of a Gaussian fit. Noting that an imperfect match of the predicted versus ideal SP phase could cause the beam profile to experience distortions in the form of aberrations or other parasitic optical effects. However, in a recent study by Pagé et al. [139], the Strehl ratio is not affected significantly by the oscillation in the phase response.

A beam with a Strehl ratio $S > 0.8$ is diffraction-limited. Therefore, if a device is above this threshold, the beam profile can be considered good and usable for application. Often, with high-performing devices with a large compression factor, the angular range is narrow, and the beam is subject to aberrations. However, the beams passing through the devices of this study did not exhibit significant distortions, except for MS2. The distortions in the beam are likely due to the very narrow linewidth of the resonance. When resonances are sharp, thermal heating can cause the beam to change shape locally due to a shift in the resonance position. However, when the beam is in thermal equilibrium, the beam should travel unaffected. We can quantify how much the transverse beam shape has been modified by using the residuals of a Gaussian beam superimposed. That is,

$$S = e^{-\delta^2}, \quad (5.2)$$

where δ represents the residuals. Fitting the beam to find the residuals, we find that MS2 showed S was no lower than 0.86, which is still reasonably above the diffraction-limited case. The dip in the Strehl ratio is observed around normal incidence and near the resonance peak position corresponding to the position of highest compression. Moreover, the transverse beam shape is also shown for SPs CR2 and MS2 in Fig. 5.9(b) and (c), respectively, showing the distortion of the beam shape. The distortions are likely due to thermal fluctuations that locally change the resonance response.

5.3.4 Full Description of Transverse Walk-off

When investigating the transverse walk-off, one can look at a different representation to further understand how the SPs work. The 3D representation could be used more directly to understand the bandwidth and numerical aperture of a device with a given compression factor, as discussed in the previous chapter. Figure 5.10 shows the transverse walk-off for the CR2, showing the three resonances expected by a device with four unit cells.

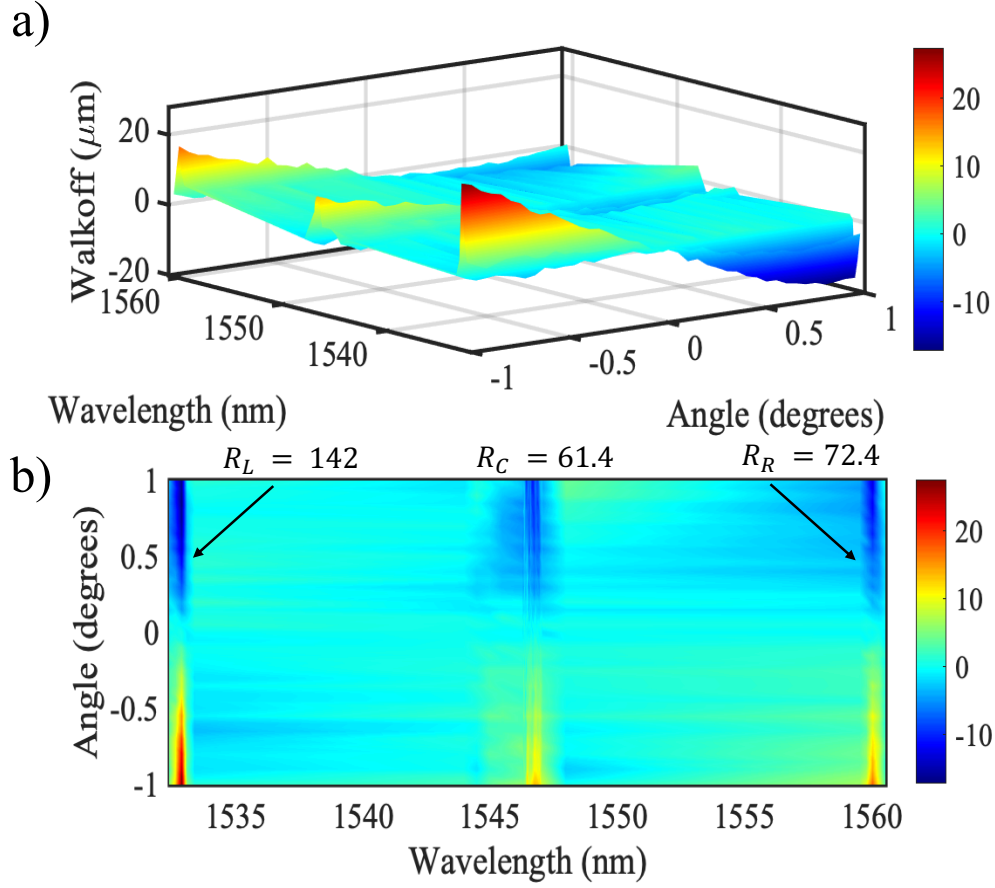


Figure 5.10: **Transverse walk-off spectral and angular response for CR2.** The transverse walk-off is shown for device CR2, highlighting the three resonance peaks resulting from four unit cells. The values Δx and R shown here are not scaled by the magnification and are, therefore, $M = 1.48$ larger than the value measured at the SP. The 3D representation highlights local changes in Δx , possibly due to fabrication intolerances. The spectral response corresponds to the measured linewidth in the compression factor in Fig. 5.7(a).

There is no clear drifting in the response of the resonances for CR2, and the resonance widths match what is shown for the transmittance and compression factor spectral response. Figure 5.11 shows more interesting features in the 3D transverse walk-off representation, where the walk is not linear around normal incidence for device MS2. In the design, the phase response of the device was fit to a global phase evolution rather than the

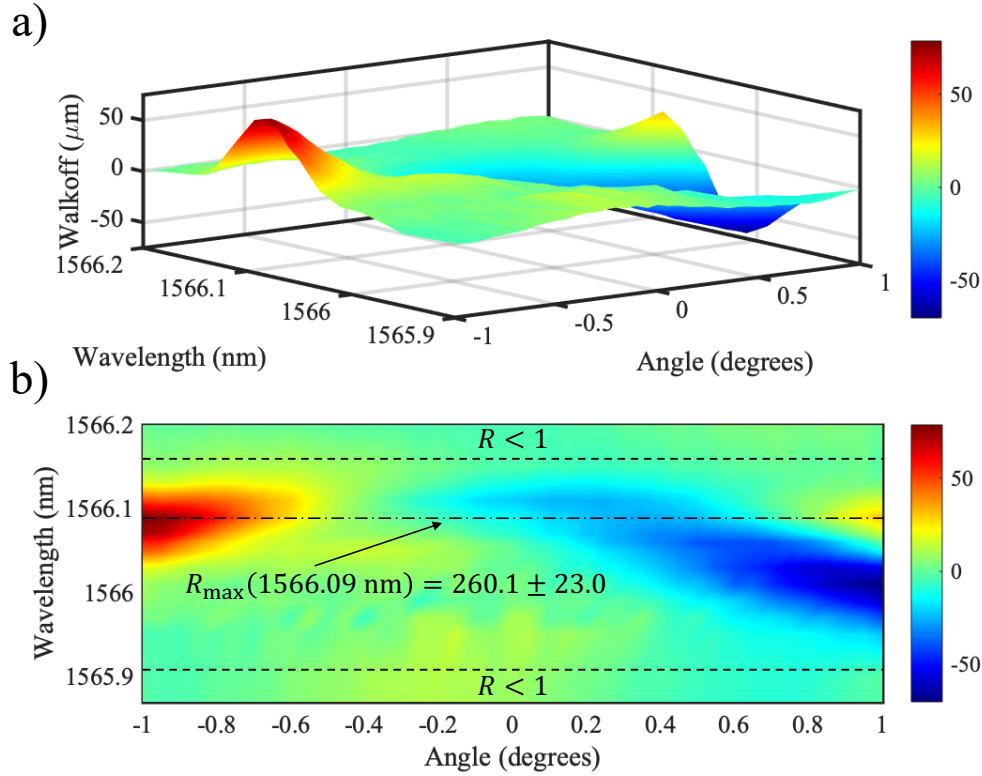


Figure 5.11: **Transverse walk-off spectral and angular response for MS2.** The transverse walk-off is shown for device MS2, highlighting one narrow resonance peak. The values Δx and R shown here are not scaled by the magnification and are, therefore, $M = 1.48$ larger than the value measured at the SP. The 3D representation highlights local changes in Δx , possibly due to fabrication intolerances. However, the design of MS2 has local changes in the phase response as a function of angle, and these are reflected in the transverse walk-off, as expected accordingly to $\Delta x \propto \frac{d\phi}{d\theta}$. The compression factor is measured as a global value over the working range of angles of the device. For a given angle, however, the value of R may be larger or smaller than the global R value. As the value is a global measure, the spectral response corresponds approximately to the measured linewidth in the compression factor in Fig. 5.7(b).

variations in phase [139].

With a very narrow resonance, thermal effects from heating by the laser could locally change the R for a given angle and wavelength but still give a large global compression

factor. This change in phase against a global phase fit for the compression factor could lead to such variation in the transverse walk-off. In any case, the device MS2 shows a large compression factor, which can drastically reduce the propagation distance needed in a modern-day imaging system.

5.4 Summary

In this chapter, we tested the performance of four SP devices based on multilayer stacks to understand the trade-offs between compression factor, bandwidth, and angular range. We found that device CR2 had three maximum compression factors $R_l = 96 \pm 2$, $R_c = 41.9 \pm 0.6$, and $R_r = 49 \pm 1.4$, with corresponding bandwidths $\Delta\lambda_l = 143 \pm 4$ pm, $\Delta\lambda_c = 282 \pm 6$ pm, and $\Delta\lambda_r = 147 \pm 5$ pm over an angular range of $\theta = \pm 1^\circ$. Furthermore, MS2 was the highest performing device with a compression factor of $R_c = 176 \pm 14$, a bandwidth of $\Delta\lambda_r = 55 \pm 7$ pm, and an angular range of $\theta = \pm 1^\circ$. We found that MS1 has a moderate compression factor of $R_c = 30 \pm 3$ with a larger angular range and bandwidth of $\theta = \pm 10^\circ$ and $\Delta\lambda = 2.8 \pm 0.3$ nm, respectively. CR1 was measured for its angular range, showing $\theta = \pm 3.5^\circ$ with low compression factors of roughly $R = 3.5$. We have shown experimentally that multilayer stack-based SPs can drastically increase the compression factor, over 10 times larger than previously reported results. Angular range and bandwidth trade-offs were discussed when designing and measuring high-performance SPs. We further showed that an image could be focally shifted backward according to the compression factor. This work shows that multilayer stack-based SPs will be an integral part of the movement toward the miniaturization of modern-day imaging systems and the realization of flat optics. It is clear that SPs are incredibly useful and can realize functionality that can advance the forefronts of optical and photonic research.

Chapter 6

Conclusion and Outlook

6.1 Conclusion

In this thesis, we have investigated the effects of slow and fast light in a rotating ruby rod and multilayer stack-based spaceplates. Starting from Maxwell's equations, we derived the nonlinear Schrödinger equation (NLSE) that describes light propagation through media, including dispersion and nonlinear effects. We derived an NLSE for a more complex system comprised of a rotating ruby rod to predict the transverse shifts and transverse trajectories at the output of a crystal. The transverse shifts and transverse trajectories were measured and compared with simulations, showing good agreement.

We then took a different approach for the latter chapters, which consisted of slow-light angular devices called spaceplates based on multilayer stacks. Using the Transfer Matrix Method (TMM), we found specific conditions from the amplitude and phase of the light that match the characteristics of free space propagation and, therefore, could spatially compress optical systems. We tested these design results from the TMM in the experiment, and the four designs successfully showed spatial compression, provided with a limited numerical aperture and bandwidth. These two media platforms, i.e. a rotating ruby rod and multilayer stack spaceplates, use dispersive properties that significantly enhance or benefit the light-matter interaction. The dispersive properties, when manipulated precisely, can be incredibly beneficial to the field of optics.

In Chapter 2, "Photon Drag Theory and Nonlinear Propagation," we developed a theory of the nonlinear propagation of light through a rotating ruby rod to model and extract transverse shift and transverse trajectories at the crystal output face. We extended the current linear photon drag theory to nonlinear, as the medium shows an intensity-dependent

group index that seeds the photon drag effect. We then discussed the importance of reference frames and how medium rotation affects optical properties, especially in the case of a birefringent medium. Then, we proceeded to discuss the effects of the nonlinear group index on the propagation equations for o- and e-beams. We provided a theory describing how rotation speed and intensity affect the nonlinear group index and how thermal and optical effects can both contribute, further complicating the trajectories and propagation. We discussed how we used SSFM in the simulations and presented results of the field evolution, the o- and e-beams trajectories, the centre of intensity trajectories, and the transverse shift due to these nonlinear effects. Although the model developed in this chapter focuses primarily on a rotating birefringent nonlinear medium in this thesis, the NLSEs can be easily manipulated to represent other media. The model can also be used to predict which conditions are most favourable for any optical applications, as the rotation speed, intensity, and other physical parameters can be tuned to choose where the beam exits the crystal. Therefore, the model in this chapter shows versatility in both application and fundamental understanding of nonlinear propagation through complex moving media.

In Chapter 3, "Photon Drag, Nonlinear Deflection, and Nonlinear Refraction," we experimentally investigated the system modelled in Chapter 2. By imaging the output facet of a 2 cm long rotating ruby rod, we observed exotic figure-eight-like transverse trajectories following the centre of intensity of two beams in linear ($P_0 = 0.2$ mW), nonlinear ($P_0 = 100$ mW), and highly nonlinear ($P_0 = 520$ mW) regimes. We found that the trajectories became distorted in the presence of an intense beam and transversely shifted from one another based on the intensity and rotation speed. The amount of transverse shift increased with an increase in intensity but reached a maximum transverse shift around a rotation speed of $\Omega = 100$ degs/s. The dynamics were attributed to the coexistence of thermal and optical nonlinear responses affecting a nonlinear group index, which impinged a nonlinear deflection on the beam. The output angle was measured by measuring the transverse shift at two other positions after the crystal, and the output angle was found to be non-zero. The non-zero angle was found as evidence to support the idea of nonlinear deflection from the nonlinear component of the group index. The strength of the nonlinear refraction was estimated and observed also by the formation of the Townes Profile. Experimentally measured transverse shifts and trajectories were found to match well with simulations and support the utility of this system to control the beam propagation for applications such as beam steering.

In the latter two chapters, the focus changed from slow light-enhanced nonlinear optics to designing, characterizing, and testing spaceplates, otherwise known as slow-light angular devices. In Chapter 4, "Theory and Design of Multilayer Stack-Based Spaceplate," we developed a basic theory of spaceplates, distinguishing between the effects of a lens

and a spaceplate. We discussed many types of schemes used to deploy spaceplate effects, promoting the advantages of multilayer stack-based spaceplates, which are focused on in this thesis. We then described how, using the TMM, we could quantify the properties of a multilayer stack, such as the transmission phase and transmittance of a device. We then used the predicted behaviour of the multilayer stacks, particularly the phase response, to mimic the phase upon free space propagation and minimize the working distance needed for images to focus, the main functionality of a spaceplate. We discussed the philosophies of four different designs that show a range of properties from large compression factors and low angular range to moderate compression factors and moderate angular ranges, as well as associated bandwidths. We characterized these four devices and extended this characterization to other spectral regions besides their design wavelength region. We hypothesized a theory to predict the resonance positions and bandwidth of devices. Finally, we discussed the theory of how the device compression factor is related to NA and bandwidth, as well as how the slow light aspect of the device is incorporated, looking at the transverse group velocity and the overall group delay.

Finally, in Chapter 5, "Experimental Observation of Spatial Compression using Multilayer Stack-Based Spaceplates," we experimentally tested the four designed spaceplates from Chapter 4 to understand their performance and ability. The transverse walk-off was measured for each device and used to quantify the compression factor as a function of wavelength. Moreover, the transverse walk-off was used to examine the numerical aperture of the device and understand the working range of each device. The largest compression factor was found to be $R = 176$, which shows a tenfold increase in performance compared to previously measured values in the experiment. The large compression factor and compactness of the design ($d \approx 10 \sim 12 \mu\text{m}$) show great promise for optical research, as these designs are easily integrated into any system. We then tested the imaging capability of the spaceplate by examining the focal retraction and found that, indeed, the focus is moved back as a result of the spaceplate. Spaceplates of this calibre could be designed to be freestanding and mounted similarly to pellicle beamsplitters and therefore do not occupy a large amount of space in an optical setup. Moreover, the spaceplate devices consist of materials that are used widely in fabrication and are not costly, showing their vast applicability. Furthermore, the use of materials like thin films of silicon and silica makes the devices relatively cost and design-effective since there is no need for expensive rare earth elements or intricate structuring of nanoparticles on the surface of the device. Overall, the compactness and utility of the materials show that spaceplates could be suitable for a wide variety of applications, but most importantly in modern-day imaging. Therefore, we will take time to discuss possible applications and follow-up experiments for multilayer stack-based spaceplates, as well as the rotating ruby rod in the context of slow light.

6.2 Outlook

The relevance of slow light in optics still shows promise today. As we have discussed, many optical effects are enhanced with slow light and allow for enhanced light-matter interaction. Although this is particularly useful to nonlinear optics, we have seen that it can be used in linear optical systems to compress space, particularly by introducing a group delay. Manipulating material dispersion and optical properties allows us to have a wide variety of optical effects and applications that were not nearly as accessible without the slow light enhancement. I would like now to highlight a few works that could be interesting follow-ups.

Firstly, we have found that spaceplates have limited bandwidth and NA when the compression factor is large. However, since the material properties can range drastically, the parameter space leaves room for a large numerical aperture device or more broadband devices that may suit other applications better. Moreover, since the spaceplates are built around the idea of resonances, there could be some interesting possibilities for nonlinear experiments. Assuming that the dispersion is relatively flat, with exceptions being the resonant peaks in question, the harmonics of design wavelength for the spaceplates also resonate with the structure and, therefore, would show some degree of spatial compression. We have shown that adding unit cells allows for multiple sideband peaks, and these effects have yet to be studied in other regions of the electromagnetic spectrum. Therefore, studying our spaceplates capability with a different laser at the harmonics or using a sufficiently intense laser to induce higher harmonics could be an interesting experiment.

Moreover, this could be useful in creating a broadband device with a higher numerical aperture at a different design wavelength. Also, since the structures can have a polarization sensitivity when going to larger angles, i.e. the Fresnel coefficients start to differ, they could provide an avenue for polarization-dependent responses and optical effects. One possible idea is to look at polarization rotation, leading to spin-orbit coupling. However, more work should be done on the field within the material and how it relates to the near-field and far-field response.

Another interesting work regarding the nonlinear response of the spaceplate is by substituting the low index layer with an ENZ medium, particularly a material such as ITO [36]. Although the absorption would have to be monitored such that light could propagate the full length of the device, an ENZ medium could give a larger index contrast which would enhance the spaceplate effect. Not only would the ENZ medium be advantageous in boosting the index contrast, but one could exploit the ultrafast nonlinearity to have ultrafast dynamic control of the focal region and, therefore, ultrafast imaging. Moreover, tilting the

structure would lead to different transverse walk-offs and could be used to realize ultrafast 3D imaging.

As for the slow-light enhanced optical effects in the ruby rod, there are other key factors that could merit further study within the system. It was shown that ruby could have a large negative group index, but the effects of nonlinear deflection complicate this measurement. It could be interesting to look at a similar experiment with a pulsed laser to investigate the time dynamics more closely. This helps with studying the Townes profile and the timescales it forms. The Townes profile formation for a continuous-wave laser is also interesting, as often long propagation distances are needed to realize solitons. In the case of our system, the soliton solution forms over the length scale of the ruby crystal, i.e. 2 cm. In either continuous-wave or pulse-laser experiments, the platform could be used to understand the conditions needed for solitons and the conditions where they break or filament.

Another idea based on the response of the ruby rod that could be implemented is an enhancement of four-wave mixing signals. In the case of photonic chips, slow light is used to enhance nonlinear interactions like four-wave mixing. However, this interaction could be extended back to the ruby rod. Since the efficiency of four-wave mixing scales to the fourth power of the slow light factor on-chip and the ruby rod has shown very large group indices, this nonlinear interaction could be very efficient. Moreover, since the sign of the group index is negative, the slow "but fast" light effect could increase the efficiency of backward four-wave mixing, rendering the need to phase match the interaction much less important.

There are many more possibilities when considering slow light, even in these two material platforms considered in this thesis. It is clear that although the media slows down light, the field is not slowing down and, indeed, has much more to explore.

Bibliography

- [1] O. Reshef, M. P. DelMastro, K. K. Bearne, A. H. Alhulaymi, L. Giner, R. W. Boyd, and J. S. Lundeen, “An optic to replace space and its application towards ultra-thin imaging systems,” *Nature communications*, vol. 12, no. 1, pp. 1–8, 2021.
- [2] R. Hogan, Y. Mamchur, D. Hutama, G. Carlow, B. T. Sullivan, O. Reshef, J. Lundeen, and R. W. Boyd, “High compression multilayer stack-based spaceplates,” *TBD*, 2023.
- [3] S. Franke-Arnold, G. Gibson, R. W. Boyd, and M. J. Padgett, “Rotary photon drag enhanced by a slow-light medium,” *Science*, vol. 333, no. 6038, pp. 65–67, 2011.
- [4] A. Safari, C. Selvarajah, J. Evans, J. Upham, and R. W. Boyd, “Strong reverse saturation and fast-light in ruby,” *arXiv preprint arXiv:2301.13300*, 2023.
- [5] R. Hogan, A. Safari, G. Marcucci, B. Braverman, and R. W. Boyd, “Beam deflection and negative drag in a moving nonlinear medium,” *Optica*, vol. 10, no. 5, pp. 544–551, 2023.
- [6] L. Brillouin, *Wave propagation and group velocity*, vol. 8. Academic press, 2013.
- [7] K. D. Hendrix and C. Carniglia, “Path of a beam of light through an optical coating,” *Applied Optics*, vol. 45, no. 11, pp. 2410–2421, 2006.
- [8] M. McGuirk and C. Carniglia, “An angular spectrum representation approach to the goos-hänchen shift,” *JOSA*, vol. 67, no. 1, pp. 103–107, 1977.
- [9] R. Klinger, C. Hulse, C. Carniglia, and R. Sargent, “Beam displacement and distortion effects in narrowband optical thin-film filters,” *Applied optics*, vol. 45, no. 14, pp. 3237–3242, 2006.

- [10] M. Gerken and D. A. Miller, “Limits on the performance of dispersive thin-film stacks,” *Applied Optics*, vol. 44, no. 16, pp. 3349–3357, 2005.
- [11] M. Gerken and D. A. Miller, “Multilayer thin-film structures with high spatial dispersion,” *Applied Optics*, vol. 42, no. 7, pp. 1330–1345, 2003.
- [12] M. Gerken and D. A. Miller, “Relationship between the superprism effect in one-dimensional photonic crystals and spatial dispersion in nonperiodic thin-film stacks,” *Optics letters*, vol. 30, no. 18, pp. 2475–2477, 2005.
- [13] A. Chen and F. Monticone, “Dielectric nonlocal metasurfaces for fully solid-state ultrathin optical systems,” *ACS Photonics*, vol. 8, no. 5, pp. 1439–1447, 2021.
- [14] K. Shastri, O. Reshef, R. W. Boyd, J. S. Lundeen, and F. Monticone, “To what extent can space be compressed? bandwidth limits of spaceplates,” *Optica*, vol. 9, no. 7, pp. 738–745, 2022.
- [15] F. Capasso, “The future and promise of flat optics: a personal perspective,” *Nanophotonics*, vol. 7, no. 6, pp. 953–957, 2018.
- [16] Y. Zhou, M. Z. Alam, M. Karimi, J. Upham, O. Reshef, C. Liu, A. E. Willner, and R. W. Boyd, “Broadband frequency translation through time refraction in an epsilon-near-zero material,” *Nature communications*, vol. 11, no. 1, p. 2180, 2020.
- [17] V. Bruno, S. Vezzoli, C. DeVault, E. Carnemolla, M. Ferrera, A. Boltasseva, V. M. Shalaev, D. Faccio, and M. Clerici, “Broad frequency shift of parametric processes in epsilon-near-zero time-varying media,” *Applied Sciences*, vol. 10, no. 4, p. 1318, 2020.
- [18] E. Galiffi, R. Tirole, S. Yin, H. Li, S. Vezzoli, P. A. Huidobro, M. G. Silveirinha, R. Sapienza, A. Alù, and J. Pendry, “Photonics of time-varying media,” *Advanced Photonics*, vol. 4, no. 1, pp. 014002–014002, 2022.
- [19] R. W. Boyd, *Nonlinear optics*. Academic press, 2020.
- [20] Y. Shen, “Optical second harmonic generation at interfaces,” *Annual Review of Physical Chemistry*, vol. 40, no. 1, pp. 327–350, 1989.
- [21] D. A. Kleinman, “Theory of second harmonic generation of light,” *Physical Review*, vol. 128, no. 4, p. 1761, 1962.

- [22] J. C. Howell, R. S. Bennink, S. J. Bentley, and R. W. Boyd, “Realization of the einstein-podolsky-rosen paradox using momentum-and position-entangled photons from spontaneous parametric down conversion,” *Physical review letters*, vol. 92, no. 21, p. 210403, 2004.
- [23] C. Couteau, “Spontaneous parametric down-conversion,” *Contemporary Physics*, vol. 59, no. 3, pp. 291–304, 2018.
- [24] M. Bass, P. Franken, J. Ward, and G. Weinreich, “Optical rectification,” *Physical Review Letters*, vol. 9, no. 11, p. 446, 1962.
- [25] S. L. Chuang, S. Schmitt-Rink, B. I. Greene, P. N. Saeta, and A. F. Levi, “Optical rectification at semiconductor surfaces,” *Physical review letters*, vol. 68, no. 1, p. 102, 1992.
- [26] R. Stolen and A. Ashkin, “Optical kerr effect in glass waveguide,” *Applied Physics Letters*, vol. 22, no. 6, pp. 294–296, 1973.
- [27] P. Ho and R. Alfano, “Optical kerr effect in liquids,” *Physical Review A*, vol. 20, no. 5, p. 2170, 1979.
- [28] R. L. Abrams and R. C. Lind, “Degenerate four-wave mixing in absorbing media,” *Optics letters*, vol. 2, no. 4, pp. 94–96, 1978.
- [29] L. Deng, E. W. Hagley, J. Wen, M. Trippenbach, Y. Band, P. S. Julienne, J. Simsarian, K. Helmerson, S. Rolston, and W. D. Phillips, “Four-wave mixing with matter waves,” *Nature*, vol. 398, no. 6724, pp. 218–220, 1999.
- [30] M. Lippitz, M. A. van Dijk, and M. Orrit, “Third-harmonic generation from single gold nanoparticles,” *Nano letters*, vol. 5, no. 4, pp. 799–802, 2005.
- [31] S.-Y. Hong, J. I. Dadap, N. Petrone, P.-C. Yeh, J. Hone, and R. M. Osgood Jr, “Optical third-harmonic generation in graphene,” *Physical Review X*, vol. 3, no. 2, p. 021014, 2013.
- [32] D. N. Christodoulides, I. C. Khoo, G. J. Salamo, G. I. Stegeman, and E. W. Van Stryland, “Nonlinear refraction and absorption: mechanisms and magnitudes,” *Advances in Optics and Photonics*, vol. 2, no. 1, pp. 60–200, 2010.
- [33] R. Adair, L. Chase, and S. A. Payne, “Nonlinear refractive index of optical crystals,” *Physical Review B*, vol. 39, no. 5, p. 3337, 1989.

- [34] C. J. Joshi and P. B. Corkum, “Interactions of ultra-intense laser light with matter,” *Physics Today*, vol. 48, no. 1, pp. 36–44, 1995.
- [35] L. Caspani, R. Kaipurath, M. Clerici, M. Ferrera, T. Roger, J. Kim, N. Kinsey, M. Pietrzyk, A. Di Falco, V. M. Shalaev, *et al.*, “Enhanced nonlinear refractive index in ϵ -near-zero materials,” *Physical review letters*, vol. 116, no. 23, p. 233901, 2016.
- [36] M. Z. Alam, I. De Leon, and R. W. Boyd, “Large optical nonlinearity of indium tin oxide in its epsilon-near-zero region,” *Science*, vol. 352, no. 6287, pp. 795–797, 2016.
- [37] O. Reshef, E. Giese, M. Z. Alam, I. De Leon, J. Upham, and R. W. Boyd, “Beyond the perturbative description of the nonlinear optical response of low-index materials,” *Optics letters*, vol. 42, no. 16, pp. 3225–3228, 2017.
- [38] F. Zernike and J. E. Midwinter, *Applied nonlinear optics*. Courier Corporation, 2006.
- [39] D. S. Hum and M. M. Fejer, “Quasi-phasematching,” *Comptes Rendus Physique*, vol. 8, no. 2, pp. 180–198, 2007.
- [40] W. Zhang, H. Yu, H. Wu, and P. S. Halasyamani, “Phase-matching in nonlinear optical compounds: a materials perspective,” *Chemistry of Materials*, vol. 29, no. 7, pp. 2655–2668, 2017.
- [41] J. H. Marburger, “Self-focusing: theory,” *Progress in quantum electronics*, vol. 4, pp. 35–110, 1975.
- [42] P. Kelley, “Self-focusing of optical beams,” *Physical Review Letters*, vol. 15, no. 26, p. 1005, 1965.
- [43] R. DeSalvo, D. J. Hagan, M. Sheik-Bahae, G. Stegeman, E. W. Van Stryland, and H. Vanherzeele, “Self-focusing and self-defocusing by cascaded second-order effects in ktp,” *Optics letters*, vol. 17, no. 1, pp. 28–30, 1992.
- [44] G. Swartzlander Jr, D. Andersen, J. Regan, H. Yin, and A. Kaplan, “Spatial dark-soliton stripes and grids in self-defocusing materials,” *Physical review letters*, vol. 66, no. 12, p. 1583, 1991.
- [45] A. Couairon and A. Mysyrowicz, “Femtosecond filamentation in transparent media,” *Physics reports*, vol. 441, no. 2-4, pp. 47–189, 2007.
- [46] S. L. Chin, *Femtosecond laser filamentation*, vol. 55. Springer, 2010.

- [47] A. Braun, G. Korn, X. Liu, D. Du, J. Squier, and G. Mourou, “Self-channeling of high-peak-power femtosecond laser pulses in air,” *Optics letters*, vol. 20, no. 1, pp. 73–75, 1995.
- [48] T. Herr, V. Brasch, J. Jost, I. Mirgorodskiy, G. Lihachev, M. Gorodetsky, and T. Kippenberg, “Mode spectrum and temporal soliton formation in optical microresonators,” *Physical review letters*, vol. 113, no. 12, p. 123901, 2014.
- [49] K. Moll, A. L. Gaeta, and G. Fibich, “Self-similar optical wave collapse: observation of the townes profile,” *Physical review letters*, vol. 90, no. 20, p. 203902, 2003.
- [50] S. M. Hernández, J. Bonetti, N. Linale, D. F. Grosz, and P. I. Fierens, “Soliton solutions and self-steepening in the photon-conserving nonlinear schrödinger equation,” *Waves in Random and Complex Media*, pp. 1–17, 2020.
- [51] B. Gu, W. Ji, and X.-Q. Huang, “Analytical expression for femtosecond-pulsed z scans on instantaneous nonlinearity,” *Applied optics*, vol. 47, no. 9, pp. 1187–1192, 2008.
- [52] R. Hellwarth, A. Owyong, and N. George, “Origin of the nonlinear refractive index of liquid ccl₄,” *Physical Review A*, vol. 4, no. 6, p. 2342, 1971.
- [53] M. Sheik-Bahae and M. P. Hasselbeck, “Third-order optical nonlinearities,” *Handbook of Optics*, vol. 4, pp. 16–1, 2000.
- [54] G. Agarwal, T. N. Dey, and S. Menon, “Knob for changing light propagation from subluminal to superluminal,” *Physical Review A*, vol. 64, no. 5, p. 053809, 2001.
- [55] D. Bortman-Arbiv, A. Wilson-Gordon, and H. Friedmann, “Phase control of group velocity: from subluminal to superluminal light propagation,” *Physical Review A*, vol. 63, no. 4, p. 043818, 2001.
- [56] M. Mahmoudi, M. Sahrai, and H. Tajalli, “Subluminal and superluminal light propagation via interference of incoherent pump fields,” *Physics Letters A*, vol. 357, no. 1, pp. 66–71, 2006.
- [57] D. F. Eaton, “Nonlinear optical materials,” *Science*, vol. 253, no. 5017, pp. 281–287, 1991.
- [58] A. Robinson, A. Arefiev, and V. Khudik, “The effect of superluminal phase velocity on electron acceleration in a powerful electromagnetic wave,” *Physics of plasmas*, vol. 22, no. 8, p. 083114, 2015.

- [59] G. Agrawal, *Nonlinear Fiber Optics (Fifth Edition)*. Academic Press, 2013.
- [60] C. Banerjee, Y. Solomons, A. N. Black, G. Marcucci, D. Eger, N. Davidson, O. Firstenberg, and R. W. Boyd, “Anomalous optical drag,” *Physical review research*, vol. 4, no. 3, p. 033124, 2022.
- [61] P. Hemmer, N. Bigelow, D. Katz, M. Shahriar, L. DeSalvo, and R. Bonifacio, “Self-organization, broken symmetry, and lasing in an atomic vapor: The interdependence of gratings and gain,” *Physical review letters*, vol. 77, no. 8, p. 1468, 1996.
- [62] R. Hogan, G. Marcucci, A. Safari, N. A. Black, B. Braverman, J. Upham, and R. W. Boyd, “Modelling nonlinear propagation effects on beam deflection and negative drag,” *TBD*, 2023.
- [63] M. M. Kash, V. A. Sautenkov, A. S. Zibrov, L. Hollberg, G. R. Welch, M. D. Lukin, Y. Rostovtsev, E. S. Fry, and M. O. Scully, “Ultraslow group velocity and enhanced nonlinear optical effects in a coherently driven hot atomic gas,” *Physical Review Letters*, vol. 82, no. 26, p. 5229, 1999.
- [64] R. Zimmermann and M. Hartmann, “Resonant and off-resonant light–matter interaction in semiconductors kinetics and transients,” *physica status solidi (b)*, vol. 150, no. 2, pp. 365–378, 1988.
- [65] P. Siddons, N. C. Bell, Y. Cai, C. S. Adams, and I. G. Hughes, “A gigahertz-bandwidth atomic probe based on the slow-light faraday effect,” *Nature Photonics*, vol. 3, no. 4, pp. 225–229, 2009.
- [66] A. Akulshin, S. Barreiro, and A. Lezama, “Electromagnetically induced absorption and transparency due to resonant two-field excitation of quasidegenerate levels in rb vapor,” *Physical Review A*, vol. 57, no. 4, p. 2996, 1998.
- [67] J. C. Camparo and J. G. Coffer, “Conversion of laser phase noise to amplitude noise in a resonant atomic vapor: The role of laser linewidth,” *Physical Review A*, vol. 59, no. 1, p. 728, 1999.
- [68] M. Notomi, K. Yamada, A. Shinya, J. Takahashi, C. Takahashi, and I. Yokohama, “Extremely large group-velocity dispersion of line-defect waveguides in photonic crystal slabs,” *Physical review letters*, vol. 87, no. 25, p. 253902, 2001.
- [69] M. N. Armenise, C. E. Campanella, C. Ciminelli, F. Dell’Olio, and V. M. Passaro, “Phononic and photonic band gap structures: modelling and applications,” *Physics Procedia*, vol. 3, no. 1, pp. 357–364, 2010.

- [70] M. S. Bigelow, N. N. Lepeshkin, and R. W. Boyd, “Observation of ultraslow light propagation in a ruby crystal at room temperature,” *Physical review letters*, vol. 90, no. 11, p. 113903, 2003.
- [71] A. L. Schawlow and C. H. Townes, “Infrared and optical masers,” *Physical Review*, vol. 112, no. 6, p. 1940, 1958.
- [72] T. Kushida, “Absorption spectrum of optically pumped ruby i. experimental studies of spectrum in excited states,” *Journal of the Physical Society of Japan*, vol. 21, no. 7, pp. 1331–1341, 1966.
- [73] A. Linz Jr and R. Newnham, “Ultraviolet absorption spectra in ruby,” *Physical Review*, vol. 123, no. 2, p. 500, 1961.
- [74] E. Hinkley and C. Freed, “Direct observation of the lorentzian line shape as limited by quantum phase noise in a laser above threshold,” *Physical Review Letters*, vol. 23, no. 6, p. 277, 1969.
- [75] R. d. L. Kronig, “On the theory of dispersion of x-rays,” *Josa*, vol. 12, no. 6, pp. 547–557, 1926.
- [76] H. A. Kramers, “La diffusion de la lumiere par les atomes,” in *Atti Cong. Intern. Fisica (Transactions of Volta Centenary Congress) Como*, vol. 2, pp. 545–557, 1927.
- [77] M. Sheik-Bahae, “Nonlinear optics basics. kramers-kronig relations in nonlinear optics,” *Encyclopedia of modern optics*, pp. 234–239, 2005.
- [78] L. Kador, “Kramers–kronig relations in nonlinear optics,” *Applied physics letters*, vol. 66, no. 22, pp. 2938–2939, 1995.
- [79] M. Erhard, R. Fickler, M. Krenn, and A. Zeilinger, “Twisted photons: new quantum perspectives in high dimensions,” *Light: Science & Applications*, vol. 7, no. 3, pp. 17146–17146, 2018.
- [80] K. Wynne, “Causality and the nature of information,” *Optics communications*, vol. 209, no. 1-3, pp. 85–100, 2002.
- [81] M. F. Yanik and S. Fan, “Stopping light all optically,” *Physical review letters*, vol. 92, no. 8, p. 083901, 2004.
- [82] M. F. Yanik and S. Fan, “Stopping and storing light coherently,” *Physical review A*, vol. 71, no. 1, p. 013803, 2005.

- [83] O. Kocharovskaya, Y. Rostovtsev, and M. O. Scully, “Stopping light via hot atoms,” *Physical review letters*, vol. 86, no. 4, p. 628, 2001.
- [84] D. A. Miller, “Why optics needs thickness,” *Science*, vol. 379, no. 6627, pp. 41–45, 2023.
- [85] C. Monat, B. Corcoran, M. Ebnali-Heidari, C. Grillet, B. J. Eggleton, T. P. White, L. O’Faolain, and T. F. Krauss, “Slow light enhancement of nonlinear effects in silicon engineered photonic crystal waveguides,” *Optics express*, vol. 17, no. 4, pp. 2944–2953, 2009.
- [86] B. Tang, L. Dai, and C. Jiang, “Electromagnetically induced transparency in hybrid plasmonic-dielectric system,” *Optics express*, vol. 19, no. 2, pp. 628–637, 2011.
- [87] A. Safari, I. De Leon, M. Mirhosseini, O. S. Magaña-Loaiza, and R. W. Boyd, “Light-drag enhancement by a highly dispersive rubidium vapor,” *Physical review letters*, vol. 116, no. 1, p. 013601, 2016.
- [88] G. Piredda and R. W. Boyd, “Slow light by means of coherent population oscillations: laser linewidth effects,” *Journal of the European Optical Society-Rapid Publications*, vol. 2, 2007.
- [89] G. M. Gehring, A. Schweinsberg, C. Barsi, N. Kostinski, and R. W. Boyd, “Observation of backward pulse propagation through a medium with a negative group velocity,” *Science*, vol. 312, no. 5775, pp. 895–897, 2006.
- [90] A. Fresnel, “Lettre d’augustin fresnel à françois arago sur l’influence du mouvement terrestre dans quelques phénomènes d’optique.,” *Annales de Chimie et de Physique*, vol. 9, pp. 57–66; 286, 1818.
- [91] M. Fizeau, “*xxxii*. on the effect of the motion of a body upon the velocity with which it is traversed by light,” *The London, Edinburgh, and Dublin Philosophical Magazine and Journal of Science*, vol. 19, no. 127, pp. 245–260, 1860.
- [92] U. Leonhardt and P. Piwnicki, “Slow light in moving media,” *Journal of Modern Optics*, vol. 48, no. 6, pp. 977–988, 2001.
- [93] S. Kubo, D. Mori, and T. Baba, “Low-group-velocity and low-dispersion slow light in photonic crystal waveguides,” *Optics letters*, vol. 32, no. 20, pp. 2981–2983, 2007.

- [94] M. S. Bigelow, N. N. Lepeshkin, and R. W. Boyd, “Superluminal and slow light propagation in a room-temperature solid,” *Science*, vol. 301, no. 5630, pp. 200–202, 2003.
- [95] K. Suzuki and T. Baba, “Nonlinear light propagation in chalcogenide photonic crystal slow light waveguides,” *Optics express*, vol. 18, no. 25, pp. 26675–26685, 2010.
- [96] I. Carusotto, M. Artoni, G. C. La Rocca, and F. Bassani, “Transverse fresnel-fizeau drag effects in strongly dispersive media,” *Phys. Rev. A*, vol. 68, p. 063819, 2003.
- [97] L. Boccia, I. Russo, G. Amendola, and G. Di Massa, “Tunable frequency-selective surfaces for beam-steering applications,” *Electronics letters*, vol. 45, no. 24, pp. 1213–1215, 2009.
- [98] Y. Zhou, *Optical communication with structured photons propagating through dynamic, aberrating media*. University of Rochester, 2021.
- [99] J.-Q. Gong, H.-G. Zhan, D.-Z. Liu, *et al.*, “A review on polarization information in the remote sensing detection,” *Spectroscopy and Spectral Analysis*, vol. 30, no. 4, pp. 1088–1095, 2010.
- [100] R. D. Allen, J. Brault, and R. D. Moore, “A new method of polarization microscopic analysis: I. scanning with a birefringence detection system,” *The Journal of cell biology*, vol. 18, no. 2, pp. 223–235, 1963.
- [101] R. Y. Chiao, E. Garmire, and C. H. Townes, “Self-trapping of optical beams,” *Physical Review Letters*, vol. 13, no. 15, p. 479, 1964.
- [102] C. Conti, M. Peccianti, and G. Assanto, “Spatial solitons and modulational instability in the presence of large birefringence: The case of highly nonlocal liquid crystals,” *Physical Review E*, vol. 72, no. 6, p. 066614, 2005.
- [103] A. Hasegawa, “An historical review of application of optical solitons for high speed communications,” *Chaos: An Interdisciplinary Journal of Nonlinear Science*, vol. 10, no. 3, pp. 475–485, 2000.
- [104] M. J. Ablowitz, G. Biondini, and L. A. Ostrovsky, “Optical solitons: perspectives and applications,” *Chaos: An Interdisciplinary Journal of Nonlinear Science*, vol. 10, no. 3, pp. 471–474, 2000.

- [105] A. Safari, I. De Leon, M. Mirhosseini, O. S. Magaña-Loaiza, and R. W. Boyd, “Light-drag enhancement by a highly dispersive rubidium vapor,” *Phys. Rev. Lett.*, vol. 116, no. 1, p. 013601, 2016.
- [106] H. H. Kusuma, B. Astuti, and Z. Ibrahim, “Absorption and emission properties of ruby (cr: Al₂O₃) single crystal,” in *Journal of Physics: Conference Series*, vol. 1170, p. 012054, IOP Publishing, 2019.
- [107] H. K. Lee and S. S. Lee, “Measurements of the anisotropic nonlinear refractive-index coefficients of ruby,” *Optics letters*, vol. 15, no. 1, pp. 54–56, 1990.
- [108] L. Cerdán, R. Weigand, J. M. Guerra Pérez, and H. Crespo, “A simple experiment on slow light in ruby,” *American Journal of Physics*, vol. 76, no. 9, pp. 826–832, 2008.
- [109] Q. Yang, J. T. Seo, B. Tabibi, and H. Wang, “Slow light and superluminality in kerr media without a pump,” *Physical review letters*, vol. 95, no. 6, p. 063902, 2005.
- [110] E. Wisniewski-Barker, G. M. Gibson, S. Franke-Arnold, Z. Shi, P. Narum, R. W. Boyd, and M. J. Padgett, “Experimental investigation of the transient dynamics of slow light in ruby,” *New Journal of Physics*, vol. 16, no. 12, p. 123054, 2014.
- [111] T. Catunda, J. P. Andreetta, and J. C. Castro, “Differential interferometric technique for the measurement of the nonlinear index of refraction of ruby and gdalo 3: Cr+3,” *Applied optics*, vol. 25, no. 14, pp. 2391–2395, 1986.
- [112] S. Kumari and A. Khare, “Studies on nonlinear response of epitaxial ruby thin film,” *IEEE Journal of Quantum Electronics*, vol. 50, no. 8, pp. 645–650, 2014.
- [113] S. Boothroyd, J. Chrostowski, and M. O’Sullivan, “Determination of the phase of the complex nonlinear refractive index by transient two-wave mixing in saturable absorbers,” *Optics letters*, vol. 14, no. 17, pp. 946–948, 1989.
- [114] G. R. Fowles, *Introduction to modern optics*. Courier Corporation, 1989.
- [115] J. Vieira, F. Fiúza, L. Silva, M. Tzoufras, and W. Mori, “Onset of self-steepening of intense laser pulses in plasmas,” *New Journal of Physics*, vol. 12, no. 4, p. 045025, 2010.
- [116] S. Doiron and A. Haché, “Time evolution of reflective thermal lenses and measurement of thermal diffusivity in bulk solids,” *Applied optics*, vol. 43, no. 21, pp. 4250–4253, 2004.

- [117] G. Marcucci, D. Pierangeli, S. Gentilini, N. Ghofraniha, Z. Chen, and C. Conti, “Optical spatial shock waves in nonlocal nonlinear media,” *Advances in Physics: X*, vol. 4, no. 1, p. 1662733, 2019.
- [118] M. I. Davidzon, “Newton’s law of cooling and its interpretation,” *International journal of heat and mass transfer*, vol. 55, no. 21-22, pp. 5397–5402, 2012.
- [119] B. S. Kumar, A. Ng, K. Yoshihara, and A. De Ruiter, “Differential drag as a means of spacecraft formation control,” *IEEE Transactions on Aerospace and Electronic Systems*, vol. 47, no. 2, pp. 1125–1135, 2011.
- [120] I. Golub, “Beam deflection and ultrafast angular scanning by a time-varying optically induced prism,” *Optics communications*, vol. 94, no. 1-3, pp. 143–146, 1992.
- [121] J. Leach, A. Wright, J. Götte, J. Girkin, L. Allen, S. Franke-Arnold, S. Barnett, and M. Padgett, ““aether drag” and moving images,” *Physical review letters*, vol. 100, no. 15, p. 153902, 2008.
- [122] R. J. Adrian, “Twenty years of particle image velocimetry,” *Experiments in fluids*, vol. 39, pp. 159–169, 2005.
- [123] J. De Oliveira, M. A. de Moura, J. M. Hickmann, and A. Gomes, “Self-steepening of optical pulses in dispersive media,” *JOSA B*, vol. 9, no. 11, pp. 2025–2027, 1992.
- [124] S. Taravati, “Giant linear nonreciprocity, zero reflection, and zero band gap in equilibrated space-time-varying media,” *Physical Review Applied*, vol. 9, no. 6, p. 064012, 2018.
- [125] C. Caloz, A. Alu, S. Tretyakov, D. Sounas, K. Achouri, and Z.-L. Deck-Léger, “Electromagnetic nonreciprocity,” *Physical Review Applied*, vol. 10, no. 4, p. 047001, 2018.
- [126] S. Manipatruni, J. T. Robinson, and M. Lipson, “Optical nonreciprocity in optomechanical structures,” *Physical review letters*, vol. 102, no. 21, p. 213903, 2009.
- [127] N. Yu and F. Capasso, “Flat optics with designer metasurfaces,” *Nature materials*, vol. 13, no. 2, pp. 139–150, 2014.
- [128] W. T. Chen, A. Y. Zhu, and F. Capasso, “Flat optics with dispersion-engineered metasurfaces,” *Nature Reviews Materials*, vol. 5, no. 8, pp. 604–620, 2020.
- [129] C. Guo, H. Wang, and S. Fan, “Squeeze free space with nonlocal flat optics,” *Optica*, vol. 7, no. 9, pp. 1133–1138, 2020.

- [130] N. J. Sorensen, M. T. Weil, and J. S. Lundeen, “Large-scale optical compression of free-space using an experimental three-lens spaceplate,” *arXiv preprint arXiv:2302.04295*, 2023.
- [131] K. Shastri and F. Monticone, “Nonlocal flat optics,” *Nature Photonics*, vol. 17, no. 1, pp. 36–47, 2023.
- [132] E. Hecht, *Optics*. Pearson Education India, 2012.
- [133] J. R. Gagnon, O. Reshef, D. H. Espinosa, M. Z. Alam, D. I. Vulis, E. N. Knall, J. Upham, Y. Li, K. Dolgaleva, E. Mazur, *et al.*, “Relaxed phase-matching constraints in zero-index waveguides,” *Physical Review Letters*, vol. 128, no. 20, p. 203902, 2022.
- [134] J. Sastry and M. Munjal, “A transfer matrix approach for evaluation of the response of a multi-layer infinite plate to a two-dimensional pressure excitation,” *Journal of sound and vibration*, vol. 182, no. 1, pp. 109–128, 1995.
- [135] R. Aylo, G. Nehmetallah, H. Li, and P. P. Banerjee, “Multilayer periodic and random metamaterial structures: analysis and applications,” *IEEE Access*, vol. 2, pp. 437–450, 2014.
- [136] Z.-Y. Li and L.-L. Lin, “Photonic band structures solved by a plane-wave-based transfer-matrix method,” *Physical Review E*, vol. 67, no. 4, p. 046607, 2003.
- [137] M. Born and E. Wolf, *Principles of optics: electromagnetic theory of propagation, interference and diffraction of light*. Elsevier, 2013.
- [138] S. Q. Duntley, “The optical properties of diffusing materials,” *JOSA*, vol. 32, no. 2, pp. 61–70, 1942.
- [139] J. T. Pagé, O. Reshef, R. W. Boyd, and J. S. Lundeen, “Designing high-performance propagation-compressing spaceplates using thin-film multilayer stacks,” *Optics Express*, vol. 30, no. 2, pp. 2197–2205, 2022.
- [140] R. Paschotta, “Bragg mirrors,” *Encyclopedia of Laser Physics and Technology*, 2009.
- [141] N. Ismail, C. C. Kores, D. Geskus, and M. Pollnau, “Fabry-pérot resonator: spectral line shapes, generic and related airy distributions, linewidths, finesses, and performance at low or frequency-dependent reflectivity,” *Optics express*, vol. 24, no. 15, pp. 16366–16389, 2016.

- [142] W. Liu, H. Cheng, J. Tian, and S. Chen, “Diffractive metalens: from fundamentals, practical applications to current trends,” *Advances in Physics: X*, vol. 5, no. 1, p. 1742584, 2020.
- [143] S.-W. Moon, Y. Kim, G. Yoon, and J. Rho, “Recent progress on ultrathin metalenses for flat optics,” *Iscience*, vol. 23, no. 12, p. 101877, 2020.
- [144] B. Li, W. Piyawattanametha, and Z. Qiu, “Metalens-based miniaturized optical systems,” *Micromachines*, vol. 10, no. 5, p. 310, 2019.
- [145] M. Y. Shalaginov, S. An, F. Yang, P. Su, D. Lyzwa, A. M. Agarwal, H. Zhang, J. Hu, and T. Gu, “Single-element diffraction-limited fisheye metalens,” *Nano Letters*, vol. 20, no. 10, pp. 7429–7437, 2020.
- [146] Y. Zhou, H. Zheng, I. I. Kravchenko, and J. Valentine, “Flat optics for image differentiation,” *Nature Photonics*, vol. 14, no. 5, pp. 316–323, 2020.
- [147] S. Banerji, M. Meem, A. Majumder, F. G. Vasquez, B. Sensale-Rodriguez, and R. Menon, “Imaging with flat optics: metalenses or diffractive lenses?,” *Optica*, vol. 6, no. 6, pp. 805–810, 2019.
- [148] S. Colburn, A. Zhan, E. Bayati, J. Whitehead, A. Ryou, L. Huang, and A. Majumdar, “Broadband transparent and cmos-compatible flat optics with silicon nitride metasurfaces,” *Optical Materials Express*, vol. 8, no. 8, pp. 2330–2344, 2018.
- [149] W. T. Chen, A. Y. Zhu, V. Sanjeev, M. Khorasaninejad, Z. Shi, E. Lee, and F. Capasso, “A broadband achromatic metalens for focusing and imaging in the visible,” *Nature nanotechnology*, vol. 13, no. 3, pp. 220–226, 2018.